Scalable techniques for graphene on glass

PhD Thesis
at the

ICFO- Institut de Ciències Fotòniques, Castelldefels
Corning Incorporated, New York
and the
Universitat Politècnica de Catalunya, Barcelona

presented by

Miriam Marchena Martín-Francés

Supervisor: Prof. Dr. Valerio Pruneri

June 14th, 2018

ICFO The Institute of Photonic Sciences
UPC UNIVERSITAT POLITÈCNICA DE CATALUNYA BARCELONATECH
CORNING

… A mis padres
y mi hermana

Acknowledgments

I consider it my privilege to acknowledge the help, assistance and support of the many individuals without whom this thesis would not have been possible.

First of all, I would like to express my gratitude to my thesis supervisor Prof. Valerio Pruneri for giving me the opportunity to do the PhD here, for his support and ideas and also for allowing me to work closely and to do an internship in Corning Incorporated.

I would like also to thank people from Corning Incorporated, especially to Robert Lee for accepting me to perform the internship during four months there and for dealing with all the formalities. It was an exceptional experience - in both a professional and personal sense - where I felt very comfortable and completely supported by all of you. The success of my work there would have not been possible without many of you. Firstly, I would like to thank my lab mate Fred for all your support and help in the lab but also for the nice discussions and jokes. Secondly, to Therese: for your supervision and your nice and close attitude to me. Thirdly, to Benedict: I really enjoyed talking to you about science, politics and life :) - I hope that the next time we can share a delicious paella! And finally, to Prantik: a very important professional reference, but also a friend. I have really enjoyed the scientific discussions with you since your first visit to ICFO, but also the nice moments here in Barcelona and in US. Thanks a lot for being so accessible to talk, also to trust me for going there and always for your nice words and advice. Also, thanks to other people that I had the privilege to know: Wageesha, Angela, Brandy, etc. And of course, to Mark Quesada, it was always very interesting (and funny) to talk to you and learn from all of your stories. I just can say that it was a pleasure to be there and working with you. I felt very productive and part of the team and really enjoyed the weekly meetings where you always tried to help me. Also, thanks for helping me dealing with the snow (I will never forget to buy a scraper), and with the cancelled/delayed flights. Hopefully, the next visit will be in summer ☺.

From the ICFO team, I would start saying thank you for their contribution and help to develop my work to: Luis, Javi and Johann (Clean room team), and to the mechanical and electronic workshop, especially to my casi paisano Xavi, for all the nice moments and jokes (going there was always funny) and José Carlos. Of course, also I would like to thank the hard-worker Carlos Dengra, for always helping me instantaneously with the CVD, and Jonas, Adri, for your help and your constant good mood. Las mismas gracias van dirigidas al equipo de la cafetería, en especial a Esther, con esa sonrisa y buena energía. It is essential to have people like you around!

Regarding my research group, the OPTO-family, I would like to start saying thanks to the ex-members who at some point contributed to make my stay and my PhD happier (or at

least easier ☺): Ilaria, Vahagn, Josep… Specially, to my ex-office (and gym) mate, friend and very nice person Nadia: I really enjoyed the time with you and remember all the laughs and confidences; and also, to my flor granaína Judith, for the same. Also, for the current people in the group, thank you, because you make each day easier and it is always a source of energy having lunch with you. One of the most important characteristics of the OPTO-group is the nice energy and atmosphere created between us. Specially, thanks to my graphene soulmate Kavitha, to be a mutual supporter and always make hilarious (and ironic) comments; and my office-mates, specially to Rinu, my little-bro, to be the definition of happiness and always trying to annoy me in a good way. Also, a special mention to the *new* "familia", a great and funny combination of people that makes my stay at ICFO and BCN more enjoyable: Juan R., Rubi, Sebastián, Sofia, and my two students Manu and Migle. From my *old* familia, I want to thank Juan M. and Roland for their continuous support and friendship, for being with me since the first year, and for always making me smile (well… maybe this only applies to Juan…). I really noticed that I was adapted to my new (PhD) life when both of you arrived to ICFO.

And last but not least, to my non-official and unconditional post-docs Davide and Vittoria. Davide, thank you for transferring me part of your knowledge, for your patience (specially teaching me how to deal with the electrical measurements), and also for your psychology sessions ☺, for not allowing me to stop and helping me to believe in what I do. Vittoria, thank you for helping me so much, especially with my last project, for your commitment even if no one forced you to, for giving me support and energy when I was blocked, and for being always available for everyone. I really think that we all should learn many things from you, mamma. Without both of you, nice professionals but better people, this thesis would have not been possible.

Also, to other ICFOnians and very good friends: Noslen (mi mamasita, gracias por tu amistad incondicional), Alberto, Miquel, Ferrán, Lisa, Silvana y Pau. All the good moments, laughs, beers and plans together (like Girona or Estartit) are unique and I really enjoyed them. Hope to continue with the traditions after ICFO ☺. Also, to other nice people that I have had the pleasure to meet during my stay at ICFO and in BCN: mis indifference Eric y Antoine, Maite, Simónnn, Nico, Gabi, Bárbara, Teresa, Peter, Morales, Giorgio, Gianvito, Pablo, Elsa, Carlota, Idoia, Rafa … I really thank you for all the good moments. And also to my second family in BCN, my ex-flatmates that had to deal indirectly with the thesis: Sandra (mi vasqui favorita), Irene, Marta, Lauri, Sara and Steffi. Thanks for injecting me with energy when I was a bit frustrated and for the nice and unforgettable moments living with you.

This thesis also has been possible due to Verónica and Sonia Fereres, as they were the key for advising me about ICFO, and helped me in an unselfish way giving me support and references to apply for the phd. I really appreciate your help and your support while I stayed in Sevilla. Also, thank you to my first mentor Sonia Gil, mi jefa of the university, to trust me and teach me at the very early stage of my life as a researcher. Thank you also to: my ex-compis from Sevilla (mis Cococobos Pau y Ramos) and from the catalysis team (los catalíticos). My friends from university (mis ingenieritos), Álvaro, mis chicas de siempre de Ciu que las adoro. En especial a: Bea, mi gran apoyo desde la uni y compañera de

andanzas inglesas ([…] por el Erasmus!![…]); Sol, mi gran descubrimiento "sevillano"; y a Mariajo, por tu amistad de tantos años y los buenos momentos que me han dado tus locuras. A la gente que me ha acompañado todo este tiempo compartiendo mi gran pasión, el baile: a Angelines y Ana, mis profes de la infancia, a Antonio, Juli y Toni. Gracias a todos por enseñarme, motivarme y ser fuente de inspiración. Por vuestro talento y los valores que comunicáis.

Finalmente, a mi familia, y en especial:
A mis padres, por estar siempre ahí, escuchándome y dándome su apoyo y amor incondicional, y por nunca cuestionar ninguna de las decisiones importantes que he tomado. Es increíble la suerte que he(mos) tenido de teneros.

A mi hermana Raquel, mi otra mitad, porque a pesar de estar en las noruegas es increíble lo unidas que estamos. Gracias por tu apoyo constante y protección. Eres un orgullo de hermana.

Finalmente, a Kevin, mi apoyo más inesperado. Wie ich dir schon gesagt habe, was für ein Glück, dass ich dich gefunden habe (und meine Sturheit überkommen habe). Danke, dass du so bist wie du bist.

Abstract

The combination of unique properties - high electrical mobility, thermal conductivity, transparency and mechanical flexibility - make graphene promising for a wide variety of applications, including transparent electrodes, flexible displays, touch-screens and wearables. One of the main reasons that prevent its wide-spread use is the difficulty to maintain all of the previously mentioned properties when grown using industrial grade techniques. The most widely used technique for growing graphene on a large scale is Chemical Vapor Deposition (CVD), where graphene is, typically, first deposited on a Cu catalyst foil and then transferred to a target substrate using additional sacrificial materials (polymers). The transfer is time-consuming and can worsen the graphene properties and its quality. For instance, residues from transfer materials can alter the doping level.

This thesis has investigated the *direct growth, dry transfer and doping control* of graphene on glass substrates, suggesting new methods and designs to improve the use of such substrates in devices, with a particular focus on optical applications where preserving the transparency is often required.

The thesis demonstrates *direct growth of graphene* on the desired target substrate using two techniques without any transfer step. In the first technique, graphene was grown on large patterned areas by using catalytic ultra-thin metal films (UTMFs) made of Ni, with thicknesses ranging from 5 to 50 nanometers. The dewetting of Ni UTMF when exposed to high growth temperatures allows graphene to deposit on the glass surface while the metal film is breaking and is retracted. In the second technique, graphene was grown on large areas covered by Cu nanoparticles, which can be arranged into different patterns and with surface densities. Tuning the Cu density by dip-coating and evaporation techniques and the possibility of etching the Cu afterwards allow the growth of flat graphene networks, but also of graphene assembled into three-dimensional shapes with high effective surface area, which opens up more potential applications.

CVD of graphene on Cu foil is a powerful growth technique, but its transfer is still a challenge. This thesis has demonstrated a successful *dry transfer* technique for graphene on glass substrates using interfacial polyimide layers, which is faster, easier and more scalable while preserving the electrical transport and optical properties.

The doping of graphene through the substrate surface or the additional top layers is not always easy to control. If not properly carried out, it can degrade the graphene properties, even when the previous growth and transfer steps have been successfully performed. This thesis has investigated a *doping control* post-processing technique, called "thermal poling" of glass, to induce the charge at the surface of the glass substrate and thus modify the electronic carrier density of graphene. The charge in the glass originates from the displacement of ions that become mobile at temperatures above 100ºC and when subjected to an electrical voltage of up to few kV. The corresponding stable and "frozen-in" electric field is responsible for the doping of graphene.

The results of this thesis widen the range of graphene applications where large-scale growth, practical transfer and doping control are required. At the same time, the thesis also opens new research avenues, especially to improve further the graphene quality when incorporated in devices.

Resumen

El grafeno es un material único y prometedor debido al conjunto de excelentes propiedades que presenta, entre las cuales destacan su elevada conductividad eléctrica y térmica, así como su transparencia y flexibilidad. La concentración de todas estas características en un único material hace que el grafeno sea objeto de estudio para su futura aplicación en diversos ámbitos, como pueden ser en electrodos transparentes, dispositivos flexibles, pantallas táctiles y "wearables", o tecnología ponible.
No obstante, una de las razones que está frenando el uso del grafeno en la actualidad, y con especial dificultad cuando esta tecnología se quiere aplicar a escala industrial, es la conservación de sus excelentes propiedades desde la etapa inicial, en la que el grafeno es fabricado, hasta que se implementa en el dispositivo para su aplicación final. En este ámbito, la técnica más prometedora para la síntesis de grafeno a escala industrial es la Deposición Química en Fase Vapor (CVD), la cual permite crecer grafeno de alta calidad normalmente sobre una lámina de cobre. No obstante, para su posterior aplicación, el grafeno ha de ser transferido al substrato final mediante un proceso durante el cual el grafeno es normalmente protegido mediante polímeros. Esta etapa puede ser perjudicial para el material, ya que además del tiempo que conlleva la transferencia, las propiedades y calidad del grafeno puede verse afectada, como por ejemplo debido al dopaje proveniente de residuos del polímero.

Esta tesis ha investigado *el crecimiento directo, transferencia por vía seca y el control de dopaje* del grafeno en vidrio, sugiriendo nuevos métodos y diseños para mejorar el uso de estos substratos en dispositivos, especialmente para aquellos con aplicaciones ópticas donde es necesaria una elevada transparencia.

La tesis demuestra el crecimiento directo de grafeno en el substrato final deseado, usando para ello dos técnicas diferentes que evitan cualquier etapa de transferencia. En la primera técnica, el grafeno se ha crecido en áreas grandes y prediseñadas usando como catalizador láminas ultra-finas (UTMFs) de níquel con espesores comprendidos entre 5 y 50 nanómetros. Cuando estas láminas metálicas son expuestas a las temperaturas elevadas necesarias para crecer el grafeno ocurre el fenómeno de *dewetting*, en el cuál la lámina se rompe y el metal se retrae, lo que conlleva que el grafeno que ha crecido en el níquel se deposite en la superficie del vidrio. En la segunda técnica, el grafeno se ha crecido sobre nanopartículas de

cobre que han sido depositadas previamente en vidrio con diferentes estructuras y densidad superficial. La variación de densidades obtenidas en las nanopartículas de cobre durante su deposición en vidrio, mediante técnicas de inmersión y evaporación, y la eliminación posterior del cobre permiten el crecimiento de grafeno en forma de red plana, pero también en estructuras tridimensionales con mayores áreas superficiales, lo que incrementa las posibles aplicaciones futuras.

El crecimiento de grafeno mediante CVD en una lámina de cobre es la técnica más prometedora a nivel industrial, pero su transferencia desde el metal hasta el substrato final es aún cuestionable y supone un reto para lograr la completa implementación de esta tecnología. Esta tesis demuestra la capacidad de una *técnica por vía seca* y escalable a nivel industrial, para transferir grafeno de manera efectiva, rápida y sencilla en substratos de vidrio, utilizando poliamida como material intermedio entre ambos y preservando las propiedades eléctricas y ópticas del grafeno.

El dopaje de grafeno que se adquiere bien por la superficie del substrato final o por la contribución de capas depositadas encima, es difícil de controlar y puede conllevar a la degradación total de las propiedades elétricas del material, incluso cuando las etapas de síntesis y transferencias se han llevado a cabo de manera correcta. Esta tesis ha investigado la aplicación de una técnica para *controlar el dopaje* del grafeno a posteriori, es decir, una vez que ha sido depositado en el vidrio. Esta técnica se conoce como polarización térmica del vidrio y consiste en la inducción de una carga en la superficie del vidrio que provocará una modificación controlada del dopaje del grafeno. Esta carga superficial del vidrio se origina por el desplazamiento de iones provenientes de aditivos del vidrio, que comienzan a moverse a temperaturas superiores a 100ºC y cuando se aplica un voltaje externo de kV. Este proceso da lugar a un campo eléctrico muy estable, confinado y "congelado" dentro del vidrio a temperatura ambiente que será el responsable de la modificación del dopaje del grafeno.

Los resultados de esta tesis amplían el rango de aplicaciones del grafeno donde es necesarios su crecimiento a gran escala, un método de transferencia efectivo y práctico y un control sobre su dopaje final. Del mismo modo, esta tesis también abre nuevas vías de desarrollo e investigación, especialmente para mejorar la calidad del grafeno cuándo éste es incorporado finalmente en dispositivos.

Publications

Journal publications

1. **M. Marchena**, D. Janner, V. Finazzi, P. Mazumder and V. Pruneri: "Doping control in graphene by thermal poling of the glass substrate". Under preparation.

2. **M. Marchena**, F. Wagner, T. Arliguie, B. Yu, M. Fernández, T. Chang, R. Lee, V. Pruneri and P. Mazumder: "Dry transfer of graphene to dielectrics and flexible substrates using polyimide as a transparent and stable intermediate layer", 2D Materials, Accepted (2018). DOI: 10.1088/2053-1583/aac12d

3. **M. Marchena**, Z. Song, W. Senaratne, C. Li, X. Liu, D. Baker, J.C. Ferrer, P. Mazumder, K. Soni, R. Lee and V. Pruneri: "Direct growth of 2D and 3D graphene nano-structures over large glass substrates by tuning a sacrificial Cu-template layer", 2D Materials 4 (2017) 025088.

4. **M. Marchena**, D. Janner, T. Chen, V. Finazzi and V. Pruneri: "Low temperature direct growth of graphene patterns on flexible glass substrates catalyzed by a sacrificial ultrathin Ni film", Optical Materials Express, Vol. 6, Issue 8, pp. 2487-2507 (2016).

5. T. Chen, D.S. Ghosh, **M. Marchena**, J. Osmond and V. Pruneri: "Nano-patterned graphene on a polymer substrate by a direct peel-off technique", ACS Applied Materials and Interfaces, 7, 10, (2015).

Invited Talks

1. K. K. Gopalan, **M. Marchena**, J. Rombaut, I. Gris, D. Rodrigo and V. Pruneri: "Graphene for transparent conductors and infrared sensing". CLEO-PR, OECC & PGC, Singapore, July-August, (2017).

2. M.A. Noyan, K.K. Gopalan, R. A. Maniyara, **M. Marchena**, V. Mkhitaryan, J. Rombaut, M. Rude, R. Sibilo, I. Manelli, J. Canet and V. Pruneri:

"Multifunctional nano-structured optical surfaces for industrial applications". Nanometa 2017, Seefeld, Austria, (2017).

3. **M. Marchena**, T. L. Chen and V. Pruneri: "Graphene directly deposited on dielectrics for transparent electrodes", Graphene World Summit 2015, Barcelona, Spain, November (2015).

4. D. Janner, **M. Marchena**, D.S. Ghosh, T.L. Chen, I. Mannelli, M. Rude, V. Mkhitaryan, A. Carrilero and V. Pruneri: "Ultrathin materials and nano-structuring for multifunctional transparent surfaces". 39th International Conference and Expo on Advanced Ceramics and Composites, Daytona, Florida, USA (2015).

5. **M. Marchena**, T. L. Chen, K. Kalavoor, D. Janner, D. S. Gosh and V. Pruneri: "Ultrathin metals and graphene for flexible optoelectronic devices". Trends in Nanotechnology International Conference (TNT2014), Barcelona, Spain (2014).

6. **M. Marchena**, T. Chen, and V. Pruneri: "Graphene combined with ultrathin metals for low cost and mechanically flexible transparent electrodes". NanoSpain Conference, Madrid, Spain (2014).

Conference publications

1. **M. Marchena**, Z. Song, W. Senaratne, C. Li, X. Liu, D. Baker, J.C. Ferrer, P. Mazumder, K. Soni, R. Lee and V. Pruneri: "Direct growth of 2D and 3D graphene nano-structures over large glass substrates by tuning a sacrificial Cu-template layer". Graphene 2017, Barcelona, Spain, (2017). Poster.

2. **M. Marchena**, D. Janner, T.L. Chen, V. Finazzi and V. Pruneri: "Direct growth of patterned graphene on dielectric and flexible substrates catalyzed by a sacrificial ultrathin Ni film". Graphene 2016, WORKSHOP 4 – Production & Applications of graphene and related materials, Genova, Italy, (2016).

3. T. L. Chen, D. S. Ghosh, **M. Marchena** and V. Pruneri: "Nano-patterned graphene on polymer substrate by direct peel-off technique". Graphene 2015, Bilbao, Spain, (2015).

4. **M. Marchena**, D. Janner and V. Pruneri: "Direct growth of graphene on transparent dielectrics XXX Trobades Científiques de la Mediterrània Josep

Miquel Vidal - Graphene and related materials. Production, Characterization, Applications, Menorca, Spain, (2014).

5. **M. Marchena** and V. Pruneri, "Ultrathin metal films for direct thermochemical vapor deposition on dielectric substrates of single and a few layered graphene". Graphene2014, Toulouse, France (2014). Poster.

Patents

1. **M. Marchena,** P. Mazumder and V. Pruneri, "Graphene doping by thermal poling", (2018). Under preparation.

2. **M. Marchena,** F. Wagner, T. Arliguie, B. Yu, T. Chang, R. Lee, P. Mazumder and V. Pruneri**,** "Direct graphene transfer and graphene-based devices" (2017).

3. **M. Marchena**, Z. Song, W. Senaratne, C. Li, X. Liu, D. Baker, P. Mazumder, K. Soni, R. Lee, V. Pruneri: "Transparent substrates comprising three-dimensional porous conductive graphene films and methods for making the same" (2016).

4. B. Johnson, X. Liu, P. Mazumder, K. Soni, T. L. Chen, **M. Marchena** and V. Pruneri, "Transfer of monolayer graphene onto flexible glass substrates" (2017). US 9.828285 B2.

Contents

Chapter 1. Introduction 1

1.1. Graphene **3**

1.1.1. Definition and structure 3

1.1.2. Electronic transport properties 5

1.1.3. Growth techniques 7

1.1.4. Graphene doping 14

1.1.5. Graphene transfer 15

1.2. Characterization techniques **18**

1.2.1. AFM topography 18

1.2.2. Bending tests 18

1.2.3. Contact angle 18

1.2.4. Energy dispersive X-ray spectroscopy (EDX) 19

1.2.5. Four-point probe measurement 19

1.2.6. Grazing incidence X-ray diffraction (GXRD) 21

1.2.7. Hall measurement 22

1.2.8. Hall measurement combined with *in situ* monitoring of R_S 24

1.2.9. Optical characterization 25

1.2.10. Raman spectroscopy 25

1.2.11. Scanning Electron Microscopy (SEM) 27

1.3. Graphene applications and future overview **28**

1.3.1. Graphene applications 28

1.3.2. Current situation and investment 29

1.4. Aim of the thesis **30**

1.5. Thesis outline **32**

Chapter 2. Direct growth of graphene by Ni dewetting 35
2.1. Introduction 35
2.2. Sample preparation 39
2.3. Ni dewetting process on glass 41
2.4. Influence of the reaction temperature 43
2.5. Growth of graphene nano-patterns on alternative substrates 54
2.6. Conclusion 60
2.7. Additional Information 61

Chapter 3. Graphene assembled into 3D-shapes by tuning the Cu density 65
3.1. Introduction 65
3.2. Sample preparation 68
3.2.1. Cu deposition on glass substrate 68
3.2.2. Graphene growth on Cu NPs by CVD 71
3.2.3. Cu removal from graphene structures 71
3.3. Characterization for graphene assembled into 2D-and 3D-structures 72
3.3.1. Graphene assembled into a 3D ball structure (3D-GB) 72
3.3.2. Graphene assembled into a 3D sponge structure (3D-GS) 77
3.3.3. Two-dimensional graphene (2D-G) 80
3.4. Conclusion 83

Chapter 4. Graphene dry transfer using polyimide as an intermediate layer 85
4.1. Introduction 85
4.2. Sample preparation 88
4.2.1. Graphene on Cu foil 88
4.2.2. Polyimide 88
4.2.3. Polyimide deposition on the target substrate 89
4.2.4. Graphene transfer step 89
4.3. Optimization of the curing level of PI to attach graphene from Cu 90
4.4. Graphene transfer to glass and PET using PI as intermediate layer 95
4.4.1. Graphene transfer to glass using the hot press 96
4.4.2. Graphene transfer to glass and PET using the laminator 99
4.4.3. Comparison of both transfer procedures 101
4.4.4. Device stability under heat, bending and aqueous media 107
4.5. Conclusions 110

Chapter 5. Tuning of graphene doping by the thermal poling of the glass substrate... 111
5.1. Introduction ... 111
5.2. Sample preparation ... 116
5.2.1. Graphene transfer and annealing ... 116
5.2.2. Graphene device fabrication ... 116
5.2.3. Thermal poling of the glass ... 119
5.2.4. Electrical measurements ... 120
5.3. Thermal poling of SDG and calibration for the introduction of graphene ... 121
5.4. Effect of SDG thermal poling on graphene doping ... 129
5.4.1. Graphene device response onto a non-poled SDG ... 129
5.4.2. Graphene device response onto a poled SDG with $\pm V_P$ ... 131
5.5. Conclusions ... 135

Chapter 6. Summary and outlook ... 137

Bibliography ... 141

Nomenclature

Ø: Diameter
μ_H: Charge carrier mobility
2D: two dimension
2D-G: Graphene film (2D structure)
3D: three dimension
3D-G: three dimensional graphene
3D-GB: Graphene nanoballs
3D-GS: Graphene sponge
A: Absorbance
AC: Alternating current
AFM: Atomic Force Microscopy
APTMS: 3-aminopropyltrimethoxy-silane
B: Magnetic field
C_1, C_2: Geometrical factor for Rs calculation
Cu NPs: Copper nanoparticles
CVD: Chemical Vapor Deposition
DC: Direct current
E: Electric field
EDX: Energy-dispersive X-ray spectroscopy
E_{IN}: Internal electric field
EM: Electromagnetic wave
FET: Field effect transistor
F_L: Lorentz force
FTIR: Fourier Transform-Infrared Spectroscopy
FWHM: Full Width at Half Maximum
GO: Graphene oxide
Gr 1: Graphene from Cu foil 18 μm
Gr 2: Commercial graphene
GXRD: Grazing incidence X-ray diffraction
h-BN: Hexagonal boron nitride
HOMO: Highest occupied molecular orbital
HOPG: High oriented pyrolytic graphite
I: Current
I_{12}: Current injected from contact 1 to 2
I_{14}: Current injected from contact 1 to 4
I_{23}: Current injected from contact 2 to 3
I_{2D}: Intensity of the 2D Raman peak
I_{34}: Current injected from contact 3 to 4
I_D: Intensity of the D Raman
I_G: Intensity of the G Raman
ITO: Indium tin oxide
LEDs: Light emitting diodes
LUMO: Lowest unoccupied molecular orbital
N.A: Numerical aperture of an objective
NMP: N-methyl-2-pyrrolidone
n_S: Charge carrier density
$P_{(HP)}$: Pressure applied by the hot press
P: Process pressure
PAA: Polyamic acid
PDMS: Polydimethylsiloxane
PECVD: Plasma Enhanced Chemical Vapor Deposition
PET: Polyethylene terephthalate
PI: Polyimide
PMMA: Poly(methyl methacrylate)
PS: Polystyrene
q_e: Electron charge ($1.602 \cdot 10^{-19}$ C)

R: Resistance
$R_{12,34}$: Resistance. Voltage measured in contacts 3-4. Current injected from contact 1-2
$R_{14,23}$: Resistance. Voltage measured in contact 2-3. Current injected from contact 1-4
$R_{23,14}$: Resistance. Voltage measured in contact 1-4. Current injected from contact 2-3
$R_{34,12}$: Resistance. Voltage measured in contact 1-2. Current injected from contact 3-4
R_B: Radii of curvature for bending
R_C: Contact resistance
R_F: Reflectance
$R_{horizontal}$: Resistance measured in horizontal position
R_S: Sheet resistance
RT: Room temperature
$R_{vertical}$: Resistance measured in vertical position
SDG: Soda lime glass
SEM: Scanning Electron Microscopy
T: Process temperature
t: time
T_C: Curing temperature
$T_{dewetting}$: Dewetting temperature
TE: Transparent electrode
t_F: Film thickness
T_F: Film transmittance without substrate contribution
Tg: Glass transition temperature
T_P: Poling temperature
t_P: Poling time
TRT: Thermal release tape
T_S: Transmittance of the substrate
T_T: Total transmittance (with substrate)
UHV: Ultra-high vacuum pressure
UTMF: Ultra-Thin Metal Film
V: Voltage
V_{12}: Voltage, measured in contact 1-2
V_{14}: Voltage, measured in contact 1-4
V_{23}: Voltage, measured in contact 2-3
V_{34}: Voltage measured in contact 3-4
V_G: Charge neutrality point
V_H: Hall voltage
V_P: External DC voltage for poling
W/L: Geometrical factor in Hall bar (W: width, L: length)
Δx: Distance between the laminator silicone rollers
Δz_{MAX}(C-C): Maximum height between two carbon atoms
Δz_{MAX}: Maximum height
θ: Contact angle
λ: Wavelength
ϱ_t: electrical resistivity
σ: standard deviation
ω_{2D}: Raman shift of 2D peak
ω_D: Raman shift of D peak
ω_G: Raman shift of G peak

List of tables

Table 1. State-of-the-art of graphene grown on Cu foil/thin films 12

Table 2. State-of-the-art of graphene grown on Ni foil/thin films 13

Table 3. State-of-the-art for direct growth of graphene on the target substrate 37

Table 4. Processing conditions and Raman signals for graphene grown on Ni UTMFs (fused silica substrates) of different thicknesses....44

Table 5. EDX measurements on graphene after Ni removal....57

Table 6. Samples S1-S9: Process conditions and Raman/electrical results for graphene deposited on Ni UTMF....61

Table 7. Samples S10-S18: Process conditions and Raman/electrical results for graphene deposited on Ni UTMF....62

Table 8. Raman results on Ni UTMFs of different thicknesses. (Raman measured on the non-dewetted areas). 63

Table 9. State-of-the-art of graphene grown on 3D-catalytic templates, indicating the process conditions and the main characteristics of the work....67

Table 10. Summary of the main properties related to 2D- and 3D-graphene structures developed by CVD technique tuning the Cu template catalyst. 83

Table 11. Variation of CVD conditions for the production of 3D-GS structures of different R_S and transmittance values 84

Table 12. Transmittance (%) at 550 nm of graphene transferred by the hot press and the laminator....104

Table 13. Summary of the conditions for transferring samples S1-S7, specifying type of graphene, substrate and equipment. 105

Table 14. Summary of θ measured on graphene and PI....109

Table 15. State-of-the-art of glass thermal poling, highlighting the type of glass and thickness, and poling conditions....115

List of figures

Figure 1. (a) Scheme of the graphene structure in a hexagonal honeycomb geometry. (b) Difference between electron occupation in orbitals. (c) Scheme of graphene showing the σ- and π-bond 4

Figure 2. Structural defects in graphene. (a-b) Point defects, and (c) Linear defects 5

Figure 3. Band structure of graphene. (a) 3D-picture of graphene band structure. (b) 2D image of graphene band where the graphene is undoped and with n- and p-doping 6

Figure 4. Graphene growth mechanism via CVD using Cu (a) and Ni (b) as catalysts . 10

Figure 5. Wet transfer of the graphene from the Cu foil to the target substrate 17

Figure 6. (a) Four-Point probe measurement set-up.(b) Scheme of the measurement . 20

Figure 7. (a) Probe station to perform Hall measurements. (b) Scheme of the Van der Pauw device. (c) Hall bar design used in Chapter 5 23

Figure 8. (a) Probe station modified to change the temperature during the Hall measurement. (b-c) Scheme of the measurement. 24

Figure 9. (a) Raman spectra of graphene and graphite. (b) 2D band of graphite comparing the evolution of the graphene peak when the number of layers is modified 27

Figure 10. Number of (a) publications and (b) filed patents related to graphene........... 30

Figure 11. (a) Sputtering system used for Ni UTMFs deposition. (b) CVD Black-Magic (AIXTRON) used for graphene growth.. 40

Figure 12. Scheme of dewetting phenomena on thin films 41

Figure 13. (a) $T_{dewetting}$ as a function of different Ni UTMF thicknesses. (b) GXRD spectra of 50 nm Ni UTMF before and after CVD growth at 1000°C..................... 43

Figure 14. (a) Optical microscope images of 50 nm dewetted samples. (b) Raman spectra measured on dewetted areas 45

Figure 15. SEM pictures of 50 nm Ni at 700°C, 800°C, 900°C, 1000°C 46

Figure 16. Growth of graphene on dewetted Ni holes (Sample A). (a) SEM image of a hole partially covered by suspended graphene. (b) AFM amplitude. (c) Height of Ni film and suspended graphene. (d) Phase image of the hole 47

Figure 17. Sample A (700°C). (a-b) Pictures by AFM and SEM, respectively. (c) Raman maps of the area in (a) 48

Figure 18. Sample B (900°C). (a-c) Raman maps. (d) FWHM (2D) statistics, plotted separately for both areas (dewetted and continuous) 50

Figure 19. AFM measurements of Sample B. (a) Height map. (b) Phase of map in (a)..50
Figure 20. SEM images and Raman maps of I_{2D}/I_G of graphene 52
Figure 21. Schematic model of graphene growth on 50 nm Ni UTMF........................53
Figure 22. Reaction time effect on graphene by (a) I_{2D}/I_G and (b) FWHM 2D peak....54
Figure 23. (a) Transmittance and absorbance at 550 nm. (b) Picture of Samples A,C...56
Figure 24. Transmittance spectra of the highest quality Ni UTMF Samples A-D and Sample S9. (a) Samples with graphene before and (b) after Ni removal.......57
Figure 25. (a) Flow chart indicating the fabrication steps. Optical images in (b-c, left) show 50 nm Ni deposited on Si/SiO_2 and Willow® glass, while in (b-c, right) graphene patterns can be distinguished after Ni removal. (d) SEM image of graphene squares grown on Si/SiO_2 after Ni removal. (e) Optical microscope image of one graphene square. (f-g) SEM images of graphene grown on Willow® glass after Ni removal 58
Figure 26. Raman of graphene grown on Willow® glass, (a) I_{2D} peak and (b) I_{2D}/I_G...59
Figure 27. Optical microscope image, and I_{2D} and shift of the G peak........................63
Figure 28. (a) Scheme of the quartz tube used for the deposition of Cu NPs. (b) Experimental data of the temperature profile along the inside of the tube ..70
Figure 29. Example of gradient color samples for 3D-GS production. (a) Cu NPs are deposited on fused silica. (b) Same after graphene growth and Cu removal.71
Figure 30. Fabrication of 3D- and 2D-graphene structures. (a) Cu template formation on the substrate. (b) CVD growth of graphene. (c) Removal of residual Cu 73
Figure 31. Characterization of the 3D-GB structure. (a) SEM image of the Cu NPs deposited on glass. (b-c) SEM at 30° of the deposited Cu NPs without and with graphene, respectively. (d) 3D-GBs after Cu removal. (e) Raman spectrum of 3D-GBs. (f) Statistical distribution of the Raman I_{2D}/I_G peak ratio. (g) Transmittance spectra of the Cu NPs, Cu NPs with graphene and 3D-GBs after Cu NPs removal 74
Figure 32. Raman mapping of 3D-GBs on glass: (a) I_{2D}/I_G ratio and (b) I_D/I_G ratio ...75
Figure 33. SEM and EDX characterization at 5kV of (a) Cu NPs that are covered with graphene, and (b) 3D-GBs on glass after performing a wet etching of Cu...76
Figure 34. Characterization of 3D-GS structures and their catalytic Cu NPs. (a-c) SEM images of Cu NPs. (b) Same Cu NPs after being heated to 800°C. (c) 3D-GS on fused silica after growing graphene and the sublimation of Cu. (d) Raman spectrum of the 3D-GS. (e) Distribution of I_{2D}/I_G extracted from the Raman mapping in (f). (f) Raman mapping showing the I_{2D} and the continuity of the 3D-GS...78
Figure 35. (a-c) SEM cross section images: (a) Cu NPs evaporated on fused silica. (b) Same Cu NPs after being heated to 800°C. (c) 3D-GS obtained after sublimating Cu NPs. (d) EDX performed on 3D-GS 79

Figure 36. Characterization of the 2D-G structure. (a) SEM image of Cu NPs embedded in glass. (b-c) Top and cross-section SEM of graphene after the sublimation of Cu NPs. (d) Raman spectrum of the 2D-G. (e) Raman distribution of the I_{2D}/I_G ratio. (f) Transmittance of the Cu NPs, 2D-G and bare substrate.....80
Figure 37. Raman mapping for 2D-G structures: (a) I_{2D}/I_G ratio and (b) I_D/I_G ratio. ..81
Figure 38. SEM images of (a) Cu NPs, and (b) 2D-G structures after Cu sublimation. EDX measurements at 15 kV have been performed on (a) the Cu NPs, and on (b) the 2D-G structure and the fused silica substrate..................................82
Figure 39. Optical measurements performed on three different samples......................84
Figure 40.(a) Commercial hot press used for the transfer of graphene to glass. (b) Commercial laminator used for the transfer of graphene to glass and PET .90
Figure 41. (a) R_S values of graphene transferred from the Cu foil to the PI film at different Tc. (b) Weight loss of PI films on glass after being treated at Tc.. 91
Figure 42. Curing process of the VTEC, where the Tc defines the reaction speed 92
Figure 43. FTIR results for PI cured at different Tc 93
Figure 44. Simulation of chemical structures for (a) defect-free graphene and (b) defective graphene layer with a vacancy and two pairs of heptagon-pentagon rings ...94
Figure 45. Graphene transfer to glass and PET: (1) Spin coating of PI; (2) Drying of PI at 40-80°C for 15 minutes; (3) Cu/graphene is located on top and placed inside the transfer equipment. (4) Cu is peeled off 96
Figure 46. R_S of Gr 1 samples transferred by hot press applying different $P_{(HP)}$ 97
Figure 47. (a) SEM characterization of Gr 1 transferred to APTMS+PI on glass by hot press. (b) AFM of Gr 1 grown on Cu. (c) AFM of the transferred sample...98
Figure 48. SEM of graphene transferred to glass under non-optimized conditions. 99
Figure 49. SEM (a-c) and AFM (d-f) characterization of the graphene samples transferred to glass/APTMS+PI (a, b, d, e) and PET/PI (c, f)...................................100
Figure 50. AFM characterization of Gr 2 grown on Cu foil (commercial)..................101
Figure 51. Raman characterization of: (a) Gr 1 on Cu foil; (b) PI on glass showing the PI peaks that are denoted by *; and graphene transferred to glass and PET...102
Figure 52. T_F measurements of: (a) Gr 1 transferred to glass/APTMS+PI by the hot press; (b) Gr 1 and Gr 2 transferred to glass/APTMS+PI by the laminator; and (c) Gr 2 transferred to PET/PI by the laminator...............................103
Figure 53. Hall measurements of samples (S1-S7). (a) n_S obtained for samples S1-S3, fabricated with Gr 1 and transferred by hot press to glass/APTMS+PI. (b) n_S obtained for samples S4-S5, fabricated with Gr 1 and transferred by laminator to glass/APTMS+PI. (c) n_S obtained for samples S6-S7, fabricated with Gr 2 and transferred by laminator to glass/APTMS+PI and PET/PI. (d) μ_H calculated..106

Figure 54. Temperature stability testing in terms of R_S for graphene transferred by the hot press method and annealed up to 350°C 107
Figure 55. Stability of the samples measuring R_S: (a) after bending tests at different radii and (b) before and after dipping the samples S1, S6 and S7 in water 109
Figure 56. Contact angle on the APTMS+PI area transferred by the hot press. 109
Figure 57. Molecular structure of (a) quartz, (b) fused silica, and (c) SDG glass. 113
Figure 58. Thermal poling of SDG, where in (a), the Na^+ charges are distributed randomly along the whole glass area. At high poling temperatures in (b), the V_P drifts the Na^+ charges to the cathode where they are neutralized. After cooling down in (c), V_P is removed and an electric field is frozen inside the glass................ 114
Figure 59. Procedure for the graphene device fabrication. (1) Initial cleaning of SDG by organic solvents and O_2 plasma. (2-3) Two UV lithography and evaporation of the metal contacts. (4-5) Graphene transfer by wet etching process. (6) Encapsulation of the graphene device. (7-9) A fourth and fifth lithography to remove the Al_2O_3 from the top of the Au contacts and to evaporate the top Au contact to apply the V_P 118
Figure 60. (a) Device pattern for performing the five lithography steps. (b) Optical image of the graphene device on glass after the whole fabrication procedure. 119
Figure 61. Description of the poling set-up. (a) Scheme showing the electric circuit. (b) Optical image of the inside of the oven 120
Figure 62. Thermal poling of glass at 270ºC, -1.6 kV and 100 minutes. (a) Scheme showing the drifting of Na^+ charges towards the cathode. (b) Raman is performed on the anode face measuring from the surface to 8 μm inside the glass.......... 122
Figure 63. Na_2CO_3 formation at the cathode after the thermal poling of SDG. (a) Optical microscope image of the cathode. (b) Raman measured on the sample 124
Figure 64. SEM and EDX measurements on the cathode. (a) Scheme and SEM of the poled area. (b) SEM and EDX performed on four different areas............ 125
Figure 65. Optimization of thermal poling of SDG when the graphene is deposited on the top face of the glass. (a-b) Monitoring of V_P applied for the poling and I created in the glass. (a) Poling of SDG at -1.6 kV at 270ºC, for 100 min without controlling I, whose maximum value is 400 μA. (b) Conditions are optimized for graphene using Kapton. (c) Contact angle measurements 127
Figure 66. Thermal poling of a graphene device, at +1.6 kV without current limitation. (a) Optical image of the Hall bar. (b) The graphene damage is confirmed by Raman 128
Figure 67. Electrical measurements performed on a graphene device. (a) Evolution of R_S when temperature is increased from RT to 280ºC. (b) R_S variation with temperature. (c) Mobility variation during the heating of the sample......... 130

Figure 68. Influence of poling time on graphene doping. (a) Charge displaced inside the SDG at different times using Kapton for current limitation at -1.6 kV. (b) n_S for the graphene, whose substrate has been poled for different times 131
Figure 69. Graphene device response after SDG poling at -1.8 kV for 2 hours. (a) Scheme of the sample indicating the displacement of the Na particles. (b) R_S evolution with temperature over time. (c) R_S , (d) n_S and (e) μ_H variation with temperature. 133
Figure 70. Graphene device response after SDG poling at +1.2 kV for 1 hour. (a) Scheme of the sample, indicating (with white arrows) the displacement of the Na particles towards the cathode. (b) R_S (orange line) evolution with temperature over time. (c) R_S variation with temperature..134

1

Introduction

In recent years, the control and manipulation of atoms and molecules have led to greater study and research in physics, chemistry, engineering and biology. This field of research is known as *nanoscience*, and allows the understanding of fundamental processes and interactions between particles occurring at the nanoscale. In other words, when a material is reduced in size down to the atomic and molecular scales, fascinating and unique interactions occur. This novelty has motivated the scientific community not only to create new materials, but also equipment and tools that can measure these extraordinary effects, which were impossible to detect with previous systems. The study, design, characterization and production of materials controlling size and shape within ranges of 0.1-100 nm is known as *nanotechnology*.
Nanotechnology is currently one of the most important fields in research and development and has achieved a rapid progress since it was first introduced in 1959 by the Physics Nobel Laureate Richard Feynman. Some potential applications involve energy production, conversion and storage, electronics, photonics, water treatment, drug delivery, pollution control, food treatment and health monitoring and control.

In particular, the following are examples where nanotechnology has provided a breakthrough or where it is a hot research topic nowadays in an extended variety of disciplines:

- Electronics: with the fabrication of transistors whose size has been decreased to the nanoscale and which can be found in millions of computer processors.

- Medicine and biology: some examples are the development of systems for efficient drug-release, and cancer treatments using nanoparticles, etc.
- Chemistry: with the fabrication of chemical nanosensors for environmental/food control or security applications. Nowadays, this is a hot topic of research based on the interaction of the detected substance when it is exposed to a nanomaterial. The advantage is the high sensitivity and low dimensions of the device, as only a very small amount is required to react or modify the properties of the nanomaterial.

Within the scope of nanotechnology, this thesis focuses in *graphene,* a novel and interesting material of only one atom thickness. Its first isolation in 2004 by A. Geim and K. Novoselov [1,2] was a breakthrough in nanoscience as they demonstrated for the first time the separation of a stable two-dimensional carbon layer of only one atom thick with gate-tunable electronic properties. This revolutionary discovery was rewarded with the Nobel Prize in Physics six years later (2010), which opened up a novel and broad scientific research line, still continuing nowadays and covering:

1. Study of new properties and potential applications of graphene, such as transparent electrodes, electronic and optoelectronic devices, composites, etc.
2. Research into improving graphene, solving issues related to fabrication, quality, electrical properties etc.
3. Fabrication of insulating, semiconducting and superconducting two-dimensional materials (e.g., MoS_2, h-BN, WS_2, $MoTe_2$, $MoSe_2$, $NbSe_2$, $TaSe_2$, etc.), which complement graphene's semi-metallic properties.
4. Research into exciting potential for new devices and applications which take advantage of the outstanding properties of these materials individually and in combination (e.g., for novel nano-optoelectronic devices).

This thesis addresses the following questions, related especially to the second point above:

- Can we find industrially compatible techniques, which improve on existing procedures for graphene fabrication while preserving its properties?

- Can we transfer graphene nanotechnology to the macro-scale and make it more suitable for large-scale production?

1.1. Graphene

1.1.1. Definition and structure

Graphene is a single layer of carbon atoms arranged in a honeycomb or hexagonal geometry, as represented in Figure 1 (a). It has been studied theoretically for many years as the building block of graphite and graphitic materials in other dimensions [3,4]. The discovery by A. Geim and K. Novoselov in 2004 [1,2] proved for the first time the isolation of stable graphene sheets.

Graphene's hexagonal structure can also be observed as two triangular lattices A and B with lattice vectors $\overrightarrow{a_1}$= (a/2) (3,$\sqrt{3}$) and $\overrightarrow{a_2}$ = (a/2) (3,-$\sqrt{3}$), with a= 0.142 nm being the distance between two carbon atoms. The bonds between carbons in graphene are in sp^2 hybridization. Here, the electrons of the second orbital 2s are mixed with only two ($2p_X$ and $2p_Y$) of the three 2p orbitals, as shown in Figure 1 (b), forming three strong σ-type covalent bonds, which contribute to a planar assembly of carbons at 120°. The $2p_Z$ orbital remains perpendicular to the planar sp^2-hybrid orbitals, forming a π-type bond, which can be seen as two lobes centered in the nucleus. This electron is delocalized over the whole graphene molecule and responds to the electric conductivity. The sp^2-hybrid orbitals form a very stable structure of only one atom thick with a very strong binding, which gives graphene its extraordinary mechanical strength, having a Young's modulus of ≈1TPa and tensile strength of ≈ 100 GPa [5–7].

If several layers, as with multilayer-graphene, or thousands of layers, in the case of graphite, are stacked together, the weak attraction between them, and consequently what causes them to be stacked together, is a weak Van-der-Waals force caused by the π-perpendicular orbital. The weakness of this force is what makes graphite a very soft material, allowing its mechanical cleaving to isolate a single layer. The overlap of the $2p_Z$ orbitals between consecutive carbon atoms produces a filled band of π orbitals (valence band) and an empty band of π^* orbitals (conduction band).

Due to the previously stated particular atomic arrangement of carbons in sp^2 hybridization, high quality graphene has unique and extraordinary properties, such as high electrical conductivity (initially found to be 10.000 $cm^2/V{\cdot}s$ [1], but recently improved up to 350.000 $cm^2/V{\cdot}s$ [8]), high mechanical resistivity as previously mentioned, high optical transmittance with an absorption of only 2.3% in the visible spectral range, and high thermal conductivity (3000-5000 $W/m{\cdot}K$ [9]), which would allow heat dissipation in large-scale integrated electronics.

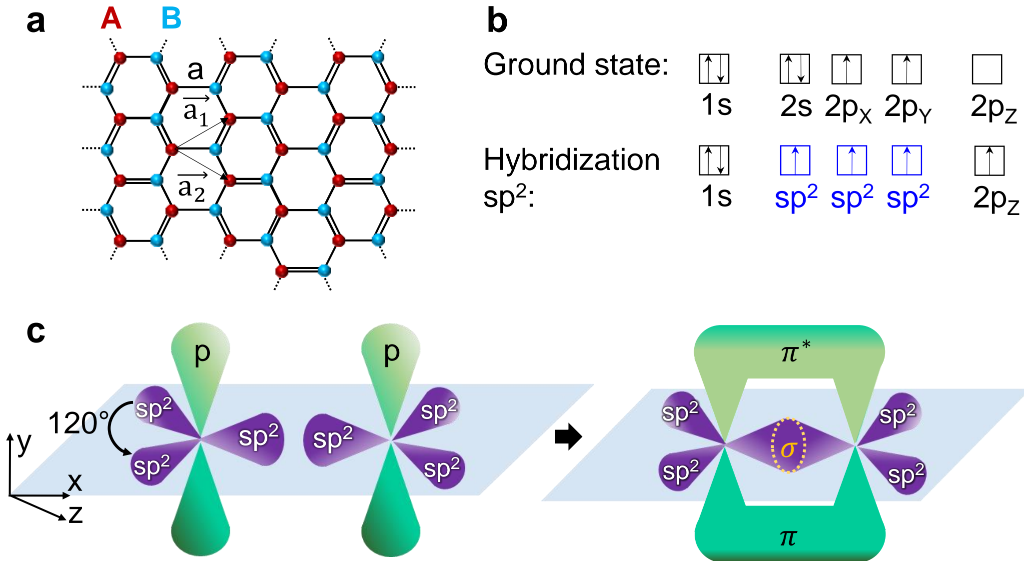

Figure 1. (a) Scheme of the graphene structure in a hexagonal honeycomb geometry of carbon atoms. Carbons forming the hexagonal structure can be divided into two types, A (red dots) and B (blue dots), which form two triangular lattices with lattice vectors $\vec{a_1}$ and $\vec{a_2}$ ($\vec{a_1}$= (a/2) (3,$\sqrt{3}$), $\vec{a_2}$= (a/2) (3,-$\sqrt{3}$), a: C-C distance = 0.142 nm). (b) Difference between electron occupation in orbitals at the valence band at the ground state and forming sp^2 hybridization of graphene. (c) Scheme of graphene where one of the sp^2 orbitals forms an σ-bond with another sp^2 orbital from the next carbon atom, and the free p-orbital perpendicular to the sp^2 forms a π-bond with the free p-orbital of the next carbon atom.

Nonetheless, during graphene growth structural defects can occur within the hexagonal lattice, which will cause the degradation of its unique properties. Examples of these defects are point (also called zero-dimensional), or linear (one-dimensional) defects (e.g., grain boundary), which are shown in Figures 2 (a, b) and Figure 2 (c), respectively [10–12]. It has been demonstrated that both types of defects serve as carrier traps and scattering centers, thus affecting graphene's electronic properties. In the case of a point defect, as it only affects a very small area it will degrade graphene to a lesser extent than a linear defect. For the latter, it has been theoretically calculated that there will be a drastic reduction in the mechanical strength of the graphene. Moreover, it dramatically degrades carrier mobility and thermal conductivity as the linear defect hampers carrier/heat flow.

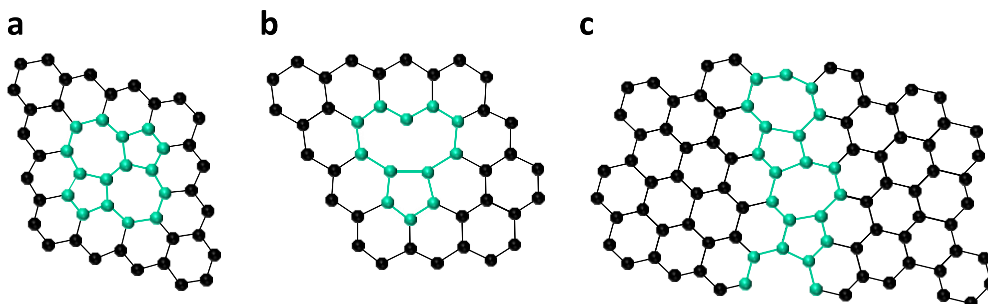

Figure 2. Examples of structural defects in graphene. (a-b) Point defects, and (c) Linear defects (grain boundary). Specific type of defect in (a) is called Stone-Wales, while (b) is due to a single-vacancy of carbon in the hexagonal structure [10–12].

1.1.2. Electronic transport properties

The hexagonal lattice of graphene give rise to a band structure with linear dispersion (Figure 3 (a)) where the valence and conduction bands meet at the, so called, Dirac points K and K'. In neutral conditions, when graphene is undoped, the Fermi energy lies at the meeting point between both bands (Figure 3 (b)).

Graphene also has an ambipolar electric field effect, which means that its doping can be tuned electrostatically between an excess of electrons (n-doping), and an excess of holes (p-doping). [1,13]. Between these two extremes, graphene exhibits a minimum of conductivity at its neutrality point where the density of charge carriers is minimum [2,13,14].

Graphene doping it is not stable with air and humidity, as species adsorb into the surface, attracted by the electrons of the π-orbital. To avoid these contamination issues, most graphene transistors are measured in a vacuum or controlled atmosphere (N_2 or Ar), and, also, the graphene is encapsulated by covering it with a thin dielectric layer, such as Al_2O_3, [15], h-BN [16], etc.. The ambipolar effect is observed when the graphene is located in a field effect transistor configuration (FET), where, typically, graphene is transferred to a Si/SiO_2 substrate, which serves as a gate electrode, and then it is contacted from the top with Au electrodes. In this case, the ambipolar effect will be measured by gating through the Si (or back) side of the substrate, which is known as back-gating of the FET. However, in the case of a different type of substrate (e.g., dielectric, polymer, etc.), the graphene can be transferred to the substrate and be covered with a dielectric and a metal on top, which will act as the gate electrode. In this case, as the gate voltage is applied over the dielectric covering the graphene from the top, the measurement is known as top-gating of the FET. In both cases, the variation of the gate voltage induces a change in the carrier concentration (n_S) in the graphene, moving the Fermi level from the equilibrium to the conduction or to the valence band. Thus, the gate voltage results in electrostatic n- or p-doping.

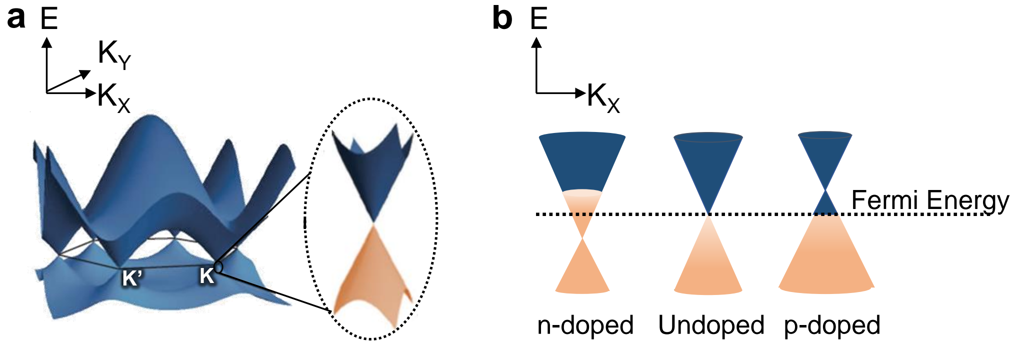

Figure 3. Band structure of graphene. (a) 3D-picture of graphene band structure with K and K' Dirac points. Zoom area shows the zero-bandgap of graphene where valence band (bottom) and conduction band (top) meet. Adapted from ref. [14,17]. (b) 2D image of graphene band structure where graphene is undoped and with n- and p-doping. In the undoped case, bands are symmetric, having the Fermi Energy at the Dirac point. For n-type graphene, conduction band is deformed, having the Fermi Energy above the Dirac point, while for p-type graphene, valence band is deformed with the Fermi Energy below the Dirac point.

Graphene mobility (μ_H) is also important as it can reach values close to 350.000 $cm^2/V\cdot s$, or even 10^6 $cm^2/V\cdot s$ for suspended graphene [18,19], which is very high compared to other semiconductors (e.g., from 480 to 1350 $cm^2/V\cdot s$ for Si,[20,21]). This would lead to much faster electronic devices compared with the Si-based industry. However, in practice the achievement and repeatability of these high values, especially when using large areas of graphene, is a challenge due to issues related to the graphene quality, growth, transfer, or effect of the desired target substrate. Apart from improving the procedure of synthesis and transfer of the graphene, a possible solution to improving mobility is the encapsulation of the graphene with an intermediate material in between the target substrate, such as hexagonal boron nitride. The wide bandgap of this semiconductor (5.97 eV), together with the advantage of having the same crystal structure as graphene, allows a good lattice matching between both materials, consequently favoring the electrical conductivity of the graphene [16].

Also important is the quantum Hall Effect in graphene, which is especially relevant in this thesis and will be further explained in section 1.2. Characterization techniques. This phenomenon allows a direct measurement of graphene n_S when the material is exposed to an external magnetic field [22,23]. The physical principle underlying the Hall Effect is the Lorentz force (F_L), a force experienced by charges that move along the electric field (E) direction and are exposed to a perpendicular magnetic field (B). The resulting F_L is perpendicular to E and B, with the actual direction determined by the right-hand rule convention. Thus, F_L can be expressed as:

$$\overrightarrow{F_L} = q_e(\vec{E} + \vec{v}x\vec{B}) \quad \text{(Eq. 1)}$$

where q_e ($1.602x10^{-19}$ C) is the elementary charge and v is the particle velocity.

As a consequence, a certain number of charge carriers will accumulate at the edge of the device and a transversal Hall voltage (V_H) will appear. V_H can be expressed as:

$$V_H = {}^{I \cdot B}/_{q_e \cdot n_S} \quad \text{(Eq. 2)}$$

If V_H is plotted versus B, n_S can be calculated using the slope of the linear fitting between both terms:

$$n_S = {}^{I}/_{q_e} \cdot (\Delta V_H/\Delta B) \quad \text{(Eq. 3)}$$

If the slope is negative, the graphene is n-type doped (excess of electrons), while if the slope is positive, it is p-type doped (excess of holes). From this calculation, μ_H can also be calculated, determining, firstly, the sheet resistance (R_S) of the graphene using the Van der Pauw method (see section 1.2. Characterization techniques). Measuring R_S at B=0, μ_H can be determined from the Drude model [24]:

$$\mu_H = {}^{1}/_{q_e \cdot n_S \cdot R_S} \quad \text{(Eq. 4)}$$

1.1.3. Growth techniques

Since graphene's novel properties were experimentally revealed in 2004 [1,2] using the mechanical exfoliation technique, several techniques have been developed and studied in order to produce large graphene sheets of high quality. These techniques are briefly summarized below, focusing mainly on Chemical Vapor Deposition (CVD), as this will be the one used to grow graphene in this thesis.

Micromechanical Exfoliation

This technique led to the first isolation of graphene in 2004. K. Novoselov *et al.* [1] were able to separate one layer of graphene from a piece of highly oriented pyrolytic graphite (HOPG) or natural graphite by peeling layers using scotch tape. By using the adhesive tape, Van der Waals forces were lower than the force applied, and the graphite layers could be separated progressively until one layer was isolated. After that, characterization of the graphene was performed by transferring it to Si/SiO_2 in order to obtain optical contrast and distinguish the number of layers. Graphene quality obtained by this method is excellent in terms of electrical properties (with μ_H values varying from 3000 to 10000 $cm^2/V{\cdot}s$ [1]), typically with lateral sizes of a few tens of microns. The main issues with this technique are the poor control of the thicknesses and sizes of the graphene flakes during production, together with its limitations in fundamental research applications, being unsuitable for large-scale production.

Chemical exfoliation

This technique consists of the chemical exfoliation, via organic solvents, of graphite powders to high quality graphene flakes[25–27]. The dispersions of graphene flakes can be later deposited onto the target substrates by spray-coating, vacuum filtration, Langmuir-Blodgett assembly [25], or drop casting. Similar work in ref. [26,28] demonstrates the exfoliation of graphene from graphite flakes by adding surfactants (e.g., sodium cholate NaC) to water. Also, ref. [29] demonstrates the graphene electrochemical exfoliation from graphite when applying voltages of ±10V.

The advantages of this method are its versatility and the possibility for it to be scaled-up at lower costs than other growth techniques, together with the wide variety of target substrates that can be used. The main application of graphene flakes obtained by this technique (graphene flakes are deposited together, finding bilayer or graphene multilayer areas), is for the production of graphene-based composites or films and in photovoltaic solar cells [30,31].

Chemical reduction of graphene oxide

This technique is similar to the previous one but, here, graphite oxide is dispersed instead of graphite. The graphite is firstly oxidized using, typically, a modified Hummers method [32]. Then, the graphite oxide is exfoliated in water by ultrasonication, producing layers of graphene oxide (GO). GO is a material consisting of graphene sheets that, due to graphite oxidation, have been chemically functionalized with compounds (e.g., hydroxyl groups, epoxides etc.), mainly at the edges of the graphene sheets or in defects positions. The presence of the hydroxyl groups is what enables the dispersion of graphite oxide in water. After this, the GO is chemically reduced with hydrazine, removing previous groups and obtaining the graphene structure. The main issue of this technique is that the initial chemical functionalization disrupts the electronic structure of the graphene, and then after the reduction of the GO, a significant number of defects are left in the structure [31–35] .

SiC sublimation

This technique consists of the use of silicon carbide commercial wafers on which to grow epitaxial graphene. The growth mechanism is based on the controlled sublimation of Si from single-crystal SiC wafers. By heating the substrate to high temperatures (1000-1600°C, atmospheric or ultra-high vacuum pressure, UHV), Si sublimates leave a few layers of free carbon on the surface, which rearrange to minimize energy forming graphene [36]. With this technique, epitaxial graphene is obtained with high mobility of up to 25.000 $cm^2/V \cdot s$ [37]. The advantage of this technique is that it can be scaled up to produce large sheets of high quality graphene and can be patterned using the nanolithography method without the need for transfer. However, the main issues are the high cost of the SiC substrates and the

costs associated with high temperature and sometimes UHV growth conditions (cost of graphene on SiC(0001)= 7.7 million $ per m^2, Graphene supermarket [38]).

Chemical Vapor Deposition (CVD)
This technique is the most promising one in terms of great versatility and high yield for production of high quality graphene over large areas [39–41]. Specifically, S. Bae *et al.* [40] demonstrated for the first time the growth and consecutive transfer of four layers of graphene in 30-inch sizes by a roll-to-roll process, thus probing the scalability of the CVD technique in the production of graphene on a large scale. The fundamental of this technique is the graphene synthesis by employing transition catalytic metals in order to reduce the activation energy of carbon decomposition from a hydrocarbon source [42–48]. The use of CH_4 and C_2H_2 gases is the most common method, although solid carbon sources have also been used [49]. The main advantage of using more reactive gases, such as C_2H_2, is the possibility of reducing the temperature growth of the graphene, which would allow the use of different types of substrates, together with a reduction of growth processing costs [50]. The use of transition metals as the catalyst comes from their reactivity due to the partially filled d-orbitals or from the formation of intermediate compounds that adsorb and activate the reacting substances.
There are three main aspects to consider for obtaining high-quality graphene by CVD: the type of catalyst, the crystal orientation and grain size, and the nucleation control of the graphene growth.

Among the possible catalysts, there are many transition metals that enable the graphene growth, including Fe, Ru, Co, Rh, Ir, Ni, Pt, Cu, Au, stainless steel and Cu-Ni alloys - further details can be found in ref.[51]. Amongst these, Cu has the lowest affinity to carbon, without carbides production and with very low carbon solubility (0.001–0.008% wt. at 1084°C) if compared to Ni (0.6% wt. at 1326°C) or Co (0.9% wt. at 1320°C). Cu's low reactivity to carbon is attributed to its filled 3d-electron shell {[Ar] $3d^{10}4s^1$}, which allows the formation of soft bonds with the carbon by a transference of charge from the p-electrons in the sp^2-carbon to the empty 4s-orbital of the Cu. This low affinity between Cu and C, together with its ability to form intermediate soft bonds, makes Cu a good catalyst for the production of graphitic materials. Co and Ni (with $3d^7$ and $3d^8$ orbitals, respectively) are also possible as they are located between the two extremes of stability, Fe being the most unstable electronic configuration and Cu the most stable [52,53].

As a result, the two most widely employed catalysts are Cu and Ni, each one producing a different growth mechanism depending on the difference in carbon solubility. As it can be seen in Figure 4 below, the low carbon solubility in Cu (a) promotes its adsorption on the surface [54], whereas the high carbon solubility in

Ni (b) promotes carbon absorption, diffusion inside the metal, and post-segregation to the metal surface when the temperature is reduced [48,54–56]. Nonetheless, the deposition of a monolayer graphene on Ni has been proven by controlling growth parameters, such as low growth times and medium values of cooling rates [51]. The highest quality CVD graphene has been obtained on µm-thick Cu foils [40] due to the fact that carbon atoms remain on the catalyst surface and, therefore, monolayer graphene sheets can be easily grown. In contrast, on Ni foils, graphene multilayer mostly grows with poor control over the number of layers [57].

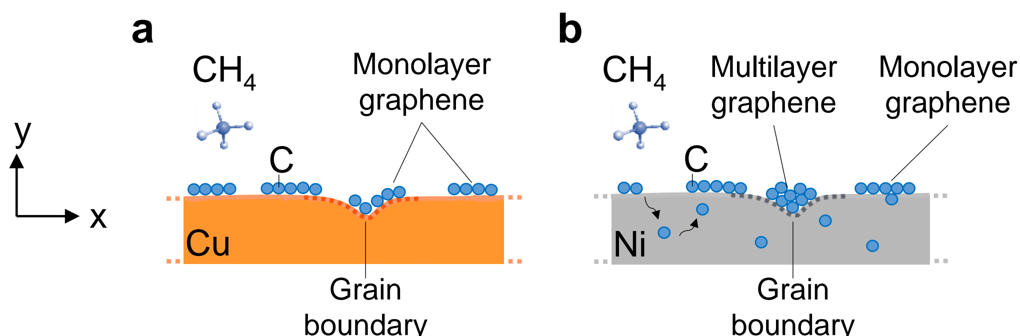

Figure 4. Graphene growth mechanism via CVD using Cu (a) and Ni (b) as catalysts. (a) CH_4 molecules dissociate at the Cu surface with carbon adsorbing on the surface and aggregating for graphene monolayer formation. (b) CH_4 molecules dissociate at the Ni surface with a consequent diffusion of carbon inside the metal and a post-segregation to the Ni surface forming graphene monolayers and multilayers at the grain boundaries.

Instead of foils, sputtered or evaporated metallic films can also be used as graphene growth catalysts. For example, on thin Ni films of a thickness 150-200 nm, a partial coverage with monolayer graphene has been obtained, although this was mixed with multilayer graphene, which starts its growth preferentially at the grain boundaries of the metal [58–61]. The reason for this is that the metallic films (Cu and Ni) deposited by these techniques have multiple grains, whose boundaries promote graphene defects, and in the case of Ni, because of carbon segregation, it deposits multilayer graphene.

In this sense, crystal orientation of the metal plays an important role for the growth of high quality graphene, and annealing of the metal film is necessary in order to improve its crystal orientation and grain size [62,63].
In the case of Cu, Cu(111) is determined to be the preferred orientation for high quality graphene growth as the lattice mismatch is very low (7°) [64] . Ref. [65] also reports the influence of Cu crystal orientation on graphene strain and doping.
In the specific case of Ni, the slow annealing of the Ni, together with the high temperatures associated with the graphene deposition, promotes large grain sizes

of Ni(111), improving the graphene quality [51]. Ref. [66] highlights the difference between graphene growth using a polycrystalline Ni foil and a crystal oriented Ni(111) wafer. While the multiple Ni boundaries promote the growth of multilayer graphene, the use of Ni(111) favors the formation of uniform monolayer and bilayer graphene domains. This increase in graphene quality is due to the absence of interface boundaries, which also provides a smoother surface if compared to the foil, and an excellent hexagonal lattice match between the graphene and Ni(111) face, being 2.497 Å and 2.46 Å for Ni(111) and graphite, respectively.

Another possible solution for the promotion of a single crystal orientation in the metallic films, consequently favoring the graphene quality, is the use of target substrates with the desired orientation. One example is ref. [67], where metallic films were deposited onto c-plane sapphire. However, the main issue with graphene production by single-crystal systems is the difficulty in producing single-crystal metals on a large scale. Because of this, the future of large-scale graphene is focused on growing it onto polycrystalline metal films or foils. When using the latter, a proper conditioning is necessary before the CVD treatment, such as cleaning with organic solvents, using acids to remove oxides and annealing in H_2 to increase the grain size and reduce the oxides from the metal surface [39,40,62]. The possibility to scale-up CVD and the low price of some current polycrystalline Cu foils (e.g.: Alfa Aesar Cu foils of 25 μm thickness cost 120€ per m^2 [68]) makes the growth costs affordable for large-scale implementation.

Regarding the growth, it is also important to limit the graphene nucleation sites in order to avoid or reduce the number of defects that can be created at the domain boundaries due to misalignment of the carbon atoms [69]. This can be achieved by reducing the carbon gas flow, allowing a slow rate of nucleation of the surface, hence larger graphene domains [70]. Also, work in ref. [71] has demonstrated that a reduction of the foil roughness via electro-polishing enhances the graphene quality as a smoother catalytic surface reduces the graphene nucleation, and, consequently, defects in the graphene structure.

Finally, pressure also has an effect on graphene. Although UHV is not suitable for large-scale production of graphene due to the high costs of the equipment and maintenance, it has been demonstrated that low pressures limit the graphene growth to a monolayer [72].

Tables 1 and 2 below show the performance of CVD growth of graphene on Cu and Ni foils or thin-films, highlighting the types of catalyst used, the CVD process conditions and the main results obtained.

Table 1. State-of-the-art of graphene grown on Cu foil/thin films indicating process conditions and main characteristics of the work

Catalyst (thickness)	Target substrate (transfer method)	Annealing conditions	CVD conditions	Main comments	Ref.
Cu foil, 30 inch length	Si/SiO_2 and PET (PMMA -transfer)	1000°C, 30 min 12 mbar, H_2	1000°C, 30 minutes 61 mbar, CH_4:H_2	4 layers. Domains 100 µm Post-doped: HNO_3. T= 90% and R_S= 30 Ω/sq.	[40]
Cu foil (25 µm) Cu/W foil (50 µm)	Si/SiO_2 (PMMA transfer)	1080°C, 30 minutes H_2 (200 sccm)	1080-1120°C 28 minute-4 hours CH_4:H_2	Cu melted. Domains= 50 µm μ_H: 1000-2500 $cm^2/V\cdot s$; R_S= 609 ± 200 Ω/sq.	[73]
Cu foil (25, 125 µm)	PET (hot press and Cu etching)	1000°C, 1 hour 1.01 bar, H_2	1000°C, 3 hours 1.01 bar, CH_4:H_2	Cu is polished. Domain: 100µm Area: 40 inch	[43]
Cu (100), (110) (111). Cu foil	-	1000°C, 20 min H_2 (50 sccm)	1000°C, 20 min $^{12}CH_4$ or $^{13}CH_4$	Doping/strain depends on Cu orientation. Domain= 20-50 µm	[65]
Cu foil (25 µm)	Si/SiO_2/h-bN PDMS/PVA/PMMA	1035°C, 20 minutes $7\cdot10^{-3}$ mbar, H_2	1035°C, 2 hours $7\cdot10^{-3}$ mbar, CH_4:H_2	μ_H=350000 $cm^2/V\cdot s$ Cu foil reused. Domain=500 µm	[8]
Cu foils (smooth: 20 µm, and 25 µm)	Resist + Cu etching. PVC +laminator + Cu etching	1035°C, 30 minutes H_2	1035°C, 10 minutes CH_4: H_2	Smooth Cu improves graphene quality Flake area: 1100 μm^2	[74]
Cu foil (25 µm), electropolished	Si/SiO_2 (Cu etching)	10°C/minute, 1050°C, 4 hours H_2	1050°C, 4 h PS evaporated, Ar/ H_2	Polished Cu. Annealing: Cu (111) Cu grains: 500 µm Graphene domains 240-560 µm	[63]

Table 2. State-of-the-art of graphene grown on Ni foil/thin films indicating process conditions and main characteristics of the work

Catalyst (thickness)	Target substrate (transfer method)	Annealing conditions	CVD conditions	Main comments	Ref.
Ni foil, (0.5 mm)	SiO_2 (sacrificial Si rubber etched with HNO_3)	1000°C, 1 hour 1.01 bar, H_2	1000°C, 20 minutes 1.01 bar, CH_4: H_2: Ar	Study of cooling rates. Medium value (10°C/s) reduces multilayer graphene	[57]
Ni (500 nm)/SiO_2/Si	Si/SiO_2 (PMMA transfer, HCl)	900-1000°C 10-20 minutes 1 atm, Ar:H_2	900-1000°C 5 - 10 minutes 1.01 bar, CH_4:H_2	1-12 layers. Ni grain:-20 μm μ_H: 100 to 2000 cm^2/ V·s; R_S= 770-1000 Ω/sq.	[58]
Ni (500 nm) /SiO_2/ Si Ni (111)	Si/SiO_2 (polycrystalline Ni)	900°C, 15 minutes 1.01 bar, H_2	900°C, 10 minutes 1.01 bar, CH_4 Cooling: 16°C/min	Carbon segregation (Ni-Ni) and precipitation. Layers: Ni(111): 1-2; Polycrystalline Ni: 3	[66]
Ni (100-300 nm) / SiO_2/Si	Si/SiO_2	700°C, H_2/Ar 1000°C, H_2/Ar,	1000°C, 50-120 s CH_4: Ar Ultra-fast cooling	Bilayer graphene low defective (low D peak)	[75]
Ni (50 nm) / SiO_2 (300 nm) /Si	Quartz	-	Plasma: 450-475°C, 100 W, 100 seconds 12 mbar, CH_4/H_2/Ar	Use of lower temperatures. R_S= 4000-9000 Ω /sq.	[55]
Ni (10-200nm)/a:SiCH PECVD (7-80 nm)/SiO_2 (300 nm)/Si (100)	SiO_2 and Si nitride grids (PMMA and Ni etching)	800°C, 15 minutes	600-800°C, 1-15 minutes 67 mbar, Ar	Rapid, simple, low cost. Transparent; R_S= 565 Ω/sq.	[49]

1.1.4. Graphene doping

As discussed previously, graphene is a zero-band gap semi-metal, but its electrical properties can be tuned by changing the doping level. This is generally carried out by one of the following three types of procedure: (1) chemical or surface transfer doping, (2) substitutional doping, or (3) electrostatic doping.

In the following paragraphs, the main results from the three techniques will be presented.

Chemical or surface transfer doping

This technique is based on the graphene's surface deposition of chemicals, which act as electron donors or acceptors. Generally, chemical or surface transfer doping does not produce defects or alter the graphene structure and it is reversible, which means that a removal of the molecules from the graphene surface will return the doping to its initial value.

This type of doping occurs due to a charge transfer from the adsorbed dopant to the graphene or from the graphene to the adsorbed dopant. The role of the electron donor or acceptor between the dopant and the graphene is determined by (1) the position of density states of the highest occupied molecular orbital (HOMO) and lowest unoccupied molecular orbital (LUMO) of the dopant, and (2) the Fermi level of the graphene. If the HOMO of the dopant is higher than the Fermi level of the graphene, the dopant will be the electron donor (graphene: n-type doping). However, if the LUMO of the dopant is lower than the Fermi level of the graphene, the dopant will be the electron acceptor (graphene: p-type doping). In other words, adsorbed dopants with electron withdrawing groups will cause graphene p-doping while dopants with electron donor groups will cause graphene n-doping.

Some examples of chemical doping are the adsorption of HNO_3 (p-doping) [76], also for the case when graphene is transferred to polyethylene terephthalate (PET) by a roll-to-roll technique [40], NO_2 (p-doping) [77], H_2O (p-doping) [77], ethanol (n-doping) [78], and NH_3 (n-doping) [79,80]. One issue related to this type of doping is the instability of the doping levels over time (e.g., HNO_3 and $AuCl_3$ on graphene surfaces). For more details about this technique, see ref. [78].

Substitutional doping

This technique is based on the substitution of graphene carbons with atoms with a different number of electrons in the valence band. This replacement of atoms in the graphene hexagonal structure is performed during the CVD growth or during the SiC decomposition to graphene. To perform n-type doping, nitrogen is typically the atom that replaces carbon in the graphene structure as it has more electrons in the valence band than carbon [81,82]. Depending on the site that the nitrogen occupies, three types of configurations can be distinguished: pyridinic or pyrolic when the nitrogen occupies sites at the edge of the graphene sheet or

defects sites, respectively, or graphitic when the nitrogen replaces a carbon on the graphene plane. The introduction of nitrogen causes graphene ripples that promote the increase of the D band in Raman characterization.

For p-doping of graphene, compounds like boron are typically used, as it has less electrons in the valence band than carbon. Graphene with boron included in the sp^2 network has been synthesized by arc discharge of graphite electrodes in the presence of H_2: He: B_2H_6 [83]. A result of Raman characterization is the increase of I_D/I_G ratios and the shift in the G band towards higher frequencies. However, the use of this doping technique has been shown to affect the graphene quality, inducing irreversible defects on the structure.

For more details about this technique, see ref. [78].

Electrostatic doping

This technique is based on the modulation of the Fermi level of graphene by modifying the gate voltage, thus allowing the n- and p-type doping. The advantage of this method is that the graphene doping is reversible and can be accurately controlled. As mentioned in section 1.1.2. Electronic transport properties*,* the most common techniques used to perform this type of doping are either back- or top-gating, depending on the substrate nature (Si/SiO_2 or a dielectric, respectively). In the case of back-gating, the polarity of the gate voltage introduced by the Si on the bottom (back) side of the device will cause the n- or p-doping of the graphene. The first issue associated with electrostatic doping is the limitation of achievable n_S for a given applied voltage, due to the low capacitance of the Si/SiO_2 (200 nm)/graphene structure. This capacitance can be increased by reducing the thickness of the SiO_2. However, this is finally limited by the breakdown of the dielectric (SiO_2) used. In this respect, the use of thinner or higher dielectric constant materials (e.g., MoS_2, h-BN etc.), oxides, ionic liquids or polymers have been studied [1,84,85]. The second issue of this technique is the influence of the target substrate on the graphene or, in the case of top-gating, the dielectric deposited on top of it.

1.1.5. Graphene transfer

For the outstanding properties of graphene to be fully utilized, it must be transferable to a wide variety of substrates, such as SiO_2, Si/SiO_2, polymer substrates or metals. Several methods have been developed toward this goal, typically depending on the graphene synthesis route. In particular, the high impact of CVD for producing large areas of graphene has promoted the development of compatible techniques to transfer graphene from the catalyst to the target substrate.

The most commonly used method relies on a polymer-assisted transfer process, which was developed firstly by Reina *et al.* [86] and then adapted with

modifications by Li *et al.* [39]. This procedure is typically known as the "wet-transfer" method, where, as shown in Figure 5, a polymeric layer - poly(methyl methacrylate) (PMMA), polystyrene (PS), polydimethylsiloxane (PDMS) or thermal-release tape (TRT) [40,87–91]- is spin-coated on graphene. The polymer serves as a support to protect the graphene while the metal catalyst underneath is etched away. Several etchants have been used for this purpose, the most typical being ammonium persulfate ($(NH_4)_2S_2O_8$) [40,92–95], as it has been shown to provide cleaner graphene surfaces. Moreover, other etchants, such as iron chloride ($FeCl_3$) [90,91,96] or iron-nitrate ($Fe(NO_3)_3$) [39], have provided good quality transferred graphene.

After the Cu is removed, the resulting floating structure (graphene/PMMA) is rinsed three times in de-ionized (DI) water to remove any etchant residues from the graphene or located on top of the target substrate. Finally, the PMMA is removed by dipping the sample in a beaker of acetone and then isopropanol for 15 minutes each. The prevention of cracks or gaps between the graphene and the substrate can be achieved by putting a droplet of PMMA on the PMMA/graphene [39] or by heating the structure above PMMA's glass transition heat level (180°C) [92]. Thus, the graphene's contact with the target substrate will be improved. This technique has been widely used by the scientific community and, as demonstrated by Bae *et al.* [40], to transfer 30 inches of graphene by a roll- to-roll process to PET and Si/SiO_2 substrates.

The main advantages of PMMA are its low cost, its versatility and its good mechanical properties; the main disadvantage is the residue left on the graphene surface after the PMMA removal. This residue poses a significant challenge as it has a detrimental effect on graphene's electrical and mechanical properties [93,95,97,98]. One possible solution is the addition of a thermal annealing step in a controlled atmosphere to reduce the contamination level [96,99,100].

Two different techniques that can be classified as "wet-transfer" type techniques are electrochemical transfer and face-to-face transfer. The former was proposed by Wang *et al.* [101] using electrochemical exfoliation to detach the graphene from the Cu foil. This technique works as an electrochemical cell, where the Cu/graphene is previously covered with PMMA, being the *cathode*, a glassy carbon rod is used as the *anode*, and both parts are immersed in the electrolyte ($K_2S_2O_8$, 0.05M). When a voltage is applied between the electrodes, H_2 is released, forming bubbles at the cathode due to the dissociation of H_2O. Due to the force induced by the H_2 bubbles, the graphene/PMMA is separated from the Cu foil, allowing Cu recycling. This represents the main advantage of this technique. However, this method is limited, restricted to electrically conductive metal substrates, and still has the challenge of using PMMA, which produces residues after its removal.

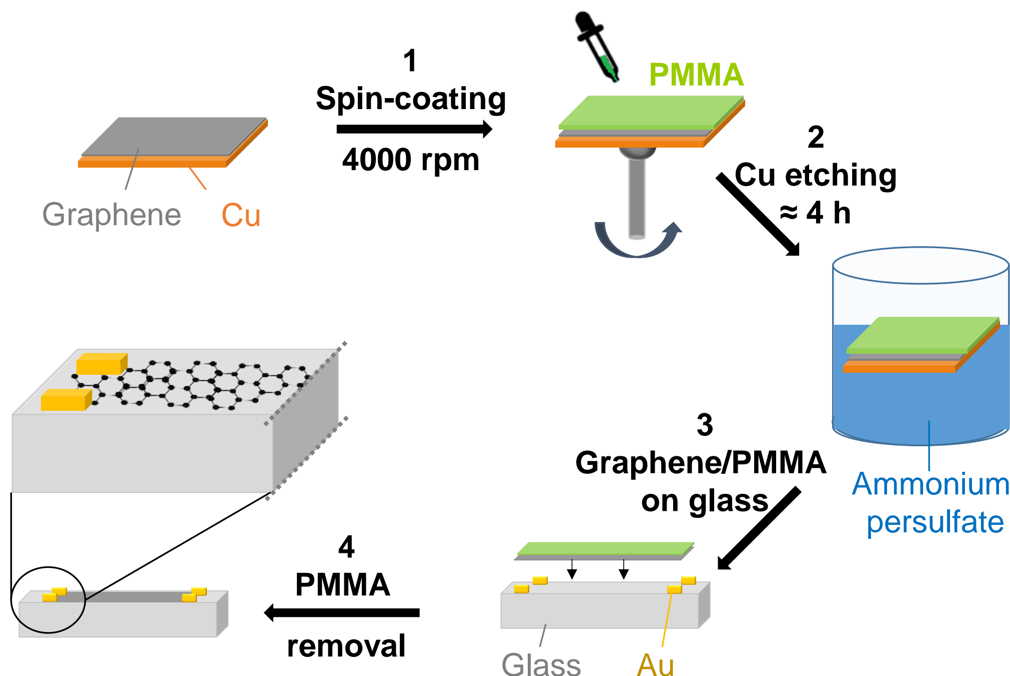

Figure 5. Wet transfer of CVD graphene from the Cu foil catalyst to the target substrate: (1) spin-coating of PMMA on Cu/graphene; (2) after PMMA drying, Cu/graphene/PMMA is floating on ammonium persulfate (3-4 hours) for Cu etching; (3) after dissolving Cu, graphene/PMMA is rinsed three times in a beaker with DI water and then placed on the target substrate. Sample is dried using N_2 gun or by storing in vacuum; (4) PMMA is removed by dipping the sample in acetone and isopropanol (15 minutes each). Zoomed area in (4) shows graphene on the target substrate with previously deposited Au contacts.

The second technique proposed by Gao *et al.* [94] is based on the pre-treatment of the substrate with N_2, where the Cu will be sputtered. After the graphene is grown and during the Cu etching process, they suggested that N_2 bubbles trapped between the substrate and graphene contribute to the formation of capillary bridges that allow the graphene to remain attached to the substrate. Finally, a very promising alternative has been the development of techniques based on graphene "dry-transfer", where the graphene is "peeled-off" from the Cu with the advantage of the catalyst recycle. This technique will be further explained in Chapter 4.

A recent review, ref. [102], provides more details in all the progress made on CVD graphene transfer by both wet and dry methods, and also on epitaxial graphene grown on SiC substrates [103].

1.2. Characterization techniques

For evaluating the quality and properties of graphene, many techniques have been established. The main characterization methods used in this thesis are atomic force microscopy (AFM), bending tests, contact angle, Energy-dispersive X-ray spectroscopy (EDX), Four point-probe measurement, grazing incidence X-ray diffraction (GXRD), Hall measurements, optical microscopy, Raman spectroscopy and Scanning Electron Microscopy (SEM).

1.2.1. AFM topography

This is used for surface roughness and topography measurements at the atomic scale. With this technique, the quality of the graphene can be measured by detecting residues, holes and graphene wrinkles. Also, because it is an extremely accurate technique, the thicknesses of the samples can be measured, thus determining the number of layers in the graphene. The simultaneous measurement of the phases is very useful because it allows for the detection of the different materials in the sample. The topography information is obtained by measuring a mechanical frequency change of an oscillating micron-scale cantilever due to interactions with the surface, such as Van der Waals, capillary or electrostatic forces. The frequency of the cantilever is recovered by modifying the amplitude of the measurements, which correlates to the height of the surface morphology.

In this thesis, we have used the AFM Bruker/Veeco Dimension 3100 in tapping mode for measuring the graphene on Ni films and glass in Chapter 1, and on Cu foil, polyimide (PI) and glass in Chapter 4.

1.2.2. Bending tests

Flexibility tests are performed using a two-point bend custom set-up connected to a motor driven by an electronic controller, which allows the arm to move back and forth in a horizontal direction. In this thesis, we have used this setup to measure graphene transferred to PET and PI substrates in Chapter 4. Samples were subjected to continuous bending and the R_S was measured after each bending cycle. The bending radii continuously varied between 2 cm and 7 mm.

1.2.3. Contact angle

This technique determines the wetting properties of a surface by measuring the angle (θ) formed by a pure liquid droplet when it is deposited on the relevant surface. Depending on the measured θ between the two interfaces (liquid-solid and liquid-vapor), the surface can be: (1) hydrophilic, if θ <90°, (2) hydrophobic, if θ>90°, or (3) superhydrophobic, if θ>150°. There exist highly hydrophobic surfaces with low surface energy (e.g. fluorinated materials), where θ≈120° [104,105].

In this thesis (Chapter 4), we have used the DSA100, KRÜSS for measuring the wetting properties of graphene transferred to glass or PET substrates covered with PI. This equipment has a high-resolution camera, which allows the profile capture and contact angle calculation.

1.2.4. Energy dispersive X-ray spectroscopy (EDX)

This is an x-ray technique used in conjunction with SEM to identify the elemental composition of materials. The resulting spectra show peaks corresponding to the elements making up the true composition of the sample being analyzed.

In this thesis, we have mainly used the EDX, Oxford INCA to evaluate a total removal of residues from the graphene surface. These evaluations can be found in in Chapters 2 and 3. The analysis corresponds to at least 10 points in the sample with voltages of 10 kV (Chapter 2) and between 5 kV and 15 kV, depending on the nature of the sample (Chapter 3).

1.2.5. Four-point probe measurement

By definition, intrinsic properties such as electrical resistivity or conductivity should be constant and independent of size for a given bulk material. This is not true for a thin film as when its thickness is compared with the characteristic length scale of a physical phenomenon, the intrinsic properties are affected by so called size-effects [106]. The limitation of size affects the electrical conductivity when the film thickness becomes comparable to the electron mean free path in the medium. Thus, the electrical resistivity between the bulk material and the thin films cannot be considered to be the same. It is very common to measure the electrical surface properties of a film through the R_S in Ω/sq. units:

$$\varrho_t = R_S \cdot t_F \qquad \text{(Eq. 5)}$$

where ϱ_t is the thin film electrical resistivity and t_F is the thickness. The R_S can be measured directly using a Four-Point probe set-up (Cascade Microtech 44/7S 2791) connected to a multimeter (Keithley 2001).

The set-up, which is shown in Figure 6 (a), has four tips aligned and set 1 mm apart, which are brought into contact with the measuring surface. A test current (I) is injected through the outer tips while the inner tips measure the voltage drop (V), as shown in Figure 6 (b). As can be observed in the circuit on the right-hand side, the separation of the current and the voltage avoids the measurement of the contact resistance (R_C), which makes the measurement more accurate.

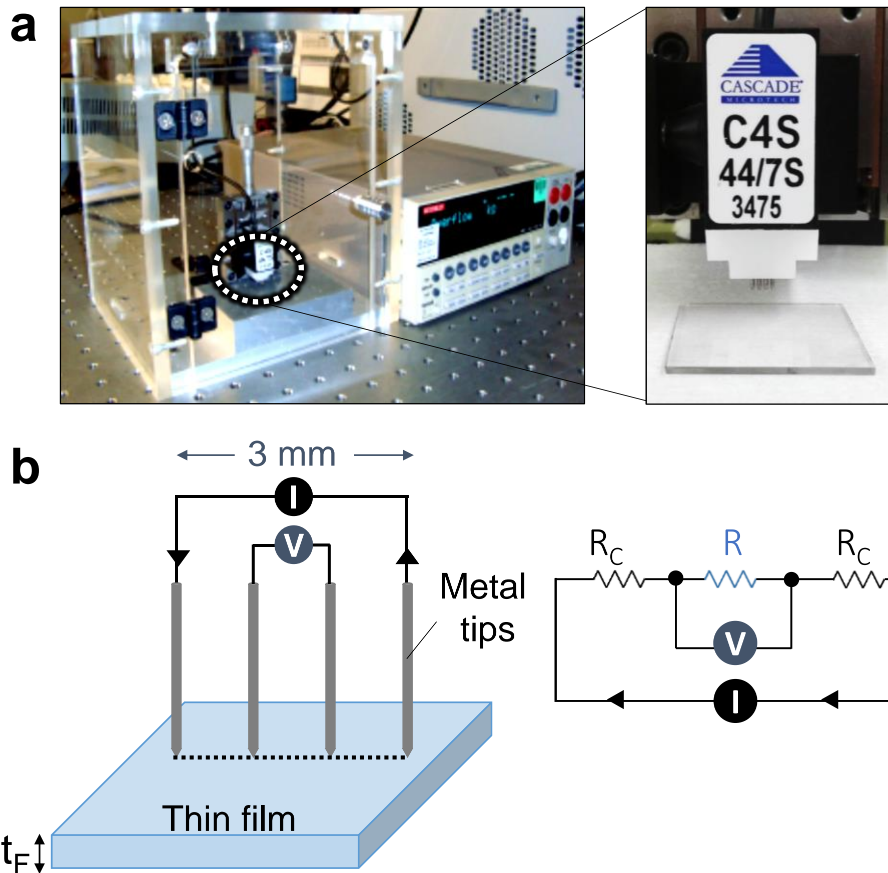

Figure 6. (a) Four-Point probe measurement set-up connected to a Keithley multimeter. The zoomed area of white-dashed line shows the four probes aligned at the Four-Point probe head, 1 mm apart. (b) Scheme of the measurement where probes are in contact with the thin film of thickness t_F. A current is injected between the outer tips while the voltage droplet is measured by the inner ones. The circuit on the right summarizes the 4-probe measurement, showing its high accuracy as the Rc is not measured.

According to the alignment of the four probes, Rs can be calculated using the following equation:

$$R_S = \left(\pi/\ln(2)\right) \cdot t_F \cdot \left(V/I\right) \cdot C_1 \cdot C_2 = 4.53 \cdot t_F \cdot R \cdot C_1 \cdot C_2 \qquad \text{(Eq. 6)}$$

where R is the calculated electrical resistance from Ohm's law, and C_1 and C_2 are two corrective coefficients that take into account the separation between the tips in the Four Point Probe Head and the substrate's dimensions [107].

In our case, where graphene is the material being measured: (1) C_1=1 as the separation between the tips (1 mm) is much higher than the graphene thickness (0.345 nm); and (2) C_2=1, as the area of the graphene measured by this method (typically 1 inch=2.5 cm) is higher than the separation between the tips (1 mm). Thus, the R_S calculation is reduced to:

$$R_S = 4.53 \cdot t_F \cdot R \qquad \text{(Eq. 7)}$$

In this thesis, we have measured the Rs using this technique for graphene on glass and Ni films in Chapter 2, for a three dimensional graphene structure in Chapter 3 and for graphene transferred to glass or PET covered with PI in Chapter 4. Typically, six measurements were taken at different positions of the sample, the mean value ($\overline{R_S}$) being the one provided as the result.

1.2.6. Grazing incidence X-ray diffraction (GXRD)

X-Ray diffraction is one of the most used tools in the analysis of the crystal structure of a material. Diffraction phenomena appear when an electromagnetic (EM) wave hits a periodic structure with the characteristic length of the order of the EM wave. At large incident angles, the x-ray beam penetrates deep into the material. Because in this thesis we are using thin metallic films and graphene, the incident beam has to be limited to the surface using grazing-incidence X-rays. At an incident angle near or below the critical angle for total reflection, the incident beam is evanescent and penetrates only the top 100 Å or less of the surface. There is also an enhancement in the intensities at the surface. At incident angles near to the critical angle, X-rays are enhanced by 2-4 times at the surface over the intensities in the bulk. Small penetration depths and intensity enhancements make possible the use of X-rays for the characterization of the surfaces, buried interfaces and thin films [108]. Besides the orientation of the single crystals of the sample, XRD also provides information about the average size of the grains composing the sample, which can be estimated by the Scherrer equation:

$$\tau = {K \cdot \lambda_{X-Ray}}/{(\beta \cdot \cos\theta)} \qquad \text{(Eq. 8)}$$

where τ is the mean grain size, K is a dimensional factor close to 1, $\lambda_{X\text{-}Ray}$ is the wavelength of the X-ray radiation, β is the broadening of the diffraction peak at half of its intensity, or full width half maximum (FWHM), and θ is the Bragg angle.

In Chapter 2 of this thesis, we have used this technique to characterize the crystallinity of Ni films using a Philips MRD goniometer equipped with four crystal Bartels Ge 220 monochromator.

1.2.7. Hall measurement

This measurement is important to semiconductor material characterization because from the V_H, the conductivity type, carrier density (n_S), and mobility (μ_H) can all be derived. The physical principle underlying the Hall Effect was explained in detail in the previous section 1.1.2. Electronic transport properties.

In our case, an alternating current (AC) flows along the x-axis from left to right in the presence of B in the z-axis direction. This charge results in the V_H, a potential drop across the two sides of the sample (see Eq. 2). With our set-up shown in Figure 7 (a), we calculate the n_S using the slope of the linear fitting between the V_H and B (see Eq. 3). By measuring the R_S at B=0, the μ_H can be also calculated (see Eq. 4) [1,22,109]

In this thesis, we work with two types of devices. For macro-sized samples, (lateral size of graphene up to 2 cm, Chapter 4), we fabricate samples as shown in Figure 7 (b). Thus, for obtaining the V_H, a current is injected from the Au contact "1-3" or "2-4", and probes are located on "2-4" or "1-3", respectively. Because the samples have a large area, the R_S can be calculated either by the previous Four-point probe method, or by the following Van der Pauw procedure where Au contacts have been deposited to measure the n_S and μ_H. The current is injected from one contact and collected from the adjacent one, while the V is measured from the opposite pair of contacts. This is repeated for all possible combinations, thus calculating the corresponding R by Ohm's law. As the geometry of the sample is always rectangular but can be different in dimensions, we average R in two groups (Eq. 9 and Eq.10), defining a vertical ($R_{VERTICAL}$) and a horizontal ($R_{HORIZONTAL}$) one by introducing the current into the device vertically or horizontally, respectively. Finally, the R_S is calculated using Eq. 11.

$$\left.\begin{aligned} R_{12,34} &= V_{3-4}/I_{1-2} \\ R_{34,12} &= V_{3-4}/I_{1-2} \end{aligned}\right\} R_{HORIZONTAL} = (R_{12,34} + R_{34,12})/2 \quad \text{(Eq. 9)}$$

$$\left.\begin{aligned} R_{14,23} &= V_{2-3}/I_{1-4} \\ R_{23,14} &= V_{1-4}/I_{2-3} \end{aligned}\right\} R_{VERTICAL} = (R_{14,23} + R_{23,14})/2 \quad \text{(Eq. 10)}$$

$$e^{-\pi \cdot R_{VERTICAL}/R_S} + e^{-\pi \cdot R_{HORIZONTAL}/R_S} = 1 \quad \text{(Eq. 11)}$$

For μ-sized samples, we use a standard Hall bar, as shown in Figure 7 (c), where the graphene area has been reduced to the central part (Chapter 5). Four probes are necessary to perform the Hall measurement: probes "1-2" for injecting the current into the circuit, and probes "3-4" or "4-5" to measure the R_S or V_H, respectively.

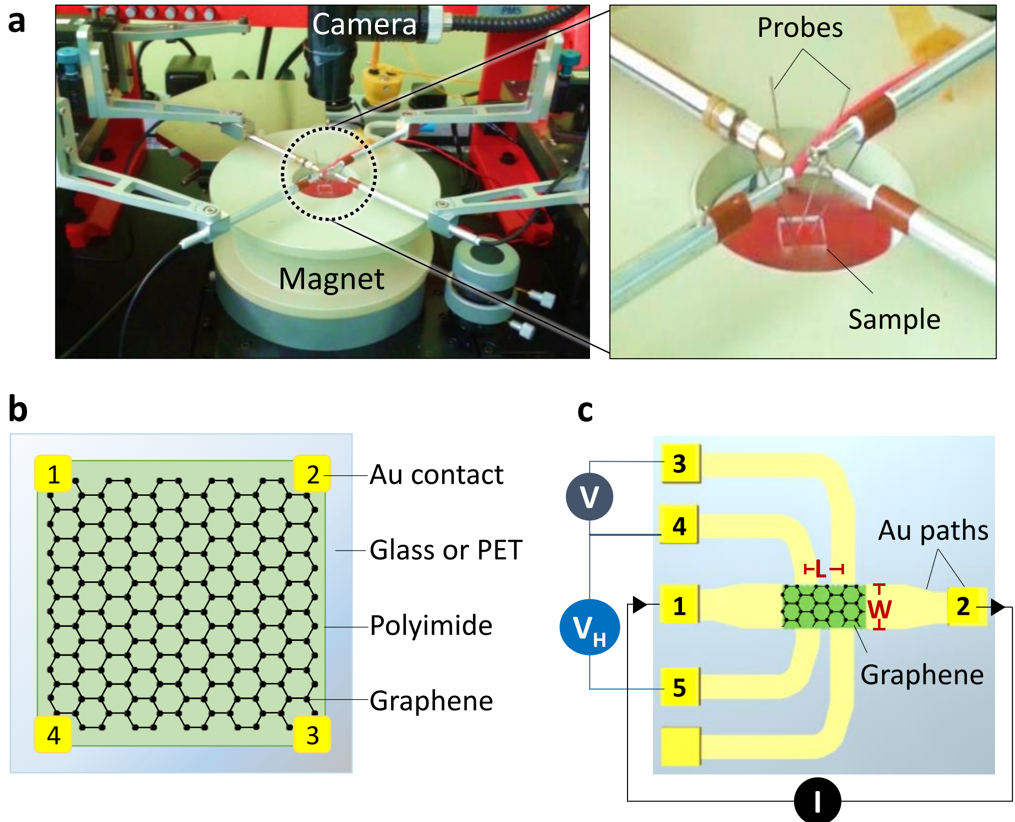

Figure 7. (a) Probe station to perform Hall measurements. (b) Scheme of the Van der Pauw device used in Chapter 4, where Au paths are contacted with 4 probes to measure V and V_H. For obtaining V_H, a current is injected from Au contacts "1-3" or "2-4", and probes are located on "2-4" or "1-3", respectively. For obtaining R_S, a current is injected from one contact and collected from the adjacent one, measuring V from the opposite pair of contacts. As the size can be different, R is measured in two groups (Eq. 9 and 10) defining an $R_{VERTICAL}$ and $R_{HORIZONTAL}$. (c) Hall bar design used in Chapter 5 where probes in Au contacts 1 and 2 inject an AC current, probes in contacts 3 and 4 measure V (to calculate R and R_S), and contacts 4 and 5 measure V_H, when a perpendicular B is applied.

As specified in the figure, by contacting the probes at opposite sides of the pattern, the V_H can be measured. However, if the probes are contacted at the same side of the pattern, the V is measured and by Ohm's law ($V = I \cdot R$), R is calculated. Then, considering a geometrical factor (W/L= 0.47), which depends on the geometry of the graphene pattern, the R_S can be calculated.

$$R_S = {}^{W}/_{L} \cdot R \qquad \text{(Eq. 12)}$$

1.2.8. Hall measurement combined with *in situ* monitoring of R_S

The physical principle is the same as with the standard Hall measurement, but the set-up, as shown in Figure 8 (a), is slightly modified for the experiment demonstrated in Chapter 5. We want to monitor simultaneously the changes in the R_S and V_H over time and also while the temperature is being modified. To this end, samples are fabricated as in Figure 7 (c) and contacted with 5 tips as shown:

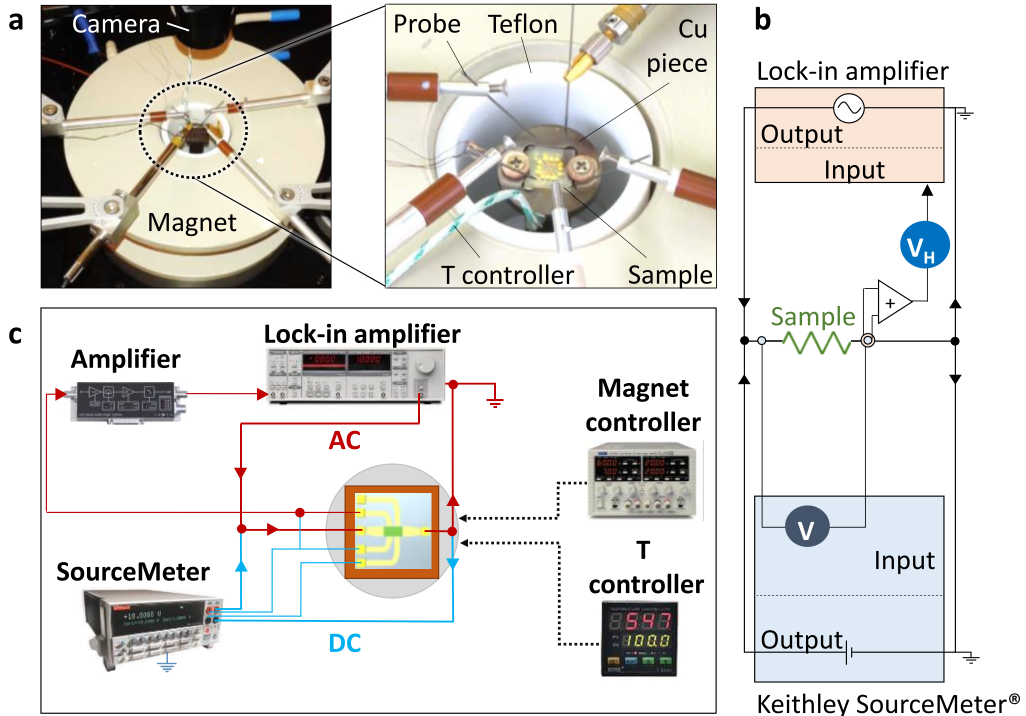

Figure 8. (a) Probe station modified with a thermal insulator and thermocouples to modify the temperature during the Hall measurement. (b-c) Scheme of the measurement: in the chip, a DC current is injected and measured by a Keithley SourceMeter® (blue circuit), while an AC current (red circuit) is injected by a Lock-in amplifier. The controlled variation of a perpendicular B generates V_H, which is amplified and measured by the Lock-in. This circuit allows the simultaneous measurement of R_S and n_S at different temperatures.

- Probes "1-2": the source and drain of the AC and direct (DC) currents. The AC is supplied by the Lock-in amplifier while the DC is injected by a Keithley SourceMeter®.
- Probes "3-5": to measure the V_H and R_S. Probe 4 is common to both measurements. Together with probe 3 it is used to measure the R_S in the Keithley SourceMeter® and with probe 5 it is used to measure the V_H in

the Lock-in amplifier. Because the V_H is very small, an amplifier is placed before the Lock-in and the gain (amplification) is taken into account for the calculations.

The previous elements can be clearly distinguished in the schemes of Figure 8 (b-c). All the equipment is controlled by a code developed with Labview®. At a certain temperature (also controlled with a temperature controller and a PT100 resistor located on top of the sample), the current of the magnet controller is modified, thus varying the B from -300 to +300G and consequently, the V_H. Also, because the DC current is continuously injected into the device, the R_S can be obtained at the same time as the AC measurement.

1.2.9. Optical characterization

This technique is applied to obtain the transmittance spectra of the samples as we are mainly working with glass substrates to obtain transparent devices. Optical characterization also allows us to determine the graphene layers. A graphene monolayer is almost transparent, with an absorption of only 2.3% in the visible spectral range. The transmittance decreases by a factor of 2.3% with each added layer up to five layers [110].

In this thesis, we have used a PerkinElmer Lambda 950 spectrometer in the UV–Visible region. Note that the substrate's contribution is always taken into account in optical transmittance measurements as:

$$T_F = T_T / T_S \quad \text{(Eq. 13)}$$

where T_T is the total optical transmittance (film and substrate), whereas T_F and T_S are, individually, the film and substrate optical transmittances, respectively.

In Chapter 4, we also have used the Fourier Transform-Infrared spectroscopy (FT-IR), a technique with several applications. One of these is its use for detecting functional groups and characterizing covalent bonding information. This is one of the objectives of the thesis - the use FT-IR (BRUKER) for PI curing reaction characterization by identifying the change of chemical compounds with temperature. When the material absorbs IR light (typically in the mid-IR region), the resulting spectrum shows specific molecular fingerprints of each chemical group, thus allowing their identification.

1.2.10. Raman spectroscopy

This is based on a phenomenon called the "Raman effect", which originates either from the interaction of an incident light beam with the phonons in a solid or from molecular vibrations in molecules, producing an inelastic scattering of light. When light hits a material, the majority of the phonons experience elastic scattering, called Rayleigh scattering, and the intensity of this portion of light is ≈

10^{-3} times the intensity of the incident light. However, the portion of light that undergoes the Raman scattering is even less at ≈ 10^{-6} times the intensity of the incident light. Thus, Raman spectroscopy requires high laser intensities. Raman is a non-destructive, fast and reliable tool for the characterization of materials, and, particularly in the case of graphene, it is essential to distinguish single-layer from multilayer graphene or graphite (Figure 9).

The quality of the produced graphene and types of defects of the material, the effect of the substrate on the graphene and doping can also be studied using this technique. For graphene, three characteristic peaks are detected, corresponding to D, G and 2D bands, at 1350, 1580 and 2700 cm^{-1}, respectively. The G band comes from the in-plane vibration of sp^2 carbon and is the most noticeable resonant phenomenon in graphitic materials. The 2D band, which is the graphene's fingerprint, belongs to a mechanism of double resonance between the excited electrons and the phonons near K. For monolayer graphene, the 2D band is single and sharp but as the number of layer increases, the 2D peak shape varies, becoming asymmetrical. The D peak rises up from the breaking of the double resonance and, thus, from the graphene defects. From Raman spectroscopy, it is possible to obtain information about doping. The shifts of the 2D and G peaks, as well as the ratio of their intensities, changes with the concentration of carriers.

Raman spectroscopy is unique for the characterization of graphene in terms of the number of layers, quality and doping. According to graphene monolayer criteria (66), the graphene quality can be measured in terms of intensity ratios between various different peaks. For example, the intensity ratio between the D peak and G peak (I_D/I_G) should be very low as the D peak is related to material defects, whereas the ratio between the 2D peak and G peak (I_{2D}/I_G) should be equal to or higher than two. The full width at half maximum of the 2D peak (FWHM (2D) varies depending on whether it is exfoliated or CVD grown graphene. For exfoliated graphene this value should be in the 25-30 cm^{-1} range while for CVD graphene it is typically larger [111–113].

In this thesis, we have used Renishaw inVia with a laser of 532 nm wavelength, with a reduction in the power radiation in order to avoid heat damage on the samples. Regarding the objectives, we have used two types: 50X and 100X lenses (with numerical apertures N.A of 0.75 and 0.85, respectively), depending on the sample needs. The 100X lenses were used for spectra and maps performed on samples in Chapters 2 and 3, where the graphene was directly grown on the surface and high definition of the surface was needed in order to detect nanoparticles and artifacts at low scale. For Chapters 4 and 5, as the graphene was transferred from the Cu foil we performed Raman measurements using the 50X lens. Laser spot sizes for 50X and 100X lenses are 865 and 764 nm, respectively.

$$\text{Laser spot} = \frac{1.22 \cdot \lambda}{N.A} \qquad \text{(Eq. 14)}$$

where λ is the excitation laser wavelength equal to 532 nm and N.A is the numerical aperture of the objective.

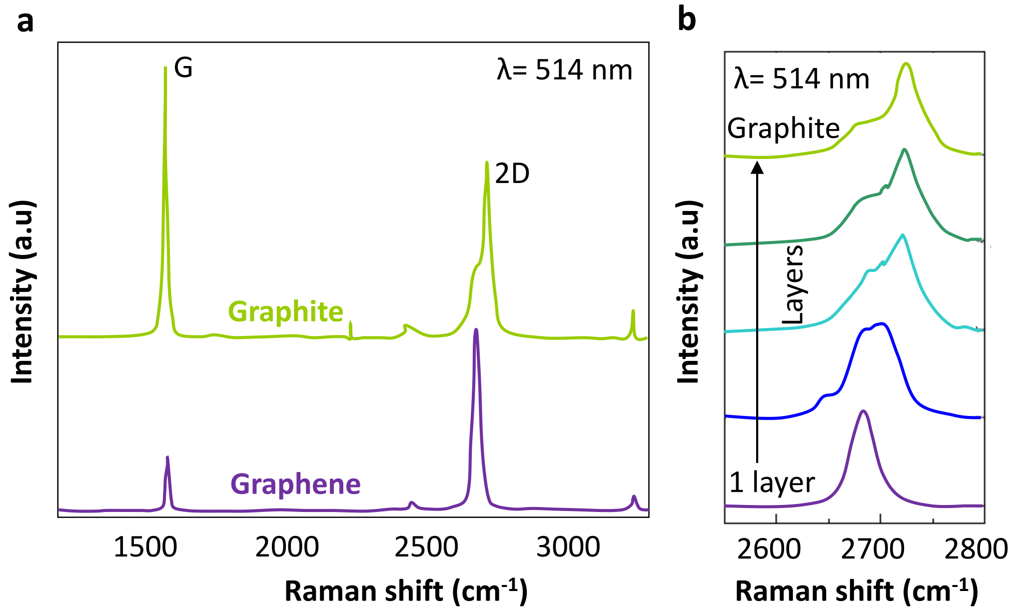

Figure 9. (a) Raman spectra of graphene (bottom) and graphite (top) at a laser wavelength of 514 nm, where two intense bands are detected, G and 2D. (b) 2D band of graphite at 514 nm laser wavelength comparing the evolution of the graphene peak when the number of layers is modified from 1 to 10. Adapted from ref. [112].

Raman maps are acquired in order to get a statistical overview of the whole sample. Data from Raman maps are treated by a custom program developed by Matlab®, where intensities of peaks, ratios and FWHM are automatically calculated. Results provided from single spectra are the mean value and standard deviation of at least 10 measurements at different sample locations.

1.2.11. Scanning Electron Microscopy (SEM)

This is important for the investigation of properties and structure of materials. The SEM provides information related to the material morphology, topography, crystallinity, composition and defects. This technique is versatile due to the numerous signals generated, the simplicity in image formation, wide magnification range and depth of field [114].

In this thesis, we have used SEM (FEI Inspect F) for the analysis of graphene structures in Chapters 2-5.

1.3. Graphene applications and future overview

1.3.1. Graphene applications

Graphene obtained by different synthesis methods (e.g., exfoliated, CVD or GO) have the following variety of potential applications, which can be divided into three main groups: electronics, energy, materials and composites [74,115].

Electronics, photonic and biomedical applications

There are several examples of graphene applications in the field of electronics, including high-frequency devices, transparent electrodes and flexible displays (e.g., touch-screen and wearable devices, etc.), ultrasensitive sensors (e.g., chemical, nano-electrochemical sensors, photodetectors, etc.), super-dense data storage (e.g., memory chips), and photonic devices, etc. In the following, we will mainly discuss application to transparent electrodes, photonic and biomedical devices.

CVD graphene films provide the optical and electrical properties needed to replace indium tin oxide (ITO), a material which has been used as a transparent electrode (TE). Graphene has been shown to achieve a low R_S from 50-300 Ω/sq. together with high optical transmittances of 90%, values that are comparable to typical TEs fabricated with ITO [40]. Specifically, graphene has greater potential than ITO for fabricating flexible displays, as graphene's mechanical resistance and flexibility are higher than those of ITO. Graphene has a ten times higher fracture strain compared with ITO's brittleness. This fact, together with the high cost of ITO and limited sources compared to carbon, makes graphene an ideal material for the fabrication of flexible and rollable electronic devices [116–118].

The combination of graphene's electronic properties, (e.g., tunable carrier transport properties), together with its wavelength independent absorption (2.3%) for normal visible light (<3 eV) makes graphene a promising option for implementation in photonic devices. Some examples are ultrafast graphene photodetectors and ultrahigh gain graphene-based photodetectors [13,115,119–121], optical modulators [115,122], and plasmonic devices [115,123–125], etc. In addition, graphene has been demonstrated to control plasmons by electrical voltages [115,126,127].

The application of graphene in the biomedical field for imaging and diagnosis, drug delivery, bioelectronics or biosensors is also important [115,128–130]. As graphene is chemically inert, it can be functionalized by other molecules as a drug delivery vehicle. Graphene's impermeability to liquid and gases makes it suitable for bio-compatible protective coatings and barrier films for the fabrication of biomedical implants and devices. Further understanding of graphene's biocompatibility and toxicity needs to be gained, however, prior to its final implementation in devices. Finally, the use of graphene as a (bio) sensor is possible due to its high sensitivity

to the electrostatic perturbations that are induced when locally charged particles are deposited on its surface.

Energy

The applications here are related to the storage and transportation of electrical power (e.g., batteries and supercapacitors) and organic solar cells [115,131–133]. Additional applications are based on the extraordinary potential of graphene to transmit light, electricity and heat. Thus, graphene can be used to improve the performance of light emitting diodes (LEDs) [134].

For current supercapacitors, the main issue is their limited energy capacity due to the materials used today. The nanofabrication of graphene supercapacitors is of great interest as more devices can be fabricated in the same area, thus improving their potential on the large scale. Another important advantage of graphene supercapacitors is the high speed at which they can charge and discharge (to transfer power to the device).

Materials and composites

Graphene can be implemented with pre-existing materials (mainly polymer- and ceramic-based composites) by improving their raw properties and transforming them to high-value composites. Some examples are ultra-lightweight composites and coatings, which take advantage of graphene's low thickness and weight combined with its high mechanical resistance. It is also important to highlight here the use of graphene (mainly graphene oxide) for the fabrication of conductive inks and pastes .[115,135–137].

Also important is the use of graphene as a nanofiltration membrane for water treatment (filtration and desalination) on a large scale [30,115]. This would allow the treatment of higher water fluxes compared to current polymer- ceramic-based filters, thereby reducing the energy used to force water through the membrane by a factor of 10.

1.3.2. Current situation and investment

The upscaling of graphene and graphene-related material production is faced with challenges related to keeping the graphene properties unaltered after mass production and wafer-scale integration. A big effort is currently being devoted to graphene standardization in order to define specifications of graphene quality depending on the application. For example, the graphene quality for high-performance electronics needs be very high and defect-free compared to that required for batteries/supercapacitors, which have been demonstrated to work even if the material has defects, cracks, voids and cavities [74,138].

Regarding the publications concerning graphene and graphene-related materials, until recently there has been an exponential growth as shown in Figure

10 (a). For the graphene patent graph in Figure 10 (b), the data comprise the patent filings in two main sectors, synthesis and electronics [139].

It is also important to mention the huge investment in graphene carried out by the European Commission through the "Graphene Flagship", a 10-year project started in 2013. With a budget of €1 billion, the Graphene Flagship is trying to meet academic and industrial researchers in order to transfer knowledge from laboratories to society. This has achieved the creation of new jobs and had a positive economic impact. The consortium has 150 academic and industrial research groups in 23 countries. The project has an increasing number of members within the different scientific and technological work packages, where ICFO leads the package number 8 (Photonics and electronics) and also is involved with others, such as Flexible Electronics, Sensors and Energy Applications [140].

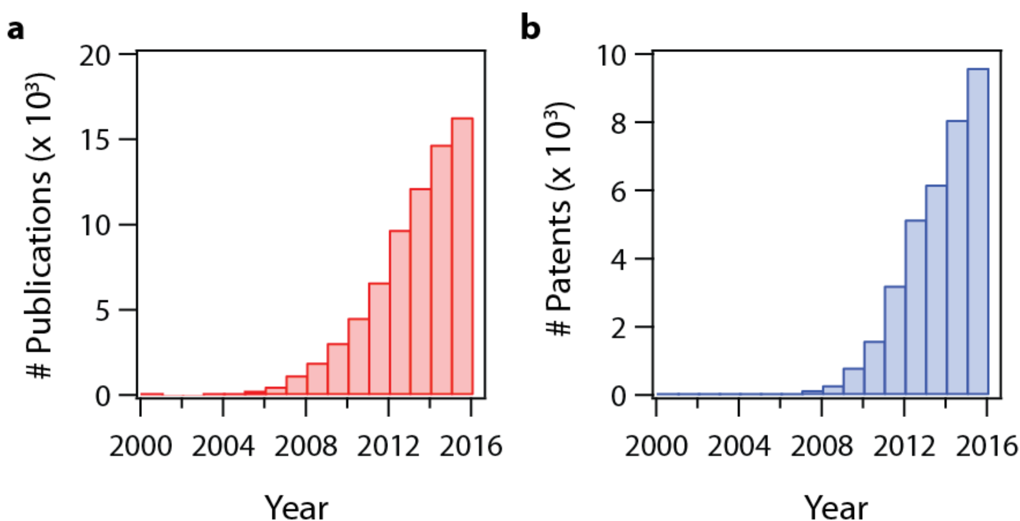

Figure 10. Number of (a) publications and (b) filed patents related to graphene until 2016 [139].

1.4. Aim of the thesis

The main objective of this thesis is the approach of graphene technology towards the large scale, whilst solving challenges related to graphene growth, and transfer and control of doping.

As discussed in previous sections, the unique properties of graphene make it promising for a wide variety of applications, with the implementation of graphene for transparent electrodes, supercapacitors or flexible displays, touch-screens and wearables being among the most important. The excellent properties that make graphene different from other materials are the combination of high electrical mobility, high thermal conductivity, high mechanical resistivity,

transparency, flexibility and impermeability, and the fact that it is chemically inert and stable in air.

However, the ability to maintain all of the previous properties of graphene when grown by a scale-up technique, different to micromechanical exfoliation, remains a challenge. The most promising technique for growing graphene on a large scale is CVD, where graphene is typically grown on a Cu catalyst. This process has been widely studied, obtaining a high quality graphene monolayer. However, transferring graphene from the Cu to the target substrate is necessary and this represents a challenge due to time consumption, and even more importantly, the risk of worsening the graphene properties and quality due to remaining residues at the end of the procedure.

To address this issue, this thesis has developed two procedures to grow graphene directly on the target substrate in large and nano-patterned sizes by avoiding two important and detrimental steps, i.e. the graphene transfer and lithography procedures. In the first case, we have performed the growth of large and patterned areas of 2D layers of graphene by using ultra-thin metal films (UTMFs) of Ni. The exposure of UTMFs at high graphene growth temperatures (700-1000ºC) leads to a well-known process called "dewetting", where the metallic films break and retract with time and temperature. The study of UTMF Ni dewetting in conjunction with graphene growth on Ni has allowed the achievement of graphene direct deposition on the target substrate while the Ni is retracted with heat, thus avoiding additional transfer steps. In the second procedure, we have combined the Cu catalyst's potential to form graphene monolayers with previous knowledge to modify the Cu density on the glass substrates. Thus, in collaboration with Corning Incorporated, we have created three different shapes of Cu catalyst where the graphene grows conformal, producing graphene in 2D and 3D dimensions, and, also, directly on the target substrate without additional transfer and lithography steps.

However, as the quality of graphene has been demonstrated to be superior and more controllable when it is grown on Cu foils, another current challenge is the transfer of graphene from the Cu to the target substrate in a clean, fast, cheap, reproducible and scalable manner. The most frequently used technique for graphene transfer, based on the use of PMMA and known as "wet-transfer", has challenges related to the PMMA residues left on the graphene surface, is a time consuming procedure and the Cu foil is etched away by the solution. The third objective of this thesis has been developed in collaboration with Corning Incorporated, and consists of the creation of a "dry-transfer" technique using a very stable polymer, PI, as an intermediate layer between the target substrate and the graphene. The study of PI and its combination with an adhesion promoter has enabled the graphene transfer by a fast, stable and residue-free technique, and with

Cu recycling and a strong adhesion of graphene to target substrates. Previously described advantages preserving the high quality of the graphene grown on recyclable Cu foils make this technique promising for graphene implementation on a large scale.

Last but not least, an important objective of this thesis is the control of transferred-graphene doping. As previously explained in section 1.1. Graphene, graphene doping can be altered by PMMA transfer, growth conditions and substrate effects, and, moreover, existing doping techniques have been shown to be sometimes uncontrollable and unstable over time. With this in mind, the fourth objective of this thesis consists of the application of a well-known technique called "thermal-poling", to alter the surface charge at the interface between the glass substrate and the graphene device in a controlled way, and consequently inducing the desired doping of the graphene. Due to the mobility of ions in glass at certain temperatures and voltages, a very intense electric field is created inside the glass and "frozen" when normal conditions return. The high electric field created at the interface of the glass and graphene device, together with the accumulation of positive charges due to Na^+, modifies the graphene doping, being stable as the graphene device is encapsulated.

1.5. Thesis outline

This thesis is organized into six chapters. Chapter 2 provides a brief introduction, collating previous work related to the direct growth of graphene on target substrates. Also, the "dewetting" concept is explained in further detail for the case of ultra-thin films. A description of sample fabrication is also provided, giving details of Ni UTMFs deposition by sputtering, CVD graphene growth parameters (temperature, pressure and time), Ni etching and the deposition of Au electrodes for electrical characterization. The chapter summarizes the main results of graphene grown at different temperatures, with the final part being dedicated to the optimal conditions to grow graphene in large and nano-patterned areas onto a wide variety of substrates, without residues or defects, but with high optical transmittances and low sheet resistances comparable to standard processes of graphene grown on Cu foils.

Chapter 3 provides a brief introduction to previous work on graphene growth in three-dimensional shapes and the additional new properties that increase the range of potential applications where graphene can be used. We provide a full description of the technique that we have developed for the creation of Cu nanoparticles (Cu NPs) catalysts of different densities - materials used for Cu NPs deposition, optimization of Cu deposition conditions and Cu etching techniques. The chapter collates the main results of graphene structures grown conformal to

previous varieties of Cu catalysts, obtaining graphene in 2D and 3D shapes and demonstrating them to be free-catalyst and nano-patterned over large areas without lithography procedures.

Chapter 4 includes a brief summary of previous state-of-the-art work performed on graphene dry-transfer. We include a full description of the technique we have developed with information on sample fabrication, previous studies and characterization of PI for optimum graphene transfer, and optimization of equipment conditions. The chapter summarizes the main results of a continuous graphene layer, free of residues and defects, which has been transferred to glass and PET, with high optical transmittances, n-doping and comparable mobility to conventional CVD graphene transferred by the PMMA wet-process.

Chapter 5 provides an introduction to the concept of thermal poling of glass with a brief summary of previous state-of-the-art work related to this. The chapter includes details of graphene device fabrication, a description of the set-up for applying poling to glass, and the complete optimization of poling conditions. The details of the set-up used for the electrical characterization are included in the above section 1.2. Characterization techniques. The chapter collates the main results of graphene doping changed after glass poling at positive and negative external voltages. Also, the reversibility of the poling effect in graphene doping is demonstrated when it is progressively erased with temperature.

2

Direct growth of graphene by Ni dewetting

This chapter includes the state-of-the-art techniques related to the direct growth of graphene on a target substrate without the need for additional transfer steps. The graphene growth mechanism developed in our work, based on dewetting on Ni ultrathin films, is explained, including the theoretical concept and optimization for our specific case. Results for graphene grown on fused silica at different temperatures are presented, together with their characterization results. For the optimum conditions (700°C for 30 minutes using 50 nm of Ni), our technique is demonstrated to directly grow graphene patterns of different sizes and shapes on different substrates. These include conventional Si /SiO_2 wafers and low strain point substrates, such as Willow® flexible glass.

Further details of this work can be found in the following publication:

M. Marchena *et al.* (2016), "Low temperature direct growth of graphene patterns on flexible glass substrates catalyzed by a sacrificial ultrathin Ni film," Opt. Mater. Express 6, 2487-2507.

2.1. Introduction

Deposition by CVD is the most promising graphene synthesis as it combines two important factors: (1) the production of high-quality graphene, which has been found to be essential for applications within electronics, and (2) the scalability of the technique using roll-to-roll processes, which would allow large-scale implementation. However, one of the main disadvantages associated with this technique is that it requires the graphene to be transferred from its catalytic template (typically Cu foils) to the target substrate. The implementation of this procedure is not trivial, as it causes not only an increase in process time and

costs, but also, very importantly, the introduction of defects and residues on the graphene, which decrease the potential of the material, for example, by affecting its electrical properties.

In order to resolve these issues, one possible solution is the development of procedures that allow the direct growth of graphene on the target substrate used for the application, thus avoiding completely the need for graphene transfer. A big effort has been devoted to this end by the scientific community, one example being ref. [41], where graphene was deposited on glass using Cu vapor as a catalyst. However, although graphene was found on the substrate, the graphene coverage was poor, not uniform and without position control.

Other works [45,141] used Cu thin films (100-300 nm as minimum thicknesses) deposited on glass to promote and catalyze the graphene growth, thus avoiding previous issues of position control. During CVD, the Cu film retracted and dewetted in a characteristic finger-like shape due to the high temperatures, leaving behind regions of the substrate surface covered by graphene. In ref.[45], the process conditions for the graphene growth were temperatures of 1000°C for 5 to 7 hours in order to achieve a complete dewetting and evaporation of the Cu. Unfortunately, this represents an important limitation for its implementation on a large scale due to the high costs associated with the equipment maintenance and sources. Another disadvantage is the fact that the target substrate is limited to fused silica, due to its high strain point, which allows it to resist high temperatures without being damaged or deformed. Moreover, after the whole process it was reported that there remained a large portion of Cu film residue on the substrate, which reduced the transparency of the sample, thus undermining the most important advantage of using glass as the target substrate.

Similar work [142] directly grew graphene on Cu films of 450 nm thick that had previously been deposited on glass. The temperature and time growth were reduced to 900°C and 5 minutes, respectively. However, a different growth mechanism was reported, where the carbon diffused through the Cu grain boundaries, forming the graphene at the interface between the Cu and the glass. After the Cu etching using $FeCl_3$, the graphene remained on the glass with a high optical transmittance (94%) and an R_S close to 2 kΩ/sq. Although these were impressive results, the main issue was the limitation of the minimum growth temperature to 900°C, thus, not allowing the use of substrates with lower strain points. The use of lower temperatures, such as 850°C, produced no graphene at the interface, while the use of temperatures higher than 900°C increased considerably the defect levels on the film.

Table 3 below collates several different works where, in some cases, metallic catalysts were mixed with different carbon sources in order to grow

graphene directly on the substrate at lower reaction temperatures, but with the disadvantage of decreasing the graphene quality. On the other hand, two works report the growth of graphene without the use of any metal catalyst at very high temperatures (1100-1180°C) and long reaction times, which, in some cases, exceed 9 hours. Besides the high costs associated with the maintenance of equipment under those conditions, the high temperature means that only a limited type of target substrates can be used, i.e., those of high strain points that can stand high temperature for long periods of time (e.g. quartz, sapphire or borosilicate glasses).

Table 3. State-of-the-art for direct growth of graphene on the target substrate with the possible addition of sacrificial metallic catalyst

Catalyst (thickness)	Carbon source	Substrate	Growth conditions	Main results	Ref.
Ni, (100 nm)	Graphite paste	PMMA, glass, Si/SiO_2	Anneal: 1000°C; Growth: 25-260°C, 10 min, Ni-C etching	μ_H=600 $cm^2/V\cdot s$, R_S = 1kΩ/sq. Glass: nano-domains	[143]
Ni, (10-30 nm)	A.C(*) (2-5 nm)	Si/SiO_2	Anneal: 750°C 10 min, H2/Ar	Islands of sizes 100 nm to 1μm.	[144]
-	CH_4	Quartz, sapphire, SiO_2/Si, Si_3N_4	1100-1180°C 9-72h	μ_H=1000-3000 $cm^2/V\cdot s$ ($Si_3N_4/SiO_2/Si$)	[145]
Ni (200 nm)	C_2H_2	Si/SiO_2	Anneal: 900°C, 5 min, He. Growth: 120 s	Ni etch by tape. Low quality (I_{2D}/I_G= 0.6)	[59]
Fe	Fe-C (20, 200 nm)	SiO_2	400-800°C, 10-30 min. Fe etching: Cl_2, 0-90 min.	6-7 layers of graphene on quartz.	[146]
-	CH_4	Quartz, sapphire	1000-1100°C, 1 to 7 hours, Ar: H_2: CH_4.	Best: 97.5% transmission at R_S = 6.7kΩ/sq.	[147]

(*) Amorphous carbon

Other works have developed the use of Plasma-Enhanced Chemical Vapor Deposition (PECVD) to grow graphene directly on the substrate without using any metal catalyst. Here, the plasma created inside the chamber by the radio frequency or the direct current discharge between the two electrodes allows the dissociation of the carbon molecules at temperatures lower than thermal CVD. Depending on the carbon source reactivity - see ref. [148,149]- the growth temperatures can be decreased to 600°C when CH_4 is used, or even to 400°C, when using more reactive gases, such as C_2H_2. However, the main challenge is the quality of the graphene, which was demonstrated to grow vertically at a lower quality than for previous standard CVD processes (R_S= 5.2 k**Ω**/sq. at the highest transmittance, 84%). For more details of work related to the direct growth of graphene on dielectrics, see the review in ref. [150], which collates complete data and details.

In view of the previously mentioned issues, the aim of our work has been the development of a technique that can grow good quality, clean and continuous graphene on large areas of the substrate without the need for a transfer step. The technique requires moderate processing conditions compatible with a wide range of target substrates, and the possibility to produce nano-patterned graphene without using lithography steps. Although our approach is based on the dewetting procedure reported by Ismach *et al.*, it differs in the use of Ni as the sacrificial metal catalyst at much lower thicknesses, from 5 to 50 nm. Moreover, we are able to reduce the temperature and reaction times to 700°C and 30 minutes, respectively. Also, the addition of a fast and polymer-free step (5-15 minutes), dipping samples in aqua regia, improves optical transmittances by up to 90%, only about 2.5% less than the bare glass substrate. Thus, under these conditions of low temperature and high transmittance properties, we demonstrate the potential for our technique to be implemented in the growth of graphene in large and patterned areas on target substrates with high strain points (e.g., fused silica and Si/SiO_2), and also on those with low strain points, such as flexible Willow® glass.

A recently published review [151] summarizes the most important direct transfer techniques developed for graphene growth, where results on the direct growth of graphene on glass using Ni thicknesses from 5 to 50 nm from this thesis have been included.

Finally, a recent work by Guo *et al.* (2018) [152] demonstrates that using Ni as a provisional template for growing graphene directly on dielectrics is still a hot topic with promising applications. In that work performed by PECVD, the growth temperatures were reduced to 700°C (which is the minimum temperature of our work) using Ni films of 25, 50 and 100 nm that had been previously deposited on quartz wafers (2.5 inch diameter). After growth, the graphene grown on the top face of Ni was etched by an oxygen plasma, and also the Ni film. The graphene used for devices was the one grown at the interface between the Ni and the quartz.

2.2. Sample preparation

The substrates employed are fused silica (High Purity Fused Silica, HPFS®) and Willow® glass (both from Corning Inc.), and Si/SiO_2 wafers. After an organic cleaning by sonication (acetone and isopropanol), the substrates are placed inside the small Chamber 2 of the magnetron sputtering machine (Orion 8, AJA) shown in Figure 11 (a-b), which allows the loading of the sample at an atmospheric pressure while the main Chamber 1 is kept isolated under high vacuum. After transferring the samples to Chamber 1, Ni UTMF films (UTMFs) of 5, 15 and 50 nm thicknesses are deposited from one of the targets shown in (b). Before that, a characterization of the Ni target is required in order to determine the rate of deposition, and consequently, the time needed to deposit each thickness. Experimental results determined 0.71 Å/s to be the Ni rate of deposition, meaning that 1.16, 3.56 and 11.98 minutes are needed in order to deposit 5, 15 and 50 nm thicknesses, respectively. The deposition steps are: (1) a first plasma pre-treatment of Ar (8 mTorr, 40 W) to clean the surface of the substrate, and (2) Ni deposition in Ar atmosphere and room temperature.

Subsequently, the graphene is grown on Ni covered substrates by means of CVD equipment (Black Magic 4-inch, AIXTRON, Figure 11 (c)). Figure 11 (d) shows the inside of the main chamber containing a 50 nm thick sample of Ni on top of the heater. The CVD conditions for growing graphene on Ni are: CH_4/H_2, 30/20 sccm, 7 mbar, 50-75°C/min heating and cooling rates, and growth temperatures ranging from 700°C to 1000°C, in steps of 100°C. Lower temperatures are not sufficient for the endothermic CH_4 decomposition reaction to occur.

Before the graphene growth, samples are annealed while heating the system from room temperature up to the reaction temperature with the addition of 15 minutes at the reaction temperature before starting the graphene growth. During annealing, Ar/H_2 gases are introduced inside the chamber to perform a double action on the Ni, namely: (1) a redox chemical reaction where possible metal oxides forming at the surface are reduced to their active phase (fundamental state: Ni(0)), and (2) an increase in the grain size and crystallization, as was previously discussed in Chapter 1, section 1.1. Graphene. When the temperature stabilizes, the reaction gases are fed into the system. Finally, the samples are cooled down under a continuous flow of H_2 in order to remove amorphous carbon from the surface. Additionally, after the graphene growth, samples are dipped in diluted aqua regia (1:2:2, HCl: HNO_3: H_2O) for 5 to 15 minutes to remove the dewetted Ni nanoparticles remaining on the surface.

We also demonstrate the possibility of growing graphene patterns directly on two types of substrates: Si/SiO_2 wafers and Willow® glass substrates. A first lithography step using laser writer (LaserWriter LW405B, MICROTECH) is performed after spin-coating the photoresist on the cleaned target substrate. This is followed by Ni sputtering and lift-off to obtain the metal patterns. For electrical measurements, a second lithography is performed to deposit Au contacts.

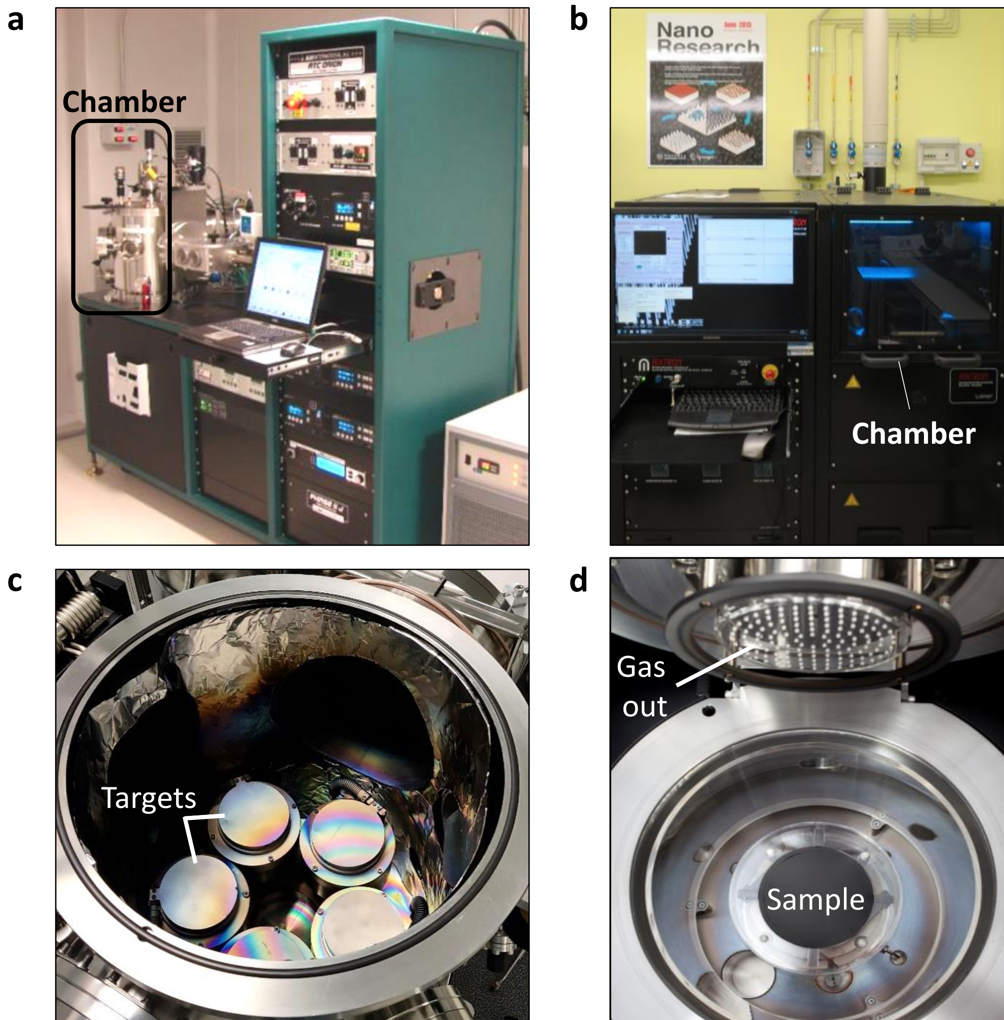

Figure 11. (a) Sputtering system used for Ni UTMFs deposition. The equipment consists of the highlighted main chamber containing the targets with the material to be deposited and where the deposition process occurs. The inside of the chamber is shown in (c). (b) CVD Black-Magic (AIXTRON) used for graphene growth where the main chamber is highlighted. The inside of the chamber is shown in (d) where the sample is located on top of the bottom heater and the gases are introduced from the top shower head.

2.3. Ni dewetting process on glass

In general, deposited thin films are grown under conditions for which atomic motion is limited and non-equilibrium structures are fabricated. The atoms that arrive at the substrate surface or growing film can usually move over distances of nanometers or less. As a consequence, most of the resulting films are unstable, which means partial stability in the equilibrium until, for example, heat is applied. When this occurs, thin films start to dewet, forming islands, as the heat provided increases the mobility of the atoms. The dewetting phenomenology on thin films is represented in Figure 12. However, it needs to be considered the substrate where depositing the thin films, due to a great interaction between them will not allow the film to dewet e.g., thin films of Ti and Cr deposited on glass do not dewet due to its rapid oxidation when contacting the SiO_2 [153,154].

Dewetting can occur at pre-existing holes or film edges, but also requires the formation of new holes. In the former case, the dewetting can be controlled in a desired direction. By increasing the temperature, or the time at a fixed temperature where the film has started to dewet, the holes created grow progressively, eventually producing a full dewetting of the entire film. Because dewetting requires atomic transport, the dewetting rate depends strongly on temperature. There is generally a characteristic temperature at which dewetting occurs, $T_{dewetting}$, which depends on several parameters, such as the type of material and the t_F. Generally, $T_{dewetting}$ decreases with t_F. Also, the size and spacing of the islands formed decrease with t_F. While these trends generally hold, there are many other factors that control the specific relationships between the $T_{dewetting}$, island shapes and the t_F. A deeper understanding of dewetting phenomenology and thermodynamics can be found in ref. [155].

As well as the application of dewetting on the direct growth of graphene demonstrated in this work, previous applications have used it to fabricate particle arrays in sensors [156]; to produce catalysts for growing carbon nanotubes [157] and semiconductor nanowires [158], and, also, to form elements in electrical memory devices [159].

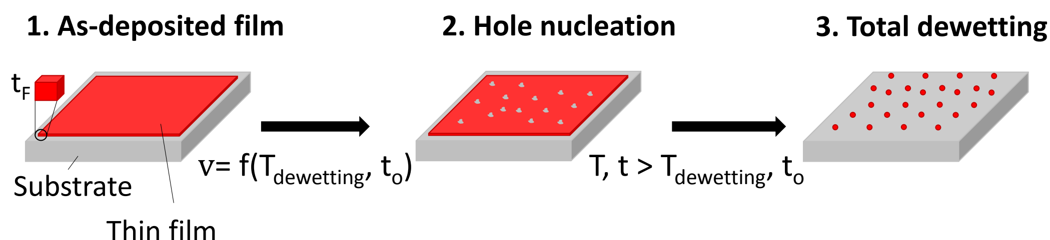

Figure 12. Scheme of dewetting phenomena on thin films. After the continuous deposited thin film is exposed to a certain $T_{dewetting}$, the film is nucleated with holes. If it exposed for longer periods or to higher temperatures, the film can totally dewet into islands [155].

In our work, within the working temperature range (700-1000°C) and given pressure (7 mbar), the Ni is well below its melting point. This means that the catalyst remains during the growth process, thus allowing control over the graphene location, which in previous works [45] was a big issue. Moreover, due to the previously mentioned instability of thin films, when temperature is applied, Ni UTMFs dewet. Using this method, it is possible to grow graphene precisely in the position where the Ni has been sputtered and in direct contact with the substrate surface, due to the subsequent Ni retraction. In this way, graphene transfer from the catalyst to the target substrate is avoided.

Regarding Ni dewetting, little work has been devoted to the study of ≤ 50 nm thick UTMF polycrystalline films, although some publications do report the interest of single crystal Ni films dewetted on oxide surfaces (e.g., MgO) [155]. Before the graphene growth, we initially studied the dewetting mechanism of Ni UTMFs, considering $T_{dewetting}$ as the temperature at which 5% of a 1 μm^2 substrate area is uncovered (same criteria as ref. [155,160]). Figure 13 (a) shows the experimental results of $T_{dewetting}$ as a function of the Ni film thickness (5 to 50 nm) compared to previous work carried out with Cu. The results indicate that, due to the small Ni thicknesses used in this work (5, 15 and 50 nm), all of the films dewet within the 700-1000°C range except for the 50 nm one processed at 700°C, where only small holes are formed in the film. This will be discussed in section 2.4. Growth at 700°C, where the characterization of SEM and AFM confirm that Ni film at this temperature is at the initial "hole nucleation" step.

Graphene quality is highly dependent on the surface properties of the substrate (in our case Ni UTMF), in particular the crystal orientation, which has been demonstrated to affect the carbon gas dehydrogenation, adsorption, diffusion and generation of H_2 [49,54,161]. As discussed previously in section 1.1.3. Growth techniques, when growing graphene on metal films, crystal orientation plays an important role in the growth of high quality material. Specifically, when using polycrystalline films, it has been demonstrated that it is essential to add an annealing step before the growth, not only to increase the size of the metal grain, but also to promote the crystal orientation, which will lead to a reduction in the grain boundaries and defects in the graphene [62,63]. For Ni, Ni (111) crystal orientation promotes the formation of graphene monolayers due to a small mismatch in the crystal lattice structure and dimensions [60,162].

In order to fully characterize the deposited Ni UTMF films before the graphene growth, we have performed a GXRD analysis to evaluate their structural modification after being exposed to the CVD growth process at 1000°C (including the additional 15 minutes of annealing at this temperature after the heating ramp in Ar:H_2). Figure 13 (b) shows a significant difference in crystallinity between a sputtered 50 nm thick Ni UTMF before and after CVD growth, thus demonstrating the promotion of Ni (111) after annealing. During the heating phase

of the process, the grains of the polycrystalline film increase in size (up to a few hundred nanometers), and also in crystal orientation, mainly on the (111) and (220) planes. Moreover, a weak peak at 2θ=25.4° ascribable to graphene [49] is present after the CVD growth, thus confirming its growth on the Ni film.

The next section collates the main results of graphene growth classified by the reaction temperatures studied here (700-1000°C in steps of 100°C) at different Ni UTMF thicknesses.

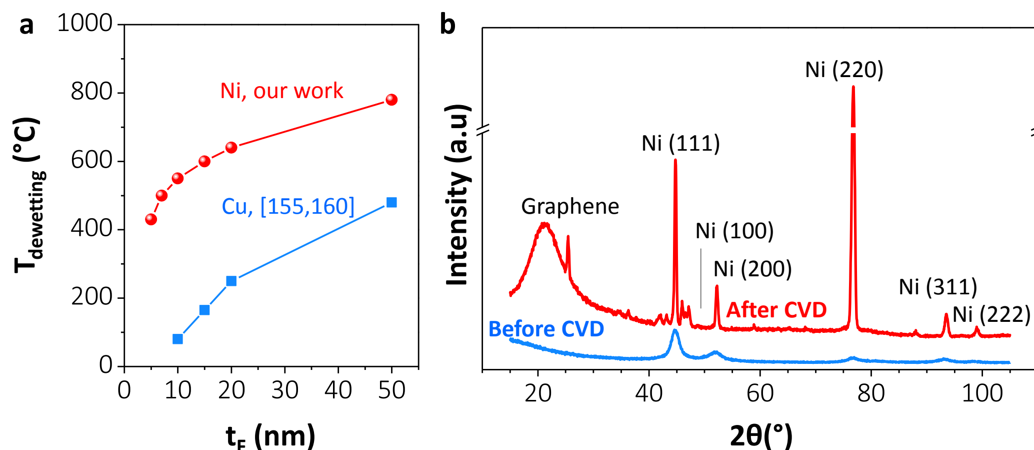

Figure 13. (a) Experimental results of $T_{dewetting}$ as a function of different Ni UTMF thicknesses (our work, red sphered line) compared with data of Cu UTMF [155,160] (blue squared line). (b) GXRD spectra of 50 nm Ni UTMF before (bottom line) and after (top line) CVD growth at 1000°C, (this sample corresponds to sample C in Table 4). A crystallinity improvement after CVD growth due to annealing is obtained, mainly to crystal orientations of (111) and (220), also with the appearance of a narrow peak at a small angle (25.4°), which is associated with graphene.

2.4. Influence of the reaction temperature

Processing conditions for the growth are fixed except for the temperatures and reaction times, which vary from 700°C to 1000°C and from 15 to 60 minutes, respectively. Details about time reaction characterization, for which the optimum value was found to be 30 minutes, are included at the end of this section (Figure 22). Table 4 summarizes the results obtained for the four most relevant samples (samples A-D) of the eighteen we prepared (see section 2.7. Additional information). Tables 6 and 7 summarize the results obtained for all eighteen samples S1-S18). However, initially we focus on Samples A-C for 50 nm Ni, as in the previous section this was determined to be the most relevant thickness as it covers the whole dewetting process combined with graphene growth.

To this end, we prepared three samples of 50 nm Ni deposited on fused silica, and exposed them to the CVD process at 700, 900 and 1000°C, respectively, for a duration of 30 minutes. In Figure 14 (a), we can observe the expected evolution of the Ni film dewetting with increased temperatures. This includes the nucleation of holes at 700°C [143] followed by the hole enlargement and propagation at 800-900°C, where dewetted areas and a still continuous Ni film are clearly distinguished (sample S8 at 800°C can be found in Table 6 in section 2.7. Additional information). Finally, a complete dewetting of the film into Ni islands occurs when the temperature is increased to 1000°C.

Table 4. Processing conditions and Raman signals for graphene grown on Ni UTMFs (fused silica substrates) of different thicknesses. Raman results include the ratios between graphene peaks: I_{2D}/I_G, I_D/I_G and the FWHM of 2D peak (σ: standard deviation). All measurements were performed on the dewetted areas, where the metal is retracted.

		Ultrathin Ni on fused silica substrates			
		Sample A	**Sample B**	**Sample C**	**Sample D**
Processing conditions	**Ni (nm)**	50	50	50	15
	T (°C)	700	900	1000	1000
	t (min)	30	30	30	30
Raman results	**I_{2D}/I_G (σ)**	3.20 (1.78)	2.28 (0.74)	2.34 (1.24)	2.37 (0.38)
	I_D/I_G (σ)	0.92 (0.54)	0.49 (0.46)	0.17 (0.12)	0.51 (0.11)
	FWHM 2D (cm^{-1}), (σ)	22.8 (5.74)	26.8 (2.11)	26.4 (4.98)	30.1 (1.65)

After this, Raman characterization was used to determine the growth of the graphene under these conditions when measuring on the tops of the fused silica, which are the dewetted areas without Ni. For further details about Raman characterization, see Chapter 1, section 1.2. Characterization techniques. Raman spectra of each sample are shown in Figure 14 (b), where the three characteristic peaks of the graphene appear, namely D, G and 2D peaks at 1350, 1580 and 2700 cm^{-1}, respectively. Data related to the Raman results are summarized in Table 2 above. Considering the monolayer criteria of $I_{2D}/I_G \geq 2$ and the narrow FWHM of the 2D peak, the best results are considered to be obtained at 700°C (Sample A) for graphene grown on the nucleation holes with an I_{2D}/I_G ratio of 3.20. Also, monolayer graphene is obtained on dewetted regions at 900 and 1000°C with I_{2D}/I_G ratios of 2.28 and 2.37, respectively. These results differ from those obtained when measuring Raman on the non-dewetted areas, as shown in the data in Table 4, where the presence of Ni decreases the I_{2D}, thus leading to lower I_{2D}/I_G ratios.

In order to obtain a better characterization of the surface morphology during the dewetting evolution, rather than only optical microscope images, SEM characterization in Figure 15 has been included for samples treated at temperatures from 700 to 1000°C. The introduction of an image of the sample at 800°C confirms that the hole-propagation occurs between 800 and 900°C.

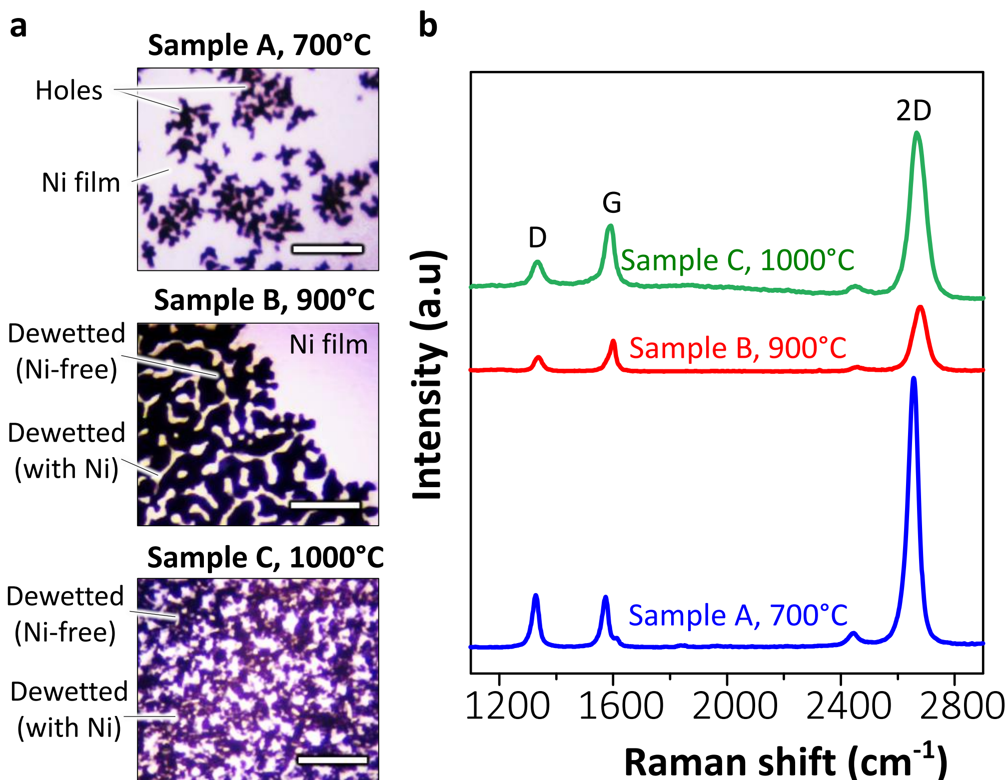

Figure 14. (a) Optical microscope images of 50 nm dewetted Samples A, B and C after graphene CVD growth at 700, 900 and 1000°C, respectively (for 30 minutes). Bright areas correspond to continuous Ni or dewetted areas with residual Ni, while dark areas correspond to Ni-free regions where graphene is deposited directly on fused silica. (b) Raman spectra measured on dewetted areas, demonstrating graphene direct deposition on fused silica. Scale bar: 10 µm.

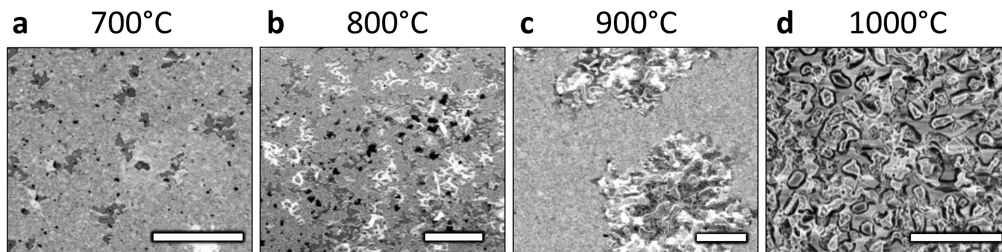

Figure 15. SEM pictures of 50 nm Ni at 700°C, 800°C, 900°C, 1000°C (Samples: A, S8, B, and C). Dewetting evolves as the process temperature is increased: (a) hole nucleation (dark dots), (b-c) hole propagation and (d) total dewetting of Ni UTMF catalyst. Scale bar: 10 μm.

The following subsections explain the most significant results and the different regimes of graphene growth classified by the reaction temperature. Results for samples performed at different thicknesses, temperatures and reaction times can be found in Tables 6 and 6 (section 2.7. Additional information), and are necessary for a full understanding of the growth mechanism of graphene.

Growth at 700°C

At this temperature, a very peculiar graphene growth occurs for 50 nm, (Sample A). As previously mentioned, at such a low temperature dewetting is at the initial state, creating irregular holes in the film. As shown in Figure 14 above, suspended graphene started to grow over the holes forming patches with areas of approximately 2 μm^2.

Figure 16 (a) shows the surface of a randomly selected hole with wrinkled graphene partially covering it. The contrasted area highlights the uncovered area of the hole. Atomic Force Microscopy (AFM) has been used to confirm the suspension of the graphene between the Ni walls in terms of height (the suspended graphene should be at similar heights to the continuous Ni film), and also with the phase mapping, which should be different for both materials (graphene and Ni). Figure 16 (b) shows the AFM measurement of a randomly selected hole that is partially covered by graphene. The same hole is represented in Figure 16 (c) delimited with a white-dotted line. The two height profiles in Figure 16 (c) correspond to the two cross-sections, one to the hole covered with graphene (bottom, red), and the other to the area of the hole free of graphene (top, blue). The comparison of both profiles confirms the presence of graphene being suspended between Ni walls, as the initial height of the red line (graphene) is similar to the Ni film (blue), and does not meet at the lowest height, which is the fused silica surface. In addition, the mapping of the hole in (d) confirms the coexistence of two different materials (graphene and Ni) as there is a big phase change between the suspended area and the continuous film.

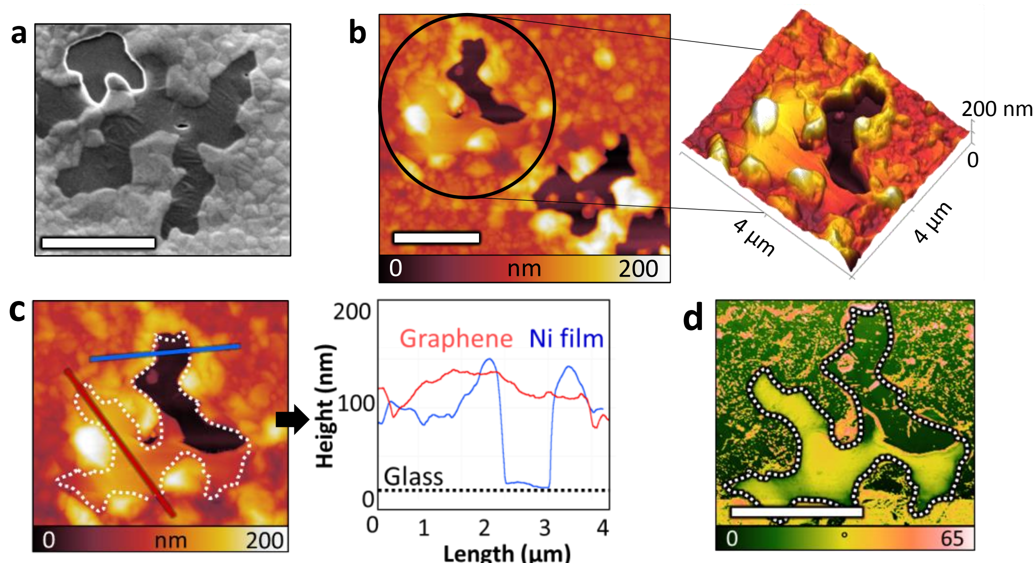

Figure 16. Growth of graphene on dewetted Ni holes (Sample A). (a) SEM image of a hole partially covered by suspended graphene. The highlighted area corresponds to the hole area without graphene. (b) AFM amplitude of suspended graphene over a different hole. The 3D-image on the right highlights the area where graphene is suspended. (c) AFM amplitude of the Ni hole where the white dotted line indicates the hole's border and the blue and red lines are cross-sections plotted on the right. The blue line corresponds to the height of Ni continuous film while the red line corresponds to suspended graphene. (d) Phase image of the hole delimited by the dotted line in (c). A change in phase is detected between the continuous film and the area covering the hole, which confirms the existence of two different materials, Ni and graphene. Scale bar: 2 µm.

A different area of the sample (10x10 μm^2, Figure 17), containing well-delimited nucleation holes, has been selected to evaluate the surface characteristics. The AFM in (a) and the SEM characterization in (b), which has been performed on the white-dashed area in (a), reveal clearly the hole edges, but the growth of the graphene suspended on top cannot be confirmed. To this end, Raman mapping is performed on the whole area of (a). As shown in Figure 17 (c), monolayer graphene is confirmed to grow on top of the dewetted hole by the high I_{2D}/I_G ratio and single sharp Lorentzian-shape of the 2D band with FWHM (2D) = 25-30 cm^{-1}. It is interesting to note that the centers of the 2D and G peaks (ω_{2D}, ω_G) are slightly shifted compared to the typical values of graphene grown on standard Cu foils (2673 cm^{-1} and 1582 cm^{-1} for 2D and G, respectively). Apart from the presence of defects, confirmed by the D peak, the shift and broadening of the 2D peak can be attributed to the strain on the graphene possibly due to the effect of the Ni grain boundaries and residual stress on the Ni film after the graphene growth (31). The metal edges have been delimited with a white line as a reference.

The electrical characterization of the R_S by a Four-point probe system gives very low values due to the contribution of continuous Ni UTMF (see Table 6 and 7, section 2.7. Additional information). In the following section, 2.5. Growth of graphene nano-patterns on alternative substrates, it will be shown that after performing a fast polymer-free etching of Ni UTMF on this sample, the R_S is equal to 2 kΩ/sq. at very high transmittances (T_T= 91.07%).

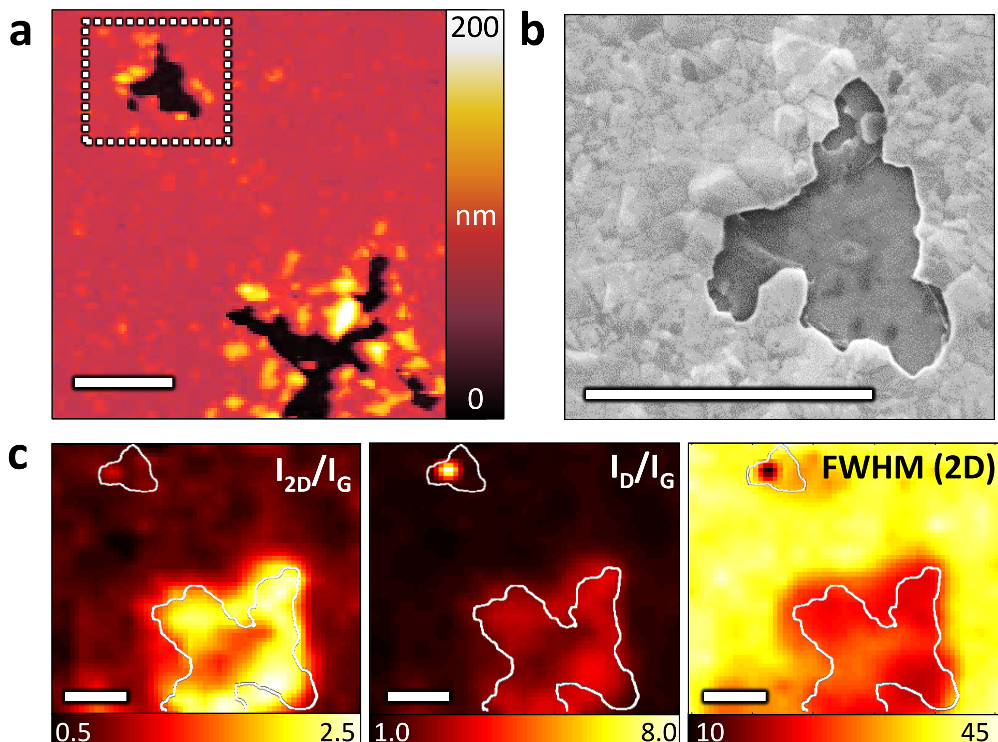

Figure 17. Sample A (700°C). (a-b) Pictures of an area with holes created on the Ni UTMF film by AFM and SEM, respectively, where (b) corresponds to the white-dashed area in (a). (c) Raman maps of the area in (a) demonstrating graphene coverage of the holes, as revealed by the ratios of I_{2D}/I_G and I_D/I_G mapping (c, left and middle, respectively), and FWHM 2D within 25-30 cm^{-1} values (c, right). Metal edges have been delimited with a white-solid line as a reference. Scale bar: 2 µm.

Growth at 800°C

Results obtained at this temperature are shown in Tables 6 and 7, section 2.7. Additional information. The obtained I_{2D}/I_G ratio and FWHM (2D) values of 0.53 and 35.6 cm^{-1} for 50 nm Ni (Sample S8) reveal a decrease in the graphene quality compared to that grown at lower (700°C, Sample A), and higher (900°C, Sample B) temperatures. A possible reason for this transition decrease in quality might be the retraction procedure of the metal.

Growth at 900°C

At this temperature, the Ni films partially dewet, leaving (after the metal retraction) a uniform graphene layer covering the whole sample. To illustrate the differences in the graphene properties between the dewetted and non-dewetted (still continuous metal film) areas, Figure 18 (a) shows the Raman mapping of a 20x20 μm^2 area across these two regions on a 50 nm Ni film (Sample B). The metal edges have been determined from the optical microscope image (see Figure 27 (d), section 2.7. Additional information) and superimposed as a reference. In the dewetted region, the graphene is almost entirely uniform and of good quality with a I_{2D}/I_G ratio of 2.28. In contrast, the continuous film Ni has a lower I_{2D}/I_G ratio due to the Ni film contribution. Similarly to that reported in ref. [45], higher quality graphene is grown on the metal-free dewetted area, which is the fused silica surface. In Figure 18 (d), we have plotted the statistic distribution separately for the two regions. In the dewetted region, monolayer graphene growth is demonstrated by means of a single and sharp Lorentzian 2D peak with a mean value of FWHM (2D) equal to 26.8 cm^{-1}. In the case of the continuous Ni film areas, the 2D peak is very broad with the FWHM (2D) ranging from 30 to 50 cm^{-1}.

AFM measurements were performed to obtain topography and phase details, as shown in Figure 19 (a-b). From the amplitude mapping in (a), one can see that the graphene wrinkles are 1-5 nm in height at areas close to the continuous Ni film. From the phase mapping in (b) and the zoomed area on the right (corresponding to the area delimited by a black-dashed line), graphene domains are observed, with sizes ranging from 130 nm to 410 nm.

The R_S measurement by the Four-point probe equipment performed on the continuous Ni film gives very low values due to the contribution of the metal (Table 6 and 7, section 2.7. Additional information). However, when measured on the dewetted area, the R_S cannot be obtained due to the high roughness of the Ni particles, which avoid the contact area between the graphene and the probes. It is important to remember that the four probes are aligned and equal in height (for more details, see Chapter 1, section 1.2. Characterization techniques).

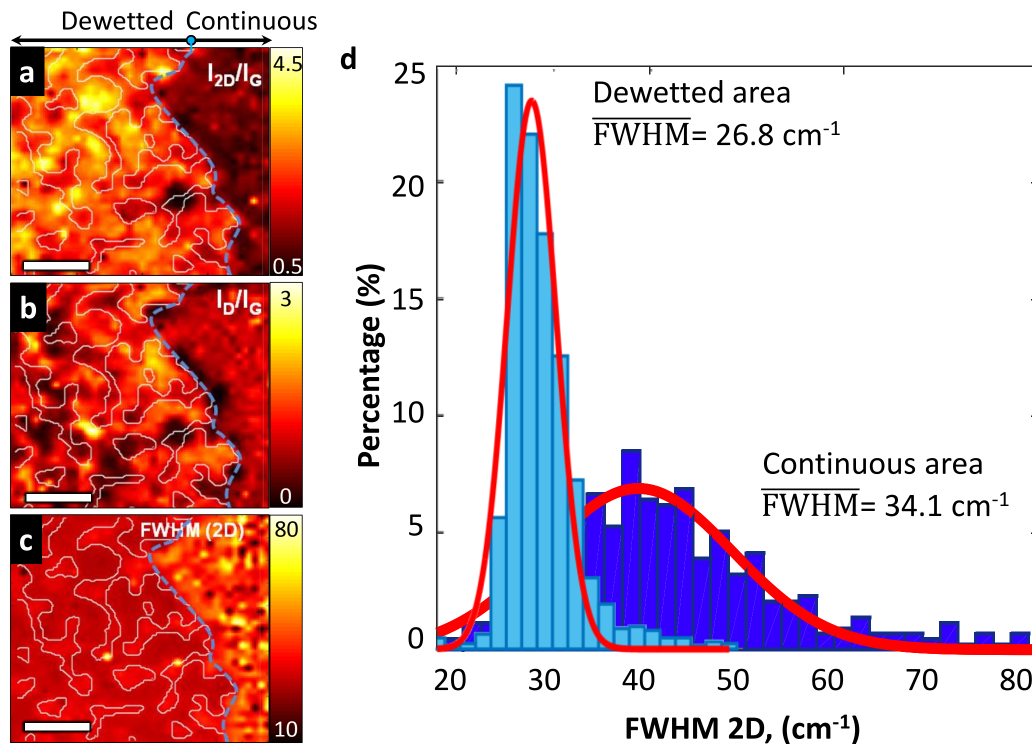

Figure 18. Sample B (900°C). (a-c) Raman maps showing I_{2D}/I_G and I_D/I_G ratios, and FWHM of 2D peak, respectively. Dewetted and continuous areas are delimited by a blue dashed line and metal edges are highlighted with a white-solid line as a reference. (d) FWHM (2D) statistics, plotted separately for both areas (dewetted and continuous) showing a different distribution and mean value. Scale bar: 5 µm.

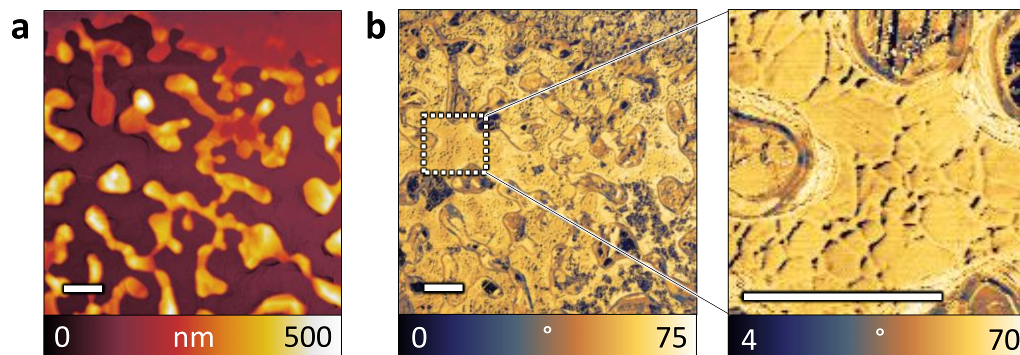

Figure 19. AFM measurements of Sample B. (a) Height map. (b) Phase of map in (a). The image on the right is the zoomed area from (b) (white-dashed line) showing graphene domains on the dewetted area of the sample, which confirms the direct growth of graphene on fused silica. Scale: 2 µm.

Although 50 nm is the most relevant thickness for the whole study of Ni dewetting combined with graphene growth, the use of a 5 nm Ni film at 900°C (Sample S9) is also discussed due to the interesting results. The SEM picture in Figure 20 (a) reveals that, as expected, a complete dewetting occurs at 900°C for this low thickness, forming Ni nanoparticles, which remain on the surface with an average diameter of 200 nm. Raman mapping shows low I_{2D}/I_G values where nano-particle features can be distinguished. These low values and the FWHM (2D) value of 43.8 cm^{-1} (Tables 6 and 7, section 2.7. Additional information) can be translated to the growth of few-layer graphene. In this case, due to the low size of Ni particles and the separation between them, R_S can be measured along the whole sample (mean value 34.2 kΩ/sq.), which indicates the presence of a continuous conducting layer different from Ni (as this has been dewetted into nanoparticles). Indeed, except for a tiny hole in the central part of the SEM picture in (a), the graphene film is continuous over the whole area. We believe that the carbon segregated by the Ni nanoparticles on the glass can act as a seed to grow graphene allowing the connection with other graphene patches originated from the surrounding Ni particles. This fact would allow the growth of the observed continuous film along the whole surface of the sample. The previous hypothesis would explain the high I_D/I_G ratio and high R_S, as defects might appear between the connection of graphene patches, together with the presence of Ni nanoparticles and the fast dynamics of metal retraction at 900°C for 5 nm thick Ni.

Growth at 1000°C

At a processing temperature of 1000°C, for both 50 and 15 nm film thicknesses (Samples C and D, respectively), graphene with a high I_{2D}/I_G Raman ratio grows on the retracted metal regions. This has been confirmed by Raman maps - Figure 20 (b and c) below - where the I_{2D}/I_G ratio is high and fairly constant. For both thicknesses, the 2D band fits to a sharp and single Lorentzian peak with FWHM values between 27 and 30 cm^{-1}. Similarly to Sample S9, the lower heights of Ni dewetted particles allow the R_S measurement on Sample D over the whole area (mean value of 8 kΩ/sq.). The information obtained in Figure 13, where $T_{dewetting} <$ 1000°C for a Ni layer of 15 nm thick, confirms a complete dewetting of the metallic film, the measured conductivity only being possible with the growth of a continuous conductive graphene layer on top of the fused silica. For Sample C, however, the R_S cannot be measured due to the roughness of the remaining Ni particles, which prevents the electrical contact between the graphene and the four -point probes.

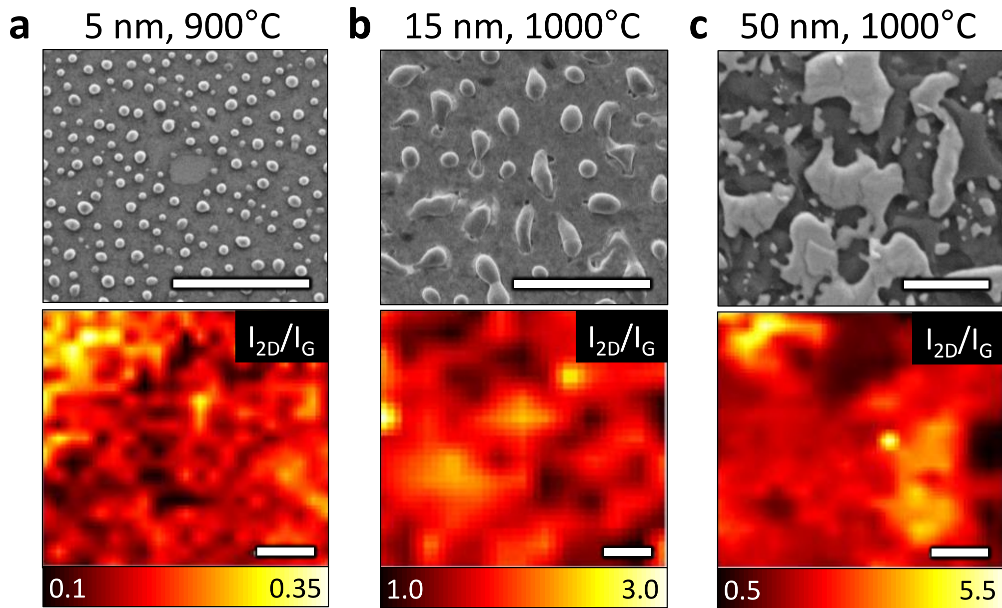

Figure 20. SEM images and Raman maps of I_{2D}/I_G of graphene grown for 30 minutes on different Ni thicknesses and at different temperatures: (a) S9 (5 nm, 900°C), (b) Sample D (15 nm, 1000°C) and (c) Sample C (50 nm, 1000°C). The central part of the SEM in (a) shows a tiny hole in the continuous area of graphene on fused silica. Scale bar: 2 µm.

After evaluating these results at different growth temperatures, we can conclude that higher quality graphene can be grown using Ni UTMFs of 50 nm thickness. In this case, the growth mechanism of the graphene can be explained with the qualitative model in Figure 21. During the heating phase, an annealing step in H_2 is performed on the Ni UTMF (a), which increases its grain size and crystallinity, with preferential crystal orientations of Ni(111) and Ni(220) [49,66]. At a $T_{dewetting}$ of 700°C, the Ni film is nucleated with holes (b). If this temperature is selected as the growth temperature, the graphene is formed on the holes and continues growing upon retraction of the metal. If higher temperatures are selected for the graphene growth (900-1000°C), the hole propagation increases, depositing graphene on the dewetted areas, i.e., directly on the substrate.

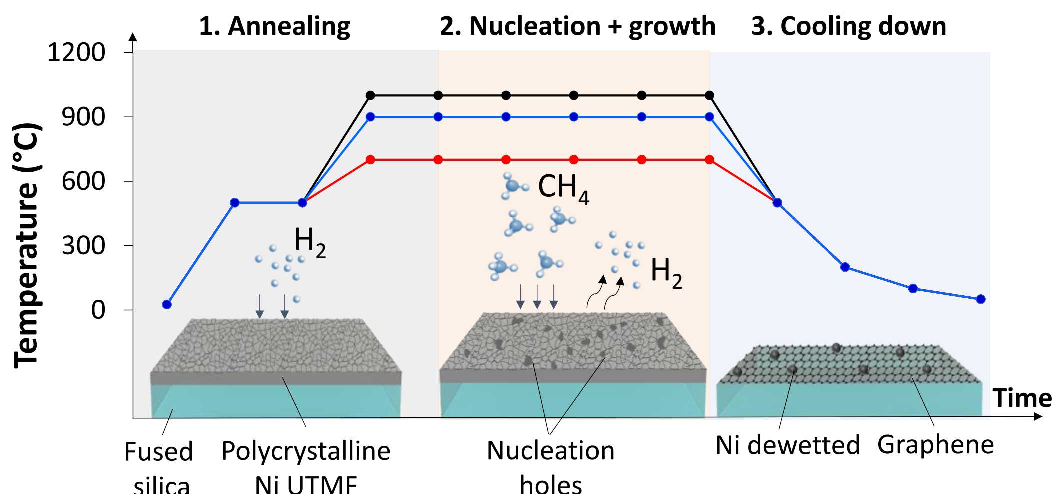

Figure 21. Schematic model of graphene growth on 50 nm Ni UTMF at temperatures from 700-1000°C consisting of three main steps: (1) annealing, where activation, reduction and crystallization of Ni UTMF polycrystalline film occur; (2) hole nucleation (at 700°C) promoting Ni dewetting and deposition of graphene upon metal retraction; (3) cooling down of the system to room temperature where graphene is deposited on the silica substrate.

Finally, to conclude this section it is necessary to comment on the characterization of the reaction time. All of the previous results were obtained for a 30-minute growth period because this proved to be the optimum value from an initial study of reaction time influence on graphene quality. Figure 22 shows the resulting Raman I_{2D}/I_G ratios in (a) and FWHM 2D values in (b) for Ni UTMFs of thicknesses of 5 and 50 nm at temperatures of 700 and 1000°C. The modification of the reaction time (from 15 to 60 minutes) revealed that at 30 minutes, the Raman parameters were within the graphene monolayer ranges (shadowed areas in both graphs) with the highest I_{2D}/I_G ratios and lowest FWHM 2D for all Ni thicknesses and all temperatures.

After only 15 minutes, the samples had low I_{2D}/I_G ratios – where the 2D band was very low and broad - and high FWHM 2D values, which may be attributed to an incomplete formation of the graphene. For 60 minutes, the I_{2D}/I_G ratios again decreased and the FWHM 2D values increased, which may indicate that at larger reaction times, more carbon is absorbed and segregated upon the metal retraction, thus promoting the growth of multilayer graphene.

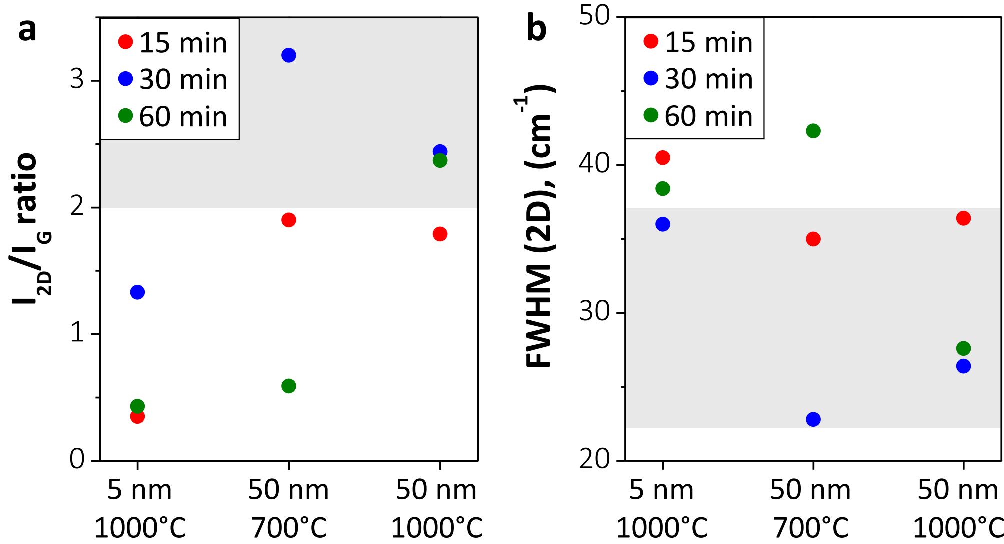

Figure 22. Reaction time effects on graphene quality, evaluating (a) I_{2D}/I_G and (b) FWHM 2D peak, at 15, 30 and 60 minutes (represented by red, blue and green circles, respectively), for different samples. Shadowed areas correspond to values for theoretical graphene monolayer.

2.5. Growth of graphene nano-patterns on alternative substrates

For many applications, especially those involving the use of light (e.g., for optical and optoelectronic devices), the transparency of the substrates with graphene is crucial. For the samples obtained in this thesis, Ni residues are still present in the sample, being responsible for most of the optical loss. Therefore, these need to be removed after the graphene growth is performed. Different removal approaches can be employed, such as thermal evaporation [163] or wet chemical etching. Thermal evaporation of the Ni, however, requires high temperatures (>2000°C at 7 mbar [164]) which would make it unsuitable for the application of low strain point substrates. This is one common issue that has limited the practical application of some previous direct growth techniques. For this reason, we have used a diluted aqua-regia solution for a duration of only 5-15 minutes, a very low time period when compared to the standard "wet-etching", and with the additional advantage of avoiding PMMA deposition on the graphene.

After Ni etching, we believe that the graphene deposited on the glass originates from the top side of the Ni for Sample A, where the graphene grows on dewetted holes. However, for samples B, C, and D, the graphene could originate from the bottom side of the Ni. For these samples, higher temperatures improve the dissolution of the carbon inside the metal. Additionally, as the Ni film is

dewetted, the catalyst surface area in contact with the carbon source will be larger, with more active sites where carbon could be dissolved.

A visible evolution in the transmission and absorbance values at 550 nm are observed in Figure 23 (a-b) for Samples A, B, C and D, before and after Ni removal. The absorbance measurements have been obtained by measuring the transmittance (T_T) and reflectance (R_F) of the samples with the spectrophotometer, and then calculating the absorbance (A) as:

$$A = 100 - T_T - R_F \quad \text{(Eq. 15)}$$

The evolution in transmission is shown in Figure 23 (b) through a series of pictures for exemplary Samples A and C. All the results confirm a significant recovery in the samples' transmittances, Sample A being the most transparent with approximately 91.07% transmission, followed by Samples D and B both with approximately 82 and 79%, and finally Sample C with 67%. The most drastic change occurs for Sample A, whose optical loss of 2.38% with respect to the bare fused silica substrate (which is also represented in the figure, with a measured transmittance of 93.45%) is very close to the expected absorption of the graphene monolayer (2.3%), thus being consistent with the effective direct growth of graphene on the fused silica. Full transmittance spectra are included in Figure 24 (a-b), both before and after the Ni removal for Samples A-D and S9 (5 nm, 900°C). Very interesting information can be extracted from them, such as the presence of Ni nanoparticles after graphene growth in (a) for Samples D and S9 due to the observable dip in transmission, i.e., the plasmonic response of the metallic particles. For Sample D, this plasmonic effect is not observable after etching in (b), which together with its high transmittance suggest that a considerable quantity of Ni particles have been removed. For Sample S9, a small increase of 10% in (b) at 550 nm has been obtained, which together with the still observable plasmonic effect of Ni particles confirm that a lower quantity of catalyst has been removed from the surface.

From these results, we can confirm the successful growth of graphene directly on fused silica, with samples treated at the lowest temperature (700°C) being the most promising as they have the highest optical transmittance after a complete Ni removal (91.07% at λ=550 nm). Taking advantage of the low temperature needed, we want to implement our technique in order to produce controlled patterned areas (ribbons and squares) on different substrates including conventional Si/SiO_2 wafers and Willow® Glass, which is very unusual due to its low strain point, ultra-thinness (100 μm) and flexibility. The wide range of target substrates where we can use our technique to grow graphene, together with the advantage of being able to also use flexible substrates, considerably expands the potential for our technique compared to previous ones, where the main limitation was the high growth temperatures required. In addition, an efficient direct growth on Willow® Glass [165] would enable large-scale and roll-to-roll production of

transparent substrates with graphene for flexible electronics and optoelectronics. The fabrication procedure is represented in Figure 25 (a), where the Ni patterns have been deposited by sputtering after performing a lithography step. For the dimensions of the patterns deposited here (with squares ranging from 0.1 mm to 1 mm and ribbons with maximum dimensions of 0.3 mm x 1.5 cm), a shadow mask could also be used, being easier, faster and without the need for a photoresist. After the Ni UTMF deposition of 50 nm, the graphene is grown under the same conditions as for Sample A (700°C, 30 minutes), and then the Ni removal step in aqua regia is carried out for 5-15 minutes. Figure 25 (b-c) shows the sample appearance after Ni sputtering (left picture), and after Ni removal showing graphene patterns (right picture), when using Si/SiO_2 wafers and Willow® Glass, respectively.

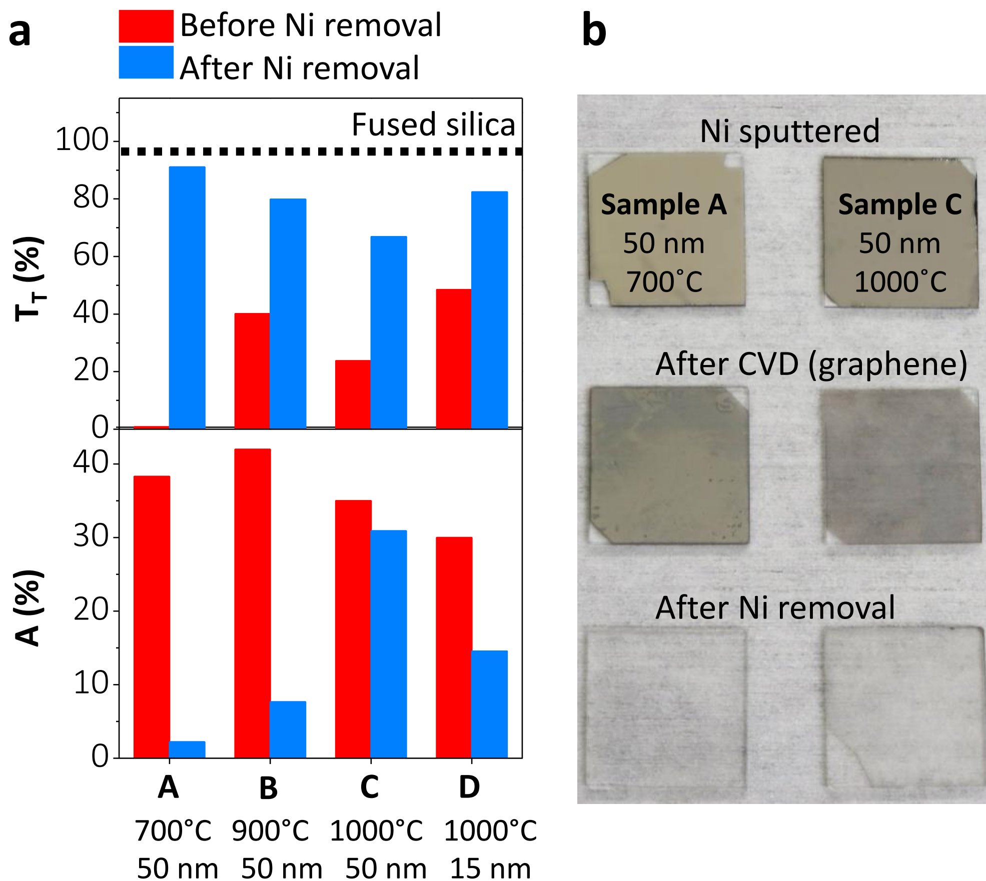

Figure 23. (a) Transmittance (including substrate) and absorbance values at 550 nm of Samples A-D before (red column) and after (blue column) Ni removal. (b) Picture of Samples A and C (50 nm Ni at 700°C and 1000°C, 1st and 2nd column, respectively), showing the appearance after Ni deposition (1st row), after graphene growth (2nd row) and after Ni removal (3rd row).

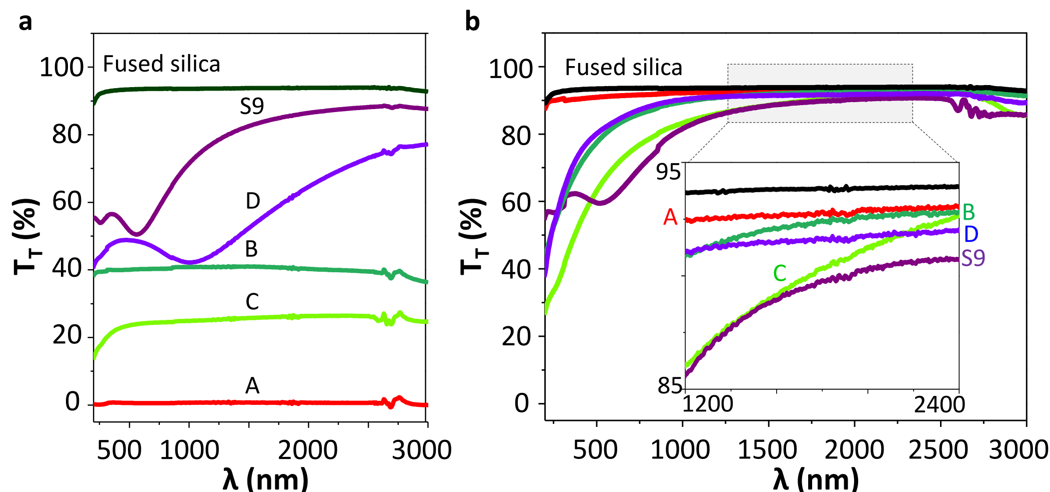

Figure 24. Transmittance spectra of the highest quality Ni UTMF Samples A-D and Sample S9. (a) Samples with graphene before the Ni removal, and (b) the same after Ni removal (15 minutes). The zoomed area in (b) shows the spectra range from 1200 to 2400 cm^{-1}. Details of each sample in terms of thickness and temperature at 30 minutes of reaction are: Sample A: 50 nm, 700°C; Sample B: 50 nm, 900°C; Sample C: 50 nm, 1000°C; Sample D: 15 nm, 1000°C; Sample S9: 5 nm, 900°C.

For all patterns, the graphene is continuous as indicated by the SEM characterization in Figure 25 (d) and Figure 25 (f-g), when grown on Si/SiO_2 and Willow® Glass, respectively. Due to the observance of two small nanoparticles in (g), an EDX has also been performed in order to detect the presence of Ni residues on top of the graphene. The EDX results collated in Table 5 confirm the total removal of the Ni as no residues are detected when measuring over the whole graphene area.

In addition, Figure 25 (e) shows an example of the Au contacts that have been evaporated on the corners of a graphene square grown directly on Si/SiO_2 in order to perform Rs measurements by the Four-point probe measurement (see Chapter 1, section 1.2. Characterization techniques for further details). The mean value of the R_S growth on both substrates is close to 2 kΩ/sq. (±0.5).

Table 5. EDX measurements on graphene after Ni removal (at Ni 50 nm 700°C, 30 minutes)

Elements	Atomic (%) detected by EDX technique	
	On graphene	On particles
C	44.79	48.07
O	29.63	29.54
Si	25.99	22.52
Ni	-	-

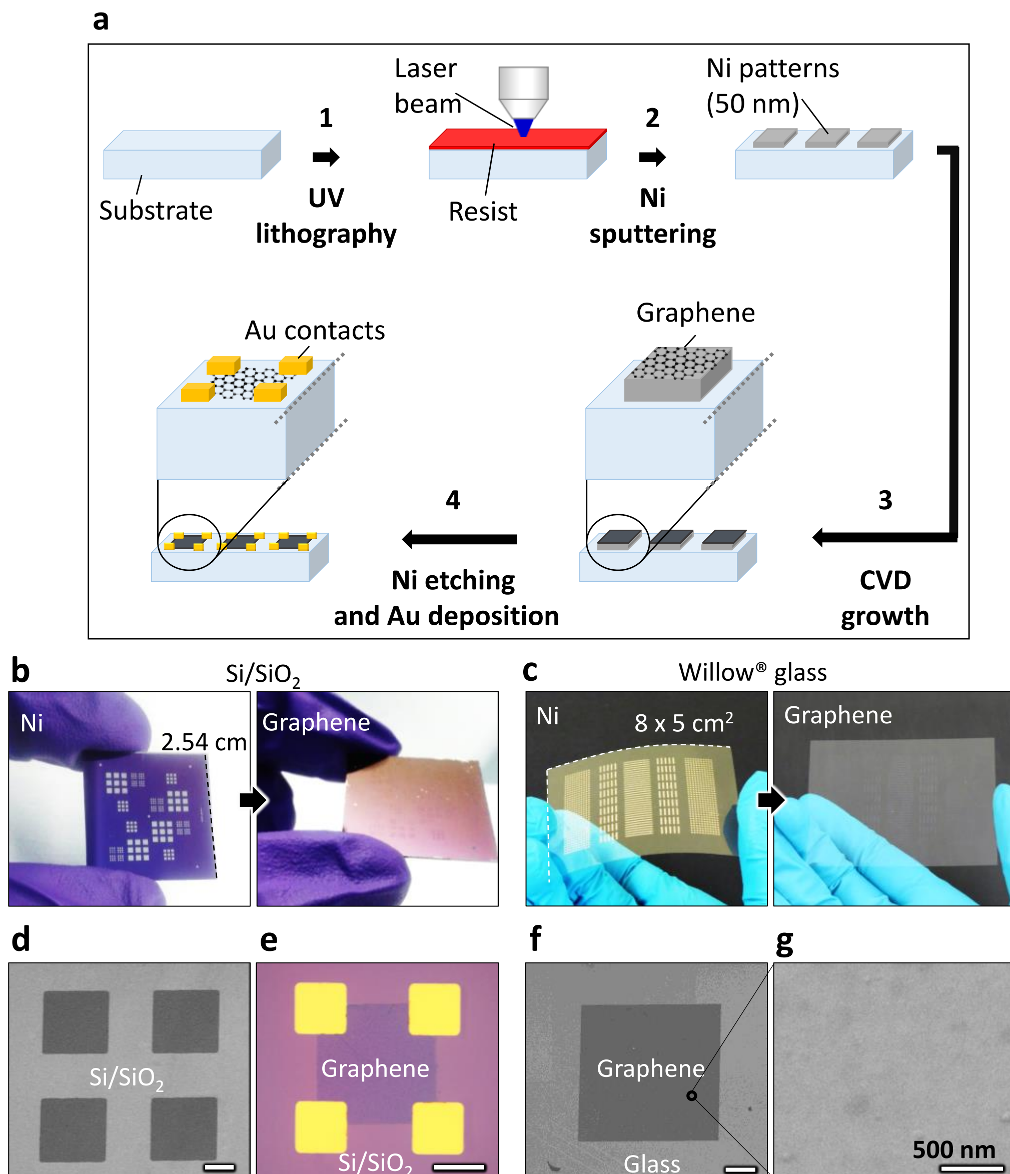

Figure 25. (a) Flow chart indicating the fabrication steps (see section 2.2. Sample preparation for further details), including: (1) lithography of Ni; (2) 50 nm Ni deposition by sputtering; (3) graphene growth on Ni via CVD technique (700°C, 30 minutes); (4) Ni removal in aqua regia and Au contact (100 nm) deposition. Optical images in (b-c, left) show 50 nm Ni deposited on Si/SiO_2 and Willow® glass in square/stripe shapes, while in (b-c, right) graphene patterns can be distinguished after Ni removal. (d) SEM image of graphene squares grown on Si/SiO_2 after Ni removal. (e) Optical microscope image of one graphene square after Au contacts deposition for R_S measurement. (f-g) SEM images of graphene grown on Willow® glass after Ni removal, where (g) is a zoomed area of the area in (f) delimited by a red circle. Scale bar: 100 μm.

Finally, Raman microscopy has been performed in order to characterize the graphene grown on Willow® glass after the Ni removal. Figure 26 (a) shows a Raman map performed on a large area of graphene (40x80 μm^2) close to the edge of the square pattern. The plot of I_{2D} allows a clear identification of the area where the graphene has grown and the high resolution of the graphene edge. When the Raman is measured outside the graphene pattern (on the glass surface) the I_{2D} is close to zero. Moreover, Figure 26 (b) shows the mapping of the same area for I_{2D}/I_G ratios, again giving a high contrast between the area where the graphene is grown and the glass surface. Two spectra from the aforementioned Raman map have been plotted separately in (c), one taken from the area covered with graphene (top, red line), and the second measured on the glass surface (bottom, black line). The 2D peak of the graphene has decreased when compared with the initial measurement performed after the CVD growth (Figure 14). This fact, together with the appearance of a small D peak, can be a consequence of the etching process with the aqua regia. Further optimization of the etchant solution (concentration and chemicals) needs to be performed in order to improve the resulting graphene quality.

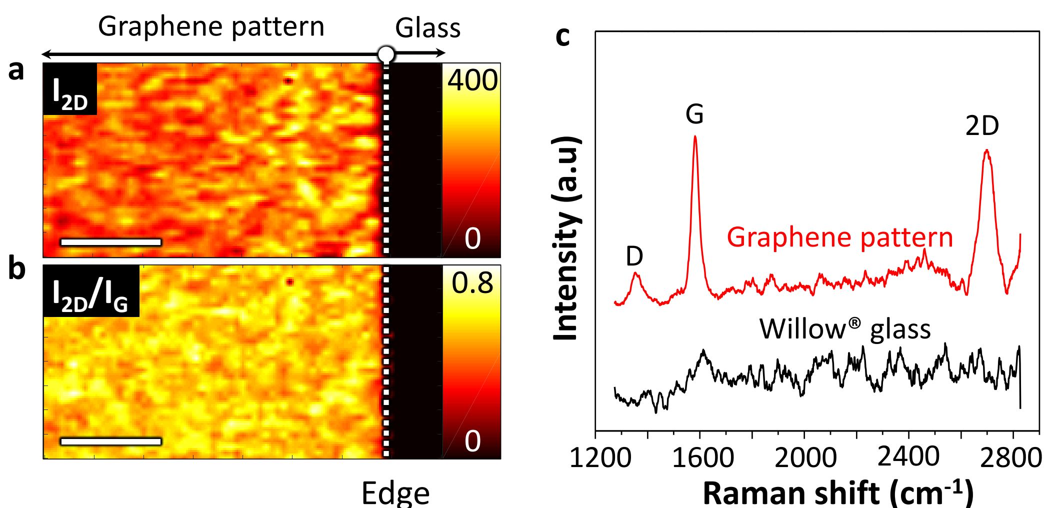

Figure 26. Raman mapping of graphene square grown on Willow® glass, plotting: (a) I_{2D} peak and (b) I_{2D}/I_G ratio. The edge of the graphene square pattern is represented by a white-dashed line, with graphene on the left side of the line and glass on the right. (c) Two Raman spectra taken from the map in (b) are plotted, the top one belonging to the graphene covered area (red line) while the bottom one belongs to the glass (black line). Scale bar: 20 μm.

2.6. Conclusion

Thin metal films of thicknesses at the nanometer scale are known to be unstable when heat is applied. After a specific temperature is achieved, holes start to appear on the film and propagate with time or higher temperatures, finally collapsing into small islands. Previous knowledge on this topic has motivated us to use dewetting in order to solve a very important issue related to graphene growth: its direct growth on the target substrate without the need for any transfer step.

With this aim in mind, we have proposed Ni as the ideal material for two reasons: its role as a good catalyst for high-quality graphene growth, and its stability during graphene synthesis as its melting/boiling points are much higher than the graphene growth temperatures (typically 700-1100°C). The last reason is important in order to accurately control the position of graphene deposition.

The dewetting dynamics of thin films depend not only on the temperature applied but also on the thickness of the film. Higher thicknesses lead to higher temperatures at which dewetting occurs. For graphene growth purposes, it is better to use minimum catalyst thicknesses in order to avoid metal residues. However, dewetting of Ni thin films of 5-20 nm occur within the 400-600°C temperature range. To study the whole phenomenology of dewetting, we extended the use of 50 nm Ni films, as their dewetting temperature is most suitable for graphene growth.

With our study, we have demonstrated the success of using Ni UTMFs as catalysts and sacrificial templates for the fast growth of high-quality graphene directly onto the target substrate, without the need for a transfer step or the addition of secondary materials.

The possibility of depositing graphene at minimum temperatures of 700°C widens the range of substrate materials on which graphene can be directly grown. This has already been demonstrated by growing graphene patterns on ultrathin glass, a functionalized substrate with great potential for flexible electronic and optoelectronic devices.

2.7. Additional Information

Table 6. Samples S1-S9: Process conditions and Raman/electrical results for graphene deposited on Ni UTMF

Results	Ni UTMF Samples								
	S1	**S2**	**S3**	**S4 (A)**	**S5**	**S6**	**S7**	**S8**	**S9**
Ni (nm)	5	15	50	50	50	5	15	50	5
T (°C)	700	700	700	700	700	800	800	800	900
t (min)	30	30	15	30	60	30	30	30	30
ω_{2D} (cm^{-1})	2665.5	2684.5	2676.3	2657.3	2698.3	2680.2	2678.8	2706.2	2676.6
ω_G (cm^{-1})	1592.5	1600.9	1592.4	1574.6	1578.5	1598.6	1600.5	1585.5	1594.6
ω_D (cm^{-1})	1335.6	1345.5	1332.5	1329.3	1351.5	1342.0	1341.1	1354.1	1344.9
I_{2D}/I_G (σ)	0.04 (0.04)	0.09 (0.06)	1.9 (0.22)	3.20 (1.78)	0.59 (0.12)	0.16 (0.03)	0.36 (0.08)	0.53 (0.27)	0.38 (0.06)
I_D/I_G (σ)	0.62 (0.33)	0.93 (0.07)	1.22 (0.11)	0.92 (0.54)	0.36 (0.21)	0.96 (0.07)	1.07 (0.16)	0.25 (0.20)	0.95 (0.13)
FWHM (2D), (σ)	44.7 (2.41)	42.2 (3.78)	35.3 (2.34)	22.8 (5.74)	42.3 (2.48)	41.2 (3.79)	43.9 (3.51)	35.6 (0.62)	43.8 (3.65)
R_S [a] (kΩ/sq.)	54.0	52.8	$1.2\cdot10^{-3}$ [b]	$1.4\cdot10^{-3}$ [b]	$1.5\cdot10^{-3}$ [b]	52.4	83.4	$2\cdot10^{-3}$ [b]	34.2

[a] Note that R_S measurements were performed with the Four-point probe system measuring directly on the graphene/Ni surface. Residual Ni affects the measurements. Also, at 1000°C, the high roughness of Ni/graphene surface makes a correct evaluation of R_S difficult.

[b] Ni film was almost continuous as the dewetting of the film was at the initial nucleation state. In Sample B, R_S was measured on continuous Ni film.

Table 7. Samples S10-S18: Process conditions and Raman/electrical results for graphene deposited on Ni UTMF

Results	Ni UTMF Samples								
	S10	S11 (B)	S12	S13	S14	S15 (D)	S16 (C)	S17	S18
Ni (nm)	15	50	5	50	5	15	50	5	50
T (°C)	900	900	1000	1000	1000	1000	1000	1000	1000
t (min)	30	30	15	15	30	30	30	60	60
ω_{2D} (cm^{-1})	2674.9	2681.4	2679.7	2675.9	2663.8	2664.6	2667.2	2666.1	2657.9
ω_G (cm^{-1})	1600.8	1603.5	1588.9	1596.2	1577.2	1593.5	1589.6	1593.5	1586.1
ω_D (cm^{-1})	1342.3	1338.0	1341.7	1335.9	1335.0	1336.6	1333.9	1340.9	1333.9
I_{2D}/I_G (σ)	1.20 (0.28)	2.28 (0.74)	0.35 (0.08)	1.79 (1.30)	1.33 (0.09)	2.37 (0.38)	2.44 (1.24)	0.43 (0.03)	2.39 (0.49)
I_D/I_G (σ)	1.11 (0.13)	0.49 (0.46)	0.90 (0.11)	0.91 (0.44)	0.87 (0.07)	0.51 (0.11)	0.17 (0.12)	1.25 (0.06)	0.53 (0.27)
FWHM (2D) (σ)	42.0 (1.25)	26.8 (2.11)	40.5 (2.86)	36.4 (4.22)	36.0 (2.56)	30.1 (2.37)	26.4 (4.98)	38.4 (2.26)	27.6 (3.34)
Rs [(a)] (kΩ/sq.)	16.8	$1.7 \cdot 10^{-3}$ [(b)]	58.9	-	17.55	8.16	-	16.9	-

[(a)] Note that R_S measurements were performed with the Four-point probe system measuring directly on the graphene/Ni surface. Residual Ni affects the measurements. Also, at 1000°C, the high roughness of Ni/graphene surface makes a correct evaluation of R_S difficult.

[(b)] Ni film was almost continuous as the dewetting of the film was at the initial nucleation state. In Sample B, R_S was measured on continuous Ni film.

Table 8. Raman results on Ni UTMFs of different thicknesses. (Raman measured on the non-dewetted areas).

Raman results	Ultrathin Ni on fused silica substrate samples			
	Sample A	Sample B	Sample C	Sample D
I_{2D}/I_G, (σ)	1.24 (0.45)	1.36 (0.68)	1.73 (0.85)	1.57 (0.30)
I_D/I_G, (σ)	0.82 (0.37)	0.88 (0.39)	0.29 (0.16)	0.57 (0.21)
FWHM 2D (cm^{-1}), (σ)	32.6 (4.45)	34.1 (10.6)	28.2 (2.72)	31.7 (1.59)

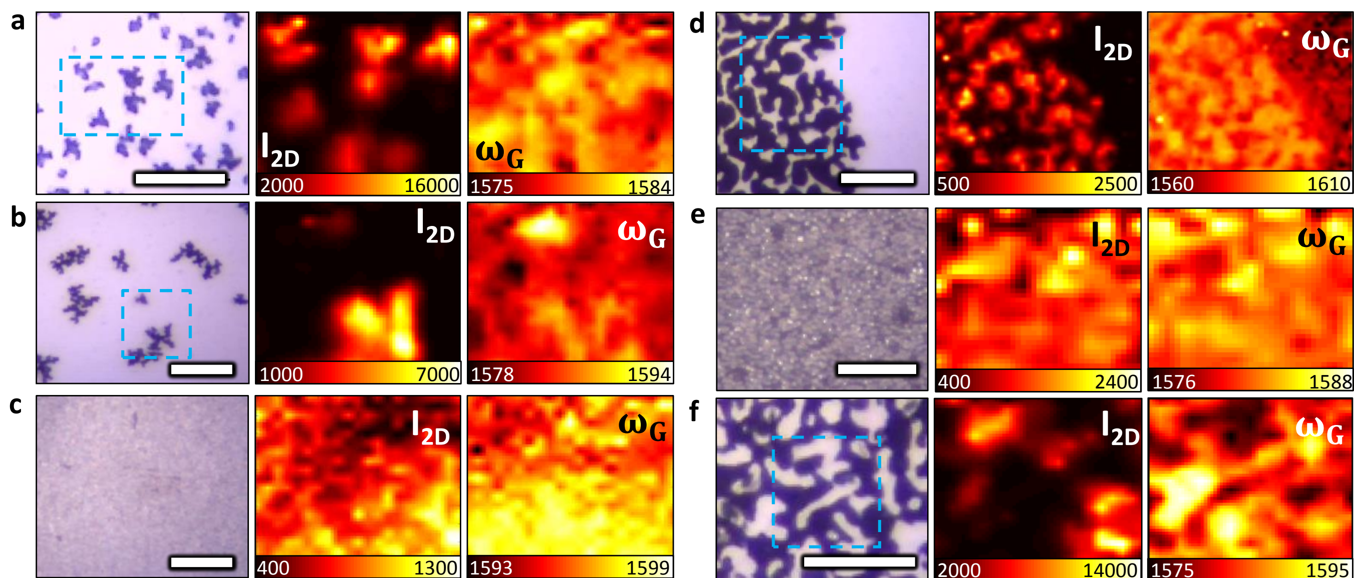

Figure 27. Optical microscope image, and I_{2D} and shift of the G peak. (a-b) G Raman maps (10x10 μm²) for two different regions of Sample A (blue dashed lines). (c) S9, (d) Sample B (map of the region delimited with dashed blue line), (e) Sample D and (f) Sample C (map of the region delimited with dashed blue line). Scale bar: 10 μm

3

Graphene assembled into 3D-shapes by tuning the Cu catalyst density

Graphene grown directly on dielectrics is a hot research topic due to being able to avoid the intermediate step of transferring the graphene from the initial catalyst to the target substrate. As well as accelerating the fabrication process, this is also useful in order to avoid the addition of other materials onto the graphene, which can degrade its electrical properties. Recently, the growth of graphene disposed in three-dimensional shapes has been exploited because this allows additional properties to be added to the intrinsic exceptional properties of graphene – e.g., higher surface areas and porosity – thus, increasing the potential applications for graphene.

In this chapter, we have developed an easy technique that allows the direct growth of graphene structures in layers – two-dimensional assembly (2D) – and also in balls and sponge-like structures – three-dimensional assembly (3D) – by a controlled modification of the Cu catalyst density. High transparency nanostructures have been obtained over large areas without the need to use expensive and time-consuming lithography steps.

This work is a collaboration with Corning Incorporated, and has resulted in the filing of a Patent application and the publication of the following paper:

M. Marchena *et al.* (2017), "Direct growth of 2D and 3D graphene nano-structures over large glass substrates by tuning a sacrificial Cu-template layer", 2D Mater. 4, 025088.

3.1. Introduction

As previously mentioned, the two-dimensional material graphene is of great interest due to its excellent and unique properties that make it suitable for a wide range of applications. Besides the growth of large graphene areas on flat metal catalysts, recent studies have demonstrated the advantages of growing graphene layers assembled into three-dimensional (3D) configurations. The great interest for synthetizing these new structures relies on the combination of typical graphene

properties (e.g., transparency, conductivity, flexibility, etc.) with additional ones that are typical of 3D-materials (e.g., large effective surface areas, porosity etc.). The added value of these novel 3D-graphene structures expands the applications for graphene. If 3D-graphene structures are combined with other functional materials, new surfaces can be developed for a wide variety of applications. These include chemistry (e.g., new catalysts, membranes, filters, etc., also with environmental applications for pollutant removal, etc. [166]), energy storage (e.g., supercapacitors, batteries, solar cells, etc. [167]), gas storage (e.g., CO_2 adsorption [2]), gas and biological sensors, anti-glare display screens, LEDs and biotechnology (e.g., drug delivery, tissue scaffold for *in vitro* neural stem cell growth, bionic nanocomposites, etc.) [168–171].

The achievement of graphene structures with large surface-to-volume ratios has been possible with the development of techniques that modify the catalytic templates into 3D shapes. After growing graphene by the CVD method on 3D catalysts, sometimes adding a step to etch the initial catalytic template, the 3D structures obtained are graphene spheres, tubes and networks [170,172]. Table 9 below shows part of the data related to the fabrication of state-of-the-art 3D-graphene structures, highlighting the wide variety of catalysts that have been used, the growth conditions and the main results. Within the possible 3D-shaped catalysts used, the Ni foams are an example that produce high quality 3D-graphene (3D-G) networks with excellent conductivity [171,173]. More specific catalysts are, for example, MgO, Ni-coated pyrolyzed films, Ni scaffold structures and metallic salts. PECVD has also been used for the production of 3D-G because vertical oriented structures of graphene, called carbon nanowalls, are obtained when a voltage is applied, sometimes without the need for a catalyst [174,175]. Several works have also reported the fabrication of 3D-graphene networks treating initial GO suspensions [167,168]. For a more complete overview of the work related to the production of 3D-graphene structures, reviews from ref. [176–178] contain further information.

There are two main challenges associated with the growth of 3D-G structures, firstly, in extending the aforementioned technique to different catalyst materials and geometries. Secondly, as with the fabrication of 2D graphene (2D-G), there is the challenge of avoiding intermediate transfer processes, which usually involve the etching of the metal catalyst, and the use of polymers and lithography steps that are expensive, time consuming and can degrade the graphene properties.

In this work, we address the previous challenges and demonstrate the direct growth of 2D-G and 3D-G structures starting from properly defined catalytic Cu templates. The use of Cu as the catalyst simplifies the graphene growth process and makes it compatible with the production of both types of graphene structures (2D-G and 3D-G). Moreover, the two following considerations serve to demonstrate the great potential of our technique for future industrialization.

Table 9. State-of-the-art of graphene grown on 3D-catalytic templates, indicating the process conditions and the main characteristics of the work

Catalyst (thickness)	Target substrate	Growth conditions	Main comments	Ref.
-	Free-standing	GO in aqueous dispersion (autoclave) 180°C, 12 h	Graphene hydrogel. 2D-G sheets assembled to a 3D network. Conductive, mechanical and thermal stable	[168]
Au (50 nm)	Si/SiO_2	PECVD (2kV), Patm,CH_4-C_2H_2 30 s-10 min	Vertical oriented p-type graphene nanosheets (10 layers) for gas detection (NH_3 and NO_2)	[174]
Ni foam (1.2 mm)	Free-standing by PDMS infiltration	CVD, CH_4 1000°C, 1 atm	Graphene foams (100-600 μm thick and area= 374 cm^2). High porosity (97%) and area=850 m^2/g. Ni etching: HCl or $FeCl_3$	[171]
Fe reduced from $FeCl_3$ solution	PS beads with –COOH and –SO_3H	CVD, 1000°C, H_2/Ar 30 min Fe etch: HCl 6h	Few-layer graphene nanoball Area= 508 m^2/g; p- doping by dipping in H_2SO_4 3h 120ºC.	[179]
-	Free-standing	GO in water mixed for 3h. Frozen for 24 hours	3D network of GO, by polymerization with glutaraldehyde and resorcinol. Application for CO_2 storage	[167]
Cu NPs (500 nm)	Si/SiO_2	Mixed with PMMA 12 h Cure 110°C 10 min 800-900ºC, H_2/Ar	Graphene balls with Cu cores inside. Graphene demonstrated to prevent Cu oxidation	[180]
3D-Ni scaffolds	Free-standing by PDMS infiltration	Ni scaffold in layers and annealed at 700°C. CH_4, 950°C	3D graphene porous networks in controllable patterns PMMA added	[170]

Firstly, our technique allows the nano-structuring of the initial Cu structures using lithography-free methods, meaning we are able to process larger areas (up to 2x2 inches) over shorter timescales. An additional advantage is that, although in this work the Cu deposition has been performed on glass, it is also compatible with

other target substrates. Secondly, our technique allows the direct growth of 2D-G and 3D-G structures on the target substrate, thus avoiding additional transfer steps, which are time consuming and risky with regard to maintaining the graphene properties, as a consequence of the remaining residues.

In order to demonstrate the versatility of our technique, we have investigated the growth of three different graphene structures - of varied optical, electrical and morphological properties - by proper tailoring of the initial Cu template. The first types of structures are 3D-graphene sponges (3D-GS), which result from the arrangement in layers of non-aggregated Cu NPs. The second types of structures are 3D-graphene nanoballs (3D-GB), which result from the arrangement of isolated Cu NPs in one layer. The third types of structures are 2D-graphene networks (2D-G), which result from the aggregation of Cu NPs into large catalytic structures.

It is worth noting that in previous work [180], the Cu NPs used for the production of 3D-G shapes tended to coalesce during the graphene growth, thus making it difficult to control the size and the shape of the resulting structures. Instead, our process allows control of the Cu NP template. In addition, we have improved adhesion by surface treatment or by partially embedding the Cu template in glass. The resulting high-quality graphene nanostructures present low defect sites, high surface to volume ratios, and high optical transmission while, in some, still preserving the electrical properties.

3.2. Sample preparation

3.2.1. Cu deposition on glass substrate

The deposition of the Cu catalyst NPs for 2D-G and 3D-G production has been carried out at Corning Incorporated.

Fused silica substrates from Corning Inc. (High Purity Fused Silica, HPFS®), 2x2 inches in size, have been used in this work as the target substrates. For a proper deposition and adhesion of the Cu NPs to the glass surface, the latter needs to be highly cleaned with contact angles below 5 degrees. To achieve this, the following cleaning procedure is performed. The glass slides are soaked in Semiclean™ KG solution at 70°C in an ultrasound wash, subsequently rinsing them in ultrasound with DI water. After drying the substrates in air at 80°C, it is necessary to perform a plasma cleaning step (March PM-100, Nordson) at 50 W for 3 minutes, using an O_2/Ar (50/50) mix to ensure the removal of any residues left on the surface following the washing or storage steps.

For the production of all graphene structures, Cu has to be firstly deposited onto the substrate. This is discussed below, differentiating the Cu deposition for 3D-GB and 2D-G production, where the Cu belongs to a solution of CuO NPs, and for 3D-GS production, where the Cu is evaporated from a Cu foil.

Specifically, for the growth of 3D-GB and 2D-G, the Cu has been deposited using a copper (II) oxide (CuO) suspension in water (Nanophase Technologies or Alpha Aesar, 46.8%) onto cleaned glass with a primary particle size of 17-23 nm. The cleaning process, the concentration of the CuO solution and the dip-coating parameters (withdrawal speed and immersion time) allow the control of the particle deposition, the Cu NP density and aggregate size. The CuO dispersion is initially mixed and sonicated for 10 minutes while the clean substrates are located inside a dipping vessel. The deposition of CuO NPs on the glass has been carried out using varying concentrations (1–10 wt. %) by diluting the stock solution and withdrawal dip speed at 224 mm/min without additional modification of the solution. The use of high concentrations of CuO have resulted in multilayer coatings while lower concentrations have promoted the deposition of a discontinuous coating – island type for 3D-GB production – with few layers of particles in some regions.

However, for the 2D-G production, we have observed that the increase in the number of runs at a lower withdrawal speed dip (50-150 mm/min) leads to an increase in particle density without the addition of CuO multilayers. In this specific case, we have increased the adhesion of the CuO NPs to the fused silica by embedding the particles in the glass. For this purpose, a Vulcan furnace was used to run various temperature profiles from 850 to 1100°C in air, where 975°C for 1 hour proved to be the optimum conditions for particle adhesion. For the 3D-G and 2D-G productions, after the complete deposition of the CuO NPs a reduction step is performed inside an oven or CVD at 600°C, for one hour or longer, in order to activate the catalyst to the Cu(0) state. If the oxide has not been totally removed, the catalyst will lose its efficiency, leading to the growth of poorer graphene in terms of quality and coverage. The achievement of a complete reduction in CuO NPs to Cu(0) can be confirmed with the spectrophotometer because the reduced Cu(0) NPs have a plasmon resonance at 586-590 nm in the absorption spectra. The ability to carry out the previous reduction step *in situ* with the graphene growth in a CVD reactor helps to reduce the sample handling and processing steps.

For 3D-GS, the Cu is thermally evaporated from a Cu foil (Sigma Aldrich, 25 μm thickness) onto the top of the fused silica slides. The samples are placed inside a quartz tube (Figure 28) or CVD equipment at vacuum ($5 \cdot 10^{-3}$ mbar) and 1100°C. Initially, we perform an optimization of the temperature gradient along the quartz reactor to control the evaporation dynamics on the samples. While the Cu foil is located at the center of the quartz tube (area 2 in Figure 28) at a mean temperature of 1100°C, the fused silica samples are at the extremity of the chamber (areas 1 and 3 in Figure 28), where the temperature changes. The temperature gradients observed in the extreme parts of the oven have an effect on the deposited Cu NPs on the fused silica by modifying the particle diameters. The controlled and accurate modification of the Cu NP sizes is of great interest because it allows the production of 3D-GS structures of varied sizes. In the specific case of the

results that have been included in this work, after locating the Cu foil in the center of the quartz tube, the fused silica samples are approximately six inches away – areas 1 and 3 – with mean temperatures of 250°C and Cu NPs with mean diameters ($\overline{\emptyset}$) of 30 nm. Although at the highest temperatures for graphene growth (around 900°C) Cu NPs tend to agglomerate, we have observed differences in the resulting 3D-GS structures depending on the diameters of the initial Cu NPs. Further work should be devoted to the improvement of the deposition of Cu NPs with more accurate control over the size of the synthetized Cu NPs.

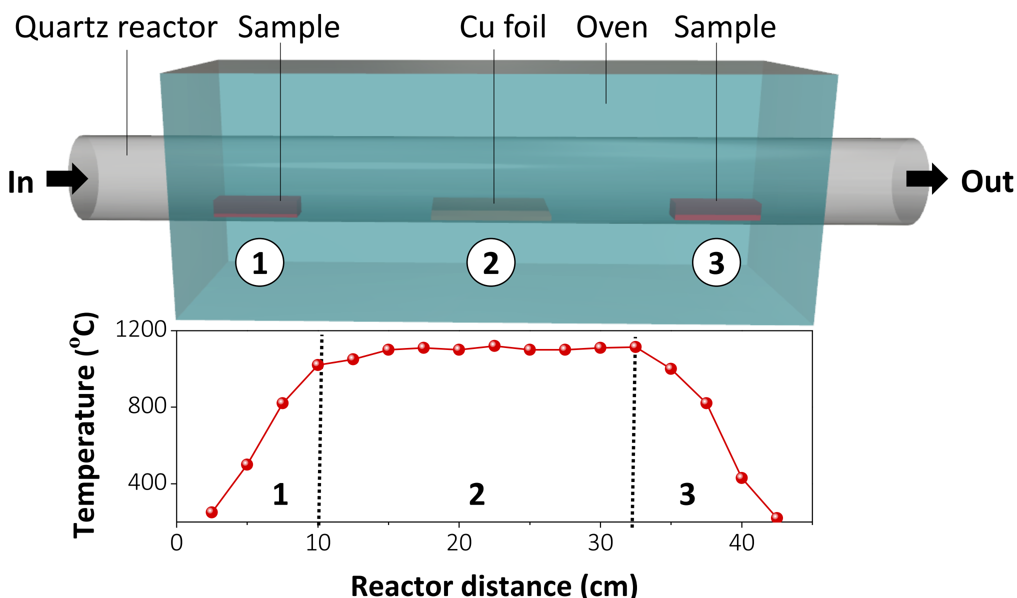

Figure 28. (a) Scheme of the quartz tube used for the deposition of Cu NPs for the CVD production of 3D-GS, indicating the location of the fused silica samples (areas 1 and 3) and the Cu foil (area 2, center of the tube). (b) Experimental data of the temperature profile along the inside of the quartz tube. Areas 1-3 are highlighted, indicating the profile temperatures corresponding to the areas where the Cu foil and substrates are located.

In sections 3.2.2. Graphene growth on Cu NPs by CVD and 3.2.3. Cu removal from graphene structures, we will comment on the growth of graphene on the previously deposited Cu NPs with the addition of a fast step to remove the Cu. Figure 29 (a) below shows an optical image of a sample where Cu NPs have been evaporated from the Cu foil onto the fused silica. A color gradient can be observed as a consequence of the temperature gradient inside the chamber, which modifies the diameter of the Cu NPs. After the Cu removal shown in (b), the same gradient is observed in the 3D-GS structures that remain on the fused silica surface. Larger diameters and more layers will lead to the growth of bigger and multilayered 3D-GS that will decrease the optical transmission of the samples.

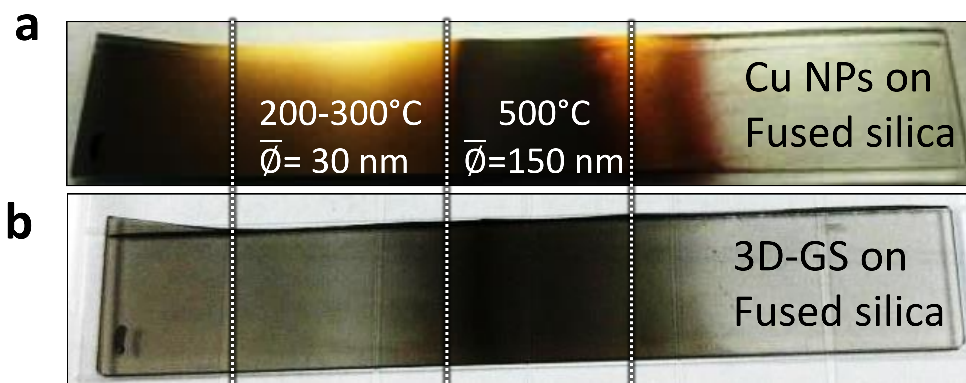

Figure 29. Example of gradient color samples for 3D-GS production, which is associated with different sized Cu NPs when the sample is subjected to different temperatures within the quartz tube. (a) Cu NPs are deposited on fused silica after the evaporation from a Cu foil. (b) Same after graphene growth and Cu removal at high temperatures.

3.2.2. Graphene growth on Cu NPs by CVD

For the production of 3D-GB and 2D-G, the graphene has been grown using the same CVD equipment as in Chapter 2 for the direct growth of graphene on dielectrics (Black Magic 4-inch, AIXTRON) at CH_4:H_2 (1:4), 1000°C, 25 mbar and 30 minutes. For the production of 3D-GS, the growth has been carried out at Corning Incorporated using the CVD equipment from Figure 28 above at C_2H_2:H_2 (1:0, 1:2, and 1:4, for 3D-GS), 900°C, 0.2 mbar and 30 minutes. The heating rate is 50-75°C/min for both CVD treatments.

3.2.3. Cu removal from graphene structures

After the graphene growth, it is necessary to remove the catalyst for further characterization of the samples and in order to achieve high optical transmittances. Because wet etching and thermal etching have been previously demonstrated to successfully remove the catalyst, we have implemented both types without the need to add any polymer for graphene protection. The Cu NPs used for the production of 2D-G and 3D-GS have been sublimated at 1100°C under Ar/H_2 for 10 minutes, whereas the Cu NPs used for the production of 3D-GB have been removed by wet etching using diluted ammonium persulfate for 10 minutes.

The synthesis of 3D and 2D graphene structures (3D-GB, 3D-GS and 2D-G), using Cu as a common catalyst for all structures, is illustrated in Figure 30. The growth procedure consists of three steps: the Cu pre-patterning by dip-coating of CuO particles on the substrate or by thermal evaporation of Cu from a Cu foil (see section 3.2.1. Cu deposition on glass substrate for more details), the CVD graphene growth on the catalyst, and the removal of the Cu NPs by a fast-wet etching or sublimation.

In the following section, we present the characterization results and main properties for the 3D- and 2D-graphene structures obtained in this work using the previously described procedures.

3.3. Characterization results for graphene assembled into 2D- and 3D-structures

3.3.1. Graphene assembled into a 3D ball structure (3D-GB)

The production of the 3D-GB structures requires a systematic control of the initial Cu template before performing the graphene growth. This is detailed in section 3.2.1. Cu deposition on glass substrate above. Figure 31 (a-b) shows top and 30° SEM pictures of the Cu NPs after deposition and subsequent H_2 reduction. It can be observed that the Cu NPs are spread over the surface, presenting a distribution similar to that in solution and, contrary to previous work [180], without large aggregation. After Cu NPs deposition and reduction, the graphene growth starts once the reaction temperature is achieved and the CH_4 is injected into the chamber. Figure 31 (b-c) shows the 30° tilted view of the Cu NPs before and after graphene deposition, respectively. One can observe the morphological changes, with the particles reducing their surface contact angles by getting closer to each other and the graphene growing in between. In order to evaluate the transparency and quality of the graphene grown on Cu NPs, the sample is dipped in a diluted ammonium persulfate solution to etch the Cu. The resulting 3D-GBs are shown in the SEM picture in Figure 31 (d), presenting diameters similar to those of the original Cu NPs in (a).

We have performed Raman mappings in Figure 32 (a-b) in order to obtain statistics of the quality and coverage of 3D-GBs over 20x20 μm^2 areas. The limited spot size of our Raman laser – 764 nm being the spot size for the 100X lens used – means that it is not possible to distinguish individually each 3D-GB shape. However, both maps confirm the homogeneous distribution of 3D-GBs over the sample.

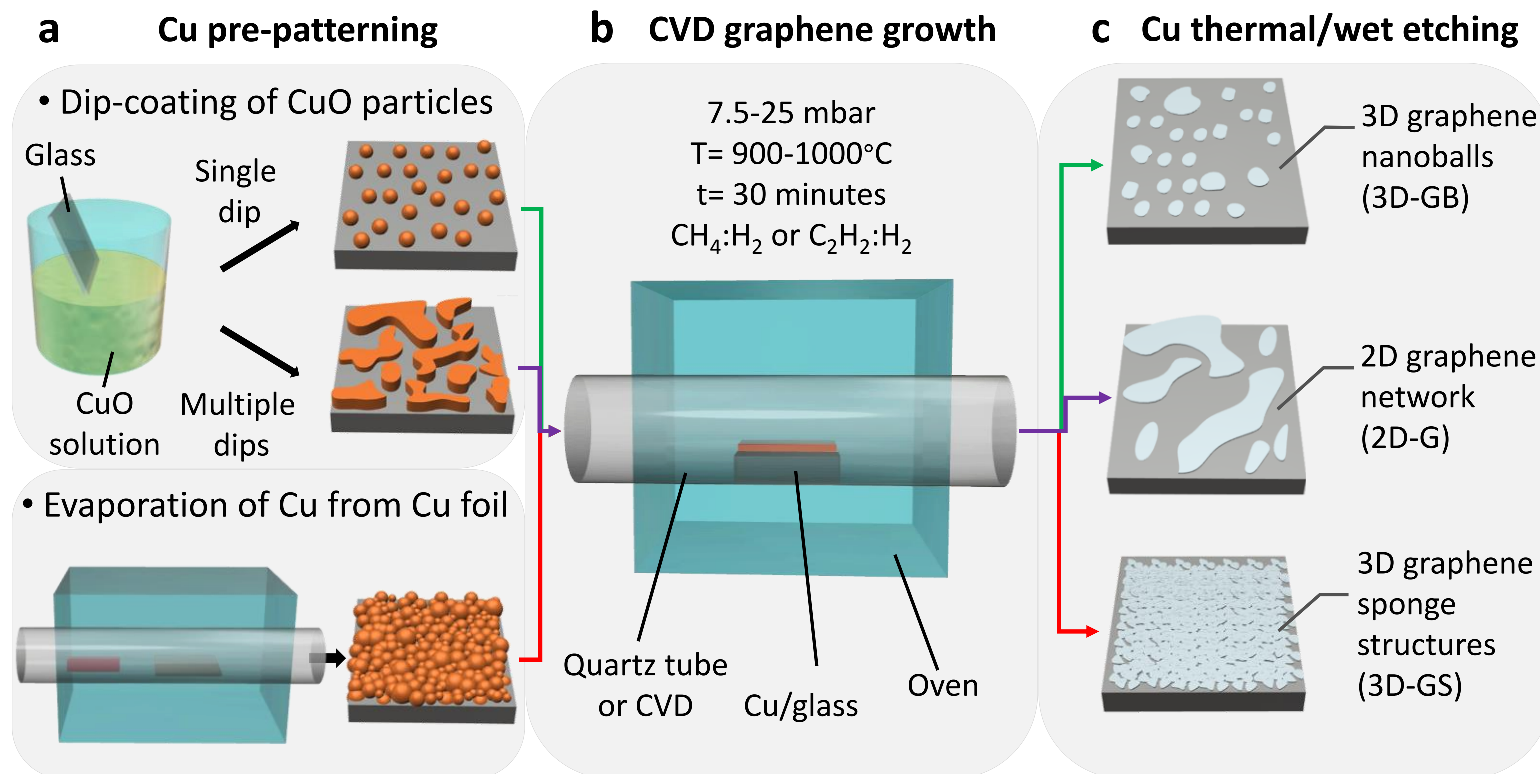

Figure 30. Fabrication of 3D- and 2D-graphene structures. (a) Cu template formation on the substrate by CuO particle dip-coating or by thermal evaporation from a Cu foil. Pictures on the right side show the final Cu structures on the substrate: isolated, large Cu NPs embedded in glass or multilayer Cu NPs. (b) CVD growth of graphene on the Cu template. (c) Removal of residual Cu by wet etching or thermal sublimation.

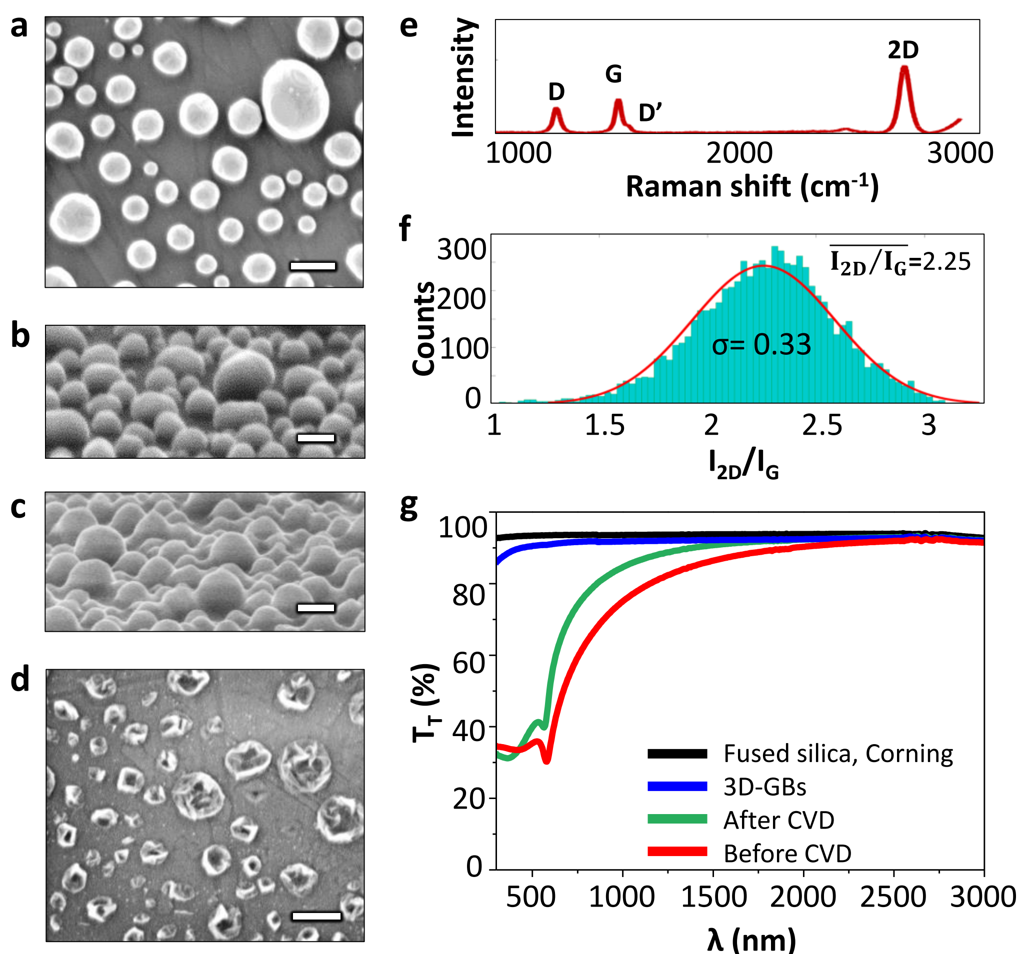

Figure 31. Characterization of the 3D-GB structure from the initial state where Cu NPs are deposited on glass until the final stage when they are removed. (a) SEM image of the Cu NPs deposited on glass after the reduction process with H_2. (b-c) SEM at 30° of the deposited Cu NPs without and with graphene, respectively. The particle profile in (c) is smoother due to the change in the NPs and the graphene coverage. (d) 3D-GBs after Cu removal with ammonium persulfate. (e) Raman spectrum of 3D-GBs where the three graphene peaks appear (D, G and 2D, and an additional D' related to structural defects). (f) Statistical distribution of the Raman I_{2D}/I_G peak ratio over an area of 20x20 μm², with an average value of 2.25 (σ=0.33). The average value of the I_D/I_G is 1.32 (σ=0.21). (g) Transmittance spectra of (from bottom to top) the Cu NPs deposited on glass after H_2 reduction, Cu NPs with graphene, 3D-GBs after Cu NPs removal and the bare substrate. Scale bar: 200 nm.

Figure 31 (e) shows a Raman spectrum extracted from the map, which corresponds to a 3D-GB structure, where the three typical graphene peaks (D, G and 2D, at 1350, 1580 and 2700 cm^{-1}, respectively) can be clearly distinguished. For further details about Raman characterization, see Chapter 1, section 1.2.

Characterization techniques. In addition, Figure 31 (f) shows a Gaussian distribution of the ratio between the peaks 2D and G (I_{2D}/I_G), with 2.25 being the mean value in a representative area of the sample. The previously mentioned high ratio confirms that 3D-GB structures are monolayer graphene. It is important to note that the graphene structures are less defective than those found in previous literature, where a high D peak value is reported [179,180]. In our case, it is worth also commenting that a tiny D' peak is present on the right side of the G peak due to structural defects, which would explain the complete removal of the Cu NPs when the etchant is added, thus allowing the contact between Cu-etchant [181].

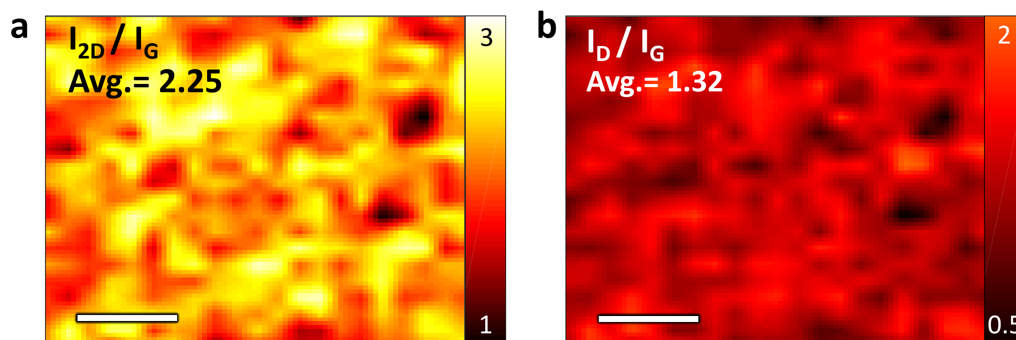

Figure 32. Raman mapping of 20x20 μm² measuring samples with 3D-GBs on glass: (a) I_{2D}/I_G ratio with an average value of 2.25, and (b) I_D/I_G ratio with an average value of 1.32. Scale bar: 5 μm.

For a complete characterization, Figure 31 (g) shows the evolution of the transmittance measurements through the different fabrication steps for the 3D-GBs. It can be observed that the initial Cu NPs (bottom red line) produce a strong plasmonic dip in the transmission, which explains the pale red color of the samples, while the high transmission in the near-infrared is expected as in that region the wavelength becomes much larger than the particle size. The growth of the graphene (green line) increases the transmission slightly, which is mainly due to the rearrangement in size and surface distribution of the Cu NPs. As expected, the most dramatic transmission change occurs after the Cu wet etching (blue line). The final 3D-GB structures show very little absorption with respect to the initial fused silica substrate (top black line) with a 90% transmittance at 550 nm. If a reflection of 7% is considered, which was measured with the spectrophotometer, the corresponding absorption value is approximately 3%, which is very close to the theoretical absorption of the graphene monolayer, i.e., 2.3%. In addition to the transmittance measurements, an EDX has also been performed to corroborate the total removal of the Cu NPs. Figure 33 (a) shows the elements detected when the EDX is performed on points 1 and 2 (Cu NPs with graphene), and on point 3 which corresponds to the fused silica surface. The results when the Cu NPs are measured – points 1 and 2 – show a Cu percentage between 40 and 60%, Si and O

belonging to the fused silica substrate (SiO_2), and carbon detection from the graphene with possible organic residues. However, when the glass surface is measured, only Si, O and carbon residues are detected. After the Cu NPs are removed with ammonium persulfate, as shown in Figure 33 (b), again three points are evaluated, where two correspond to the 3D-GBs (points 1 and 2) and one is measured on the fused silica surface (point 3). The results show a negligible detection of Cu when measuring on the 3D-GB substrates with almost constant percentages of carbon, Si and O, which are related to graphene and fused silica substrates, respectively.

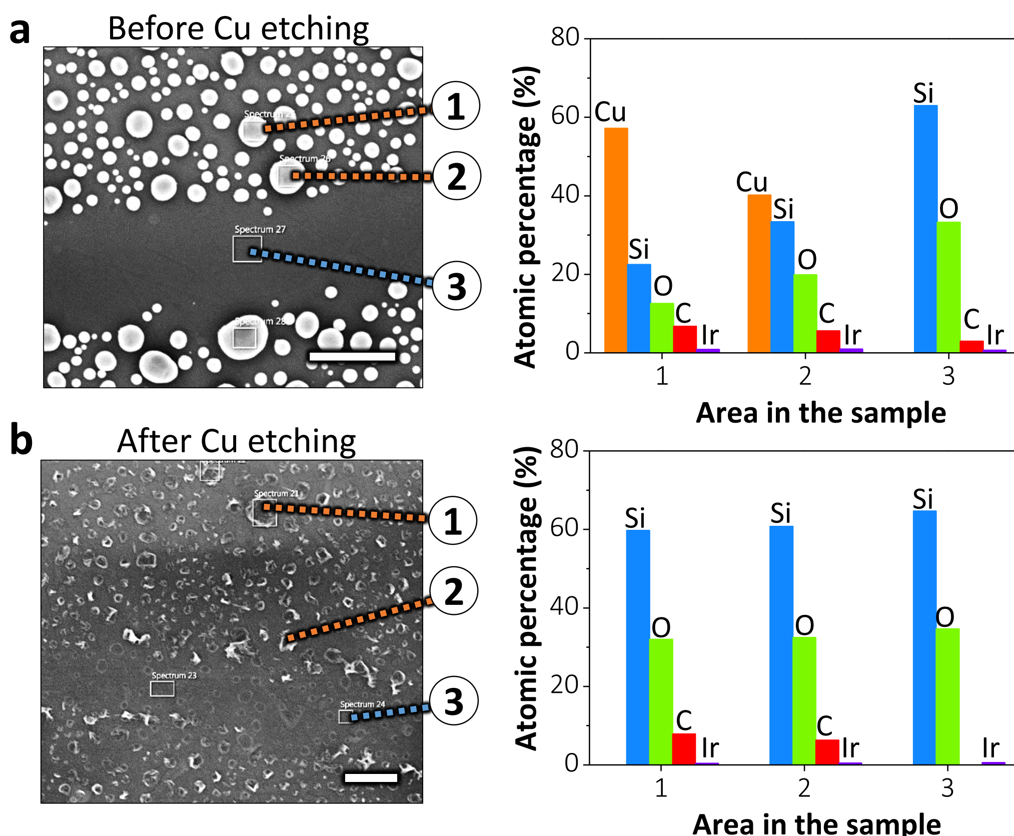

Figure 33. SEM and EDX characterization at 5kV of (a) Cu NPs that are covered with graphene, and (b) 3D-GBs that have been deposited on glass after performing a wet etching of Cu. The areas denoted by numbers in both SEM images correspond to the areas where EDX analysis has been performed. Points 1 and 2 have been measured on graphene deposited on Cu NPs in (a), and on Cu-etched 3D-GBs in (b). Point 3 corresponds to the fused silica substrate in both cases. After Cu etching in (b), no traces of Cu are detected, which is translated into the fabrication of catalytic-free 3D-GBs, and also a constant signal of SiO_2. An UTMF coating of Ir has been added to enhance the contrast of the SEM images. Scale bar: 1 μm.

Thus, the growth of monolayer and catalytic-free 3D-GB structures can be confirmed. It should be mentioned that a thin layer of iridium has been added as a coating conductive layer to improve the quality of the SEM images. This promotes the detection of a very low percentage of iridium in both cases. Due to the fact that the 3D-GBs are isolated and the substrate is not electrically conductive, the R_S cannot be measured.

The large surface to volume ratios of the 3D-GBs make them suitable for a variety of applications, such as supercapacitors, electrochemistry and catalysis by surface functionalization. Moreover, the electron confinement associated with the nanoballs could also produce localized surface plasmon resonances (LSPRs), which would be very interesting for chemical and biochemical sensing [128]. We have not observed these as they are only expected at large wavelengths - in the mid infrared region - and require graphene doping beyond the intrinsic levels. In the future, we plan to electrically gate the nanoballs by, for example, adding an additional graphene layer to create a common electrical contact and thereby obtain the doping level required to observe the LSPRs.

3.3.2. Graphene assembled into a 3D sponge structure (3D-GS)

3D-GS can meet the requirements of large-scale applications in terms of high quality, uniformity, transparency and conductivity. As previously noted, an accurate control over the evaporation time and the location of the sample within the quartz tube allow the size of the resulting Cu NPs to be tailored. Figure 34 (a) shows the Cu NPs evaporated on fused silica with a narrow size distribution centered at a diameter of 30 nm and a height of 75 nm – see the SEM cross-section in Figure 35 (a). The increase in temperature up to 900°C (the reaction temperature for graphene growth) leads to the sintering of particles with larger diameters. This can be observed in Figure 34 (b), where the sample has been taken out of the CVD chamber at 800°C, before the graphene growth process. The Cu NPs obtained at this intermediate temperature have mean diameters of 150 nm and heights of up to 200 nm, as can be seen in Figure 35 (b). After the graphene is grown on top of the Cu NPs at 900°C, the temperature is increased to 1100°C for 30 minutes to sublimate the Cu. The resulting 3D-GS structures, with a sponge finger-like structure, remain on the glass surface as shown in the top and cross-section SEM images in Figure 34 (c) and Figure 35 (c), respectively. The thickness has decreased slightly due to the removal of the Cu from the inside, making the structures more compact. The performance of EDX on the 3D-GS in Figure 35 (d) confirms the detection of Si and O from the substrate, and carbon from the graphene. However, no trace of Cu is detected, thus confirming that the 3D-GS structures are catalytic-free after the whole process.

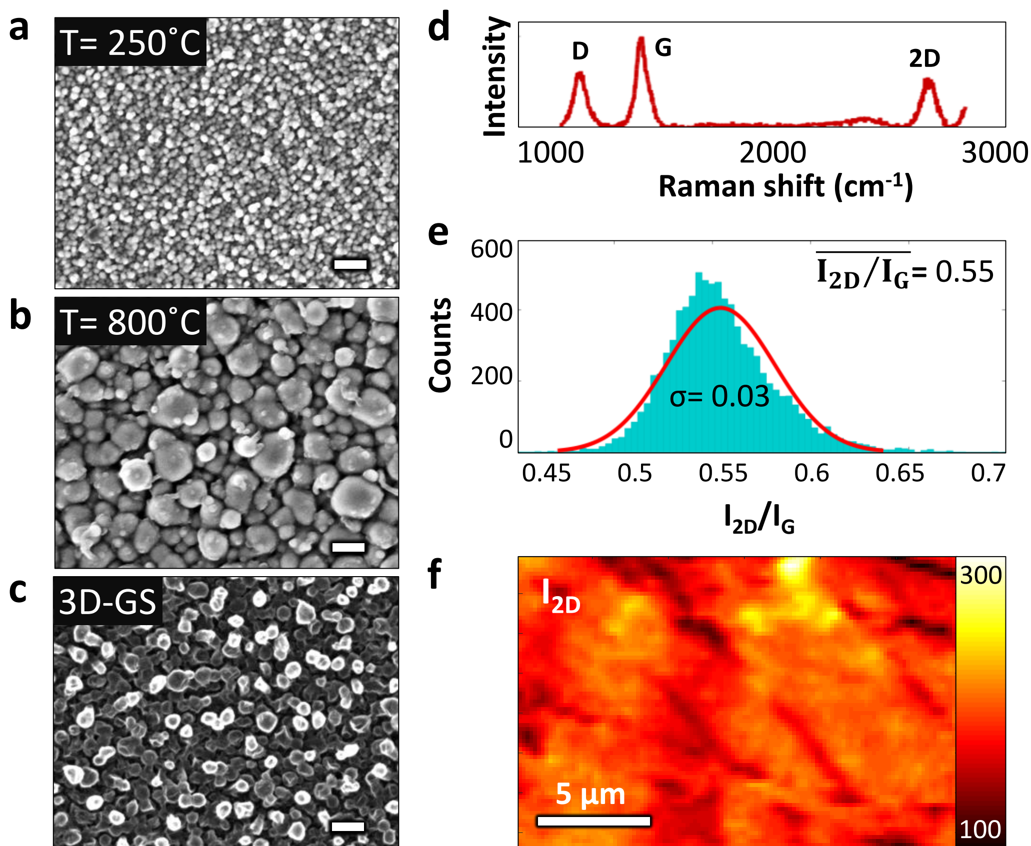

Figure 34. Characterization of 3D-GS structures and their catalytic Cu NPs. (a-c) SEM images of Cu NPs evaporated and deposited at 250°C. (b) Same Cu NPs after being heated to 800°C, showing an increase in diameter due to the sintering of particles. (c) 3D-GS on fused silica after growing graphene by CVD at 900°C for 30 minutes and the consequent thermal sublimation of Cu at 1100°C for 30 minutes. (d) Raman spectrum of the 3D-GS where the three graphene peaks are clearly distinguished (D, G and 2D). (e) Distribution of I_{2D}/I_G extracted from the Raman mapping in (f), with an average value of 0.55 (σ=0.03). For I_D/I_G ratio, the average value was 0.80 (σ=0.05). (f) Raman mapping over 20x20 µm² area showing the I_{2D} and the continuity of the 3D-GS. Scale bar: 200 nm.

The performance of Raman mapping on these structures is also needed to confirm the successful growth in terms of quality and coverage. Figure 34 (d) shows a representative Raman spectrum of 3D-GS where the three graphene peaks can be observed. Moreover, the high D peak reveals the presence of structural defects in the 3D-GS, which could be caused by the Cu sublimation. Figure 34 (e) shows the corresponding Gaussian distribution of I_{2D}/I_G extracted from the map in (f), where the center and mean value corresponds to 0.5. The decrease in the previous ratio can be explained by the presence of few-layer graphene as the initial Cu NPs are closely packed and stacked in layers. The plot of the intensity of the 2D peak

I_{2D} in Figure 34 (f) shows the continuity and homogeneity of the graphene over the whole area.

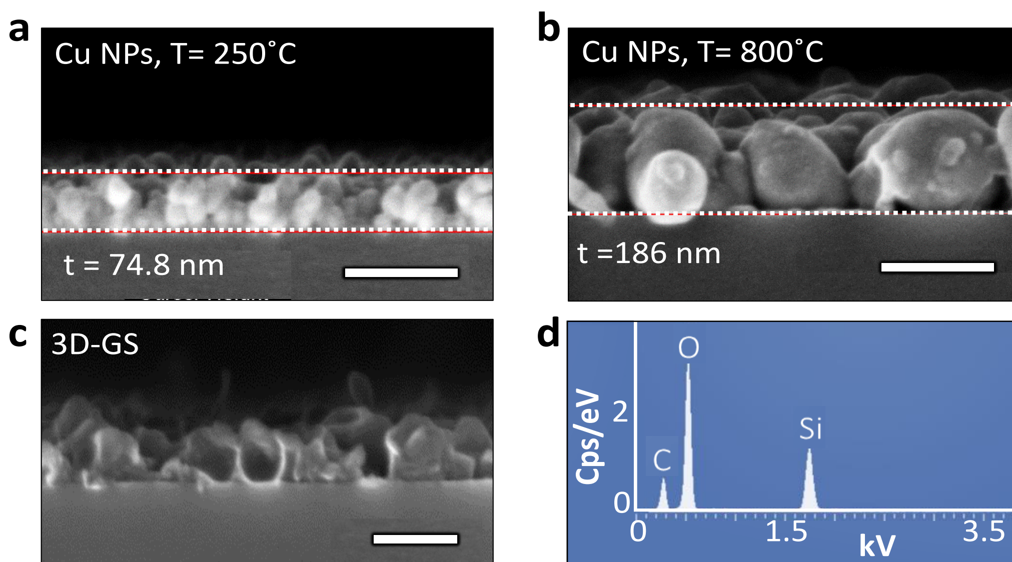

Figure 35. (a-c) SEM cross section images: (a) Cu NPs evaporated on fused silica at temperatures of 250°C, with mean diameters of 30 nm and thicknesses of 75 nm. (b) Same Cu NPs after being heated to 800°C, showing particle sintering with mean diameters of 150 nm and thicknesses of 186 nm. (c) 3D-GS obtained after sublimating Cu NPs at 1100°C for 30 minutes, with slightly lower thickness after Cu removal as the graphene structures are more compact. (d) EDX performed on 3D-GS, showing the contributions of the fused silica substrate (Si and O peaks), the graphene (C peak), and a negligible Cu peak, which demonstrates the growth of catalytic-free 3D-GS. Scale bar: 200 nm.

Finally, a very interesting consequence of the overlapping of the different layers forming the 3D-GS is the electrical conductivity. Several tests have demonstrated that the R_S of 3D-GS can be tuned from 1 to 20 kΩ/sq. by modifying the initial Cu NPs thicknesses, morphology and CVD conditions. We provide evidence of these variations when exposing the initial Cu NPs to the conditions described in Table 11 (section 3.5. Additional information). As can be observed in the results, the optical transmittance and the R_S are closely related, the R_S typically being higher for the most transparent samples. This can be observed in Figure 39 where the spectra of three samples has been plotted. The structures that have been discussed in this work have been obtained at C_2H_2:H_2 1:1, which gives transmittance values of 47-70% at 2-5 kΩ/sq. Further work needs to be carried out in order to understand the change in transmittance (up to 80%) and R_S variation (from 3 to 20 kΩ/sq.) when the gas ratio is modified.

3.3.3. Two-dimensional graphene (2D-G)

The modification of the initial Cu template has allowed us to promote the growth of graphene into a flat layer – two-dimensional shape – using almost the same process conditions as those described above for the production of 3D-GBs. The increase in the dip- coating steps of the CuO particles on glass and their consequent reduction under H_2 has resulted in the large Cu isolated motifs shown in Figure 36 (a).

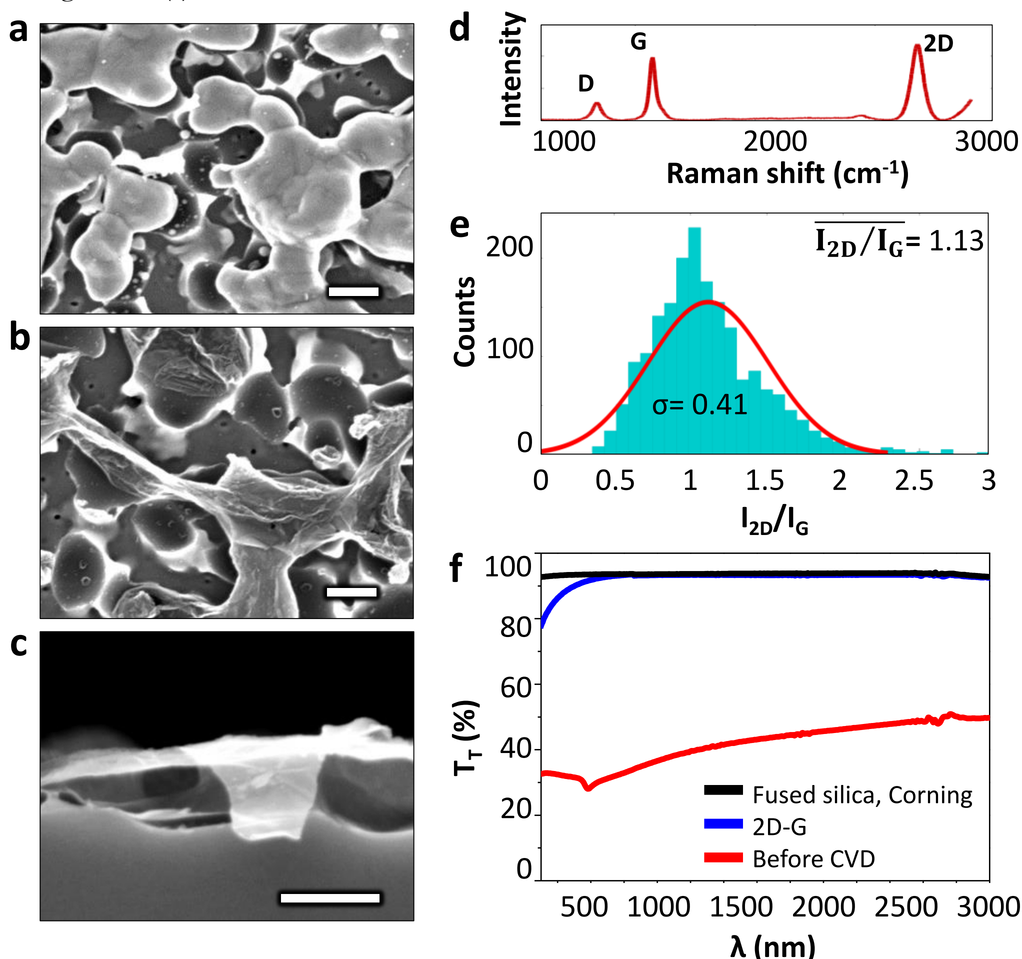

Figure 36. Characterization of the 2D-G structure. (a) SEM image of Cu NPs embedded in glass before the graphene deposition. (b-c) Top and cross-section SEM of graphene after the sublimation of Cu NPs. (d) Raman spectrum of the 2D-G where the three graphene peaks are clearly distinguished (D, G and 2D). (e) Raman distribution of the I_{2D}/I_G ratio with an average value of 1.13 (σ=0.41) over an area of 20x20 μm². For I_D/I_G ratio the average value is 0.79 (σ=0.16). (f) Transmittance measurements of (from bottom to top) the embedded Cu NPs, 2D-G after the Cu sublimation at 1100°C and the bare substrate. Scale bar: 200 nm.

The thicknesses of these structures are approximately 300 nm, as is revealed by the SEM cross-section images in Figure 38 (a). In this case, due to larger areas of Cu being exposed for graphene growth, we want to prevent their evaporation when the temperature is raised to 1000°C. To this end, we have performed a thermal treatment as described in section 3.2.1. Cu deposition on glass substrate in order to embed the Cu NPs in the glass. After this, the graphene is grown on top of the Cu NPs at 1000°C, and once this step is finished, Cu sublimation is performed for 30 minutes at 1100°C. The resulting structure is a flat 2D-G network, which is shown in the top and cross-section SEM images in Figure 36 (b-c), respectively. The slight curvature of the fused silica substrate in (c) confirms the successful embedding of the Cu NPs. In addition, Raman mapping characterization in Figure 36 (d-e) show the corresponding Raman spectrum of the 2D-G structure – extracted from the maps of Figure 37 – and a Gaussian distribution for the I_{2D}/I_G ratio, with 1.13 being the average value. The low D peak confirms the high quality of the material. The full maps, which denote a homogeneous distribution of the 2D network, are shown in Figure 37 (a-b).

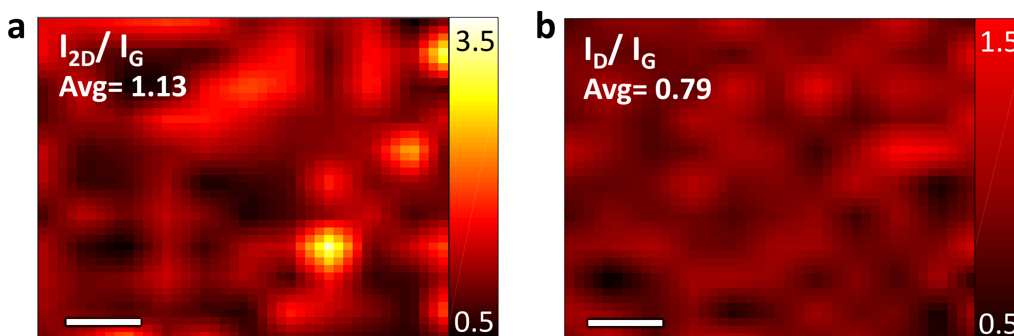

Figure 37. Raman mapping of 20x20 μm² area for 2D-G structures: (a) I_{2D}/I_G ratio with an average value of 1.13 and (b) I_D/I_G ratio with an average value of 0.79. Scale bar: 5 μm.

The optical transmittances of the samples during the whole process have been measured. Figure 36 (f) shows the spectra of (from bottom to the top) the Cu NPs before graphene growth by CVD, the 2D-G structure after Cu sublimation and the measurement of the bare fused silica. Values of up to 90% (at 550 nm wavelength) have been observed, which are very close to those for the fused silica. EDX characterization in Figure 38 (b) has confirmed that the high optical transmittance is due to a complete removal of the Cu template. This is demonstrated by comparing the EDX results performed on the initial Cu template - which is shown in the SEM cross-section in Figure 38 (a) - with the resulting 2D-G structure shown in the SEM image in Figure 38 (b). While in the first case, an intense peak of Cu is detected, the measurement of the 2D-G structure does not show any trace of Cu, which is promising for a wide range of applications, such as transparent electrodes and interfacial layers.

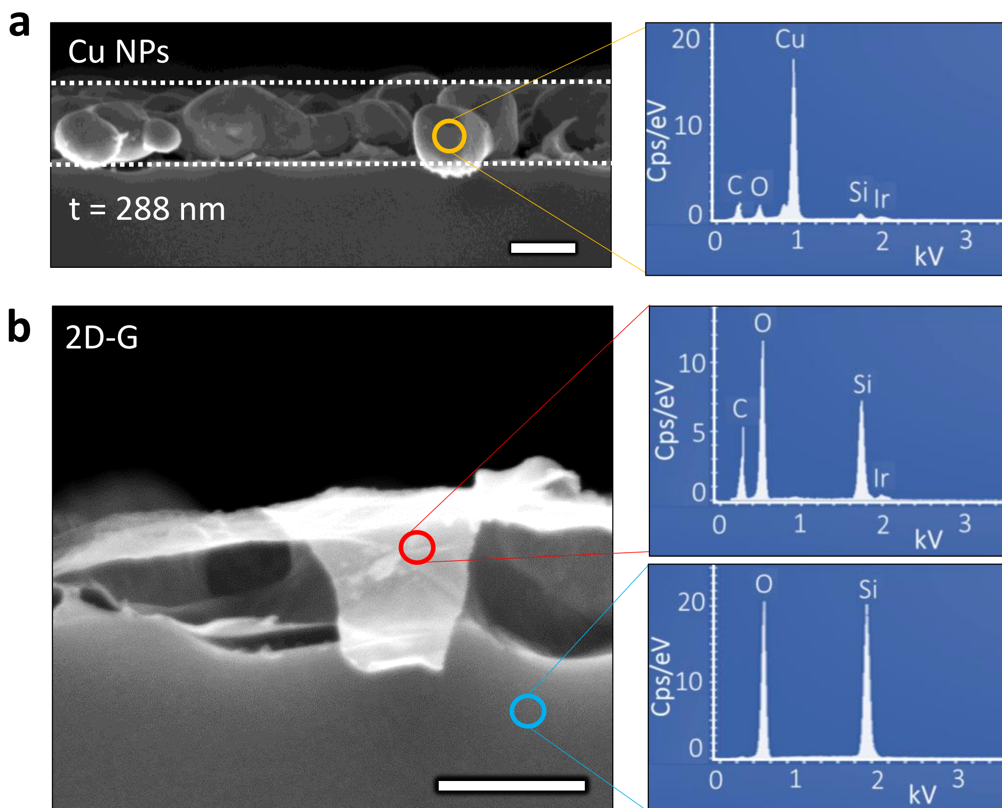

Figure 38. SEM images of (a) Cu NPs evaporated on fused silica, and (b) 2D-G structures after Cu sublimation, respectively. EDX measurements at 15 kV have been performed on (a) the evaporated Cu NPs on the fused silica, and on (b) the 2D-G structure and the fused silica substrate (top and bottom EDX measurements, respectively). EDX confirms the catalytic-free nature of 2D-G structures by negligible detection of Cu in (b). Scale bar: 200 nm.

Regarding the electrical measurements, the R_S of the 2D network cannot be measured as it is not possible to back-gate the dielectric substrate. Future work could contemplate the gating of the graphene nanostructures by using Si/SiO_2 as the initial substrate.

Finally, Table 10 below gives a summary of the main differences between the three types of structures discussed in this chapter, highlighting the type of Cu NPs deposited, the growth processing conditions and the main results obtained by Raman, transmittance and R_S.

Table 10. Summary of the main properties related to 2D- and 3D-graphene structures developed by CVD technique tuning the Cu template catalyst.

Properties	Graphene structure		
	3D-GB	**3D-GS**	**2D-G**
Catalyst	Isolated Cu NPs	Layered Cu NPs	Large Cu NPs
Graphene Growth	1000°C, 30 min, CH_4:H_2 (1:4)	900°C, 30 min, C_2H_2:H_2 (1:1)	1000°C, 30 min, CH_4:H_2 (1:4)
I_{2D}/I_G (σ)	2.25 (0.33)	0.55 (0.03)	1.13 (0.41)
I_D/I_G (σ)	1.32 (0.21)	0.80 (0.05)	0.79 (0.16)
T_T, (%)	91.2	46.5	92.2
Rs (kΩ/sq.)	- (*)	2.2	- (*)

(*) The Rs cannot be measured because the structures are isolated, i.e., not continuous over the dielectric.

3.4. Conclusion

By modifying the shape of copper nano-particles, we have demonstrated a new technique for growing graphene structures assembled into three-dimensional shapes and as a flat layer. A wide range of morphologies, with high surface to volume ratios, have been produced, from sponge-like to nanoball and conformal graphene structures. The properties of these novel structures combine high quality structural characteristics with high optical transparency. These may find important application in anti-glare display screens, solar cells, light-emitting diodes, gas and biological plasmonic sensors.

3.5. Additional information

Table 11. Variation of CVD conditions for the production of 3D-GS structures of different R_S and transmittance values (the shadowed rows are the samples for which the transmittance spectra are shown in Figure 12)

Gas composition	T (°C)	P (Torr)	t (min)	Rs (kΩ/sq.)	T_T, 550 nm (%)
C_2H_2	900	0.1	30	2.2	46.6
	1000	0.1	30	9.6	77.4
	1000	0.1	60	10.7	80.3
	1100	0.1	30	2.9	67.6
	1100	0.1	30	2.6	71.7
	1100	0.1	60	17.3	86.1
C_2H_2:H_2 1:1	900	0.2	30	2.2	46.5
	1000	0.2	30	1.8	52.1
	1000	0.2	30	3.42	47.7
	1100	0.2	30	4.6	69
C_2H_2:H_2 1:2	1000	0.3	30	7.4	69.5
	1000	0.3	30	11.8	69.9
C_2H_2:H_2 1:4	1000	0.5	30	30.5	68.2
	1000	0.5	60	27.4	81.9

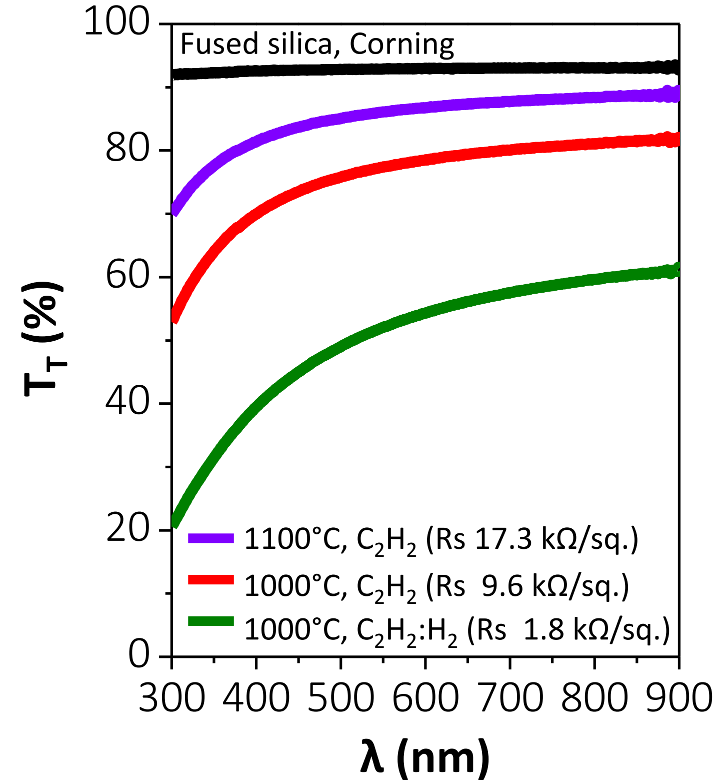

Figure 39. Optical measurements performed on three different samples included in Table 11.

4

Graphene dry transfer using polyimide as an intermediate layer

Although the direct growth of graphene on dielectrics is a very ambitious target currently under research, the most controllable technique nowadays is the use of Cu foils as catalytic templates. For the unique properties of graphene to be fully utilized, it must be transferable to a wide variety of substrates. To this end, several procedures have been developed, with wet etching by PMMA being the most standardized. However, dry transfer procedures represent a breakthrough with regard to reducing the processing times, waste and material consumption (by Cu recycling), and the residues left by PMMA on the graphene. Our approach involves the use of a chemically and thermally stable, light material such as polyimide, as an intermediate thin layer between the target substrate and the graphene to allow its mechanical peeling from the Cu. As a result, a transparent graphene device on a rigid and flexible substrate is obtained, stable up to 350°C and in aqueous media. The easy, fast and scalable method used here, using current industrial technology, demonstrates its feasibility for device fabrication.

This work has been partially developed during an internship at Corning Incorporated, which has resulted in the filing of a patent application and the following publication:
M. Marchena *et al.* (2018), "Dry transfer of graphene to dielectrics and flexible substrates using polyimide as a transparent and stable intermediate layer", 2D Materials.

4.1. Introduction

As previously explained in Chapter 1, (section 1.1.5. Graphene transfer), in order to exploit graphene properties in applications, it needs to be transferrable to a wide range of substrates. To this end, several techniques have been developed, depending on the graphene synthesis route. In our case, we focus on that developed for transferring CVD graphene on Cu catalytic templates. Although the

direct growth of graphene is an important research topic, and also one of the objectives of this thesis because it pursues a complete removal of additional transfer steps, to date the highest controlled quality of graphene has been achieved by CVD on Cu foils.

In particular, the most standardized transfer method is the wet transfer technique, typically using PMMA as a protective graphene layer while the Cu is etched using a chemical solution [39,86,88]. However, besides the fact that this technique is time consuming and involves the waste of Cu foils at each run of graphene growth, the main issue is that after PMMA removal by organic solvents, residues are very difficult to remove, thus causing degradation to the graphene electrical properties [96,182]. To solve this issue, additional annealing steps at 200-350°C for 3 hours are performed on the graphene devices in order to remove PMMA residues and improve the mobility. The work by L. Gammelgaard *et al.* reported in ref. [97] is of great interest as the PMMA and heat contribution to the electrical properties of the graphene have been measured using back-gating at each fabrication step. They observed hysteresis in the electrical measurement, possibly due to adsorbed water molecules below and on top of the graphene after fabrication. They also observed an increase in the charge neutrality point (V_G) of approximately 9V after venting the chamber, an increase of 16V when the device was baked in ambient air, and a decrease of almost 14V when the device was annealed in N_2 at 250°C. The positive variation V_G corresponds to an increase in p-type graphene doping where, consequently, the graphene mobility decreases. They attributed this behavior to the interplay between the contamination of the graphene surface and its mechanical conformation to the substrate. The particles adsorbed into the graphene (mainly oxygen and water, both inducing a strong p-doping) increased the n_S with a consequent μ_H degradation. In addition, they also found that the graphene conformation to the substrate was enhanced by heat, which increased the contact and the reactivity between the graphene and the oxygen molecules, leading to an increase in the n_S and μ_H degradation. The substrate and water effects on the graphene were controlled by the use of hydrophobic coatings on the target substrate. They also demonstrated that graphene interaction with air at temperatures above 200°C leads to an irreversible degradation of the electrical properties, due to high reactivity to oxygen.

More recently, in the work by W. Choi *et al.* reported in ref. [98], by removing PMMA residues mechanically with an AFM tip in contact mode under a normal force of 20 nN, they have demonstrated how these residues contribute to the p-doping of graphene. They observed that after mechanical cleaning was performed on the graphene surface, the V_G moved from 21-33V toward lower gate voltages, thus increasing the graphene μ_H by approximately 200 $cm^2/V\cdot s$.

In order to solve the previously mentioned issues related to PMMA residues, two main alternatives have been considered. The first one is known as

"hydrophobic transfer" [5], where the graphene on the Cu foil is slightly pressed onto a substrate covered with a hydrophobic coating. Since graphene is also intrinsically hydrophobic, it remains attached to the substrate during the Cu etching procedure in a polar liquid. The three main issues related to this technique are the introduction of air bubbles between the Cu foil and the etchant (leading to graphene breakage or the removal of the Cu being unsuccessful), the induction of doping due to the long exposures between the graphene and the etchant, and the Cu foil wastage.

The second technique is known as graphene "dry transfer", which consists of the transfer of the graphene from the Cu foil to the target substrate with the advantage of Cu recycling for a future growth catalyst. In previous works, Yoon *et al.* [183] demonstrated for the first time the mechanical peeling of graphene from Cu with the calculation of the adhesion energies between the graphene and the Cu. Na *et al.* [184] continued the study, using a similar custom set-up with the optimization of the separation speed, allowing the transfer a graphene layer of good quality and avoiding cracks. The graphene was peeled from the Cu where it was located between two Si slides covered with epoxy adhesives of approximately 20 μm thickness and low thermal resistance. A more recent example developed by our group consisted of the mechanical peeling of graphene from Cu using a flexible, light and chemically stable material such as polyimide (PI), where the adhesion strength between suitably cured PI-graphene is higher than that between graphene-Cu, thus making possible the graphene detachment [185]. Further examples include the use of UV light for graphene transfer to an ultraviolet adhesive on PET [186,187], and the transfer of graphene between two polymeric films using a hot press [188].

In this work, we have considered the strong adhesion of graphene to PI [185], specifically for a particular type of polyimide called VTEC®, with good properties in terms of high thermal stability up to 500°C, and good mechanical and chemical stability at high temperatures. Additionally, they are flexible and robust after at least three thermal cycles up to 400°C and have low solubility in common organic solvents. All of these properties have made them suitable for incorporation in industry in high temperature applications, such as enamel coatings for wires [189]. We propose the direct dry transfer of graphene from the Cu foil to rigid and flexible substrates, such as glass and PET, using PI as a thin intermediate layer between the graphene and the substrate. This is possible to achieve by exploiting the high adhesion energies between the graphene and the PET, between the graphene and the surface modified glass, and between the PI and the graphene. In order for the process to be successful on glass, an adhesion promoter (3-aminopropyltrimethoxysilane, APTMS) is added to the PI precursor solution, thus increasing the glass to PI adhesion and avoiding its detachment when applying force for the Cu mechanical peeling. This allows us to produce three types of samples: graphene on PI by detaching it from the glass when the adhesion

promoter is not added, graphene strongly attached to PI/glass when the adhesion promoter is added, and graphene on PET with PI as an intermediate layer.

Our technique, when compared to existing work, is the first step towards making a substrate ready for device fabrication. The use of a thin polyimide layer as an intermediate adhesive layer leads to a structure that is transparent, thermally stable up to 350°C and free of polymer residue on the device side of the graphene – a great advantage compared to the PMMA residues left by the wet transfer. In addition, our technique is easy to handle, faster than previous techniques with a reduction in curing times, and less complicated, as we use industrial equipment (a hot press and a laminator). It also demonstrates a high interfacial stability in aqueous media. Moreover, although our work is based on a specific polyimide (VTEC), we also provide initial results using polyamic acid (PAA), which demonstrates that our technique is not limited to one specific material. All these achievements represent a feasible process that enables device fabrication.

4.2. Sample preparation

4.2.1. Graphene on Cu foil

The graphene has been grown on a smooth Cu foil of 18 μm thickness (Taiwan Copper Foil Co. LTD) using CVD (Black Magic 4-inch, AIXTRON) under the following conditions: CH_4:H_2 (1:4), 25 mbar and 10 minutes. Prior to the graphene growth, the Cu foil needs to be cleaned by rinsing it in organic solvents and deionized water (acetone: isopropyl alcohol: H_2O, 2 minutes each), and finally in 0.1 M aqueous acetic acid (CH_3COOH) for 2 minutes to remove the oxides that have formed on the Cu foil surface. After that, the Cu foil is placed inside the CVD chamber and is heated at 50°C·min^{-1} from room temperature to 1000°C under an Ar/H_2 flow. Before initiating the growth of the graphene, the temperature is held at 1000°C for 15 minutes to anneal the foil, thus increasing its crystallinity and grain size, which has been determined to improve the graphene quality [62]. The graphene transferred from this Cu foil will be referred to as "Gr 1" in the following sections. For the graphene transfer using the laminator, previous Gr 1 and a commercial one will be used (Graphenea, 18 μm foil), which will be referred as "Gr 2".

4.2.2. Polyimide

This work is based on the use of polyimide VTEC-080-051 (Richard Blaine International, Inc. [RBI, Inc.]) as the intermediate material to detach the graphene from the Cu foil. The VTEC is received as a solution of the PAA precursor in N-methyl-2-pyrrolidone (NMP), which means that the solution is not polyimide itself. An additional thermal step is required to transform the PAA into PI, also known as "curing" of the polymer, which will occur at a certain curing temperature

(T_C). This will be widely explained in the following sections. The specific structure for the VTEC polymer is RBI, Inc. proprietary information. As mentioned at the beginning of the chapter, experiments are currently being performed at Corning Incorporated using another PAA precursor instead of VTEC (PAA-431176 from Sigma Aldrich), thus demonstrating that the technique is not limited to one unique material.

4.2.3. Polyimide deposition on the target substrate

The target substrates chosen for this work are Corning® EAGLE XG® glass (Corning Incorporated), of 1 mm thickness, as an example of rigid substrates able to withstand temperatures of up to 675°C, and PET slides (Goodfellow Inc.) of 125 μm thickness, as an example of flexible substrates that can withstand temperatures up to 250°C. Both substrates are diced into 2x2 inch dimensions and cleaned using acetone and isopropyl alcohol, followed by O_2/Ar (50:50) plasma cleaning at 50 W for 3 minutes. The cleanliness of the glass is checked with contact angle measurements, assuming good cleaning for contact angles below 5 degrees. As previously discussed, to prepare the samples on glass, an adhesion promoter needs to be added to the VTEC. A mixture of VTEC-080-051 and APTMS, m_{APTMS}= 0.5%wt. × m_{PI} or "as-received" VTEC-080-051 are spin coated at room temperature at 3000 rpm, for 1 minute, on the glass and the PET, respectively. After the spin coating step, the samples need to be pre-dried inside an oven at temperatures from 40-80°C for 15 minutes to remove initial volatiles that can interfere with the graphene transfer.

4.2.4. Graphene transfer step

Two types of industrial equipment – a hot press and a laminator – are used for the graphene transfer, to demonstrate the feasibility of scale-up and of roll-to-roll processing. Both types are shown in Figure 40, and are also described in detail below.

Hot press

The graphene dry transfer to glass is performed using an industrial hot press (Wabash MPI, GENESIS Hydraulic 30 ton press) at 150°C. The pressure ($P_{(HP)}$) is modified in this study from 25-350 psi, with 150-300 psi being the optimum range at which a proper transfer is obtained. During the transfer step, the samples are under temperature and pressure for 10 minutes. In order to achieve a constant $P_{(HP)}$ distribution over the whole area to prevent defects and discontinuous areas on the transferred graphene, it is important to add a silicone rubber sheet on top of the sample.

Laminator

The graphene dry transfer to glass and PET is performed using a commercial laminator to simulate a roll-to-roll process (Catena 65, GBC). The pressure is modified by changing the distance (Δx) from 0.038 mm to 2 mm, which by a previous calibration would correspond approximately to a range between 6 and 100 psi, being the maximum pressure applied at the minimum Δx. During the transfer step, the samples are placed several times between the silicone rollers at low speed, with 12 and 6 being the optimum number of cycles for a proper graphene transfer to glass and PET, respectively. Regarding the optimum conditions for the laminator, the transfer is performed at 140°C, with the Δx between 1 and 2 mm for the transfer to glass and between 0.038 and 1 mm for the transfer to PET.

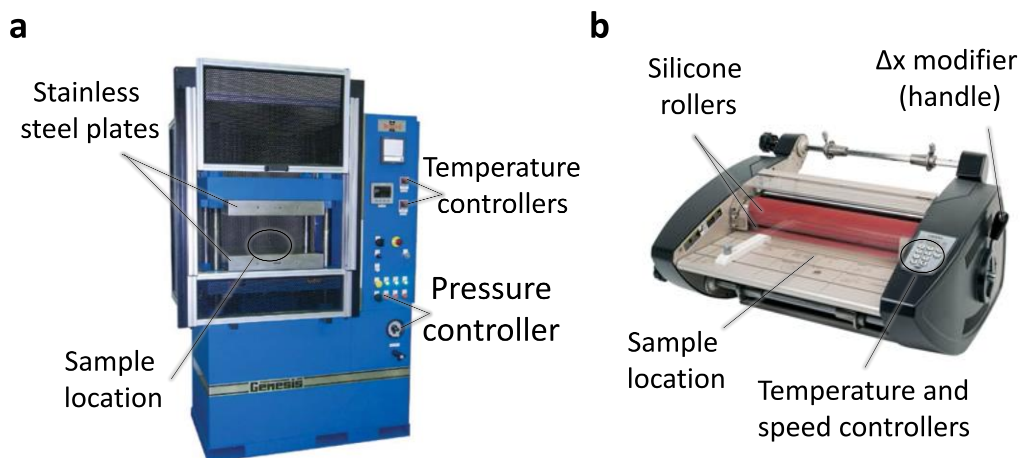

Figure 40. (a) Commercial industrial hot press (Wabash MPI, GENESIS Hydraulic 30 ton press) used for the transfer of graphene to glass. The controllers for Tc and $P_{(HP)}$ are highlighted, as well as the sample location between the two stainless steel plates that will automatically apply Tc and $P_{(HP)}$ - picture adapted from ref. *[190]*. (b) Commercial laminator (Catena 65, GBC) used for the transfer of graphene to glass and PET. Controllers for temperature, speed and distance between the silicone rolls are highlighted, as well as the location where the sample will later be introduced between the silicone rollers.

4.3. Optimization of the curing level of PI to attach graphene from the Cu foil

Firstly, a study is carried out in order to understand the variation in the results for the graphene transfer upon curing temperature (Tc) variations. Following on from previous work by our group [185], after growing the CVD graphene on Cu we have spin coated PI films onto them at 1000 rpm for 1 minute. We have cured the samples at different Tc for 10 minutes, and then proceeded to

the mechanical peeling off the PI from the Cu foil. The measurement of the R_S on the peeled PI films is chosen as an indicator to confirm the successful transfer of the graphene, thus identifying the Tc at which graphene transfer to PI occurs reliably.

Figure 41 (a) shows the most successful transfer of graphene to PI when the Tc is modified between 90 and 130°C, with the majority of R_S results within 2-3 kΩ/sq. At 180°C, a variation of the R_S from 6 kΩ/sq. to MΩ is found, denoting poorer graphene adhesion or graphene damage. For a further understanding of the results, we also performed a weight loss – Figure 41 (b) – and FTIR characterization on the PI films that were spin coated on glass and cured at different temperatures.

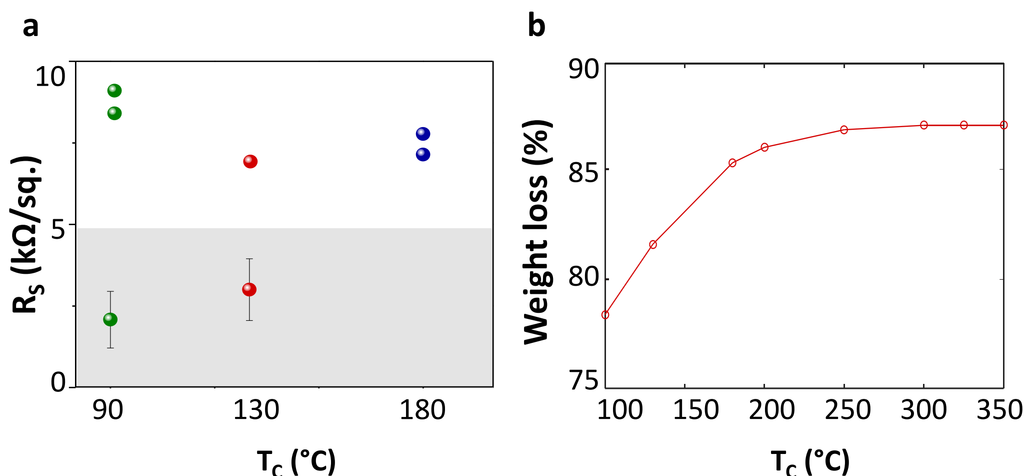

Figure 41. (a) R_S values of graphene transferred from the Cu foil directly to the PI film at different Tc. The shadowed area indicates the R_S range considered for a successful transfer of graphene to PI, with 90-130°C being the optimum Tc at which graphene transfer occurs. (b) Weight loss evolution of PI films deposited on glass after being treated at different Tc. The maximum weight loss where the film has been fully cured is 87%, which occurs at Tc of 250-350°C.

As explained previously in section 4.2.2. Polyimide, the initial precursor polymer solution contains VTEC in its PAA form, which produces imides as it dehydrates, as shown in Figure 42 below. As can be observed, for each constituent monomer of PAA, two molecules of water are removed, thus closing the polymeric chain into a five-ring, incorporating nitrogen. The stable chemical structure of the monomer gives the extraordinary properties to the PI in terms of thermal, chemical and mechanical resistance.

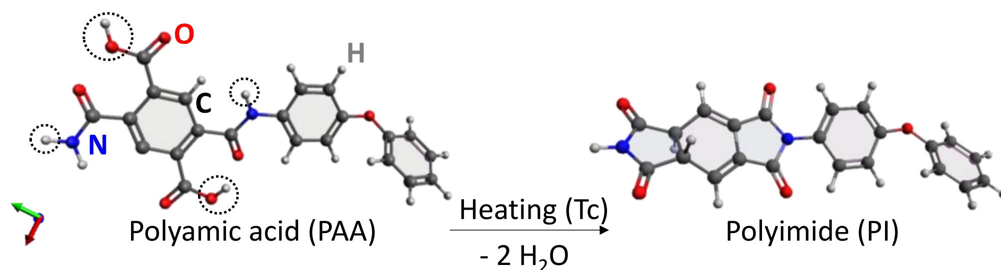

Figure 42. Curing process of the VTEC, where the applied Tc defines the reaction speed at which PAA converts to PI by the dehydration of the PAA monomer. The 3D image of PI shows a stable, flatter and compact structure. Images are simulated using Avogadro®

In Figure 43, the imidization progression of the PAA as a function of the Tc has been followed by monitoring the increase in the imide IR absorption bands (at 1380, 1724 and 1774 cm^{-1}) and the decrease of the amide bands (at 1530 and 1650 cm^{-1}) [191,192]. At 80-100°C, there is minimal to no absorption of the imide group at 1380 and 1774 cm^{-1}, which are associated with C-N stretching and C=O asymmetrical stretching, respectively. This means that at these low temperatures, the PAA remains the main component of the film. From 100 to 180°C, conversion of the PAA to PI starts to occur, which is confirmed by FTIR, as the imide bands increase with temperature while the ones for amide decrease. Finally, after 250°C the PI has been fully cured, which means that all of the PAA has been converted into PI, as revealed by the intense imide FTIR peaks together with the maximum weight loss of the film in Figure 41 (b), 87%. This is consistent with previous literature, where thermogravimetric analysis performed on VTEC films determined its degradation above 500°C and the curing (also called "polyimide condensation reaction") above 240°C. Also, by dynamic mechanical analysis, the VTEC polyimide glass transition was determined to be 250°C [189].

In accordance with these data, we hypothesize that the R_S oscillation at 180°C might be due to the variability in the degree of imidization, and that the failure to transfer graphene at Tc ≥ 180°C may be due to the PI lacking carboxylic groups that can interact with graphene. This hypothesis can be confirmed by three important facts. Firstly, the disappearance above 180°C of the FTIR peak at 1410 cm^{-1} is related to carboxylic groups. Secondly, there have been previous failed attempts to transfer graphene onto several types of already formed polyimides which have been diluted in organic solvents, such as NMP, with a chemical composition similar to the one shown in Figure 42 (e.g., P84, Kapton, etc.). Thirdly, there has been a successful transfer of graphene onto another PAA precursor (PAA-431176 from Sigma Aldrich), which demonstrates comparable values for graphene coverage and R_S. The latter is currently under investigation at Corning Inc. by evaluating the robustness of the transfer using another intermediate thin material.

The hypothesis would not be correct if we considered a high-quality hexagonal structure without defects (e.g., from micromechanical exfoliation), where the interaction between the PAA and the graphene should be negligible. However, in practice (and for the CVD technique) the appearance of defects is usual, and, depending on their nature, can alter the chemistry and shape of the material, adding carboxylic and hydroxyl groups. The most typical are non sp^2 carbon defects caused by vacancies, dangling bonds, carbon chains, edges or interstitials, and structural defects such as heptagon-pentagon pairs that distort the curvature of the carbon lattice (Stone—Thrower—Wales type transformations). For a better understanding of defect types, please see Chapter 1 and ref. [10–12].

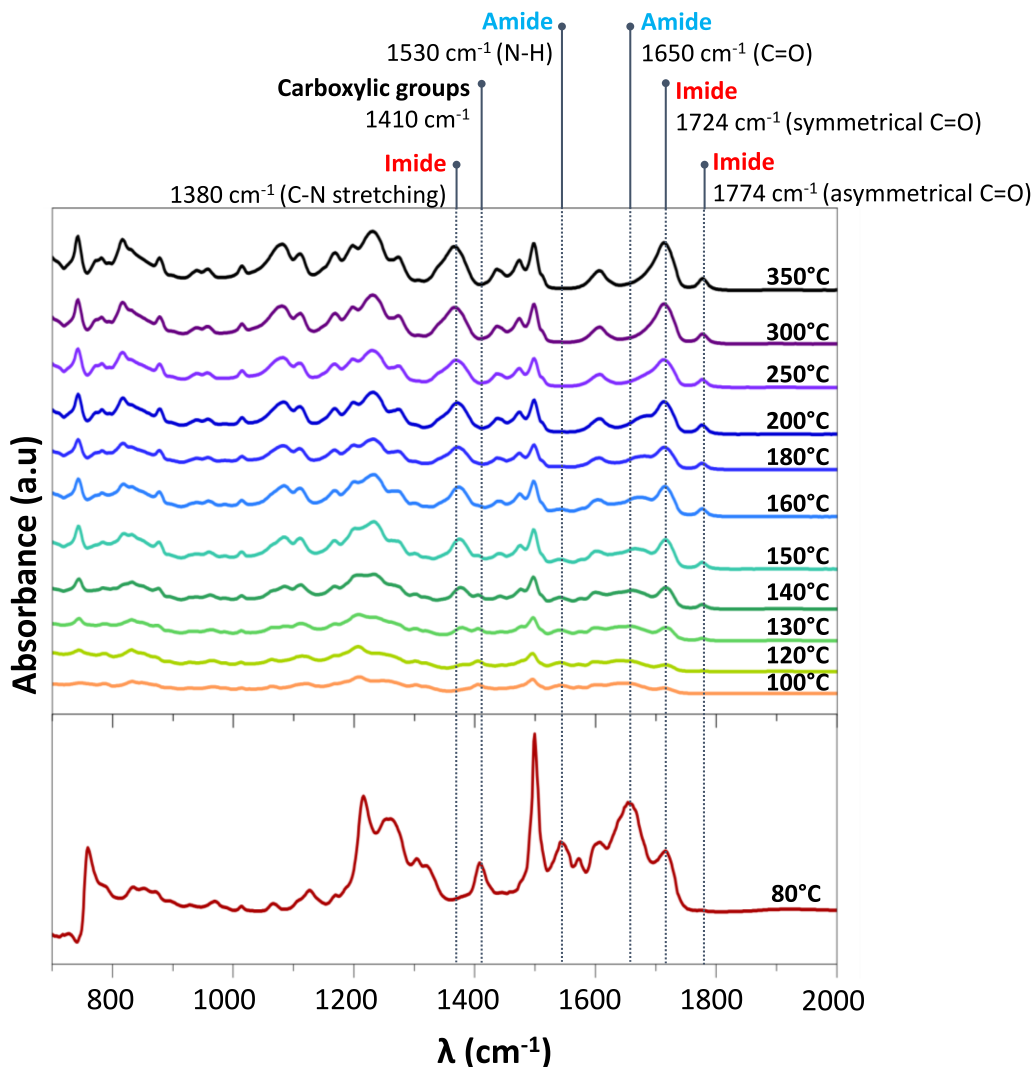

Figure 43. FTIR results for PI cured at different Tc - at 80°C (bottom) and 100-350°C (top). The highlighted peaks correspond to the imide (1380, 1724 and 1174 cm^{-1}), amide (1530 and 1650 cm^{-1}) and carboxylic (1410 cm^{-1}) groups.

Figure 44 below shows the comparison between two simulated structures using Avogadro® [193], an advanced software for building, editing, visualizing and analyzing chemical data. The two structures below are a defect-free graphene layer (a) and a defective graphene layer (b) that includes a vacancy in the center and two pairs of heptagon-pentagon defects. As a result of the defects, some oxygen groups can bond the structure, forming, for example, -C=O, -COOH, and -OH groups. As can be observed, these groups are out of the plane of the graphene layer, and are in theory available to react with the carboxylic groups of the PAA, further confirming our hypothesis. The figure shows the maximum height found in the structure, between the two most separated elements (Δz_{MAX}), and, specifically, between the two carbons (Δz_{MAX}(C-C)), which proved to be slightly lower (i.e., flatter) for the high-quality graphene in (a).

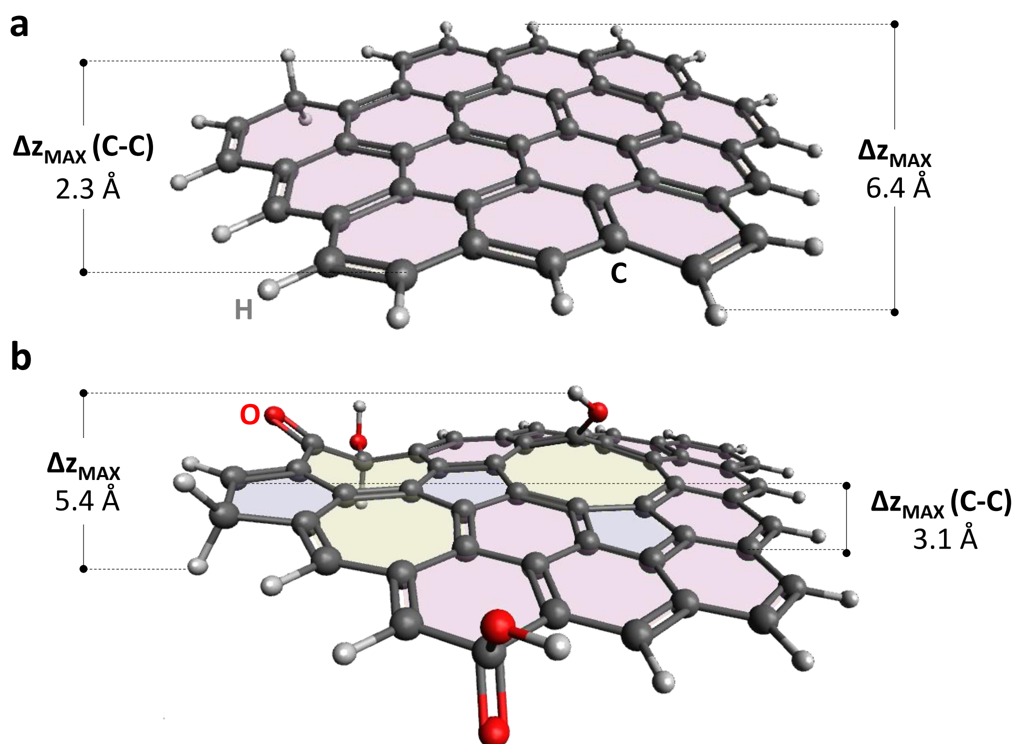

Figure 44. Simulation using Avogadro® of molecular structures for (a) defect-free graphene layer and (b) defective graphene layer with a vacancy and two pairs of heptagon-pentagon rings. In both, Δz_{MAX} and Δz_{MAX}(C-C) are indicated.

This is due to the heptagon-pentagon pairs and the vacancy-induced torsion in the molecule. As will be shown in section 4.4. Graphene transfer to glass and PET using PI as an intermediate layer, the graphene quality measured by Raman on the Cu is very high, without the detection of a D peak, but defects could be created later as a consequence of the mechanical peeling of the Cu. However, as we will discuss, SEM images and electrical measurements reveal that the

transferred graphene is of good quality. Further work should be dedicated to verifying this hypothesis by evaluating the creation of defects, their nature and their possible contribution to the limitations in electrical mobility.

In conclusion, after confirming the successful transfer of graphene at temperatures from 90°C to 180°C, we have defined the Tc set points for the hot press and laminator as 150 and 140°C, respectively. The difference in temperature is due to a limitation in the laminator designed to prevent damage to the silicon rollers.

4.4. Graphene transfer to glass and PET using PI as an intermediate layer

This transfer procedure involves four main steps as shown in Figure 45. Firstly, we spin coat the VTEC-APTMS or "as-received" VTEC onto glass or PET respectively (1). Next, the PI is dried at 40°C-80°C for 15 minutes to remove volatiles (2), after which the graphene is transferred by locating Cu/graphene on top of the sample with the graphene face in direct contact with the PI (3). Finally, the Cu is mechanically peeled, leaving the graphene attached to the substrate/(APTMS+)PI structure (4). The transfer is performed at the desired Tc by applying $P_{(HP)}$ with the hot press, or with a laminator modifying the Δx. In order to achieve a constant $P_{(HP)}$ distribution over the whole area of the sample, we have placed a silicone rubber sheet between the sample and the stainless steel top plate at the third step.

The optimization of both terms, $P_{(HP)}$ and Δx, is crucial for a successful transfer of high quality graphene. The optimized parameters for the hot press are Tc=150°C and $P_{(HP)}$=150-300 psi for a period of 10 minutes when Gr 1 is used, while for the laminator they are Tc= 140°C, and Δx =1-2 mm for the transfer to glass and 0.038-1 mm for the transfer to PET when Gr 2 is used. As will be discussed in sections 4.4.1. Graphene transfer to glass using the hot press and 4.4.2. Graphene transfer to glass and PET using the laminator, the Cu foil roughness is imprinted onto the graphene/PI. The transfer mechanism when using the laminator – applying compressive and shear forces to the sample - will create defects on these imprinted features, so, for this reason, a Gr 2 of lower roughness is used in the case of the laminator.

In the following sections, we will analyze separately the graphene quality obtained for the hot press and laminator, respectively, in terms of the morphology and cleanness. In section 4.4.3. Comparison of both transfer procedures, both techniques will be compared in terms of electrical and transparency results. Finally, in section 4.4.4. Device stability under heat, bending and aqueous media we will demonstrate the stability and resistance of the samples in terms of R_S when exposed to high temperatures, bending cycles and aqueous media.

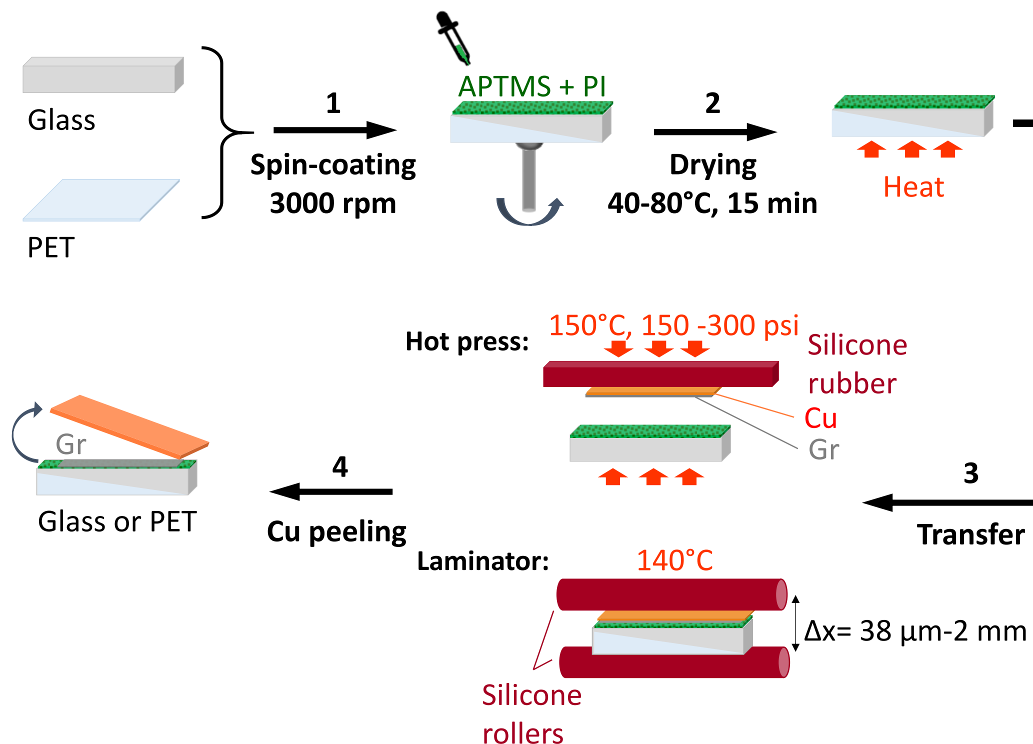

Figure 45. Graphene transfer to glass and PET using PI as an intermediate layer: (1) Spin coating of PI at 3000 rpm for 1 minute; (2) Drying of PI at 40-80°C for 15 minutes; (3) Cu/graphene is located on top of the sample and placed inside the transfer equipment (hot press or laminator). (4) Cu is peeled off, leaving graphene deposited on top of the target substrate with PI. Note that APTMS is only added to VTEC (0.5% APTMS+PI) when transferring graphene to glass. For the transfer to PET, only VTEC is spin coated.

4.4.1. Graphene transfer to glass/APTMS+PI using the hot press

In order to optimize the $P_{(HP)}$, a wide range of pressures are tested, showing different behaviors and transfer qualities. Indeed, two regimes can be identified, the first one occurring at low pressures from 25-75 psi, while the second occurs at high pressures from 150-350 psi. Figure 46 below shows results where the R_S at the first regime is highly variable. This might be due to a lack of contact between the graphene and the substrate, and the contribution of the volatiles trapped between them. For the second regime, the R_S decreases to a mean value of 1.91 kΩ/sq., being almost constant until 300 psi. According to the results, we can conclude that for a $P_{(HP)}$ between 150 and 300 psi, the graphene quality is not affected. However, as will be discussed in section 4.4.3. Comparison of both transfer procedures, the transfer at high pressures, such as 350 psi, might affect the graphene quality due to a decrease in mobility.

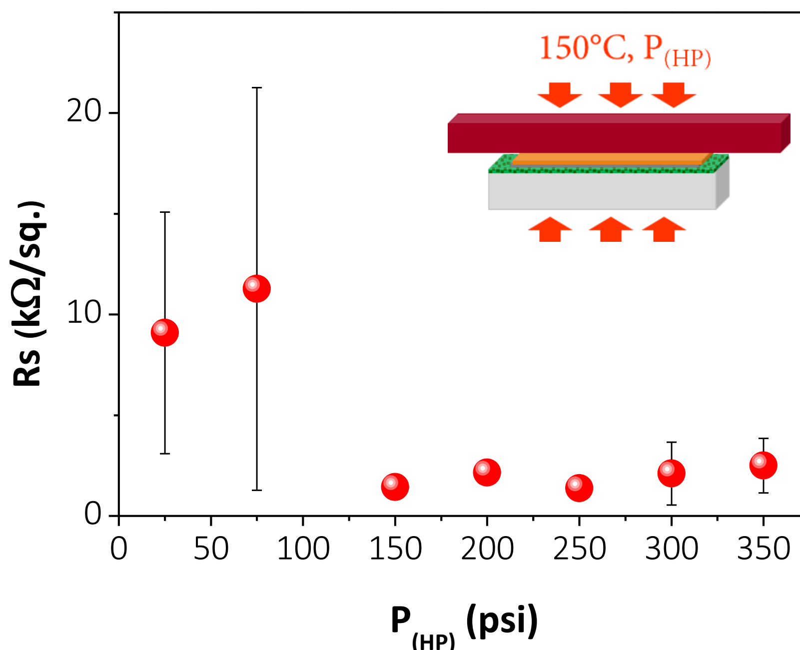

Figure 46. R_S of Gr 1 samples transferred by hot press, applying pressures of $P_{(HP)}$=25-350 psi. R_S is higher at lower pressures due to poor contact between the press and the sample. Above 150 psi, R_S remains almost constant.

The surface morphology of the transferred graphene samples is determined by SEM and AFM characterization. Figure 47 (a) consists of two SEM images showing a defect-free and clean graphene transfer. The high-resolution SEM image on the right shows two types of artifacts on the transferred graphene.

The first type of artifact corresponds to the imprinted large grain boundaries that are originated on the Cu foil (in this case, Gr 1) as confirmed by the AFM mapping in (b) performed on the Cu foil after the graphene growth. The Cu grain measured by the AFM is similar to the one observed in the SEM, thus confirming that during the PI curing step, the Cu foil roughness is imprinted onto the graphene/PI.

The second type of artifact observed in the SEM image (a) corresponds to graphene wrinkles. The presence of graphene cracks is easily detectable due to a high contrast in the SEM between the conductive layer (graphene) and the non-conductive materials (PI and glass). In particular, if the PI is exposed to the electron-beam of the SEM, a very strong charging effect appears. This charging effect, due to graphene cracks after transference when using a thick epoxy layer to detach the graphene from the Cu foil, has been previously reported in ref. [184]. Also, during the optimization of our technique, we measured samples containing both types of defect, i.e., cracks in the whole structure - Figure 48 (a) - and cracks

in the graphene leading to the previously mentioned charging effect by PI exposure to the SEM, shown in Figure 48 (b). Therefore, under the optimum conditions shown in Figure 47, we can confirm that a continuous layer of graphene has been successfully transferred.

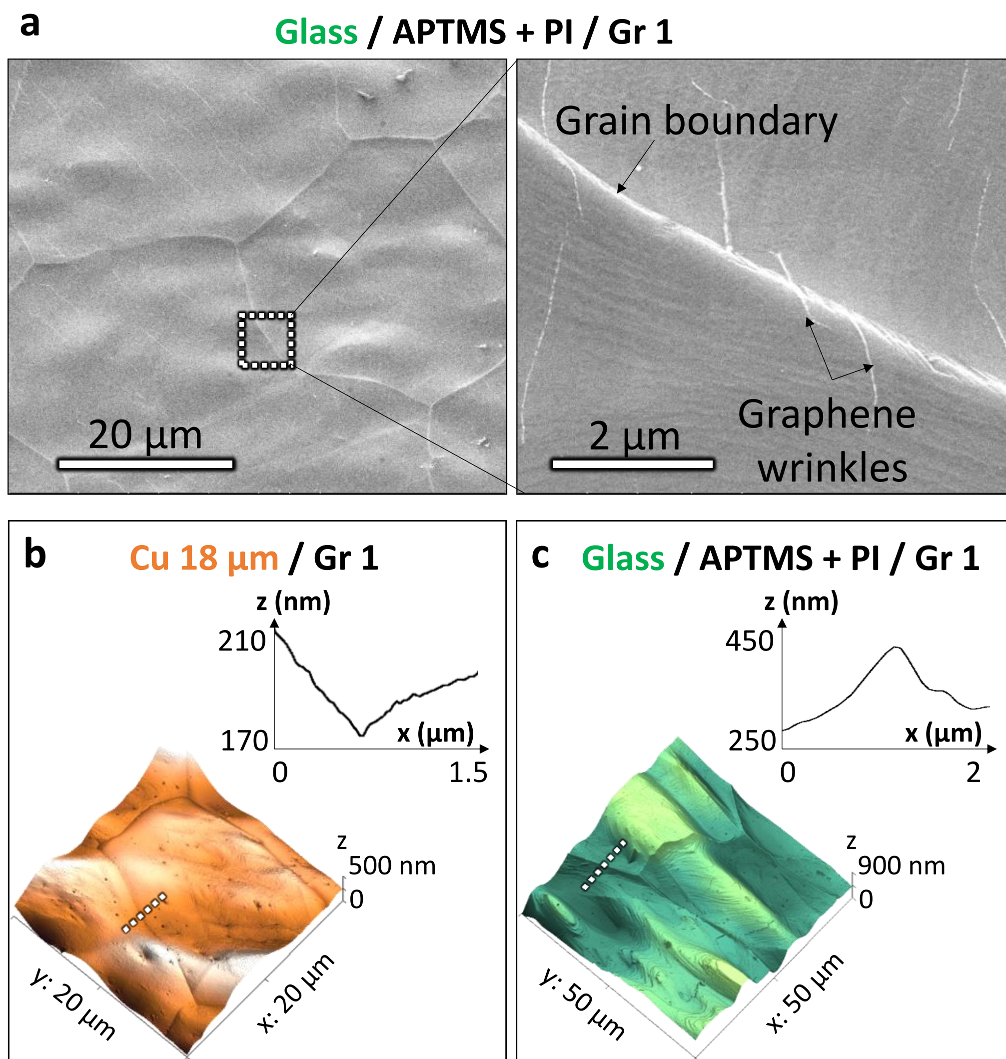

Figure 47. (a) SEM characterization shows clean and continuous Gr 1 transferred to APTMS+PI on glass by the hot press. Graphene wrinkles together with imprinted Cu grain boundaries -originated on the Cu foil - can be observed. (b) AFM characterization of Gr 1 grown on Cu. The inset shows the section of the area marked on the map (grain boundary depth) by a squared dashed line. (c) AFM mapping of the transferred sample showing the imprinted Cu grain boundary. The inset corresponds to the section marked on the AFM map by a squared-dashed line, which shows that the imprinted boundary is lifted up due to the mechanical peeling of Cu.

The inset in Figure 47 (b) shows the section of the grain boundary marked on the mapping with a squared-dashed line. This morphology has an opposite direction in height to the transferred samples in Figure 47 (c) due to the mechanical peeling of the Cu. These results together with the SEM show that the Cu foil roughness imprints onto APTMS+PI/ graphene during the curing step. However, contrary to the results obtained when using Gr 1 in the laminator, the electrical characterization in terms of mobility demonstrates that the imprinted features here are not critical to the graphene quality.

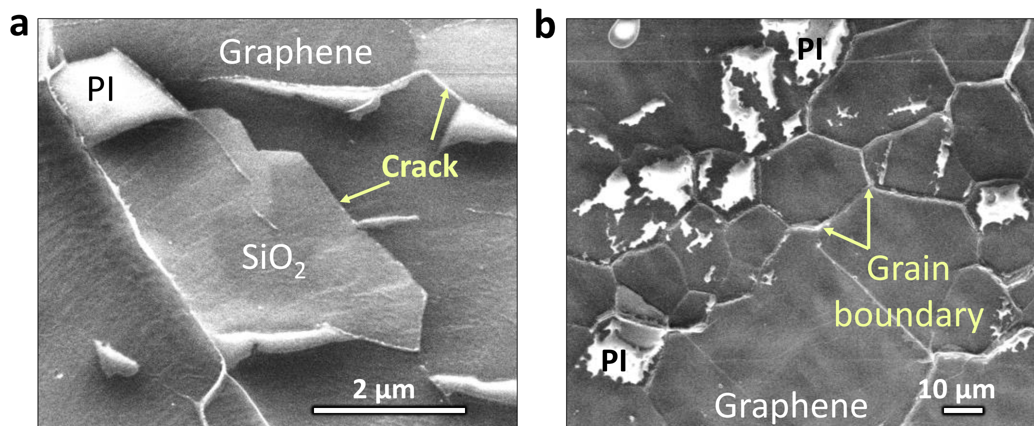

Figure 48. SEM images of graphene samples transferred to glass under non-optimized conditions. (a) Two big cracks are observable due to the large contrast between the dark conductive area – graphene – and the glass substrate. The PI film is observed to be lifted up on the top left corner, with PI being white due to its charging effect. (b) Very pronounced and defective imprinted grain boundaries can be seen, with large white areas of graphene holes that leave the PI directly exposed to the SEM electron beam. Because of this, a strong charging effect is measured. The darker areas correspond to the transferred graphene layer.

4.4.2. Graphene transfer to APTMS+PI/glass and PI/PET using the laminator

In this case, the parameter Δx has been optimized to enhance the quality of the transferred graphene when using glass and PET as the target substrates. At Tc=140°C, and considering the substrate thicknesses, the optimum values for Δx are 2 mm and 38 µm for glass and PET, respectively. It should be noted that these Δx values are optimized for the specific thicknesses of our substrates (1 mm and 125 µm for glass and PET, respectively). The use of substrates of different thicknesses would need a modification of the Δx.

The SEM and AFM characterization for the laminator reveal differences to the results obtained for the hot press. Figure 49 (a,d) shows Gr 1 transferred to

APTMS+PI/glass with more remarkable imprinted grain boundaries than the ones observed for the hot press transfer. According to the height profile in (d) of the area marked by the squared-dashed white line on the map, the imprinted grain boundary is almost three times higher when using the laminator than when transferring it with the hot press. For this reason, graphene grown on a less rough Cu foil (Gr 2) has been tested to evaluate whether there is a reduction in the imprinted features, which will potentially improve the graphene quality. In the case of Gr 2, the initial morphology of the Cu foil presents terraces instead of the large Cu grain boundaries found with Gr 1, as demonstrated by the AFM measurement in Figure 50. The differences in morphology of the transferred graphene are shown in the SEM and AFM measurements in Figure 49 (b,e) and Figure 49 (c,f), where the Gr 2 has been transferred to glass and PET, respectively. As before, the Cu terraces are imprinted onto the PI/graphene during the curing step, but show less pronounced artefacts.

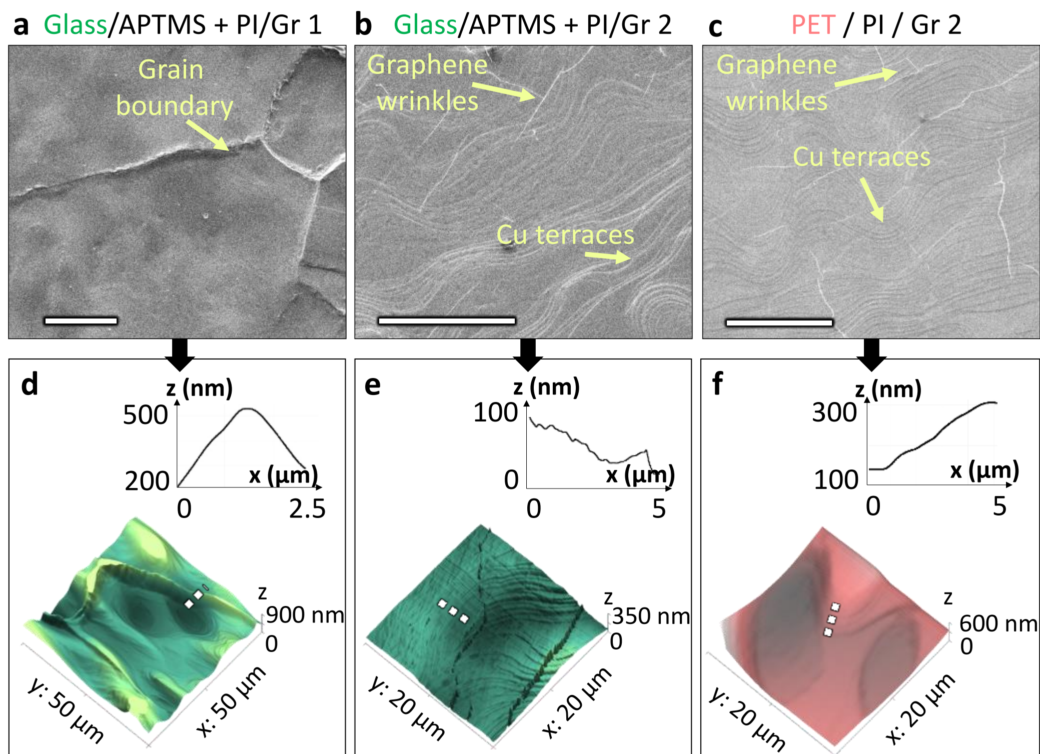

Figure 49. SEM (a-c) and AFM (d-f) characterization of the graphene samples transferred to glass/APTMS+PI (a, b, d, e) and PET/PI (c, f) using a laminator. Gr 1 is used for the transfer in (a,d), showing imprinted Cu grain boundaries with greater heights than for the hot press. Gr 2 is used for the transfer to glass (b, e) and PET (c, f), showing imprinted Cu terraces originated in the Cu foil (see Figure 50 below). The insets of each AFM correspond to the section marked on the mapping (squared-dashed line).

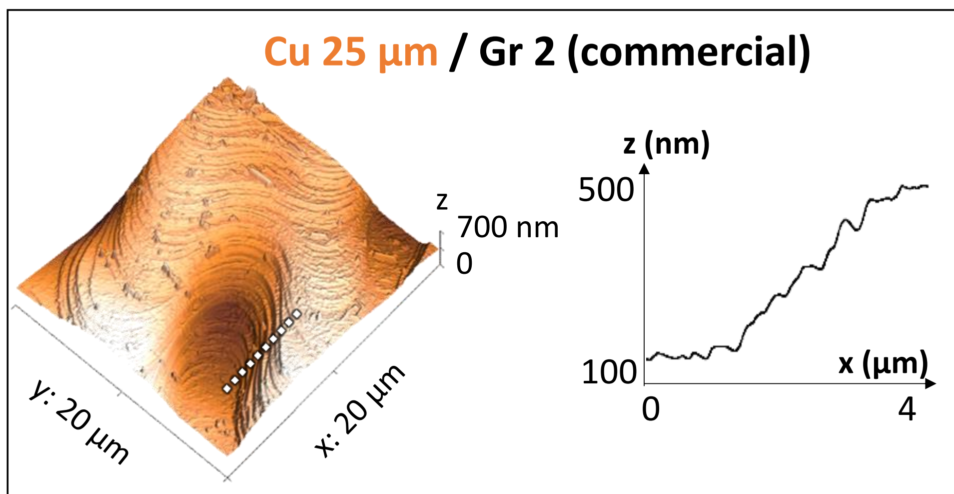

Figure 50. AFM characterization of Gr 2 grown on Cu foil (commercial). Inset shows the section of the area indicated by the squared-dashed line on the map. The foil morphology shows Cu terraces.

As will be shown in section 4.4.3 with the transmittance and electrical results, for lamination it can be concluded that the use of graphene grown on a less rough Cu foil is crucial for obtaining proper results.

4.4.3. Comparison of both transfer procedures

In order to assess the quality of the graphene on Cu foils (Gr 1) and the presence of graphene on the final structure, Raman analysis is performed. This is carried out, firstly, on the graphene grown on the Cu foil and, secondly, on the VTEC spin coated on glass and cured at 150°C without graphene on top, and finally, on the graphene samples transferred to glass/APTMS+PI and PET/PI by hot press and laminator. Figure 51 (a) shows the Raman spectra of Gr 1 grown on the Cu foil, where the two typical peaks, G and 2D, are detected at 1580 cm^{-1} and 2680 cm^{-1}, respectively. The absence of a D peak and the I_{2D}/I_{G} ratio equal to 2 reveal the growth of high quality monolayer graphene. After performing the graphene dry transfer by our technique, it can be observed in Figure 51 (b) that the previous intense 2D peak is now very weak as a consequence of the high absorption of PI – previously reported in literature [185]– which also masks detection of the G peak. Because of this, Raman is only used to confirm the presence of graphene as the ratio between the 2D and G peaks cannot be obtained. The other peaks that have been detected in the measurements (at 1325, 1376, 1614 and 1777 cm^{-1}) are attributed to the PI - Figure 51 (b), bottom blue line -, while the one at 1726 cm^{-1} is attributed to the PET substrate - top green line.

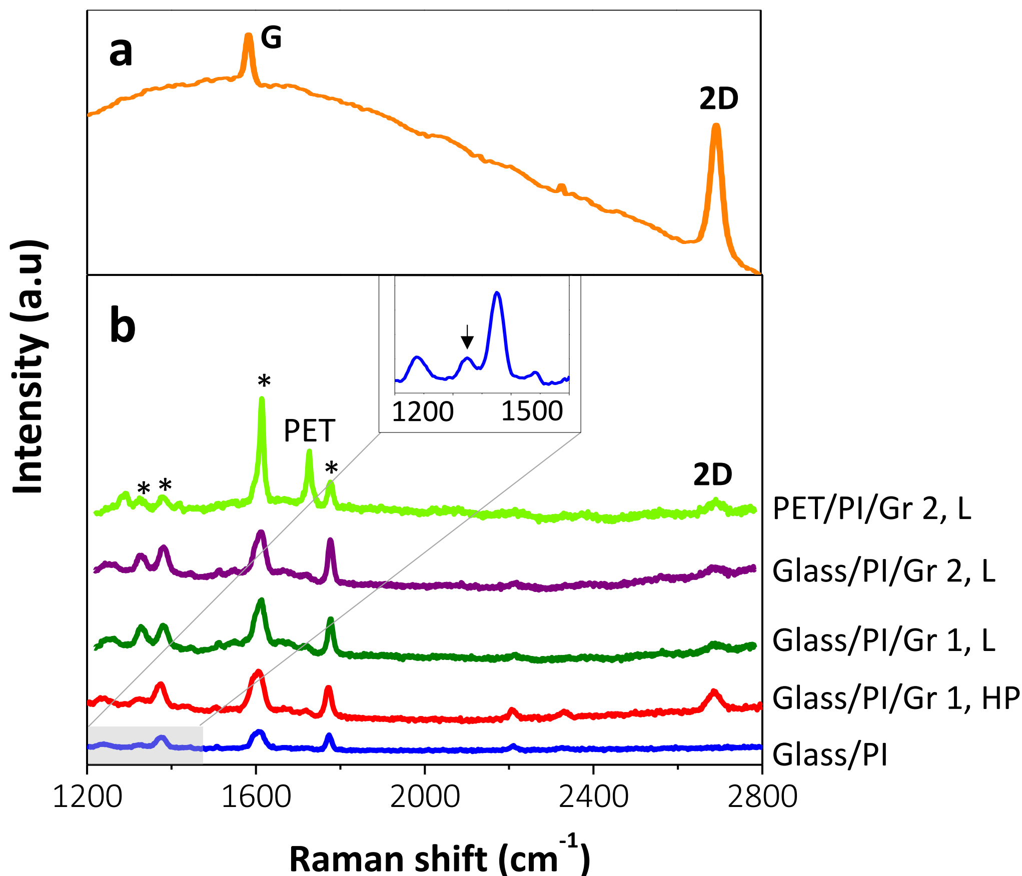

Figure 51. Raman characterization of: (a) Gr 1 on Cu foil, showing the graphene peaks, G and 2D; (b) from bottom to top: PI on glass (blue) showing the PI peaks that are denoted by *; graphene transferred to glass (red, green and purple) and PET (light green) by hot press (HP) and laminator (L) where a low 2D graphene peak and the corresponding substrate peaks are detected. The inset shows an amplification of the bottom measurement on glass/PI, showing the presence of the peak at 1325 cm^{-1}, which should not be confused with the graphene D peak. Note that APTMS is added to VTEC when the graphene is transferred to glass.

Optical measurements have been also carried out, as the transparency of the whole structure is important for such applications as flexible displays or solar cells. Results are collated in Figure 52 below for samples transferred by (a) the hot press to glass/APTMS+PI, (b) the laminator to glass/APTMS+PI, and (c) the laminator to PET/PI substrates. All graphs include the transmittance of the bare substrate with and without PI, shown by purple and black lines, respectively. To determine the order of transparency of the samples, the transmittances are calculated at 550 nm by removing the contribution of the substrate using the equation 16 below. The data is collated in Table 12.

$$T_{CALCULATED} = (T_T \text{ x } 100)/\ T_{SUBSTRATE}) \qquad \text{(Eq. 16)}$$

According to the results, the order of the samples in respect of transmittance is:

Gr 2/PET (L)> Gr 2/Glass (L)> Gr 1/Glass (HP)> Gr 1/Glass (L).

If we compare the results obtained by lamination, the graphene grown on the less rough Cu foil (Gr 2) is more transparent.

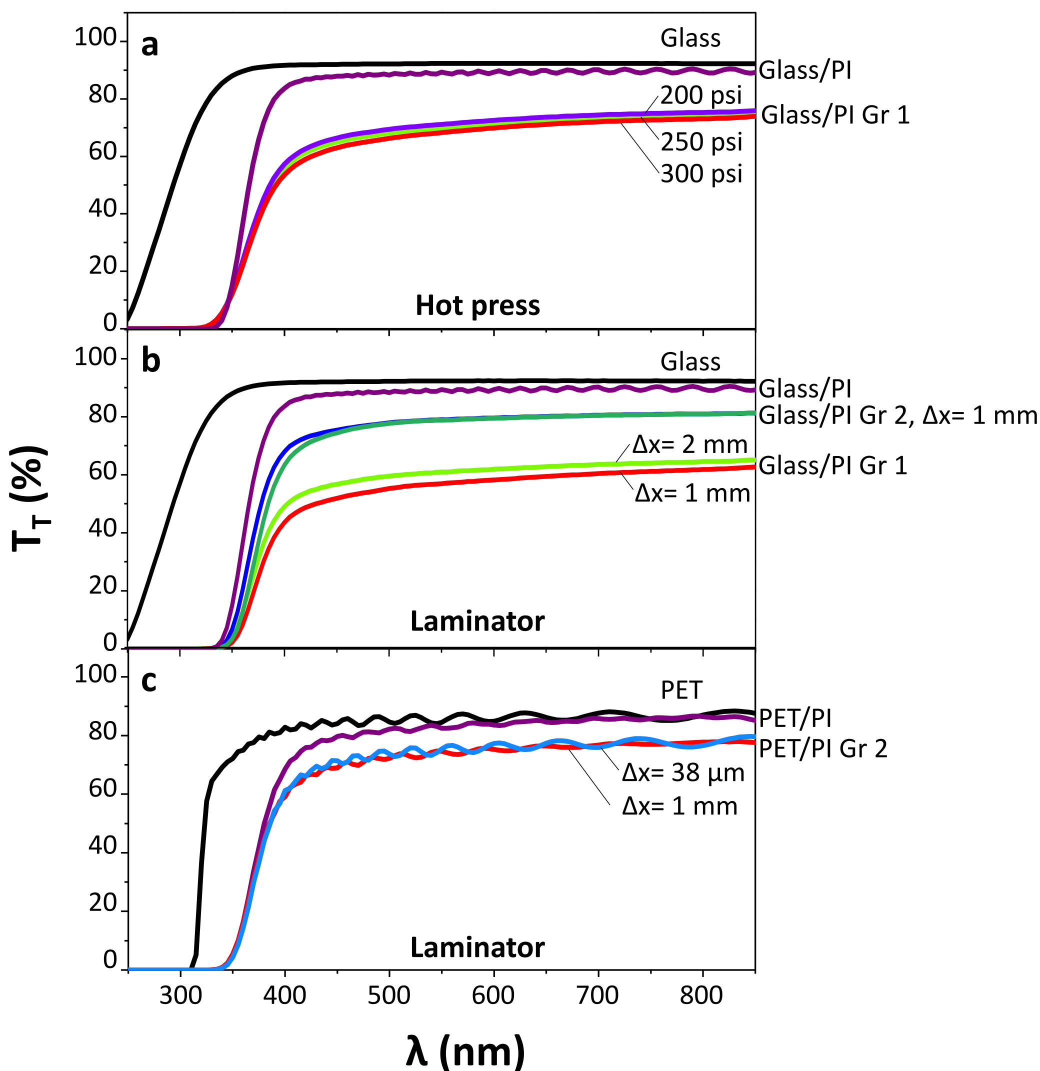

Figure 52. T_F measurements of: (a) Gr 1 transferred to glass/APTMS+PI by the hot press at $P_{(HP)}$ from 200 to 300 psi; (b) Gr 1 and Gr 2 transferred to glass/APTMS+PI by the laminator modifying Δx from 1 to 2 mm; and (c) Gr 2 transferred to PET/PI by the laminator modifying Δx from 38 µm to 1 mm. For all graphs, the transmittance spectra of the bare substrate with and without PI are included (purple and black lines, respectively).

As shown previously by the SEM and AFM images in Figure 49 (a,d), the imprinted grain boundaries using Gr 1 are more pronounced with the laminator technique. The increase in height at the grain boundary can scatter the light, thus reducing the transmittance of the sample. The transfer mechanism could be the main cause of this issue: while it is static for the hot press, the process is dynamic for the laminator, with the sample being introduced 12 times. The continuous and progressive displacement of volatiles after each cycle might induce strain and defects in the graphene at the imprinted Cu grain boundaries. We also speculate that the combined effects of shear and compressive forces in the laminator could worsen the defect structures, while only compressive force is at play in the hot press.

Table 12. Transmittance (%) at 550 nm of graphene transferred by the hot press and the laminator. The measured values (1st row) correspond to the whole structure, while the calculated ones (2nd row) are obtained by removing the substrate contribution with Eq. 1. Transmittance at 550 nm of: Glass= 92,36%; Glass/APTMS+PI= 89%; PET= 84.7%; PET/PI=82%.

T (%) at 550 nm	Hot press [(a)]			Laminator [(b)]				
	To glass			To glass			To PET	
	Gr 1, (250)	Gr 1, (200)	Gr 1, (300)	Gr 2 Δx=1	Gr 1 Δx=2	Gr 1 Δx=1	Gr 2 Δx=0.038	Gr 2 Δx=1
T_T	71	70	68	79	61	57	76	74
$T_{CALCULATED}$	77	76	74	86	66	62	90	87

[(a)] (Value): $P_{(HP)}$ used for graphene transfer [psi]
[(b)] Δx [mm]

For the electrical characterization, the R_S has been measured by depositing Au/Ag paste electrodes on top of the graphene corners to measure the n_S and μ_H by the Hall Effect. For further details of the measurement, see Chapter 1, section 1.2. Characterization techniques.

For this study, seven samples (S1-S7) were obtained under different conditions that are specified in Table 13, highlighting the type of graphene used, the substrate and the equipment used for the transfer.

Table 13. Summary of the conditions for transferring samples S1-S7, specifying type of graphene, substrate and equipment.

Properties	**Samples**						
	S1	**S2**	**S3**	**S4**	**S5**	**S6**	**S7**
Graphene	1	1	1	1	1	2	2
Substrate	Glass	Glass	Glass	Glass	Glass	Glass	PET
Hot press $P_{(HP)}$ (psi)	200	250	300	-	-	-	-
Laminator Δx (mm)	-	-	-	1	2	1	0.038

In Figure 53 below, we have plotted separately the obtained n_S (red bubbles) for the hot press at different $P_{(HP)}$ values from 200 to 350 psi in (a), and for the laminator at Δx from 0.038 to 2 mm in (b,c). For a clear understanding of the results, we have indicated the graphene type used for each sample, Gr 1 being the only one used for the hot press transfer. In the case of the laminator, both graphene types have been used, Gr 1 in samples S4 and S5 in (b), and Gr 2 in samples S6 and S7 in (c). The corresponding calculated values of μ_H calculated using the Drude model are plotted in (d), again making a distinction between the equipment and type of graphene used.

In all cases (S1-S7), the graphene presents electron doping, with a stronger n-doping for the samples transferred with the laminator (S4-S7) as shown in Figure 53 (b-c). The reason for the n-type doping is that the graphene is transferred on PI, a material that could be positively charged due to unreacted amine groups from the aminosilane. This is contrary to the direct transfer of graphene to glass, a substrate that tends to be negatively charged due to deprotonated SiOH groups on the surface, thus leading to p-type doping into graphene.

For the samples obtained by the hot press in Figure 53 (a) at $P_{(HP)}$ from 250 to 350 psi, the mean value of R_S is equal to 1.9 kΩ/sq. According to the results, the pressure does not seem to strongly affect the graphene doping, whose mean value is $\overline{n_S} = -1.6 \cdot 10^{12}$ cm^{-2}. However, at 350 psi, at a constant doping level, the μ_H slightly decreases (Figure 53 (d)), which might suggest that such high pressures can induce defects into the structure. Nevertheless, the maximum value of μ_H equal to 1250 cm^2/V·s confirms the fact that the imprinted features by the hot press do not degrade the high quality of the transferred graphene. Further work could contemplate the use of less rough foils to further improve the μ_H results.

For the samples obtained by the laminator in Figure 53 (b-c), it can be observed that the use of different substrates - glass and PET- do not have an effect

on the graphene n-doping, whose mean value is $\overline{n_S}$= -1.4·10^{13} cm^{-2}, as both target substrates are covered with PI. However, as previously mentioned, the laminator technique can induce defects onto the PI/graphene film due to the application of compressive and shear forces during the curing process, especially to the graphene grown on rougher Cu foils – Gr 1, (b) – which is confirmed by the SEM and AFM results in Figure 49 (a,d) above. These defects also contribute to the R_S, whose mean value is 3.5 kΩ/sq., which is high if we consider the high doping measured. However, when the graphene grown on the less rough Cu foil - Gr 2, (c) - there is a great improvement in the transfer quality, as shown by the SEM and AFM results in Figure 49 (b,c) and Figure 49 (e,f) above. This is also confirmed by the R_S measurement, which has decreased to 770 Ω/sq. This result is consistent due to the high level of carriers, as high doping reduces the R_S [1,13]. The μ_H calculated for Gr 2 varies from 600 to 850 cm^2/V·s, as can be observed on the right side of Figure 53 (d). Having selected a suitable Cu foil, we believe that the low μ_H observed is caused by the high carrier density.

Further work needs to be devoted to understanding the origins of the strong n-doping caused by lamination, which might be related to the charges trapped during the process. An accurate control and reduction of graphene doping in this technique will lead to an increase in μ_H.

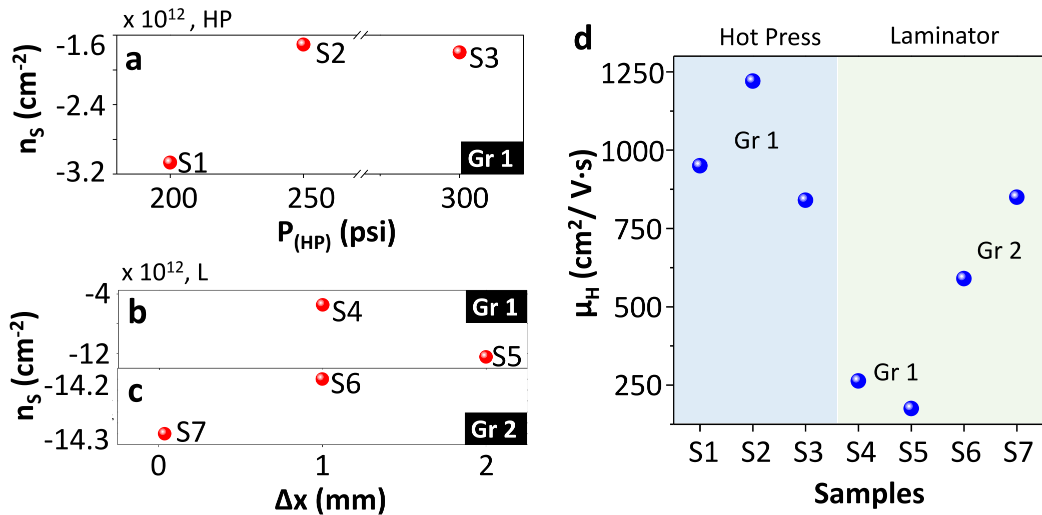

Figure 53. Hall measurements of the transferred graphene samples (S1-S7). The obtained n_S is plotted for the different transfer methods. (a) n_S obtained for samples S1-S3, fabricated with Gr 1 and transferred by hot press to glass/APTMS+PI at $P_{(HP)}$ of 200, 250 and 300 psi. (b) n_S obtained for samples S4-S5, fabricated with Gr 1 and transferred by laminator to glass/APTMS+PI at Δx of 1 and 2 mm. (c) n_S obtained for samples S6-S7, fabricated with Gr 2 and transferred by laminator to glass/APTMS+PI and PET/PI at Δx of 1 and 0.038 mm, respectively. (d) μ_H calculated for previous samples, specifying the type of transfer mechanism and type of graphene.

4.4.4. Device stability under heat, bending and aqueous media

Due to the exceptional properties of PI, we want to demonstrate its potential to provide stability to the graphene samples when they are exposed to high temperatures, bending cycles and aqueous media. R_S has been chosen as an indicator to demonstrate that the graphene remains on the surface and that it does not degrade under harsh conditions.

The *temperature stability* of an already transferred sample by hot press is tested, after depositing Au/Ag paste contacts on top of the graphene corners to measure the R_S immediately after each change in temperature. Three temperature cycles are carried out, from RT to 350°C, typically in steps of 50°C, and the samples are cooled down to RT before starting the next cycle. Figure 54 shows the R_S calculated immediately after each temperature change by measuring the resistance between all the contacts shown in the scheme on the left, thus obtaining the $R_{horizontal}$ and $R_{vertical}$. For further details about the measurement process, see Chapter 1, section 1.2. Characterization techniques.

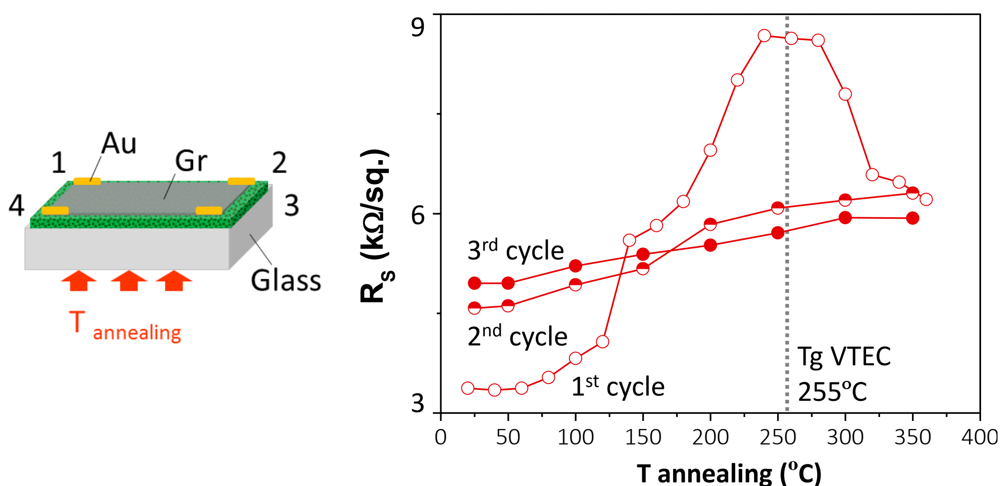

Figure 54. Temperature stability testing in terms of R_S for graphene transferred by the hot press method and annealed up to 350°C. The scheme on the left represents the sample configuration where four Au/Ag contacts are deposited to measure R_S. Three cycles of annealing are performed, modifying the temperature from 25°C to 350°C, typically in steps of 50°C. The R_S is measured after each temperature change and before starting a new cycle, the sample is cooled down to RT. The graph on the right shows the R_S at each temperature with a high slope during the first cycle. After achieving the Tg of the VTEC, the R_S decreases and remains stable after two additional cycles.

As can be observed, for the first cycle - empty red circle - there is an increase in the R_S from 150°C to approximately 250°C-275°C, after which the R_S decreases when the temperature is raised to 350°C. This increase is likely due to

the shrinking of the PI. As shown initially in Figure 41 (b), at 150°C the PI film contains approximately 4% of compounds that will evaporate at higher temperatures, with 4% being the difference between the weight loss of the PI film at 150°C (83%) and the maximum weight loss of 87% at temperatures above 250°C. This fact would explain the increase in the R_S, as the PI shrinks during the evaporation of volatiles, thus affecting the graphene that has been transferred onto it. Beyond 255°C, which is the glass transition temperature (Tg) of PI [189], the PI film likely flattens due to increased relaxation dynamics. We hypothesize that this effect also flattens the graphene, thereby reducing the resistance. For the next two cycles, the initial R_S values are very similar to each other but higher than for cycle 1 by approximately 1.3 kΩ/sq. During the heating process for cycles 2 and 3, the R_S variation with temperature is linear, which is typical for conductive materials. The reason for this behavior is that raising the temperature increases the collision of free electrons with atoms, which worsens the conductivity of the material, i.e., the resistivity increases. Since the PI has lost all volatiles at the end of the first cycle, no such sharp increase in R_S is observed in cycles 2 or 3. Thus, the mechanical and thermal stability of a glass/APTMS+PI/graphene composite at high temperatures after a first cycle of annealing can be confirmed.

The *bending stability* is evaluated on PET/PI/graphene samples at different radii of curvature (R_B) in order to evaluate any possible damage to the graphene after several cycles. Figure 55 (a) shows the R_S evolution of samples that are bent at R of approximately 2 cm, 9 mm and 7 mm. Initially, the R_S increases at R= 2 cm from 1.13 to 1.58 kΩ/sq. but remains constant after 25 cycles. After 100 cycles at the lowest R_B, the R_S increases again by a factor of 1.5.

The *adhesion tests* are performed in order to check the R_S after dipping the samples in water for a period of 5 minutes. When graphene is transferred directly to glass, after water immersion and due to the hydrophilic behavior of glass, the graphene usually starts to wrinkle and detach itself from the glass surface as the water penetrates between the layers. In our case, however, we demonstrate that the graphene transferred to glass and PET, with a PI layer in between, remains almost stable in an aqueous environment without delaminating. This can be observed in Figure 55 (b) where R_S slightly increases in S1 and S7, while it remains constant for S6. Although more statistics would be necessary in order to determine a possible increase in the R_S after water immersion, the results already point out that graphene does not physically delaminate from the substrate.

The reason for this is the hydrophobic nature of polyimide, which is confirmed by the contact angle measurements collated in Table 14. The angle formed between the water droplet and the PI is 95 degrees. When the APTMS is added, the wettability does not change. Although the APTMS is slightly positively charged due to possible unreacted amine groups, which would provide hydrophilic

behavior, when it is added to VTEC (0.5% wt.) the surface remains strongly hydrophobic. This is confirmed by the measurements performed on the APTMS+PI, whose values are above 100 degrees as shown in Figure 56. In the case of graphene, the contact angles are approximately 95 degrees. The proposed technique has thus great potential for real product implementation since device fabrication often involves wet processes.

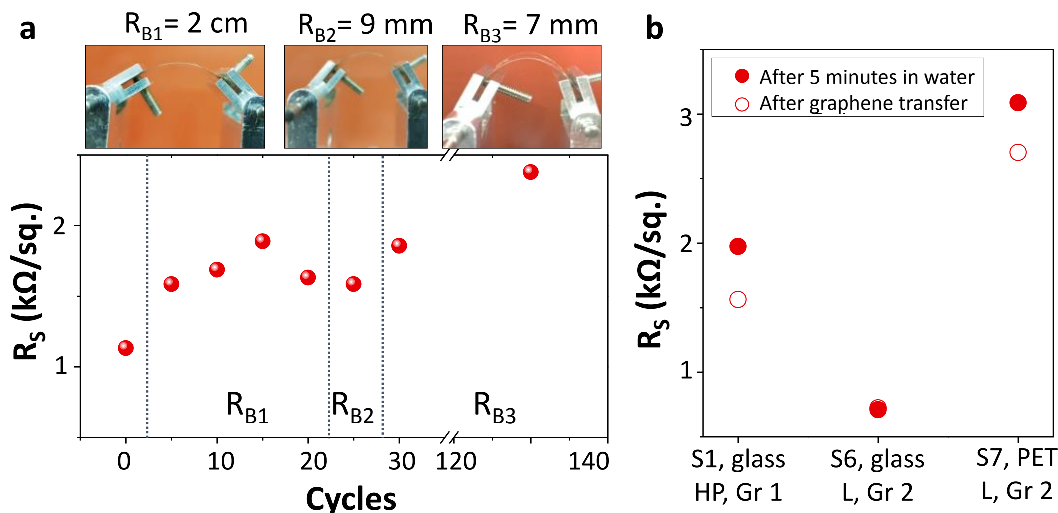

Figure 55. Stability of the transferred samples measuring R_S: (a) after bending tests on PET/PI/graphene at different radii, R_S increases by a factor of 2 after 130 cycles. Top pictures show the set-up where samples have been bent, indicating the bending radii at each step; (b) before and after dipping the samples S1, S6 and S7 in water for 5 minutes, demonstrating that graphene does not delaminate from the substrate/PI. For S6, R_S is constant after water immersion.

Table 14. Summary of θ measured on graphene and PI of different transferred samples.

Sample		θ (°)
Hot press (Glass)	APTMS+PI	102
	Graphene	97
Laminator (Glass)	APTMS+PI	105
	Graphene	92
Laminator (PET)	PI	95
	Graphene	95

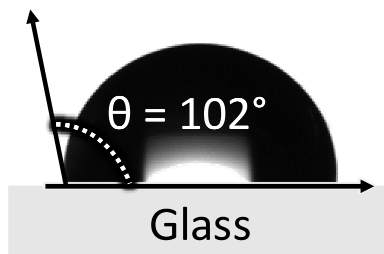

Figure 56. Example of contact angle measurement on the APTMS+PI area of the sample transferred by the hot press.

4.5. Conclusions

We have demonstrated a new technique to transfer graphene to glass and flexible substrates such as PET, using a mixture of polyimide and APTMS as an intermediate layer. Our technique is the first step towards making a substrate ready for device fabrication. The use of an intermediate thin layer leads to a device which is transparent, thermally stable (350°C) and free of polymer residues (such as PMMA for the wet transfer method) on the device side of the graphene. In addition, it has considerable important aspects for industrial implementation, such as lower processing times than previous techniques (by a reduction in curing times), the Cu recyclability, the use of current industrial technology (a hot press and a laminator), and the demonstration of a high interfacial stability in aqueous media. While for the hot press method, the initial Cu foil structure does not influence the process, in the case of the lamination technique, we have found the use of less rough Cu foils to be crucial, otherwise foil artifacts imprinted onto the graphene/PI structure lead to poor performance. Although this work is based on a specific polyimide, it has been demonstrated that our technique can be extended to other materials, such as PAA. Further work would enhance understanding of graphene doping by the lamination technique and improvement of the electrical mobility of graphene.

5

Tuning of graphene doping by thermal poling of the glass substrate

Graphene doping, i.e. changing the carrier concentration, is essential for its use in real devices. Controlling the doping can be achieved by applying an electrostatic field (gate voltage) which, depending on its sign, can either inject (n-doping) or remove (p-doping) electrons. Instead of applying an external field, our doping approach consists in creating and storing an electric field inside the glass by displacing ions. The ions move within the sample through the application of an external voltage at relatively high temperature, the latter increasing the ionic conductivity. This phenomenon is known as "thermal poling" of glass. With this technique, we demonstrate not only the doping change of the graphene after thermal poling, but also its evolution as the poling is progressively erased with temperature, showing that the poling effect on the doping is reversible. We provide the calibration of our technique and the results when negative and positive external voltages are applied.
This work is currently under consideration for patent filing with Corning Incorporated and submission of a journal paper.

5.1. Introduction

Controlling graphene doping is essential for electronic and optoelectronic applications. For instance, unintentional doping by residues, substrates and possible additional top layers residues carrier mobility. On the other hand, applications such as graphene plasmonics require high yet controlled doping levels [194]. Therefore, the development of a technique that provides stable and accurate control of doping is of great interest for research and industry applications.

There are three main types of doping: chemical or surface transfer doping, substitutional doping, and electrostatic doping. The last method is the most

commonly used as it allows a reversible and accurate control of the doping, but the main issues are the low reachable n_S due to the low capacitance of the Si/SiO_2 (200 nm)/graphene and the dependence on the type of target substrate. The latter effect has been widely demonstrated in literature when graphene is transferred to glass, a process which, together with the PMMA residues left after the wet-transfer method, induces p-doping to the graphene as the glass has a potentially negative charge due to the hydroxyl groups on the surface. In Chapter 4, where we demonstrated a clean, fast and scalable dry-transfer technique using PI as an intermediate layer, we observed an intrinsic n-doping due to the slightly positive charge of the unreacted amines in the PI.

The aim of this work is to demonstrate electron and hole doping (n- and p-doping, respectively) of graphene in a reversible mode by means of changing the polarity of the dielectric substrate where the graphene device is fabricated. In order to achieve this, we have implemented a technique called thermal poling, which has been widely studied for wavelength conversion and electro-optic modulation in glass fibers [195].

Thermal poling is a phenomenon based on the creation of two charged layers at a certain temperature (T_P) caused by the displacement of ions inside the glass when an external electric field (V_P) is applied. The most interesting aspect is that after the displacement of the charges, when the system is cooled down while applying the V_P, a frozen-in voltage is created inside the glass (V), which is stable over a specific period of time dependent on the type of glass [196,197].

When we talk about ions inside the glass, we are referring to the glass additives that can be introduced during its synthesis, mainly for modifying the glass properties. These elements are called *modifiers*, with Na and Ca being those typical added, belonging to Na_2O and CaO, respectively.

Figure 57 (a-b) show the difference between the perfect crystalline network of quartz (a), where the unit cell is repeated along the whole structure of the glass, and fused silica (b), whose structure is compact without the presence of modifiers but whose unit cell can have different shapes. Figure 57 (c) shows an example of glass, such as soda lime glass (SDG), with the presence of Na as the network modifier. For quartz and fused silica, the absence of modifiers and the strong covalent bond between each silicon to four oxygens, provides an extremely stable structure. On the contrary, the presence of modifiers, such as Na^+ in SDG (c), causes weak ionic bonds, which allows the ions mobility at temperatures much lower than the glass transition temperature.

As can be seen in Figure 57 (c), the introduction of Na during the glass synthesis promotes the breaking of some Si-O-Si bridges, which leaves non-bridging oxygens in the glass network. As a result, these oxygens will be anions (O^-) for the sodium cations (Na^+), which is incorporated at these locations.

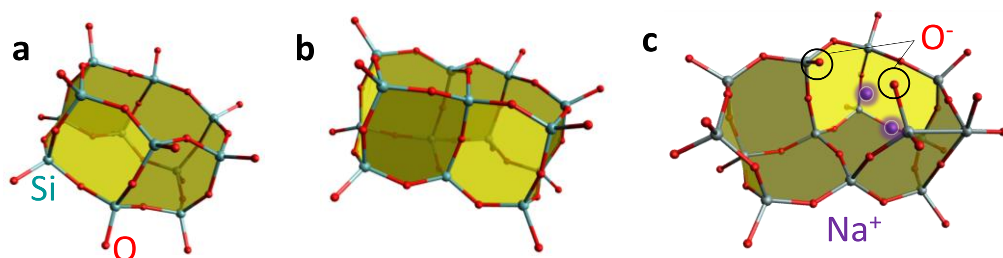

Figure 57. Molecular structure of (a) quartz, (b) fused silica, and (c) SDG glass.

The thermal poling of glass containing Na+ as a modifier, such as SDG, is explained in Figure 58 below. At temperatures above 100°C, the ionic mobility of Na+ is activated, which causes the drifting of ions towards the negative electrode (cathode) where they are neutralized by the electrons injected through the electrodes, when the electrodes are evaporated or sputtered onto the glass – usually known as *blocking electrodes* – or by negative OH^- residues when the electrode is not blocking for water – usually the electrode is a metallic piece located on top of the glass, usually known as *non-blocking electrodes*. The nature of the movement is based on thermal agitation and the potential differences across the glass. For further details about the fundamental mechanism, see ref. [198,199]. The diffusion mechanism is favored by the glass structure, where the silicon vacancies enhance the flux of Na^+, which drifts towards the cathode leaving a vacancy that will be occupied by the following Na^+. In this work, we are interested in applying a negative V_P as can be observed in Figure 58. However, if a positive V_P were applied, the phenomena would be the same, with the charges drifting towards the cathode on the bottom side of the glass. This displacement of charges along the glass propagates, creating a small current of ions. When the ions arrive at the cathode, they are neutralized into metallic sodium, Na_2CO_3 or Na_2O, which is deposited at the cathode-glass or cathode-air interfaces, depending on the type of electrode, and this is always observed as a white powder. As a consequence of the sodium migration and the absence of ions to substitute the sodium from the positive electrode (anode), a region with a negative charge is created, typically being several microns thick and located some microns below the anode. This is known as the depletion region [200,201].

The progressive increase in the thickness of the depletion region produces an increase in the potential difference (voltage) across the depletion region and a decrease in the potential difference (voltage) across the bulk of the glass. This process slows down with the reduction of voltage across the bulk and becomes stationary (i.e., an equilibrium and maximum poling are achieved) when the voltage is almost totally across the depletion region and equal to the external applied voltage. Finally, after the process, if the system cools down while applying the V_P,

the depletion region remains because the ions have lost their mobility and stay displaced inside the glass, creating a permanent internal electric field E_{IN} [200,201].

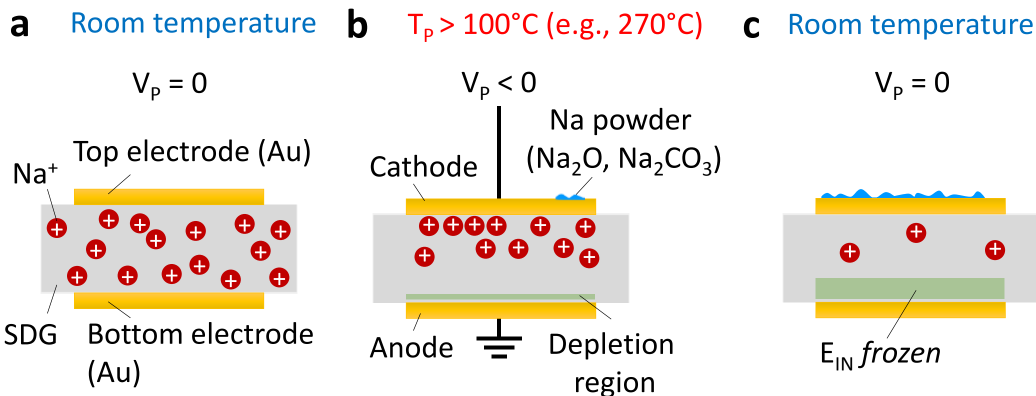

Figure 58. Thermal poling of SDG, where, at room temperature (RT) in (a), the Na^+ charges are distributed randomly along the whole glass area. At high poling temperatures e.g., 270ºC in (b), the V_P is introduced from the top electrode, drifting the Na^+ charges to the cathode where they are neutralized, forming a white powder. Simultaneously, a negative depletion region (green region in the pictures) is created. After completing the poling of the SDG and cooling down the system in (c), at RT again, V_P is removed and an electric field is frozen inside the glass, in the depletion region under the anode.

While at the beginning, the E_{IN} is constant along the glass, and can be calculated by:

$$V_P = E_{IN} \cdot t_G \quad \text{(Eq. 17)}$$

where t_G is the thickness of the glass, in this case of SDG, the formation of the depletion region alters its value.

The development of thermal poling models that consider the creation of the depletion layers allows the calculation of the depletion region thickness and the time required to achieve it [196,200,202]. In this thesis, the depletion region will be determined experimentally using Raman spectroscopy.

Previous work has demonstrated the poling effect on a wide variety of glasses containing different concentrations of impurities, such as SDG (14% wt. Na_2O) and Herasil, where the Na^+ concentration is much lower (approximately 10 ppm). According to these works, the huge differences in Na^+ concentrations produce different poling evolutions. A very important difference is the V_P applied between both glasses, with the one applied to SDG being smaller (approximately 1.4 kV) in order to avoid high currents that would cause thermal runaway and electric breakdown through the sample. Also, as it has been published, the ionic current should be limited to much below the miliampere scale in order to avoid the heating of charges by the Joule effect, which would cause an increase in

temperature at the depletion region, thus changing the breakdown value and altering the poling process [200].

Table 15 below collates data related to the poling of different glasses, highlighting parameters such as the type of glass, the temperature and the time of poling (t_P). In this work, we have decided to use SDG to achieve the poling effect with the most moderate V_P values, because other glasses, such as Herasil, typically require the application of 4 kV. Also, a very important advantage related to this type of glass is the lower cost compared to Herasil or fused silica substrates. In this work we use SDG samples diced into 1x1 cm^2 pieces with 1 mm thicknesses. For this SDG thickness, typical parameters reported in literature are T_P from 200 to 300°C, V_P from 1 to 2 kV and t_P from 5 minutes to 5 hours.

Table 15. State-of-the-art of glass thermal poling, highlighting the type of glass and thickness, and poling conditions, such as the temperature, voltage and duration of poling.

POLING PARAMETERS					REFERENCE
Glass type	**t_G (mm)**	**T_P (°C)**	**V_P (kV)**	**t_P (min)**	
Herasil	3	280	-	-	[203]
SDG	3	280	3 - 5	13 hours	[204]
SDG	-	210, 310	2.5, 1	30	[205]
Sol-gel	0.5	280	4	2 - 15	[206]
SDG	1	200, 250	1	60	[207]
SDG	1	230, 280	1, 2	5 - 50	[208]
Synthesized	1	230	2	30	[209]
SDG	1	210	1.5	40	[210]
SDG	1	250	0.1 - 1.7	-	[211]
Bulk	1	300	3	30	[212]
SDG	-	325	1	-	[213]
SDG	0.7	200	2	-	[214]

As will be later commented on, we perform the poling of the SDG at T_P of 270°C, at V_P of ±1.4-1.6 kV, and for t_P from 1 to 5 hours, depending on the doping level desired.

With this technique, we demonstrate that changing the polarity of the dielectric substrate by thermal poling, applying positive and negative V_P, changes the graphene doping into p- and n-type, respectively. Moreover, we show that a post-annealing step to the poled device can progressively erase the poling, thus modifying n_S until a change of doping is achieved, which demonstrates that the poling effect might be reversible. To this end, Hall measurements are performed in order to evaluate the change in n_S of the poled samples and those after heating

(after erasure of poling effect). The simultaneous measurement of R_S and n_S with temperature and time show the difference between the samples with and without poling treatments.

5.2. Sample preparation

5.2.1. Graphene transfer and annealing

Commercial CVD graphene samples (Graphenea) have been purchased, which have been grown on Cu foils and covered by PMMA. The graphene is then transferred to glass using the wet transfer method previously described in Chapter 1, section 1.1.5. Graphene transfer. After PMMA removal, the samples are annealed at 350ºC for 2 hours and under Ar: H_2 gases to get rid of the PMMA residues.

5.2.2. Graphene device fabrication

The target substrates chosen for this work are soda lime glass slides (Menzel-Glaser, Thermo Fisher Scientific), which have been diced into 1x1 cm^2 dimensions. According to the glass specifications, the chemical composition is 72.2% SiO_2, 14.3% Na_2O, 6.4% CaO, 4.3% MgO, 1.2% Al_2O_3, 1.2% K_2O, 0.3% SO_3 and 0.03% Fe_2O_3. As can be observed, the SLG also contains small percentages of other modifiers, such as Ca, Mg Al and K. In the following we will refer mainly to the displacement of Na due to its higher mobility and higher concentration, even though the displacement of other alkaline elements, such as Ca, can occur.

The fabrication procedure is explained in Figure 59. Initially, the glass slides are cleaned in an ultrasonic bath using acetone and isopropyl alcohol for 5 minutes in each solvent, followed by an O_2/Ar (50:50) plasma cleaning at 50 W for 3 minutes. After this, we separately perform two UV lithography steps by laser writer (LW405B, MICROTECH), the first one to fabricate the Hall bar pattern, while the second is devoted to making thicker contacts where the Hall probes will be located.

The device design can be observed in Figure 60 (a), where we have introduced two Hall bars in the same glass sample, with dimensions of length and width of 300 and 140 μm, respectively (W/L=0.47). The total area of the glass covered by the Hall bars is 5x5 mm^2. The reinforcement of the contacts is always necessary in order to avoid them breaking when the probes touch their surface. However, for this work in particular, we have had to design Au contacts with larger surface areas due to the probes moving slightly during the measurements, because of the sample heating.

For the lithography, a positive photoresist (AZ5214E, MicroChemicals) is spin coated on top of the glass and cured at 90ºC for 1.30 minutes. After the first lithography, we evaporate a thin layer of Ti (UNIVEX 350, Leybold, 2 nm) to increase the adhesion between the Au-glass and the Au (40 nm) for the Hall bar fabrication. After the second lithography, we directly evaporate the Au (100 nm) only onto the specific area of the contacts. After the Hall bar fabrication is completed, we proceed to transferring the graphene as described in section 5.2.1. Graphene transfer and annealing with an additional annealing step to get rid of the PMMA residues. Due to the graphene transferred area being much larger – typically 5x5 mm^2 – than the Hall bar, for easier handling during the transfer, a third lithography is necessary to etch the excess of the graphene by an O_2/Ar plasma using RIE (Reactive Ion Etching technique, Plasmalab System 100, Oxford Instruments).

Figure 60 (a) shows the pattern performed on the graphene during this step, with the white area corresponding to the graphene. The blue areas are the ones exposed to the RIE where the graphene has been etched. Thus, we have delimited the area of graphene to the Hall bar for proper measurements. However, we have left graphene on the rest of the sample in order to reduce possible issues arising during poling, such as dielectric breakdown. It is important to mention that the two Hall bars are completely independent due to the etching of the graphene in the middle of the sample. In order to avoid contamination to the graphene surface, and, consequently, a random alteration to the graphene doping, the device is encapsulated, depositing Al_2O_3 (40 nm) on top of the graphene for 3 hours, at 80ºC by ALD (Savannah, Cambridge Nanotech). For a better quality Al_2O_3 layer as demonstrated by [215,216], we first evaporate Ti (2 nm), which rapidly oxidizes over the whole sample. After that, we perform a fourth lithography to etch the Al_2O_3 deposited on top of the Au contacts, in order to avoid future issues during the Hall measurements. The etching is performed by dipping the samples in a buffered HF oxide etchant solution (BOE, HF: NH_4F, 1:7) for 1 minute. Finally, a fifth lithography step is carried out in order to deposit the top gold contact – Ti (2 nm, adhesion layer) and Au (100 nm) – where the tip to apply the V_P will be located.

As it can be observed in Figure 60 (a), the pattern of the Au contact touches the Au contacts of the Hall bar. In this way, the graphene will be contacted by the V_P and will adopt the role of top electrode during the glass poling process. Figure 60 (b) shows the real aspect of the device after the whole fabrication procedure. As can be distinguished, a square of Au – Ti (2 nm, adhesion layer) and Au (50 nm) – is also evaporated onto the opposite face of the glass, in order to enhance a homogeneous distribution of the E_{IN} during the poling of the glass.

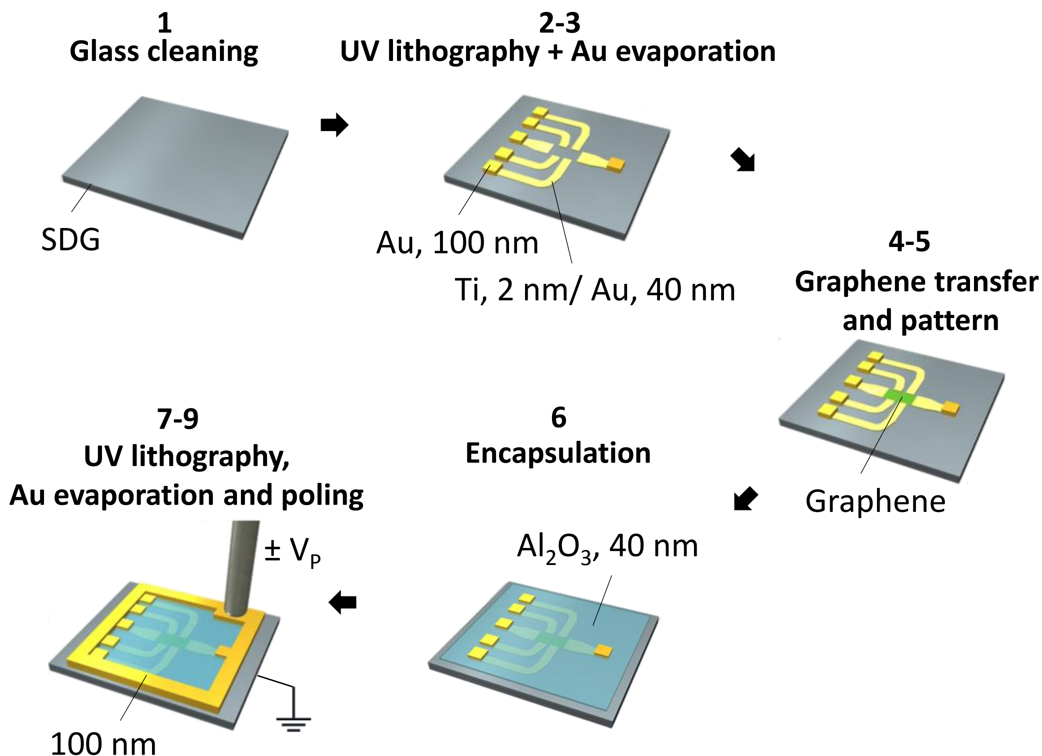

Figure 59. Procedure for the graphene device fabrication. (1) Initial cleaning of SDG by organic solvents and O_2 plasma. (2-3) Two UV lithography and evaporation of the metal contacts - the first one for the Hall bar and the second to increase the thicknesses of the contacts. (4-5) Graphene transfer by wet etching process and post-annealing. A third lithography for graphene patterning to the Hall bar area, removing the excess by RIE. (6) Encapsulation of the graphene device with Al_2O_3 by ALD deposition. (7-9) A fourth lithography to remove the Al_2O_3 from the top of the Au contacts by dipping the samples into a BOE solution. A fifth lithography to evaporate the top Au contact that will serve to apply the V_P with the poling set-up. For the electrical measurements, the top electrode (or, at least, the small connections that contact it to the device) needs to be removed using an Au etchant.

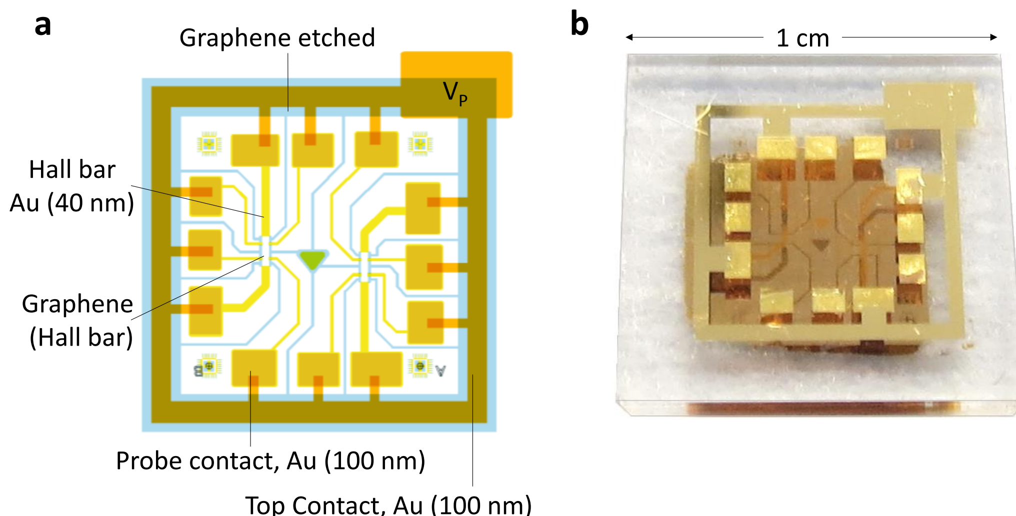

Figure 60. (a) Device pattern for performing the five lithography steps, highlighting the design of each structure – Hall bar, thicker Au contacts for Hall probes location, areas where graphene is etched and top Au electrode for V_P application. (b) Optical image of the graphene device on glass after the whole fabrication procedure.

5.2.3. Thermal poling of the glass

The SDG is poled inside a vacuum oven (Heraeus VT6060P, ThermoFisher Scientific) that allows the application of a voltage. Figure 61 (a) describes the circuit of the experimental set-up where an external DC supply is connected to the oven where the sample is located. A high resistance is connected in series to the device in order to monitor the current that will be generated in the glass due to the displacement of the ions. Figure 61 (b) shows the real set-up used for performing the glass poling inside the oven. A cable can be observed connecting the external DC supply to the metallic tip that will connect to the device. The piece where the tip is introduced contains a spring that allows the tip to be fixed to the graphene device, thus preventing its movement. For proper control of the glass poling, it is necessary to include a metallic surface below the device that is smaller than the metallic plate of the oven. Both metallic surfaces are separated by an insulator, but connected with a ground cable. The image on the right clearly shows the connection between the metallic tip and the top Au contact of the graphene device. The poling conditions are T_P of 270ºC, t_P from 1 to 5 hours (depending on the doping level to be achieved) and at 800 mbar under N_2 to avoid breakdown in air.

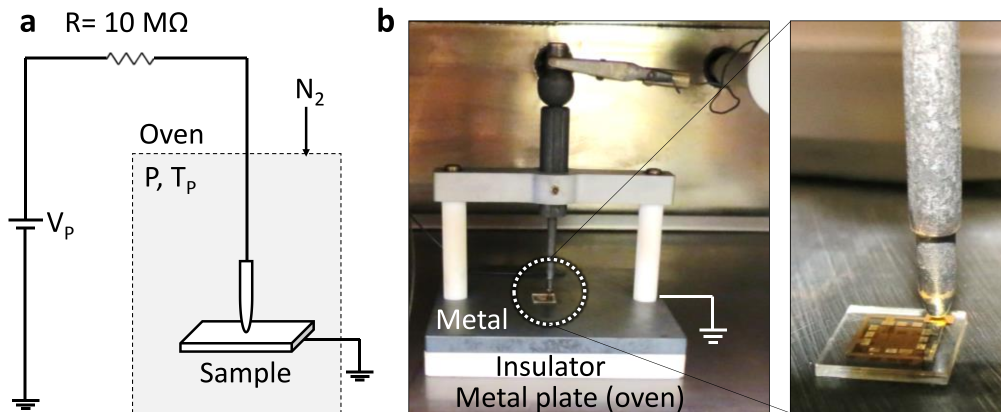

Figure 61. Description of the poling set-up. (a) Scheme showing the electric circuit where V_P is applied to the sample located inside an oven under certain pressure and temperature conditions. (b) Optical image of the inside of the oven, showing the set-up used for connecting the glass sample to V_P voltage supply. A cable coming from the outside DC supply is connected to the metallic tip. , which will apply V_P to the graphene device through the top Au electrode. The image on the right shows the connection between the tip and the top Au contact of the graphene device.

5.2.4. Electrical measurements

The electrical measurements have been previously explained in Chapter 1, section 1.2. Characterization techniques. After glass poling, four-point probe and standard Hall measurements are performed in order to obtain the R_S, and the n_S and μ_H, respectively. After the first characterization, we perform the Hall measurement combined with in situ monitoring of the R_S using five probes. Thus, the simultaneous changes to the R_S, n_S and μ_H are obtained over time as the temperature is progressively applied to gradually erase the poling effect. A LabView® code has been developed in order to control the parameters of the AC and DC currents introduced into the device and the modification of B at each Hall measurement, and to register the measured values of the R_S, V_H, time and temperature of the device.

In section 5.3. Thermal poling of SDG and calibration below, we will firstly demonstrate the successful poling of SDG in the absence of a graphene device. After that, we will show a slightly modified version of the set-up (with the addition of a thin Kapton layer below the glass for further control of the current) when the graphene device is fabricated on top of the glass. Finally, we will demonstrate the different behavior of graphene R_S and n_S in three cases: when the glass has not been poled, when it has been poled with a positive V_P and when poled with a negative V_P. For the poled samples, we will show the initial n_S measured after poling and its evolution toward opposite doping type when poling is erased using temperature increase.

5.3. Thermal poling of SDG and calibration for the introduction of the graphene

Initially, we perform the thermal poling only of SDG, in order to characterize it for combining with the graphene device later on. As previously discussed, the poling conditions are selected according to literature, where typically the T_P is from 200 to 325ºC, the V_P from 1 to 2 kV and the t_P from 5 to 60 minutes. In this work, we have established the optimum conditions, for T_P about 270ºC, V_P is ±1.4-1.6 kV, and t_P is within 1 to 5 hours range, depending on the desired doping level.

Figure 62 (a) shows the sample used to demonstrate the SDG poling. Two Au electrodes (50 nm thickness), with Ti (2 nm) as an adhesion layer, are evaporated onto both faces of the glass to enhance the formation of a homogeneous electric field inside the glass. As explained previously in section 5.1. Introduction, after the sample is located inside the oven, contacting the metallic tip with the sample (as shown in Figure 61 above), the temperature of the oven is increased to 270ºC in N_2 atmosphere at V_P=0. Once the T_P is achieved, the V_P is progressively applied in order to avoid the thermal runaway of the charges (and consequent high peak of current and non-stable poling process) that would occur if it were applied at very high speed. The Na^+ charges drift towards the cathode, and, in the case where V_P <0, such as in Figure 62 (a), the top side of the glass.

The creation of the depletion region on the bottom side of glass close to the anode can be observed. If a V_P >0 were applied, the drifting of the Na^+ charges would occur in the opposite direction, towards the cathodic bottom side of the glass, with the depletion region being created at the anodic top side. The poling conditions for the sample shown in Figure 62 (a) are: T_P=270ºC, V_P= -1.6 kV and t_P=5 hours, 800 mbar in N_2 atmosphere.

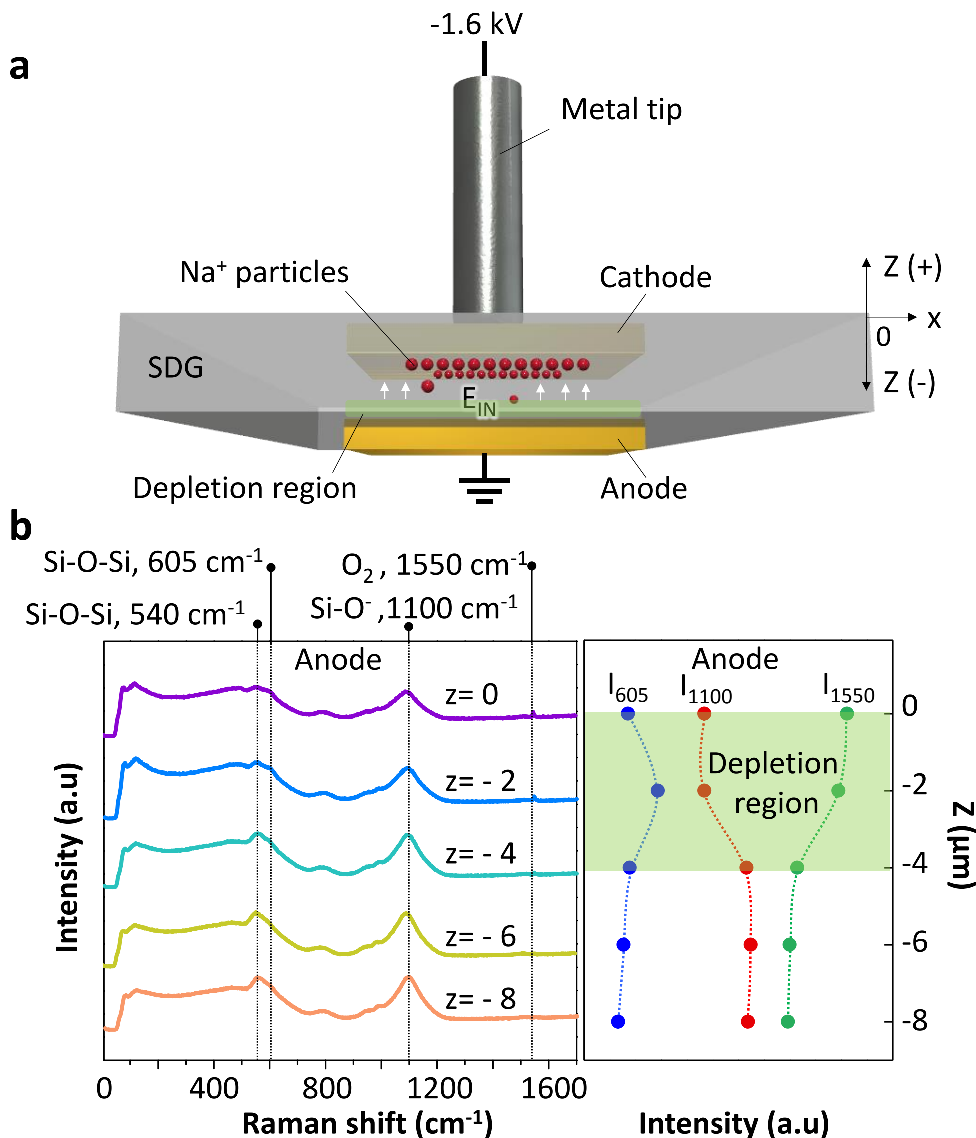

Figure 62. Thermal poling of glass at 270ºC, applying a V_P of -1.6 kV for 100 minutes. (a) Scheme showing the drifting of Na^+ charges towards the cathode (top side of the glass). The figure highlights the lines of the created electric field and the depletion region formed close to the anode. (b) Raman is performed on the anode face measuring from the glass surface (Z=0) to a distance of 8 µm inside the glass (Z= - 8 µm). The poling is confirmed by the detection of two weak peaks at 605 and 1550 cm^{-1}. The disappearance of both peaks when measuring deeper into the glass confirms a depletion region thickness of about 4 µm.

In accordance with ref. [210,211], the poling effect on the glass can be detected by Raman, and, very importantly, this allows the experimental measurement of the depletion region thickness. Typically, SDG exhibits two peaks, the first one occurring at 540 cm^{-1}, with a broad shoulder at around 450 cm^{-1}, both being related to the stretching and bending vibrational modes of the Si-O-Si bridges in the glass. The second typical peak for SDG is detected at 1100 cm^{-1}, which is related to the non-bridging bonds Si-O^{-} - see Figure 57 (c). After thermal poling of SDG, the Raman measurement on the anodic face of the glass, which corresponds to the side where the depletion region has been created, provides different spectra when it is measured exactly at the poled surface (at Z=0) and when it is measured progressively deeper in the glass. In the latter case, it is measured in steps of 2 μm, up to a maximum of 8 μm (at Z=-8 μm), where the typical Raman spectra of non-poled SDG is observed. The results obtained from our sample in Figure 62 (b) are consistent with ref. [210,211], where the spectrum differences that can be found between the poled surface (at Z=0) and the one corresponding to non-poled glass (at Z=-8 μm) are discussed below.

Firstly, when measuring on the poled surface of the glass – the anodic face – lower intensities of the peaks at 540 and 1100 cm^{-1} are observed and there is a wider shoulder of Si-O-Si stretching-bending bands, with a tiny peak at 490 cm^{-1}. However, the most determinant peak to confirm the poling effect is the weak shoulder appearing at 605 cm^{-1}. This and the one at 490 cm^{-1} are attributed to the symmetric stretching vibration of Si-O-Si bridges in three and four-member rings of SiO_4 tetrahedron, respectively. Moreover, a weak but noticeable peak appears at 1550 cm^{-1}, which is exclusively in the depletion region, and this is attributed to molecular oxygen dissolved in the glass matrix during the glass synthesis [217]. When the measurements are performed deeper in the glass, both peaks at 605 and 1550 cm^{-1} are detectable until approximately Z=-4 μm. This can be clearly observed in the graph on the right of the Raman spectra, where the intensities of the most interesting three peaks – at 605, 1100 and 1550 cm^{-1} – have been plotted at the different heights in glass. As previously mentioned, the intensity peaks at 605 and 1550 cm^{-1} are high but decrease at 4 μm. This can be translated into the experimental measurement of a depletion region thickness of about 4 μm.

The thermal poling of SDG is also visually confirmed by the deposition of a white powder on the cathode, as described in Figure 58 (b-c). According to ref. [208], the Na^+ displaced at the cathode reacts with CO_2, forming Na_2CO_3. For the SDG poled sample shown in Figure 62, we have performed Raman measurements on the white powder deposited on the cathode side of the glass, observed with the optical microscope (Figure 63 (a)). Raman data are collated in Figure 63 (b), showing the presence of Na_2CO_3 by an intense and narrow peak at 1076 cm^{-1} for both, when the current through the glass is not limited (as is the case for the sample in Figure 62), being 400 μA, and also when the current is limited to 50 μA.

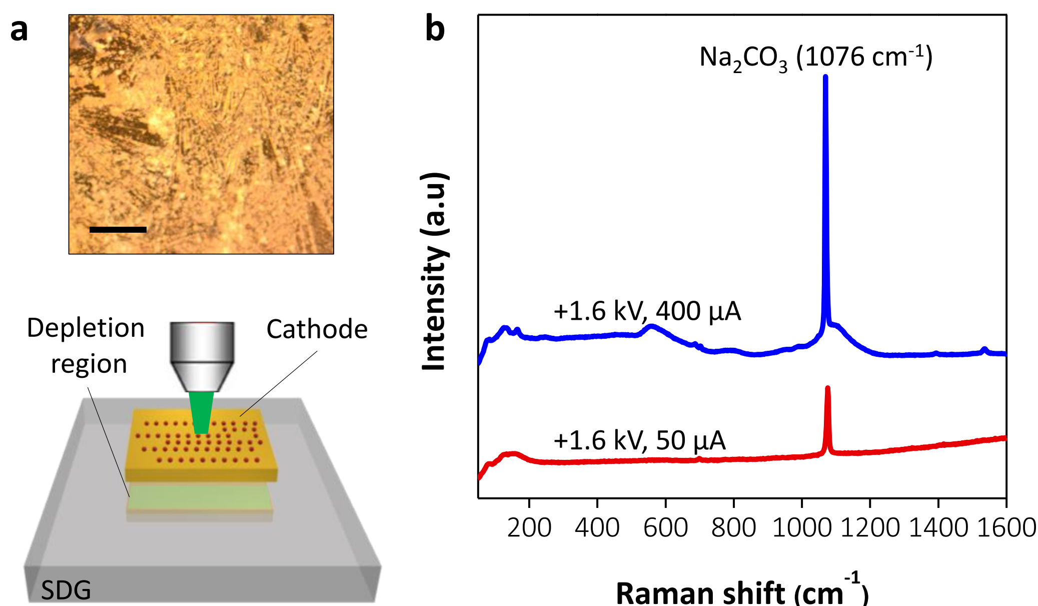

Figure 63. Na_2CO_3 formation at the cathode after the thermal poling of SDG. (a) Optical microscope image of the cathode showing white particles, which correspond to the Na^+ charges that have been neutralized into Na_2CO_3, and damaged areas. The bottom scheme shows the cathode face where the optical image and Raman in (b) have been measured. The depletion region that forms close to the anodic face (bottom) of the SDG is highlighted. (b) Raman spectra measured on the sample previously shown in Figure 62 (top, blue) where the current was not limited, and to a sample where the current was limited to 50 µA (bottom, red). Both spectra show an intense peak at 1076 cm^{-1} is detected, corresponding to Na_2CO_3. Scale bar: 100 µA.

As previously discussed, we are more interested in building the graphene device on the cathode face of the glass in order to take advantage of the highly positive charges that accumulate close to the surface, which provide a high level of doping to the graphene. However, because of Na_2CO_3 being deposited onto the glass surface, it is necessary to optimize the poling conditions for the SDG with graphene transferred onto it, in order to try to reduce the effect of Na_2CO_3 (if graphene does not completely block CO_2), Na_2O (oxidation) or Na (if electronic neutralization occurs). These compounds might otherwise damage graphene. Figure 64 (a) shows the SEM characterization of the previous sample cathode as indicated by the scheme on the bottom side. The cathode surface where the poling has been performed has a non-homogeneous surface. We have performed high resolution SEM images and EDX measurements on different areas of the sample where different morphologies can be observed (1-4), which are shown in Figure 64 (b).

The measurement on *area 1*, close to the edge of the Au electrode, shows a big difference between the poled and non-poled regions. EDX measurement on

the non-poled area, denoted by a circled-dashed line, show only Si and O belonging to the substrate.

The measurement on *area 2*, close to the center of the cathode, reveals the formation of compounds that have been passed through the Au electrode. EDX measurements detect the substrate contribution, but in this area also Au is detected - belonging to the electrode- and Na. The presence of the latter demonstrates the neutralization of the charges on the cathode.

The measurements on *areas 3* and *4* are especially interesting as they reveal the formation of two specific compounds of Na, which, according to the EDX measurements, could be related to Na_2CO_3 and Na_2O, respectively. In both cases, the Na is detected when measuring on the formed compounds, but the Si belonging to the substrate is not detected. This fact confirms the formation of Na compounds on the surface of the cathode.

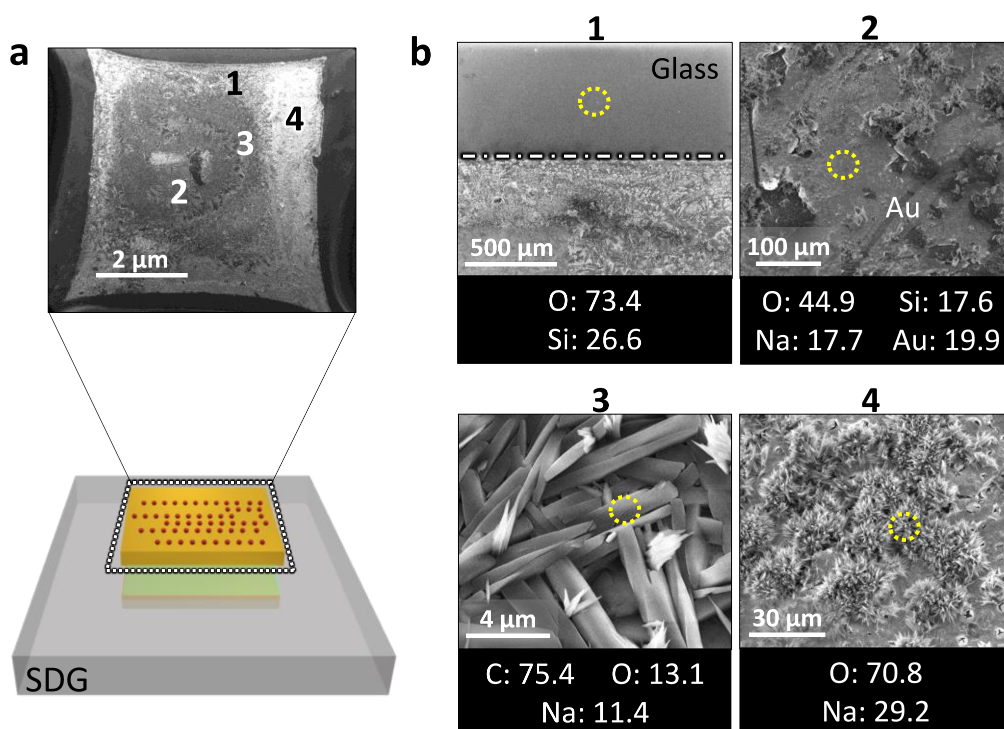

Figure 64. SEM and EDX measurements performed on the cathode area of the glass. (a) Scheme of the sample and SEM of the poled area of the cathode. (b) SEM and EDX performed on four different areas of the cathode, where the formation of compounds with Na are detected.

As previously mentioned, due to the formation of sodium compounds, it is necessary to optimize the poling of the SDG in the case where graphene is transferred onto it, as the release of Na will damage the graphene. To this aim, we have built samples similar to that shown in Figure 62 (a), but with the Au top electrode this time being a frame onto which the graphene is transferred. In order to evaluate the poling performed on the SDG, we monitor the V_P applied to the sample and the current (I) generated through the glass due to the Na^+ displacement.

Figure 65 (a) shows the poling process for the conditions used in the sample in Figure 62, where the V_P is -1.6 kV and the current, whose maximum value is 400 μA, has not been limited. It can be observed that the current immediately increases very quickly compared to the V_P, which has been applied slowly in order to avoid thermal runaway of the Na^+ charges. The current achieves a maximum and after 12 minutes, approximately, it starts to decrease. The phenomenon occurring here is that after the V_P is applied, the displacement of charges starts, which is translated in the measurement of the current. At the same time, the depletion region is created and keeps growing in thickness until the current starts to decrease after 20 minutes. At this point, the voltage across the depletion region created inside the glass is equal to the external V_P. The shoulder observed in the current curve at 70 minutes is due to the cooling down of the system while the V_P is still being applied, with the current being 72 μA. The reason for this is that the decrease in temperature reduces the mobility of the charges that are still moving. After the whole poling procedure, Raman confirms that the graphene is broken, being unable to detect the G and 2D peaks (without measuring the R_S). Further optimization is performed, limiting the current to 50, 10 and 5 μA, with damage to the graphene being observed in all the cases due to the Na release. However, as demonstrated in Figure 66, damage also occurs to the graphene if V_P is positive (+1.6 kV) and the Na is released on the opposite face. Figure 66 (a) shows the optical image of a graphene device after poling without current limitation, where it can be observed that both the Au Hall bars and the graphene are damaged after the process. In Figure 66 (b), the Raman performed on the device shows the typical graphene peaks before poling the SDG, while after poling none of these are detected. However, the detection of the peak at 605 cm^{-1} confirms the poling of the SDG.

For a more accurate limitation of current, we introduce a thin layer of Kapton (25 μm + adhesive) between the sample and the set-up, reducing the maximum current to 370 nA. Under these moderate current conditions, the graphene properties are successfully preserved when the V_P has either a positive or negative value. Figure 65 (b) shows the current generated after the application of a negative V_P, which achieves a maximum of 370 nA and decreases after 20 minutes of poling, as in the case without limitation to the current. A shoulder can be observed at 2 minutes, where the current achieves a value of 227 nA, stabilizes for approximately 5 minutes and then increases again to 370 nA. We believe that this

is related to the adhesive layer of the Kapton. For a further understanding of this artifact, we perform experiments changing the intermediate layer to Kapton without adhesive and the shoulder in the current curve disappears. Although the graph shows the poling for 1000 minutes, the experiment continues for approximately 26 hours, in order to record the whole current decrease to 10 nA, after which we cool down the system.

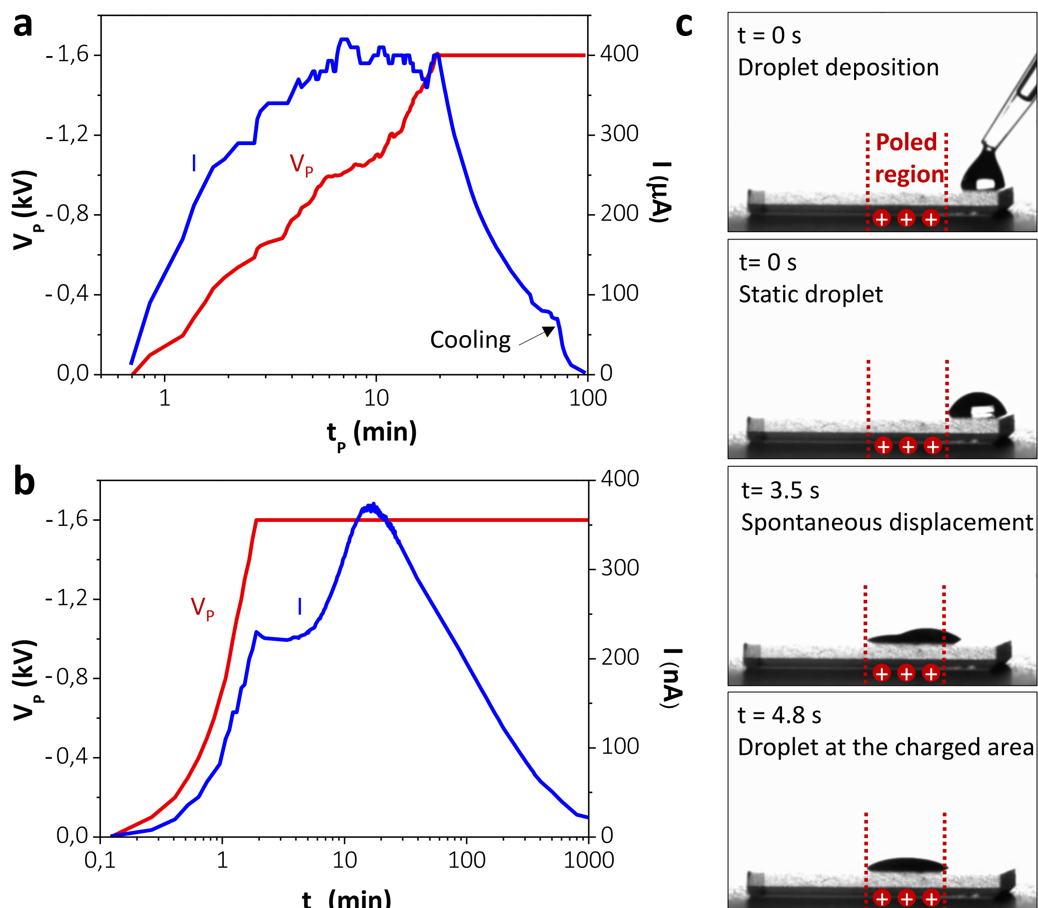

Figure 65. Optimization of thermal poling of SDG when the graphene is deposited on the top face of the glass. (a-b) Monitoring of V_P applied for the poling and I created in the glass due to the Na^+ displacement. (a) Poling of SDG under the same conditions as the sample poled previously in Figure 62, where the V_P applied is -1.6 kV at 270ºC, for 100 min without controlling I, whose maximum value is 400 µA. (b) Conditions are optimized for the introduction of graphene on the top face of glass, where the poling conditions are constant, with a longer poling time due to the current limitation and the use of a Kapton layer between the glass and the set-up. The maximum current is approximately 370 nA. (c) Contact angle measurements demonstrate a change in the surface charge by spontaneously displacing a water droplet from the external side of the glass to the area where the poling of SDG has been performed.

If both procedures are compared, the current achieved in the former – Figure 65 (a) - is much higher, thus causing a stronger poling effect on the SDG, which is confirmed by the poling and Na_2CO_3 detection by Raman. In the case of Kapton, a lower current is achieved through the glass (approximately 1000 times less), which is translated into a moderate poling of the SDG. Because of this, the poling effect cannot be detected by Raman (peak at 605 cm^{-1}) and Na is not observable on the cathode. However, a very simple procedure, such as the contact angle characterization, serves to verify if the surface charge of the glass has been altered. This is represented in Figure 65 (c) where a water droplet is deposited close to the edge of the glass, and after 3.5 seconds it spontaneously moves towards the region where the thermal poling of the glass has been performed. Moreover, if the droplet if observed from above, it can be seen how its shape is modified to the square shape of the electrode used in the poling of the SDG. The use of this simple technique serves to indicate the success of the glass poling under soft conditions.

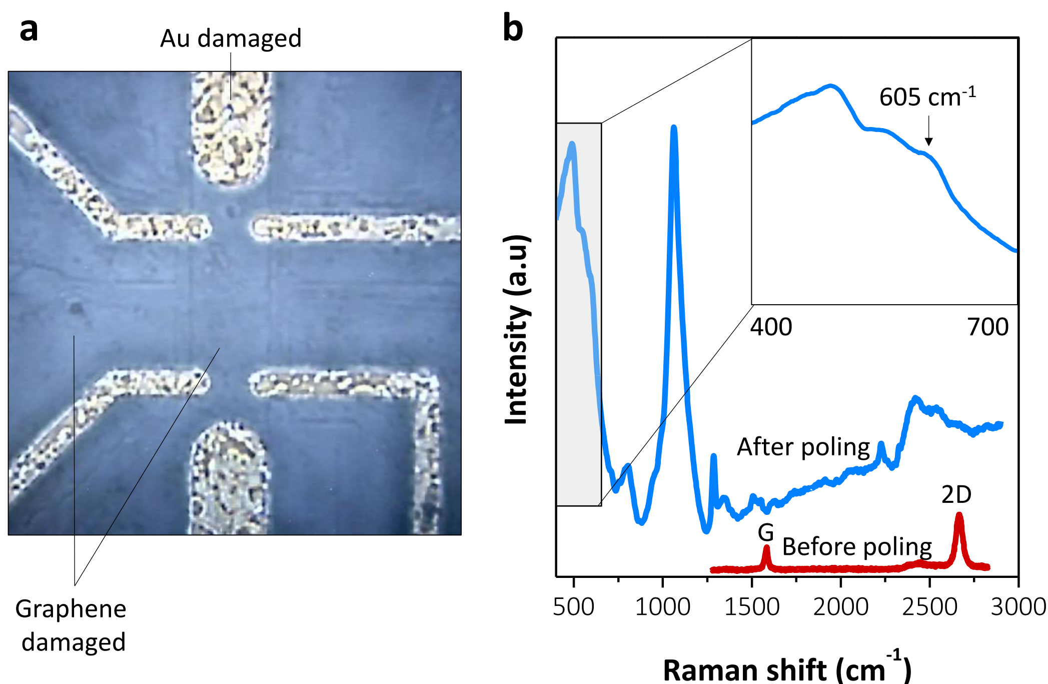

Figure 66. Thermal poling of a graphene device, at V_P of +1.6 kV, without current limitation. (a) Optical image of the Hall bar of the device where both the Au contacts and the graphene in the middle can be seen to be damaged. R_S measurements are not possible on this device. The damage to the graphene after poling is confirmed by Raman in (b), which is performed on the Hall bar before (red, bottom line) and after (blue, top line) poling. After poling, the detection of the peak at 605 cm^{-1}, and the absence of the G and 2D graphene peaks (which can be detected before poling) confirm the damage to the graphene device and the need to control the current.

A successful optimization of the SDG thermal poling when the graphene device is built onto it allows us to better understand R_S, n_S and μ_H changes under varied poling conditions, and the graphene behavior when it is deposited onto a non-poled substrate. We will discuss these results in the following section, demonstrating the change in the graphene doping depending on the charge of the V_P.

5.4. Effect of SDG thermal poling on graphene doping

For a clear understanding of the effect of thermal poling of SDG on graphene doping, firstly, we will measure n_S of a graphene device built onto a non-poled SDG and its response after thermal treatment (section 5.4.1). Secondly, we will study the response of a graphene device built onto a thermally poled glass at negative V_P (-1.6 kV), and, finally, when applying a positive V_P (+1.2 kV).

5.4.1. Graphene device response onto a non-poled SDG

After fabricating the graphene device onto a non-poled SDG following the procedure described in section 5.2.2. Graphene device fabrication above, Hall measurements are performed in order to evaluate R_S and μ_H evolution with temperature. Figure 67 (a) shows the variation in R_S when the temperature is increased from RT to 280ºC, in steps of 50ºC, and later decreased to RT again. The typical behavior of a conductive layer exposed to heat can be observed, firstly with the R_S increasing gradually with temperature, due to the enhancement of electron collisions in the material (which reduce its conductivity) and, secondly, with the R_S decreasing once the sample is cooled down.

For a better understanding of R_S results, Figure 67 (b) represents the variation in R_S at each temperature step – with the R_S being the mean value calculated for each step where the temperature is held constant – highlighting the values measured during the heating (bottom, red line) and cooling (top, blue line) of the sample. As can be observed, the R_S gradually increases until the maximum temperature is achieved, immediately decreasing when the sample is cooled down. Although the cooling down trend of the R_S shows hysteresis, the R_S finally returns to almost its initial value, being 1.23 kΩ/sq. Figure 67 (c) shows the calculated μ_H during the heating of the sample. The two initial measurements in grey are approximate due to a non-stable measurement of the ns. However, from 100 to 300ºC, the μ_H strongly decreases from 1400 to 400 $cm^2/V{\cdot}s$ for a nearly constant hole carrier density, whose mean value is 3.13×10^{12} cm^{-2}. The graphene p-doping achieved is consistent with literature, as the glass charge is potentially negative due to the deprotonated SiOH groups on the surface. According to the results, the change in R_S is purely a thermal effect and not related to a doping change. The

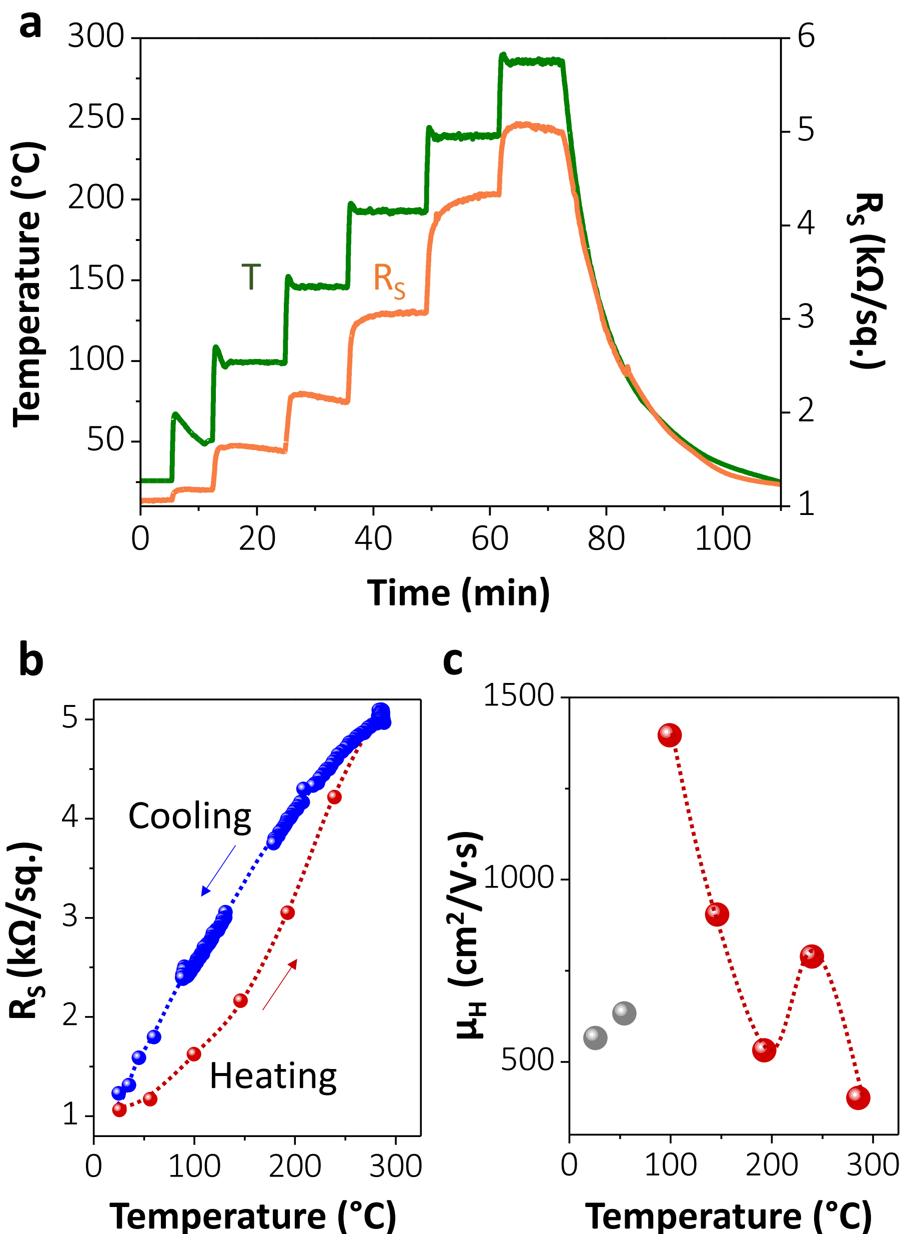

Figure 67. Electrical measurements performed on a graphene device built onto a non-poled SDG. (a) Evolution of R_S (orange line) when temperature is increased from RT to 280ºC in steps of 50ºC (green line). R_S gradually increases and decreases following the temperature trend, which corresponds to the normal behavior of a conductive layer exposed to temperature. (b) R_S variation with temperature during the heating (red line) and cooling (blue line) of the sample. (c) Mobility variation during the heating of the sample (red bubbles). The two former values in grey are approximate as measurements at these temperatures are not stable. From 100-300ºC, the μ_H strongly decreases for a nearly constant hole carrier density of 3.13 x 10^{12} cm^{-2}. The dotted lines in (b) and (c) act as guides for the eye.

decrease in mobility with temperature can be explained in ref. [97], as the graphene becomes conformal to the glass surface, allowing its reaction with oxygen.

5.4.2. Graphene device response onto a poled SDG with $\pm V_P$

As we initially discussed, we are more interested in building the device on the cathode's face in order to take advantage of the strong positive charges accumulated close to the surface of the SDG. However, as will be shown below, we will demonstrate the poling contribution to the graphene doping for both cases, i.e, when $\pm V_P$ are applied.

Before that, we want to calculate the charge (Q) that has been displaced during the thermal poling of the SDG, thus taking into consideration the current curve obtained in Figure 65 (b) for an electrode area of 25 mm^2.

Figure 68 (a) below shows the evolution of Q over time, where Q has been calculated using the following equation:

$$Q = \int_{to}^{t} I \cdot dt \qquad \text{(Eq. 18)}$$

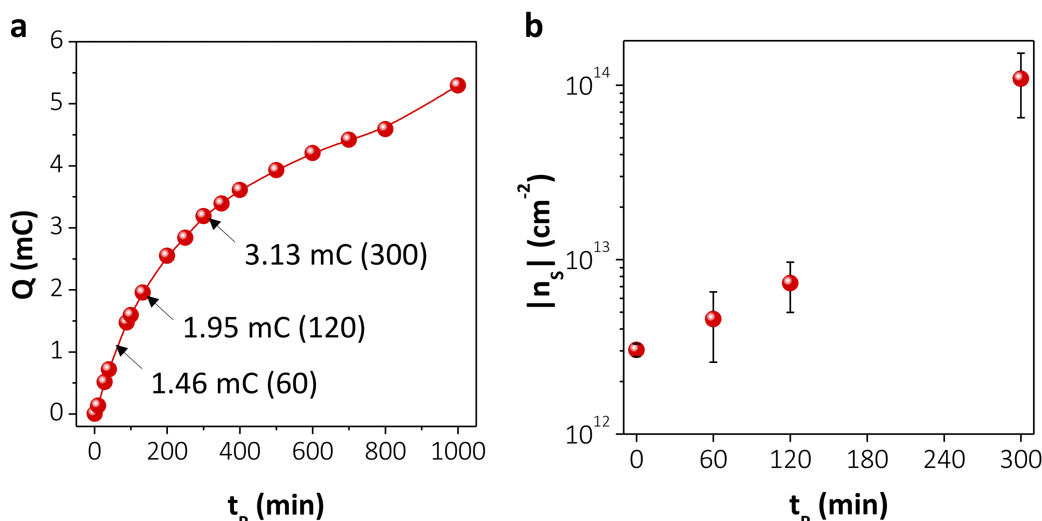

Figure 68. Influence of poling time on graphene doping. (a) Calculation of the charge displaced inside the SDG at different poling times using Kapton for current limitation and -1.6 kV. Data for Q are calculated from the current curve in Figure 65 (b) for an electrode area of 25 mm^2. (b) Summary of the absolute value of n_S for the graphene devices, whose substrate has been poled for different lengths of time at 270ºC and applying $\pm$ 1.6 kV. This shows a huge difference between the n_S for the non-poled SDG (t_P=0) and for the SDG poled for 300 min (t_P=300), with each having mean values of $3x10^{12}$ and $1.4x10^{14}$ cm^{-2}, respectively.

Although the trend is initially linear, the increase in Q slows down after 200 minutes. The increase in Q over time is related to higher doping levels in the graphene, as represented in Figure 68 (b). Here, the results obtained for the graphene devices that have been poled for 60, 120 and 300 minutes are summarized. The doping levels increase with time independently of the carrier density type (n- or p- doping; note that n_S is an absolute value). Thus, a huge change in graphene doping is observed when comparing the values obtained for non-poled SDG (t_P=0) and the samples that have been poled for 300 minutes, with mean n_S values of 3 x 10^{12} and 1.4 x 10^{14} cm^{-2}, respectively.

After evaluating the influence of t_P on the achieved doping, we include two samples that have been poled for different lengths of time – 2 hours and 1 hour – applying a negative and a positive V_P, respectively. While we demonstrate the change in graphene doping in both cases, we also show in detail the ns and mobility change during the whole procedure for our most interesting case, when the V_P is negative and the Na is displaced towards the cathode, which is the face where the graphene device is located.

When a *negative* V_P of -1.8 kV is applied for 2 hours to the SDG, as expected, the graphene is electron doped with a mean value of -1 x 10^{13} cm^{-2}. As previously discussed and shown in Figure 69 (a), the reason for this is that the displacement of the Na ions towards the cathode, which is the SDG surface where the graphene device is located, provides a strong positive charge to the substrate.

In order to evaluate the reversible behavior of the graphene device when the thermal poling is progressively erased, we heat up the sample in steps, simultaneously measuring the R_S and the n_S. Figure 69 (b) shows the evolution of R_S when the sample is heated from RT to 200ºC, and then cooled down again to RT. In this situation, the behavior of R_S is very different to the case where the SDG has not been poled - Figure 67 (a). Here, the high R_S immediately decreases after only increasing the temperature to 50ºC, demonstrating that the Na^+ at this low temperature starts to have mobility. If the temperature is further increased to 150ºC, R_S decreases to a minimum value of 250 Ω/sq. This value is constant until the end of the process, with the temperature being increased to a maximum of 200ºC and then decreased to RT. This variation is best observed in Figure 69 (c) where the heating and cooling steps can be distinguished.

Figure 69 (d) very clearly shows the change in graphene doping before and after the temperature treatment, where the poling is achieved and eventually erased, respectively. Due to the poling effect, the sample initially has electron doping – n type – which progressively changes as the temperature is increased. This is because heat once more allows the mobility of the Na particles that are accumulated on the top side of the SDG, and close to the graphene device. These particles move over the whole SDG, causing the p-doping to re-occur. The doping type changes at

approximately 60ºC and a maximum p-doping is achieved at 155ºC, after which it decreases again and remains practically constant until the sample is cooled down. The overall change in n_S before and after erasing the poling effect is from -1.4x10^{13} to 3.2x10^{13} cm^{-2}. Figure 69 (e) shows the evolution of the calculated μ_H over the whole process. Similarly to the situation with graphene on a non-poled SDG - Figure 67 (c) - an increase in μ_H can be observed when the temperature is raised from 50 to 100ºC, after which it decreases again due to the high doping level measured at 150ºC. After that, it increases when the temperature is raised to the maximum 200ºC, but then decreases when the sample is cooled down again, recovering its initial value (500 $cm^2/V\cdot s$).

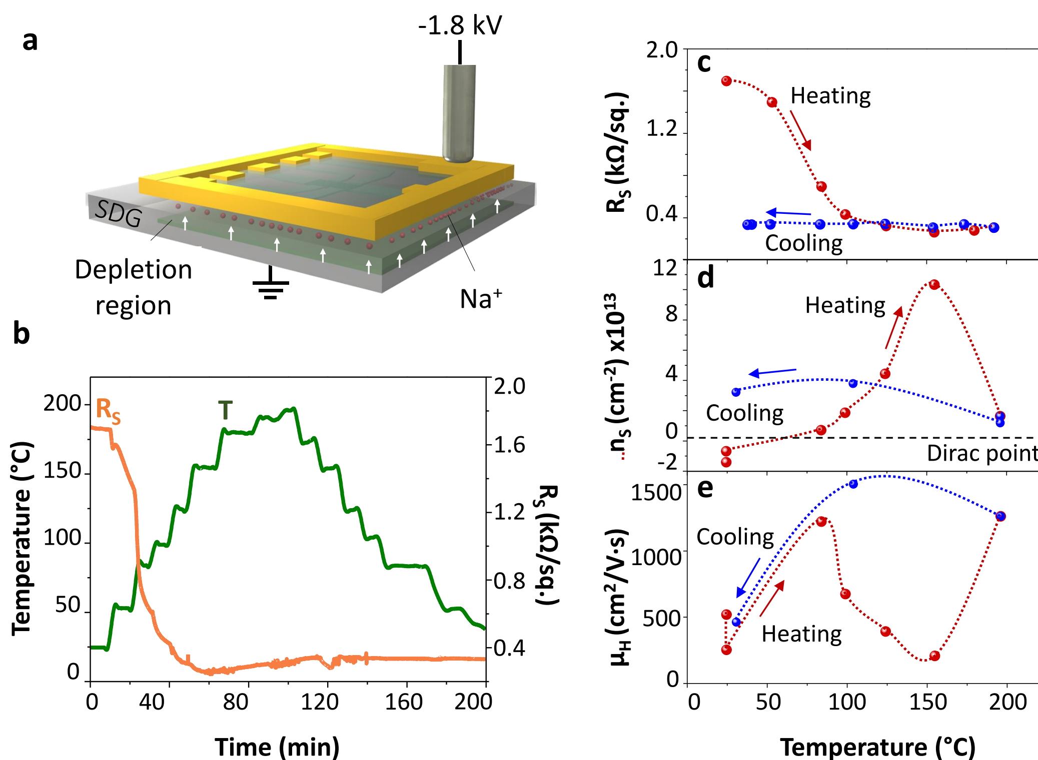

Figure 69. Graphene device response after SDG poling at -1.8 kV for 2 hours. (a) Scheme of the sample indicating (with white arrows) the displacement of the Na particles towards the cathode, the SDG face where the graphene device is located. (b) R_S (orange line) evolution with temperature, which is increased from RT to 200ºC (green line). R_S decreases after 10 minutes as the temperature is increased. After one hour, a minimum R_S of 250 Ω/sq. is achieved, which is fairly constant until the temperature decreases to RT once more. (c) R_S variation with temperature, showing a huge decrease from 1.7 kΩ/sq. to 250 Ω/sq. (d) n_S variation with temperature, where the graphene doping changes after erasing the poling effect (from n- to p-type). (e) μ_H variation with temperature, showing an increase at 100ºC and 200ºC, returning to its initial value after cooling down the sample. In (c-e) the data are plotted separately for heating (red bubbles) and cooling (blue bubbles) the sample. The dotted lines are guides for the eye.

From the above, we can conclude that the poling effect changes the doping and is reversible. Moreover, we have demonstrated that its progressive erasing modifies the doping back to the glass' original values without damaging the device, as the mobility remains the same at the end of the whole procedure.

Finally, when a *positive* V_P of +1.2 kV is applied to the SDG for 1 hour, as expected, the graphene is hole doped with a mean value of 3.5 x 10^{12} cm^{-2}. As previously discussed and shown in Figure 70 (a), the reason for this is the displacement of the Na charges towards the cathode, which is on the opposite surface to the graphene device.

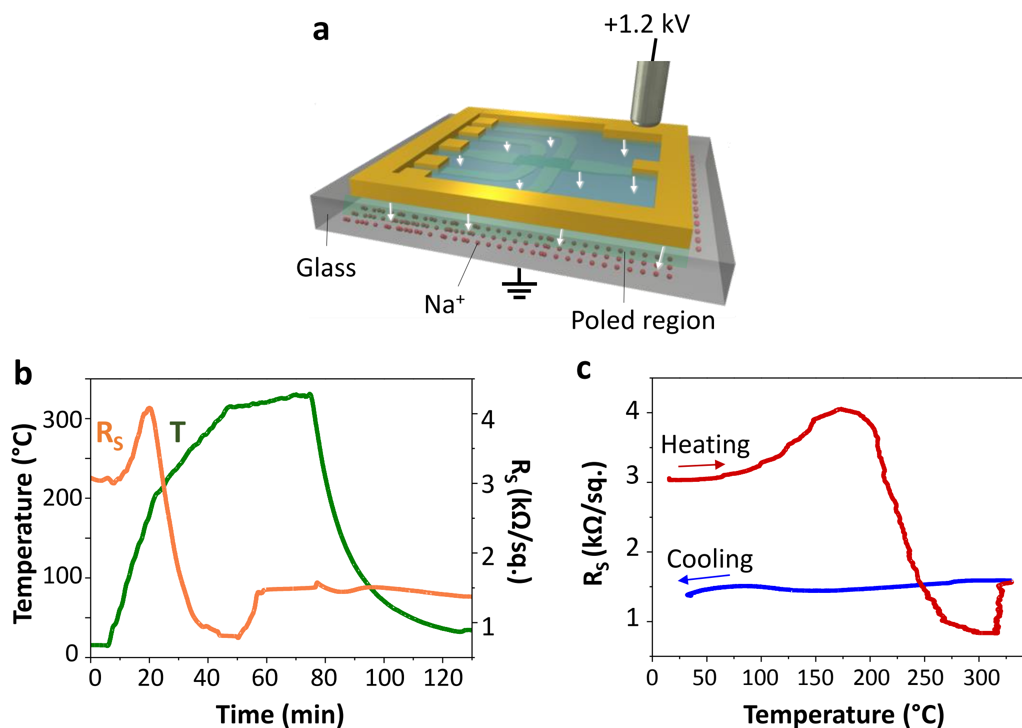

Figure 70. Graphene device response after SDG poling at +1.2 kV for 1 hour. (a) Scheme of the sample, indicating (with white arrows) the displacement of the Na particles towards the cathode, the opposite face to where the graphene device is located. (b) R_S (orange line) evolution with temperature, which is increased from RT to 320ºC (green line). R_S increases slightly until it starts to decrease after 20 minutes as the temperature is increased. After 50 minutes, a minimum R_S of 807 Ω/sq. is achieved, which then increases and remains constant until the temperature is again decreased to RT. (c) R_S variation with temperature, showing a huge decrease from 4 kΩ/sq. to 807 Ω/sq. and a constant value of 1.4 kΩ/sq. as the sample is being cooled. The data are plotted separately for heating (red line) and cooling (blue line) the sample. The measurements before and after the thermal treatment demonstrate a change in n_S from p- to n-type, with values of 3.5 x 10^{12} and -3.42 x 10^{13} cm^{-2}, respectively.

The presence of the negative depletion region close to the graphene induces its p-type doping. Here, the R_S increases and then, after 20 minutes, immediately decreases from 4 kΩ/sq. to 807 Ω/sq., the sample being constant at 1.4 kΩ/sq. after cooling – Figure 70 (b). This variation can be observed in Figure 70 (c) where the heating and cooling steps are distinguished. The measurement of the carrier density at the end of the process reveals that the carrier density has changed to n-type with a value of -3.42 x 10^{13} cm^{-2}.

It can be concluded that the poling effect on graphene doping is reversible and the graphene can be doped to both types by modifying the V_P applied.

5.5. Conclusions

We have demonstrated the possibility of altering graphene doping in a controlled and stable way by modifying the polarity of the dielectric substrate. By applying a well-known technique, called *thermal poling* of glass, we have been able to create a very stable electric field inside the glass, which, depending on the charge proximate to the graphene device, induces a different type of doping. We have provided the calibration of the thermal poling to the glass and when the graphene device was introduced. The duality of the graphene doping is possible by applying a positive and a negative external voltage to the glass, which induces p- and n-doping, respectively. We have shown the changes in doping after performing the poling in both cases (with positive and negative voltages) and also demonstrated the reversibility of the poling when the temperature is increased and the poling is erased. Future work will consider the isolation of Na charges on the cathode to enhance the poling effect and consequently the effect on the graphene doping. Another very promising aspect would be the partial erasing of the poling at the highest mobility and the checking of its stability over time.

6

Summary and outlook

The exceptional and unique properties of graphene make it a very promising material for a wide variety of applications, such as transparent electrodes, supercapacitors, flexible displays, touch-screens and wearables. The chemical vapor deposition (CVD) technique allows the growth of high quality graphene over large areas, typically on Cu foils. For its application in industry, transfer of the material from the foil to the target substrate is critical, especially for preserving the high quality of the graphene and leaving its properties unaltered. To this end, this thesis has investigated transfer, direct growth and doping alternatives, which enhance the graphene quality and contribute towards its future mass-scalable applications.

The main objectives and challenges associated with this thesis are summarized in the following figure, and the main outcomes are listed below:

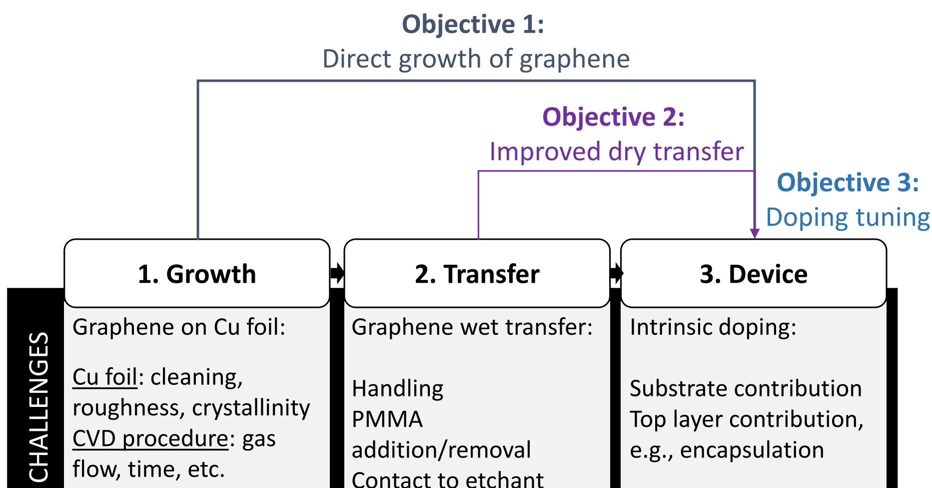

- **Direct growth of graphene on glass**. An investigation has been carried out into the direct growth of graphene on the dielectric target substrate with the removal of the intermediate and cumbersome transfer step. The use of a standard Cu foil catalyst was substituted with the deposition of a UTMF layer of Ni on top the substrate. The study covered a wide range of UTMF Ni layers (5-50 nm) that dewet at high temperatures, allowing the deposition of graphene onto the substrate, and the optimum conditions were found to be 50 nm of Ni at 700ºC. The lower temperature allows the direct growth of large areas of graphene or patterned graphene on substrates with low and high strain points, such as the flexible and thin Willow© glass and fused silica, respectively.

- **Direct growth of 2-D and 3-D carbon structures on glass**. Related to the direct growth of graphene, an innovative and versatile procedure has been developed to grow graphene under similar CVD conditions in a two-dimensional flat layer and, also, assembled into a three-dimensional shape. This second option increases the effective surface area of the material, and consequently, the potential applications. The achievement of these structures is possible by an easy and controllable tuning of the density of the catalytic Cu nanoparticles (NPs). The different arrangement of Cu NPs allows the production of two dimensional graphene networks, and three-dimensional graphene balls and sponge structures over large substrate areas without the need for lithography steps.

- **Transfer on glass using polyimide as intermediate layer**. Focusing on the issue related to the transfer of CVD graphene grown on a Cu foil, a novel technique has been demonstrated, which performs the dry transfer of the graphene onto flexible and rigid target substrates by mechanically peeling the Cu, thus allowing it to be recycled for future use. This is possible by means of an intermediate stable polyimide layer between the substrate and graphene that has a higher adhesion to graphene than the one between the graphene and the Cu foil. The transfer was carried out using two types of industrial equipment, a hot press and a laminator, with the former achieving higher quality graphene without much dependence on the roughness of the Cu foil. For the laminator, the graphene transfer was also successful, with a higher quality of graphene grown on the Cu foils with low roughness. This technique has been demonstrated to be fast, easy-handling and scalable, with the production of graphene devices with high transmittance, high resistance to bending, good stability with high temperatures (up to 350ºC without degradation), and high stability with aqueous media without delamination.

- **Doping through thermal poling of glass**. Finally, once the device had been fabricated and intrinsically doped by the contribution of, for example, the substrate or the top layer material used for encapsulation, the use of thermal poling to create an electric field in the glass was investigated, which was found to induce doping into the graphene device. The electric field created by the application of an external voltage displaced the charges of the glass, modifying the charge under the graphene device. The doping of graphene to n- and p-type was demonstrated, also showing the evolution of the carrier density when the poling effect was progressively removed.

Although this thesis has contributed to providing alternative solutions to the current issues related to the implementation of graphene on the large scale, for each technique developed here there remain aspects to be improved in order to achieve a real implementation. Future work should focus on the study of the electrical properties of devices fabricated with direct grown graphene (assembled into 2D and 3D structures), and the demonstration of application in plasmonics and membranes for the novel structures developed here, 3D-GB and 3D-GS, respectively. Moreover, the stability of the poling effect for a controlled tuning of graphene doping will be of great importance for the scientific community and for future applications.

Bibliography

1. K. S. Novoselov, A. K. Geim, S. V. Morozov, D. Jiang, Y. Zhang, S. V. Dubonos, I. V. Grigorieva, and A. A. Firsov, "Electric Field Effect in Atomically Thin Carbon Films," Science **306**(5696), 666–669 (2004).
2. A. K. Geim and K. S. Novoselov, "The rise of graphene," Nat. Mater. **6**(3), 183–191 (2007).
3. R. Peierls, *Quelques Propiétés Typiques Des Corps Solides*, Annales de l'I.H.P No. 3 (n.d.), **5**.
4. N. D. Mermin, "Crystalline Order in Two Dimensions," Phys. Rev. **176**(1), 250–254 (1968).
5. C. Lee, X. Wei, J. W. Kysar, and J. Hone, "Measurement of the elastic properties and intrinsic strength of monolayer graphene," Science **321**(5887), 385–388 (2008).
6. F. Liu, P. Ming, and J. Li, "Ab initio calculation of ideal strength and phonon instability of graphene under tension," Phys. Rev. B **76**(6), 064120 (2007).
7. K. Min and N. R. Aluru, "Mechanical properties of graphene under shear deformation," Appl. Phys. Lett. **98**(1), 013113 (2011).
8. L. Banszerus, M. Schmitz, S. Engels, J. Dauber, M. Oellers, F. Haupt, K. Watanabe, T. Taniguchi, B. Beschoten, and C. Stampfer, "Ultrahigh-mobility graphene devices from chemical vapor deposition on reusable copper," Sci. Adv. **1**(6), (2015).
9. A. A. Balandin, S. Ghosh, W. Bao, I. Calizo, D. Teweldebrhan, F. Miao, and C. N. Lau, "Superior Thermal Conductivity of Single-Layer Graphene," Nano Lett. **8**(3), 902–907 (2008).
10. A. Hashimoto, K. Suenaga, A. Gloter, K. Urita, and S. Iijima, "Direct evidence for atomic defects in graphene layers," Nature **430**(7002), 870–873 (2004).
11. J. Ma, D. Alfè, A. Michaelides, and E. Wang, "Stone-Wales defects in graphene and other planar s p 2 -bonded materials," Phys. Rev. B **80**(3), (2009).
12. F. Banhart, J. Kotakoski, and A. V. Krasheninnikov, "Structural Defects in Graphene," ACS Nano **5**(1), 26–41 (2011).
13. F. Bonaccorso, Z. Sun, T. Hasan, and A. C. Ferrari, "Graphene photonics and optoelectronics," Nat. Photonics **4**(9), 611–622 (2010).
14. A. H. Castro Neto, F. Guinea, N. M. R. Peres, K. S. Novoselov, and A. K. Geim, "The electronic properties of graphene," Rev. Mod. Phys. **81**(1), 109–162 (2009).
15. L. Jiao, L. Zhang, X. Wang, G. Diankov, and H. Dai, "Narrow graphene nanoribbons from carbon nanotubes," Nature **458**(7240), 877–880 (2009).
16. L. Wang, I. Meric, P. Y. Huang, Q. Gao, Y. Gao, H. Tran, T. Taniguchi, K. Watanabe, L. M. Campos, D. A. Muller, J. Guo, P. Kim, J. Hone, K. L. Shepard, and C. R. Dean, "One-Dimensional Electrical Contact to a Two-Dimensional Material," Science **342**(6158), 614–617 (2013).
17. F. Molitor, J. Güttinger, C. Stampfer, S. Dröscher, A. Jacobsen, T. Ihn, and K. Ensslin, "Electronic properties of graphene nanostructures," J. Phys. Condens. Matter **23**(24), 243201 (2011).

18. M. C. Lemme, T. J. Echtermeyer, M. Baus, and H. Kurz, "A Graphene Field-Effect Device," IEEE Electron Device Lett. **28**(4), 282–284 (2007).
19. X. Du, I. Skachko, F. Duerr, A. Luican, and E. Y. Andrei, "Fractional quantum Hall effect and insulating phase of Dirac electrons in graphene," Nature **462**(7270), 192–195 (2009).
20. G. W. Ludwig and R. L. Watters, "Drift and Conductivity Mobility in Silicon," Phys. Rev. **101**(6), 1699–1701 (1956).
21. P. Gaubert and A. Teramoto, "Carrier Mobility in Field-Effect Transistors," Differ. Types Field-Eff. Transistors - Theory Appl. (2017).
22. C. Dimitrakopoulos, Y.-M. Lin, A. Grill, D. B. Farmer, M. Freitag, Y. Sun, S.-J. Han, Z. Chen, K. A. Jenkins, Y. Zhu, Z. Liu, T. J. McArdle, J. A. Ott, R. Wisnieff, and P. Avouris, "Wafer-scale epitaxial graphene growth on the Si-face of hexagonal SiC (0001) for high frequency transistors," J. Vac. Sci. Technol. B Nanotechnol. Microelectron. Mater. Process. Meas. Phenom. **28**(5), 985–992 (2010).
23. H. Xu, Z. Zhang, R. Shi, H. Liu, Z. Wang, S. Wang, and L.-M. Peng, "Batch-fabricated high-performance graphene Hall elements," Sci. Rep. **3**, (2013).
24. N. W. Ashcroft and N. Mermin, *Solid State Physics* (Brooks/Cole, 1976).
25. X. Li, G. Zhang, X. Bai, X. Sun, X. Wang, E. Wang, and H. Dai, "Highly conducting graphene sheets and Langmuir–Blodgett films," Nat. Nanotechnol. **3**(9), 538–542 (2008).
26. A. B. Bourlinos, V. Georgakilas, R. Zboril, T. A. Steriotis, and A. K. Stubos, "Liquid-Phase Exfoliation of Graphite Towards Solubilized Graphenes," Small **5**(16), 1841–1845 (2009).
27. X. Geng, Y. Guo, D. Li, W. Li, C. Zhu, X. Wei, M. Chen, S. Gao, S. Qiu, Y. Gong, L. Wu, M. Long, M. Sun, G. Pan, and L. Liu, "Interlayer catalytic exfoliation realizing scalable production of large-size pristine few-layer graphene," Sci. Rep. **3**, 1134 (2013).
28. M. Lotya, P. J. King, U. Khan, S. De, and J. N. Coleman, "High-Concentration, Surfactant-Stabilized Graphene Dispersions," ACS Nano **4**(6), 3155–3162 (2010).
29. C.-Y. Su, A.-Y. Lu, Y. Xu, F.-R. Chen, A. N. Khlobystov, and L.-J. Li, "High-Quality Thin Graphene Films from Fast Electrochemical Exfoliation," ACS Nano **5**(3), 2332–2339 (2011).
30. Y. Hernandez, V. Nicolosi, M. Lotya, F. M. Blighe, Z. Sun, S. De, I. T. McGovern, B. Holland, M. Byrne, Y. K. Gun'Ko, J. J. Boland, P. Niraj, G. Duesberg, S. Krishnamurthy, R. Goodhue, J. Hutchison, V. Scardaci, A. C. Ferrari, and J. N. Coleman, "High-yield production of graphene by liquid-phase exfoliation of graphite," Nat. Nanotechnol. **3**(9), 563–568 (2008).
31. V. C. Tung, M. J. Allen, Y. Yang, and R. B. Kaner, "High-throughput solution processing of large-scale graphene," Nat. Nanotechnol. **4**(1), 25–29 (2009).
32. H. Chen, M. B. Müller, K. J. Gilmore, G. G. Wallace, and D. Li, "Mechanically Strong, Electrically Conductive, and Biocompatible Graphene Paper," Adv. Mater. **20**(18), 3557–3561 (2008).
33. S. Stankovich, D. A. Dikin, R. D. Piner, K. A. Kohlhaas, A. Kleinhammes, Y. Jia, Y. Wu, S. T. Nguyen, and R. S. Ruoff, "Synthesis of graphene-based nanosheets via chemical reduction of exfoliated graphite oxide," Carbon **45**(7), 1558–1565 (2007).
34. W. Lee, J. U. Lee, J. Yi, S.-B. Lee, J.-H. Byun, and B.-S. Kim, "Graphene paper which reduced graphene oxide layers and coating layers are stacked in sequence and

preparation method thereof," United States patent US20130065060A1 (March 14, 2013).

35. S. Wang, P. K. Ang, Z. Wang, A. L. L. Tang, J. T. L. Thong, and K. P. Loh, "High Mobility, Printable, and Solution-Processed Graphene Electronics," Nano Lett. **10**(1), 92–98 (2010).
36. A. Al-Temimy, C. Riedl, and U. Starke, "Low temperature growth of epitaxial graphene on SiC induced by carbon evaporation," Appl. Phys. Lett. **95**(23), 231907 (2009).
37. W. A. de Heer and C. Berger, "Electronic confinement and coherence in patterned epitaxial graphene," J. Phys. Appl. Phys. **45**(15), 150301 (2012).
38. "Graphene Supermarket :: 2. Research Materials :: 12. Graphene on Silicon Carbide (SiC) :: Monolayer Graphene on SiC substrate (Epitaxially grown)," https://graphene-supermarket.com/Graphene-Film-on-SiC.html.
39. X. Li, W. Cai, J. An, S. Kim, J. Nah, D. Yang, R. Piner, A. Velamakanni, I. Jung, E. Tutuc, S. K. Banerjee, L. Colombo, and R. S. Ruoff, "Large-Area Synthesis of High-Quality and Uniform Graphene Films on Copper Foils," Science **324**(5932), 1312–1314 (2009).
40. S. Bae, H. Kim, Y. Lee, X. Xu, J.-S. Park, Y. Zheng, J. Balakrishnan, T. Lei, H. Ri Kim, Y. I. Song, Y.-J. Kim, K. S. Kim, B. Özyilmaz, J.-H. Ahn, B. H. Hong, and S. Iijima, "Roll-to-roll production of 30-inch graphene films for transparent electrodes," Nat. Nanotechnol. **5**(8), 574–578 (2010).
41. H. Kim, I. Song, C. Park, M. Son, M. Hong, Y. Kim, J. S. Kim, H.-J. Shin, J. Baik, and H. C. Choi, "Copper-Vapor-Assisted Chemical Vapor Deposition for High-Quality and Metal-Free Single-Layer Graphene on Amorphous SiO_2 Substrate," ACS Nano **7**(8), 6575–6582 (2013).
42. X. Li, L. Colombo, and R. S. Ruoff, "Synthesis of Graphene Films on Copper Foils by Chemical Vapor Deposition," Adv. Mater. **28**(29), 6247–6252 (2016).
43. I. Vlassiouk, P. Fulvio, H. Meyer, N. Lavrik, S. Dai, P. Datskos, and S. Smirnov, "Large scale atmospheric pressure chemical vapor deposition of graphene," Carbon **54**, 58–67 (2013).
44. C. Mattevi, H. Kim, and M. Chhowalla, "A review of chemical vapour deposition of graphene on copper," J Mater Chem **21**(10), 3324–3334 (2011).
45. A. Ismach, C. Druzgalski, S. Penwell, A. Schwartzberg, M. Zheng, A. Javey, J. Bokor, and Y. Zhang, "Direct Chemical Vapor Deposition of Graphene on Dielectric Surfaces," Nano Lett. **10**(5), 1542–1548 (2010).
46. S. J. Chae, F. Güneş, K. K. Kim, E. S. Kim, G. H. Han, S. M. Kim, H.-J. Shin, S.-M. Yoon, J.-Y. Choi, M. H. Park, C. W. Yang, D. Pribat, and Y. H. Lee, "Synthesis of Large-Area Graphene Layers on Poly-Nickel Substrate by Chemical Vapor Deposition: Wrinkle Formation," Adv. Mater. **21**(22), 2328–2333 (2009).
47. J. Lahiri, T. S. Miller, A. J. Ross, L. Adamska, I. I. Oleynik, and M. Batzill, "Graphene growth and stability at nickel surfaces," New J. Phys. **13**(2), 025001 (2011).
48. C.-M. Seah, S.-P. Chai, and A. R. Mohamed, "Mechanisms of graphene growth by chemical vapour deposition on transition metals," Carbon **70**, 1–21 (2014).
49. A. Delamoreanu, C. Rabot, C. Vallee, and A. Zenasni, "Wafer scale catalytic growth of graphene on nickel by solid carbon source," Carbon **66**, 48–56 (2014).

50. Y. Yao, Z. Li, Z. Lin, K.-S. Moon, J. Agar, and C. Wong, "Controlled Growth of Multilayer, Few-Layer, and Single-Layer Graphene on Metal Substrates," J. Phys. Chem. C **115**(13), 5232–5238 (2011).
51. R. S. Edwards and K. S. Coleman, "Graphene Film Growth on Polycrystalline Metals," Acc. Chem. Res. **46**(1), 23–30 (2013).
52. A. Earnshaw; T. J. Harrington., *Chemistry of the Transition Elements*, Oxford University Press (1972).
53. P. Sutter, M. S. Hybertsen, J. T. Sadowski, and E. Sutter, "Electronic Structure of Few-Layer Epitaxial Graphene on Ru(0001)," Nano Lett. **9**(7), 2654–2660 (2009).
54. J. H. Warner, F. Schaffel, M. Rummeli, and A. Bachmatiuk, *Graphene: Fundamentals and Emergent Applications* (Newnes, 2012).
55. K.-J. Peng, C.-L. Wu, Y.-H. Lin, Y.-J. Liu, D.-P. Tsai, Y.-H. Pai, and G.-R. Lin, "Hydrogen-free PECVD growth of few-layer graphene on an ultra-thin nickel film at the threshold dissolution temperature," J. Mater. Chem. C **1**(24), 3862–3870 (2013).
56. Y. Zhang, L. Zhang, and C. Zhou, "Review of Chemical Vapor Deposition of Graphene and Related Applications," Acc. Chem. Res. **46**(10), 2329–2339 (2013).
57. Q. Yu, J. Lian, S. Siriponglert, H. Li, Y. P. Chen, and S.-S. Pei, "Graphene segregated on Ni surfaces and transferred to insulators," Appl. Phys. Lett. **93**(11), 113103 (2008).
58. A. Reina, X. Jia, J. Ho, D. Nezich, H. Son, V. Bulovic, M. S. Dresselhaus, and J. Kong, "Large Area, Few-Layer Graphene Films on Arbitrary Substrates by Chemical Vapor Deposition," Nano Lett. **9**(1), 30–35 (2009).
59. D. Q. McNerny, B. Viswanath, D. Copic, F. R. Laye, C. Prohoda, A. C. Brieland-Shoultz, E. S. Polsen, N. T. Dee, V. S. Veerasamy, and A. J. Hart, "Direct fabrication of graphene on SiO_2 enabled by thin film stress engineering," Sci. Rep. **4**, 5049 (2014).
60. R. Addou, A. Dahal, P. Sutter, and M. Batzill, "Monolayer graphene growth on Ni(111) by low temperature chemical vapor deposition," Appl. Phys. Lett. **100**(2), 021601 (2012).
61. A. Dahal and M. Batzill, "Graphene–nickel interfaces: a review," Nanoscale **6**(5), 2548–2562 (2014).
62. S. Thiele, A. Reina, P. Healey, J. Kedzierski, P. Wyatt, P.-L. Hsu, C. Keast, J. Schaefer, and J. Kong, "Engineering polycrystalline Ni films to improve thickness uniformity of the chemical-vapor-deposition-grown graphene films," Nanotechnology **21**(1), 015601 (2010).
63. K. P. Sharma, S. M. Shinde, M. S. Rosmi, S. Sharma, G. Kalita, and M. Tanemura, "Effect of copper foil annealing process on large graphene domain growth by solid source-based chemical vapor deposition," J. Mater. Sci. **51**(15), 7220–7228 (2016).
64. L. Gao, J. R. Guest, and N. P. Guisinger, "Epitaxial Graphene on Cu(111)," Nano Lett. **10**(9), 3512–3516 (2010).
65. O. Frank, J. Vejpravova, V. Holy, L. Kavan, and M. Kalbac, "Interaction between graphene and copper substrate: The role of lattice orientation," Carbon **68**, 440–451 (2014).
66. Y. Zhang, L. Gomez, F. N. Ishikawa, A. Madaria, K. Ryu, C. Wang, A. Badmaev, and C. Zhou, "Comparison of Graphene Growth on Single-Crystalline and Polycrystalline Ni by Chemical Vapor Deposition," J. Phys. Chem. Lett. **1**(20), 3101–3107 (2010).
67. H. Ago, Y. Ito, N. Mizuta, K. Yoshida, B. Hu, C. M. Orofeo, M. Tsuji, K. Ikeda, and S. Mizuno, "Epitaxial Chemical Vapor Deposition Growth of Single-Layer Graphene over Cobalt Film Crystallized on Sapphire," ACS Nano **4**(12), 7407–7414 (2010).

68. "Alfa Aesar," https://www.alfa.com/en/search/?q=copper+foil.
69. K. Kim, Z. Lee, W. Regan, C. Kisielowski, M. F. Crommie, and A. Zettl, "Grain Boundary Mapping in Polycrystalline Graphene," ACS Nano **5**(3), 2142–2146 (2011).
70. X. Li, C. W. Magnuson, A. Venugopal, J. An, J. W. Suk, B. Han, M. Borysiak, W. Cai, A. Velamakanni, Y. Zhu, L. Fu, E. M. Vogel, E. Voelkl, L. Colombo, and R. S. Ruoff, "Graphene Films with Large Domain Size by a Two-Step Chemical Vapor Deposition Process," Nano Lett. **10**(11), 4328–4334 (2010).
71. Z. Luo, Y. Lu, D. W. Singer, M. E. Berck, L. A. Somers, B. R. Goldsmith, and A. T. C. Johnson, "Effect of Substrate Roughness and Feedstock Concentration on Growth of Wafer-Scale Graphene at Atmospheric Pressure," Chem. Mater. **23**(6), 1441–1447 (2011).
72. S. Bhaviripudi, X. Jia, M. S. Dresselhaus, and J. Kong, "Role of Kinetic Factors in Chemical Vapor Deposition Synthesis of Uniform Large Area Graphene Using Copper Catalyst," Nano Lett. **10**(10), 4128–4133 (2010).
73. D. Geng, B. Wu, Y. Guo, L. Huang, Y. Xue, J. Chen, G. Yu, L. Jiang, W. Hu, and Y. Liu, "Uniform hexagonal graphene flakes and films grown on liquid copper surface," Proc. Natl. Acad. Sci. **109**(21), 7992–7996 (2012).
74. E. O. Polat, O. Balci, N. Kakenov, H. B. Uzlu, C. Kocabas, and R. Dahiya, "Synthesis of Large Area Graphene for High Performance in Flexible Optoelectronic Devices," Sci. Rep. **5**, 16744 (2015).
75. A. Umair and H. Raza, "Controlled synthesis of bilayer graphene on nickel," Nanoscale Res. Lett. **7**(1), 437 (2012).
76. L. D'Arsié, S. Esconjauregui, R. S. Weatherup, X. Wu, W. E. Arter, H. Sugime, C. Cepek, and J. Robertson, "Stable, efficient p-type doping of graphene by nitric acid," RSC Adv. **6**(114), 113185–113192 (2016).
77. T. O. Wehling, K. S. Novoselov, S. V. Morozov, E. E. Vdovin, M. I. Katsnelson, A. K. Geim, and A. I. Lichtenstein, "Molecular Doping of Graphene," Nano Lett. **8**(1), 173–177 (2008).
78. H. Liu, Y. Liu, and D. Zhu, "Chemical doping of graphene," J. Mater. Chem. **21**(10), 3335–3345 (2011).
79. Y. Shi, K. K. Kim, A. Reina, M. Hofmann, L.-J. Li, and J. Kong, "Work Function Engineering of Graphene Electrode *via* Chemical Doping," ACS Nano **4**(5), 2689–2694 (2010).
80. H. Park, J. A. Rowehl, K. K. Kim, V. Bulovic, and J. Kong, "Doped graphene electrodes for organic solar cells," Nanotechnology **21**(50), 505204 (2010).
81. D. Wei, Y. Liu, Y. Wang, H. Zhang, L. Huang, and G. Yu, "Synthesis of N-Doped Graphene by Chemical Vapor Deposition and Its Electrical Properties," Nano Lett. **9**(5), 1752–1758 (2009).
82. E. Velez-Fort, C. Mathieu, E. Pallecchi, M. Pigneur, M. G. Silly, R. Belkhou, M. Marangolo, A. Shukla, F. Sirotti, and A. Ouerghi, "Epitaxial Graphene on 4H-SiC(0001) Grown under Nitrogen Flux: Evidence of Low Nitrogen Doping and High Charge Transfer," ACS Nano **6**(12), 10893–10900 (2012).
83. L. S. Panchakarla, K. S. Subrahmanyam, S. K. Saha, A. Govindaraj, H. R. Krishnamurthy, U. V. Waghmare, and C. N. R. Rao, "Synthesis, Structure, and Properties of Boron- and Nitrogen-Doped Graphene," Adv. Mater. **21**(46), 4726–4730 (2009).

84. I. Meric, C. Dean, A. Young, J. Hone, P. Kim, and K. L. Shepard, "Graphene field-effect transistors based on boron nitride gate dielectrics," in (IEEE, 2010), pp. 23.2.1-23.2.4.
85. F. Schwierz, "Graphene transistors," Nat. Nanotechnol. **5**(7), 487–496 (2010).
86. A. Reina, H. Son, L. Jiao, B. Fan, M. S. Dresselhaus, Z. Liu, and J. Kong, "Transferring and Identification of Single- and Few-Layer Graphene on Arbitrary Substrates," J. Phys. Chem. C **112**(46), 17741–17744 (2008).
87. K. S. Kim, Y. Zhao, H. Jang, S. Y. Lee, J. M. Kim, K. S. Kim, J.-H. Ahn, P. Kim, J.-Y. Choi, and B. H. Hong, "Large-scale pattern growth of graphene films for stretchable transparent electrodes," Nature **457**(7230), 706–710 (2009).
88. X. Li, Y. Zhu, W. Cai, M. Borysiak, B. Han, D. Chen, R. D. Piner, L. Colombo, and R. S. Ruoff, "Transfer of Large-Area Graphene Films for High-Performance Transparent Conductive Electrodes," Nano Lett. **9**(12), 4359–4363 (2009).
89. J. Kang, D. Shin, S. Bae, and B. H. Hong, "Graphene transfer: key for applications," Nanoscale **4**(18), 5527–5537 (2012).
90. J. Song, F.-Y. Kam, R.-Q. Png, W.-L. Seah, J.-M. Zhuo, G.-K. Lim, P. K. H. Ho, and L.-L. Chua, "A general method for transferring graphene onto soft surfaces," Nat. Nanotechnol. **8**(5), 356–362 (2013).
91. U. J. Kim, J. Hur, S. Cheon, D.-Y. Chung, H. Son, Y. Park, Y.-G. Roh, J. Kim, J. Lee, S. W. Kim, K. Im, N. Park, J. Kim, S. Hwang, W. Park, and C.-W. Lee, "Enhancement of integrity of graphene transferred by interface energy modulation," Carbon **65**, 165–174 (2013).
92. J. W. Suk, A. Kitt, C. W. Magnuson, Y. Hao, S. Ahmed, J. An, A. K. Swan, B. B. Goldberg, and R. S. Ruoff, "Transfer of CVD-Grown Monolayer Graphene onto Arbitrary Substrates," ACS Nano **5**(9), 6916–6924 (2011).
93. A. Pirkle, J. Chan, A. Venugopal, D. Hinojos, C. W. Magnuson, S. McDonnell, L. Colombo, E. M. Vogel, R. S. Ruoff, and R. M. Wallace, "The effect of chemical residues on the physical and electrical properties of chemical vapor deposited graphene transferred to SiO_2," Appl. Phys. Lett. **99**(12), 122108 (2011).
94. L. Gao, G.-X. Ni, Y. Liu, B. Liu, A. H. Castro Neto, and K. P. Loh, "Face-to-face transfer of wafer-scale graphene films," Nature **505**(7482), 190–194 (2014).
95. T. Hallam, N. C.Berner, Y. Chanyoung, and G. S. Duesberg, "Strain, Bubbles, Dirt, and Folds: A Study of Graphene Polymer-Assisted Transfer," Adv. Mater. Interfaces **1**, (2014).
96. Y.-C. Lin, C.-C. Lu, C.-H. Yeh, C. Jin, K. Suenaga, and P.-W. Chiu, "Graphene Annealing: How Clean Can It Be?," Nano Lett. **12**(1), 414–419 (2012).
97. L. Gammelgaard, J. M. Caridad, A. Cagliani, D. M. A. Mackenzie, D. H. Petersen, T. J. Booth, and P. Bøggild, "Graphene transport properties upon exposure to PMMA processing and heat treatments," 2D Mater. **1**(3), 035005 (2014).
98. W. Choi, M. A. Shehzad, S. Park, and Y. Seo, "Influence of removing PMMA residues on surface of CVD graphene using a contact-mode atomic force microscope," RSC Adv. **7**(12), 6943–6949 (2017).
99. S. Tanaka, H. Goto, H. Tomori, Y. Ootuka, K. Tsukagoshi, and A. Kanda, "Effect of current annealing on electronic properties of multilayer graphene," J. Phys. Conf. Ser. **232**, 012015 (2010).

100. E. Pallecchi, F. Lafont, V. Cavaliere, F. Schopfer, D. Mailly, W. Poirier, and A. Ouerghi, "High Electron Mobility in Epitaxial Graphene on 4H-SiC(0001) via post-growth annealing under hydrogen," Sci. Rep. **4**, 4558 (2014).
101. Y. Wang, Y. Zheng, X. Xu, E. Dubuisson, Q. Bao, J. Lu, and K. P. Loh, "Electrochemical Delamination of CVD-Grown Graphene Film: Toward the Recyclable Use of Copper Catalyst," ACS Nano **5**(12), 9927–9933 (2011).
102. Y. Chen, X.-L. Gong, and J.-G. Gai, "Progress and Challenges in Transfer of Large-Area Graphene Films," Adv. Sci. **3**(8), (2016).
103. S.-H. Bae, X. Zhou, S. Kim, Y. S. Lee, S. S. Cruz, Y. Kim, J. B. Hannon, Y. Yang, D. K. Sadana, F. M. Ross, H. Park, and J. Kim, "Unveiling the carrier transport mechanism in epitaxial graphene for forming wafer-scale, single-domain graphene," Proc. Natl. Acad. Sci. U. S. A. **114**(16), 4082–4086 (2017).
104. A. Lafuma and D. Quéré, "Superhydrophobic states," Nat. Mater. **2**(7), 457–460 (2003).
105. G. Bracco and B. Holst, *Surface Science Techniques* (Springer, 2013).
106. G. Govindaraj and V. Devanathan, "Quantum size effect in thin metal films," Phys. Rev. B **34**(8), 5904–5906 (1986).
107. "Semiconductor Material and Device Characterization, 3rd Edition," https://www.wiley.com/en-us/Semiconductor+Material+and+Device+Characterization%2C+3rd+Edition-p-9780471739067.
108. I. K. Robinson and D. J. Tweet, "Surface X-ray diffraction," Rep. Prog. Phys. **55**(5), 599 (1992).
109. L. J. Van der Pauw, "A method of measuring the resistivity and Hall coefficient on Lamellae of Arbitrary shape," Philips Tech. Rev. (20), (1958).
110. R. R. Nair, P. Blake, A. N. Grigorenko, K. S. Novoselov, T. J. Booth, T. Stauber, N. M. R. Peres, and A. K. Geim, "Fine Structure Constant Defines Visual Transparency of Graphene," Science **320**(5881), 1308–1308 (2008).
111. A. C. Ferrari, J. C. Meyer, V. Scardaci, C. Casiraghi, M. Lazzeri, F. Mauri, S. Piscanec, D. Jiang, K. S. Novoselov, S. Roth, and A. K. Geim, "The Raman Fingerprint of Graphene," Phys. Rev. Lett. **97**(18), (2006).
112. A. C. Ferrari, J. C. Meyer, V. Scardaci, C. Casiraghi, M. Lazzeri, F. Mauri, S. Piscanec, D. Jiang, K. S. Novoselov, S. Roth, and A. K. Geim, "Raman Spectrum of Graphene and Graphene Layers," Phys. Rev. Lett. **97**(18), (2006).
113. A. Das, S. Pisana, B. Chakraborty, S. Piscanec, S. K. Saha, U. V. Waghmare, K. S. Novoselov, H. R. Krishnamurthy, A. K. Geim, A. C. Ferrari, and A. K. Sood, "Monitoring dopants by Raman scattering in an electrochemically top-gated graphene transistor," Nat. Nanotechnol. **3**(4), 210–215 (2008).
114. L. Donovan N., C. Gary W., and S. Supapan, *Scanning Electron Microscopy*, Characterization of Materials (2012).
115. A. C. Ferrari, F. Bonaccorso, V. Fal'ko, K. S. Novoselov, S. Roche, P. Bøggild, S. Borini, F. H. L. Koppens, V. Palermo, N. Pugno, J. A. Garrido, R. Sordan, A. Bianco, L. Ballerini, M. Prato, E. Lidorikis, J. Kivioja, C. Marinelli, T. Ryhänen, A. Morpurgo, J. N. Coleman, V. Nicolosi, L. Colombo, A. Fert, M. Garcia-Hernandez, A. Bachtold, G. F. Schneider, F. Guinea, C. Dekker, M. Barbone, Z. Sun, C. Galiotis, A. N. Grigorenko, G. Konstantatos, A. Kis, M. Katsnelson, L. Vandersypen, A. Loiseau, V. Morandi, D. Neumaier, E. Treossi, V. Pellegrini, M. Polini, A. Tredicucci, G. M.

Williams, B. Hee Hong, J.-H. Ahn, J. Min Kim, H. Zirath, B. J. van Wees, H. van der Zant, L. Occhipinti, A. Di Matteo, I. A. Kinloch, T. Seyller, E. Quesnel, X. Feng, K. Teo, N. Rupesinghe, P. Hakonen, S. R. T. Neil, Q. Tannock, T. Löfwander, and J. Kinaret, "Science and technology roadmap for graphene, related two-dimensional crystals, and hybrid systems," Nanoscale **7**(11), 4598–4810 (2015).

116. T. Minami, "Present status of transparent conducting oxide thin-film development for Indium-Tin-Oxide (ITO) substitutes," Thin Solid Films **516**(17), 5822–5828 (2008).
117. O. Inganäs, "Organic photovoltaics: Avoiding indium," Nat. Photonics **5**(4), 201–202 (2011).
118. D. S. Ghosh, *Ultrathin Metal Transparent Electrodes for the Optoelectronics Industry*, Springer Theses (Springer International Publishing, 2013).
119. S. Goossens, G. Navickaite, C. Monasterio, S. Gupta, J. J. Piqueras, R. Pérez, G. Burwell, I. Nikitskiy, T. Lasanta, T. Galán, E. Puma, A. Centeno, A. Pesquera, A. Zurutuza, G. Konstantatos, and F. Koppens, "Broadband image sensor array based on graphene–CMOS integration," Nat. Photonics **11**(6), 366–371 (2017).
120. A. D. Sanctis, G. F. Jones, D. J. Wehenkel, F. Bezares, F. H. L. Koppens, M. F. Craciun, and S. Russo, "Extraordinary linear dynamic range in laser-defined functionalized graphene photodetectors," Sci. Adv. **3**(5), e1602617 (2017).
121. S. Nanot, C. Peng, D. Efetov, M. Batzer, R. Parret, D. R. Englund, and F. H. L. Koppens, "Dual-gated graphene with ion gel gates as mid-infrared photodetectors," in *2016 41st International Conference on Infrared, Millimeter, and Terahertz Waves (IRMMW-THz)* (2016), pp. 1–1.
122. M. Liu, X. Yin, E. Ulin-Avila, B. Geng, T. Zentgraf, L. Ju, F. Wang, and X. Zhang, "A graphene-based broadband optical modulator," Nature **474**(7349), 64–67 (2011).
123. A. Y. Nikitin, P. Alonso-González, S. Vélez, S. Mastel, A. Centeno, A. Pesquera, A. Zurutuza, F. Casanova, L. E. Hueso, F. H. L. Koppens, and R. Hillenbrand, "Real-space mapping of tailored sheet and edge plasmons in graphene nanoresonators," Nat. Photonics **10**(4), 239–243 (2016).
124. G. Konstantatos, M. Badioli, L. Gaudreau, J. Osmond, M. Bernechea, F. P. G. de Arquer, F. Gatti, and F. H. L. Koppens, "Hybrid graphene–quantum dot phototransistors with ultrahigh gain," Nat. Nanotechnol. **7**(6), 363–368 (2012).
125. I. Nikitskiy, S. Goossens, D. Kufer, T. Lasanta, G. Navickaite, F. H. L. Koppens, and G. Konstantatos, "Integrating an electrically active colloidal quantum dot photodiode with a graphene phototransistor," Nat. Commun. **7**, 11954 (2016).
126. M. B. Lundeberg and F. Koppens, "Graphene plasmonics: From terahertz to mid-infrared in less than a micron," in *2016 41st International Conference on Infrared, Millimeter, and Terahertz Waves (IRMMW-THz)* (2016), pp. 1–2.
127. A. Woessner, Y. Gao, I. Torre, M. B. Lundeberg, C. Tan, K. Watanabe, T. Taniguchi, R. Hillenbrand, J. Hone, M. Polini, and F. H. L. Koppens, "Electrical 2π phase control of infrared light in a 350-nm footprint using graphene plasmons," Nat. Photonics **11**(7), 421–424 (2017).
128. D. Rodrigo, O. Limaj, D. Janner, D. Etezadi, F. J. García de Abajo, V. Pruneri, and H. Altuj, "Mid-infrared plasmonic biosensing with graphene | Science," Science **349**(6244), (2015).
129. Dankerl Markus, Hauf Moritz V., Lippert Andreas, Hess Lucas H., Birner Stefan, Sharp Ian D., Mahmood Ather, Mallet Pierre, Veuillen Jean-Yves, Stutzmann Martin,

and Garrido Jose A., "Graphene Solution-Gated Field-Effect Transistor Array for Sensing Applications," Adv. Funct. Mater. **20**(18), 3117–3124 (2010).

130. P. K. Ang, W. Chen, A. T. S. Wee, and K. P. Loh, "Solution-Gated Epitaxial Graphene as pH Sensor," J. Am. Chem. Soc. **130**(44), 14392–14393 (2008).
131. B. Lung-Hao Hu, F.-Y. Wu, C.-T. Lin, A. N. Khlobystov, and L.-J. Li, "Graphene-modified $LiFePO_4$ cathode for lithium ion battery beyond theoretical capacity," Nat. Commun. **4**, 1687 (2013).
132. S. Yang, X. Feng, S. Ivanovici, and K. Müllen, "Fabrication of graphene-encapsulated oxide nanoparticles: towards high-performance anode materials for lithium storage," Angew. Chem. Int. Ed Engl. **49**(45), 8408–8411 (2010).
133. X. Miao, S. Tongay, M. K. Petterson, K. Berke, A. G. Rinzler, B. R. Appleton, and A. F. Hebard, "High efficiency graphene solar cells by chemical doping," Nano Lett. **12**(6), 2745–2750 (2012).
134. J. Wu, M. Agrawal, H. A. Becerril, Z. Bao, Z. Liu, Y. Chen, and P. Peumans, "Organic light-emitting diodes on solution-processed graphene transparent electrodes," ACS Nano **4**(1), 43–48 (2010).
135. B. Z. Jang and A. Zhamu, "Nano graphene platelet-based conductive inks," United States patent US20100000441A1 (January 7, 2010).
136. R. Murphy, O. Rozhin, A. C. Ferrari, J. Robertson, and W. I. Milne, "Methods and systems for creating a material with nanomaterials," United States patent US20070275230A1 (November 29, 2007).
137. F. Torrisi, T. HASAN, F. Bonaccorso, and A. C. FERRARI, "Functional inks based on layered materials and printed layered materials," World Intellectual Property Organization patent WO2014064432A1 (May 1, 2014).
138. "Science and technology roadmap for graphene, related two-dimensional crystals, and hybrid systems - Nanoscale (RSC Publishing)," http://pubs.rsc.org.recursos.biblioteca.upc.edu/en/content/articlelanding/2015/nr/c4nr01600a#!divAbstract.
139. "Global Science & Technology Report: Graphene Research & Development | CAS," https://www.cas.org/resources/whitepapers/global-science-technology-report-graphene-research-development.
140. "Graphene Flagship | Graphene Flagship," https://graphene-flagship.eu/.
141. T. Kaplas, D. Sharma, and Y. Svirko, "Few-layer graphene synthesis on a dielectric substrate," Carbon **50**(4), 1503–1509 (2012).
142. C.-Y. Su, A.-Y. Lu, C.-Y. Wu, Y.-T. Li, K.-K. Liu, W. Zhang, S.-Y. Lin, Z.-Y. Juang, Y.-L. Zhong, F.-R. Chen, and L.-J. Li, "Direct Formation of Wafer Scale Graphene Thin Layers on Insulating Substrates by Chemical Vapor Deposition," Nano Lett. **11**(9), 3612–3616 (2011).
143. J. Kwak, J. H. Chu, J.-K. Choi, S.-D. Park, H. Go, S. Y. Kim, K. Park, S.-D. Kim, Y.-W. Kim, E. Yoon, S. Kodambaka, and S.-Y. Kwon, "Near room-temperature synthesis of transfer-free graphene films," Nat. Commun. **3**, 645 (2012).
144. K. Gumi, Y. Ohno, K. Maehashi, K. Inoue, and K. Matsumoto, "Direct Synthesis of Graphene on SiO2 Substrates by Transfer-Free Processes," Jpn. J. Appl. Phys. **51**(6S), 06FD12 (2012).
145. J. Chen, Y. Guo, L. Jiang, Z. Xu, L. Huang, Y. Xue, D. Geng, B. Wu, W. Hu, G. Yu, and Y. Liu, "Near-Equilibrium Chemical Vapor Deposition of High-Quality Single-

Crystal Graphene Directly on Various Dielectric Substrates," Adv. Mater. **26**(9), 1348–1353 (2014).
146. M. Kosaka, S. Takano, K. Hasegawa, and S. Noda, "Direct synthesis of few- and multi-layer graphene films on dielectric substrates by “etching-precipitation” method," Carbon **82**, 254–263 (2015).
147. J. Sun, Y. Chen, M. K. Priydarshi, Z. Chen, A. Bachmatiuk, Z. Zou, Z. Chen, X. Song, Y. Gao, M. H. Rümmeli, Y. Zhang, and Z. Liu, "Direct Chemical Vapor Deposition-Derived Graphene Glasses Targeting Wide Ranged Applications," Nano Lett. **15**(9), 5846–5854 (2015).
148. D. Wei, Y. Lu, C. Han, T. Niu, W. Chen, and A. T. S. Wee, "Critical Crystal Growth of Graphene on Dielectric Substrates at Low Temperature for Electronic Devices," Angew. Chem. Int. Ed. **52**(52), 14121–14126 (2013).
149. J. Sun, Y. Chen, X. Cai, B. Ma, Z. Chen, M. K. Priydarshi, K. Chen, T. Gao, X. Song, Q. Ji, X. Guo, D. Zou, Y. Zhang, and Z. Liu, "Direct low-temperature synthesis of graphene on various glasses by plasma-enhanced chemical vapor deposition for versatile, cost-effective electrodes," Nano Res. **8**(11), 3496–3504 (2015).
150. H. Wang and G. Yu, "Direct CVD Graphene Growth on Semiconductors and Dielectrics for Transfer-Free Device Fabrication," Adv. Mater. **28**(25), 4956–4975 (2016).
151. V. P. Pham, H.-S. Jang, D. Whang, and J.-Y. Choi, "Direct growth of graphene on rigid and flexible substrates: progress, applications, and challenges," Chem. Soc. Rev. **46**(20), 6276–6300 (2017).
152. L. Guo, Z. Zhang, H. Sun, D. Dai, J. Cui, M. Li, Y. Xu, M. Xu, Y. Du, N. Jiang, F. Huang, and C.-T. Lin, "Direct formation of wafer-scale single-layer graphene films on the rough surface substrate by PECVD," Carbon **129**, 456–461 (2018).
153. D. Gentili, G. Foschi, F. Valle, M. Cavallini, and F. Biscarini, "Applications of dewetting in micro and nanotechnology," Chem. Soc. Rev. **41**(12), 4430–4443 (2012).
154. M. Todeschini, A. Bastos da Silva Fanta, F. Jensen, J. B. Wagner, and A. Han, "Influence of Ti and Cr Adhesion Layers on Ultrathin Au Films," ACS Appl. Mater. Interfaces **9**(42), 37374–37385 (2017).
155. C. V. Thompson, "Solid-State Dewetting of Thin Films," Annu. Rev. Mater. Res. **42**(1), 399–434 (2012).
156. J. Mizsei, "Activating technology of SnO2 layer by metal particles from ultrathin metal films," Sensors and Actuators B: Chemical **16**, (1993).
157. M. Chhowalla, K. B. K. Teo, C. Ducati, N. L. Rupesinghe, G. A. J. Amaratunga, A. C. Ferrari, D. Roy, J. Robertson, and W. I. Milne, "Growth process conditions of vertically aligned carbon nanotubes using plasma enhanced chemical vapor deposition," J. Appl. Phys. **90**(10), 5308–5317 (2001).
158. V. Schmidt, J. V. Wittemann, S. Senz, and U. Gösele, "Silicon Nanowires: A Review on Aspects of their Growth and their Electrical Properties," Adv. Mater. **21**(25–26), 2681–2702 (2009).
159. J.-H. Chen, T.-F. Lei, D. Landheer, X. Wu, J. Liu, and T.-S. Chao, "Si Nanocrystal Memory Devices Self-Assembled by In Situ Rapid Thermal Annealing of Ultrathin a -Si on SiO2," Electrochem. Solid-State Lett. **10**(10), H302–H304 (2007).
160. P. R. Gadkari, A. P. Warren, R. M. Todi, R. V. Petrova, and K. R. Coffey, "Comparison of the agglomeration behavior of thin metallic films on SiO2," J. Vac. Sci. Technol. Vac. Surf. Films **23**(4), 1152–1161 (2005).

161. L. Baraton, Z. B. He, C. S. Lee, C. S. Cojocaru, M. Châtelet, J.-L. Maurice, Y. H. Lee, and D. Pribat, "On the mechanisms of precipitation of graphene on nickel thin films," EPL Europhys. Lett. **96**(4), 46003 (2011).
162. L. L. Patera, C. Africh, R. S. Weatherup, R. Blume, S. Bhardwaj, C. Castellarin-Cudia, A. Knop-Gericke, R. Schloegl, G. Comelli, S. Hofmann, and C. Cepek, "In Situ Observations of the Atomistic Mechanisms of Ni Catalyzed Low Temperature Graphene Growth," ACS Nano **7**(9), 7901–7912 (2013).
163. J. Yoo, S. P. Patole, and H. Lee, "Method for fabricating three dimensional graphene structures using catalyst templates," United States patent US8663593B2 (March 4, 2014).
164. R. C. Weast, D. R. Lide, and U. of R. I. C. R. Center, *CRC Handbook of Chemistry and Physics* (Cleveland, Ohio : CRC Press, 1978).
165. S. Garner, S. Glaesemann, and X. Li, "Ultra-slim flexible glass for roll-to-roll electronic device fabrication," Appl. Phys. A **116**(2), 403–407 (2014).
166. Y. Shen, Q. Fang, and B. Chen, "Environmental Applications of Three-Dimensional Graphene-Based Macrostructures: Adsorption, Transformation, and Detection," Environ. Sci. Technol. **49**(1), 67–84 (2015).
167. P. M. Sudeep, T. N. Narayanan, A. Ganesan, M. M. Shaijumon, H. Yang, S. Ozden, P. K. Patra, M. Pasquali, R. Vajtai, S. Ganguli, A. K. Roy, M. R. Anantharaman, and P. M. Ajayan, "Covalently Interconnected Three-Dimensional Graphene Oxide Solids," ACS Nano **7**(8), 7034–7040 (2013).
168. Y. Xu, K. Sheng, C. Li, and G. Shi, "Self-Assembled Graphene Hydrogel *via* a One-Step Hydrothermal Process," ACS Nano **4**(7), 4324–4330 (2010).
169. X. Cao, Z. Yin, and H. Zhang, "Three-dimensional graphene materials: preparation, structures and application in supercapacitors," Energy Env. Sci **7**(6), 1850–1865 (2014).
170. M. Xiao, T. Kong, W. Wang, Q. Song, D. Zhang, Q. Ma, and G. Cheng, "Interconnected Graphene Networks with Uniform Geometry for Flexible Conductors," Adv. Funct. Mater. **25**(39), 6165–6172 (2015).
171. Z. Chen, W. Ren, L. Gao, B. Liu, S. Pei, and H.-M. Cheng, "Three-dimensional flexible and conductive interconnected graphene networks grown by chemical vapour deposition," Nat. Mater. **10**(6), 424–428 (2011).
172. Y. Xu, G. Shi, and X. Duan, "Self-Assembled Three-Dimensional Graphene Macrostructures: Synthesis and Applications in Supercapacitors," Acc. Chem. Res. **48**(6), 1666–1675 (2015).
173. N. Li, Q. Zhang, S. Gao, Q. Song, R. Huang, L. Wang, L. Liu, J. Dai, M. Tang, and G. Cheng, "Three-dimensional graphene foam as a biocompatible and conductive scaffold for neural stem cells," Sci. Rep. **3**, 1604 (2013).
174. K. Yu, P. Wang, G. Lu, K.-H. Chen, Z. Bo, and J. Chen, "Patterning Vertically Oriented Graphene Sheets for Nanodevice Applications," J. Phys. Chem. Lett. **2**(6), 537–542 (2011).
175. S. Mao, K. Yu, J. Chang, D. A. Steeber, L. E. Ocola, and J. Chen, "Direct Growth of Vertically-oriented Graphene for Field-Effect Transistor Biosensor," Sci. Rep. **3**, 1696 (2013).
176. X. H. Xia, D. L. Chao, Y. Q. Zhang, Z. X. Shen, and H. J. Fan, "Three-dimensional graphene and their integrated electrodes," Nano Today **9**(6), 785–807 (2014).

177. Y. Ma and Y. Chen, "Three-dimensional graphene networks: synthesis, properties and applications," Natl. Sci. Rev. **2**(1), 40–53 (2015).
178. S. Mao, G. Lu, and J. Chen, "Three-dimensional graphene-based composites for energy applications," Nanoscale **7**(16), 6924–6943 (2015).
179. J.-S. Lee, S.-I. Kim, J.-C. Yoon, and J.-H. Jang, "Chemical Vapor Deposition of Mesoporous Graphene Nanoballs for Supercapacitor," ACS Nano **7**(7), 6047–6055 (2013).
180. S. Lee, J. Hong, J. H. Koo, H. Lee, S. Lee, T. Choi, H. Jung, B. Koo, J. Park, H. Kim, Y.-W. Kim, and T. Lee, "Synthesis of Few-Layered Graphene Nanoballs with Copper Cores Using Solid Carbon Source," ACS Appl. Mater. Interfaces **5**(7), 2432–2437 (2013).
181. A. Eckmann, A. Felten, A. Mishchenko, L. Britnell, R. Krupke, K. S. Novoselov, and C. Casiraghi, "Probing the Nature of Defects in Graphene by Raman Spectroscopy," Nano Lett. **12**(8), 3925–3930 (2012).
182. Y. Ahn, H. Kim, Y.-H. Kim, Y. Yi, and S.-I. Kim, "Procedure of removing polymer residues and its influences on electronic and structural characteristics of graphene," Appl. Phys. Lett. **102**(9), 091602 (2013).
183. T. Yoon, W. C. Shin, T. Y. Kim, J. H. Mun, T.-S. Kim, and B. J. Cho, "Direct Measurement of Adhesion Energy of Monolayer Graphene As-Grown on Copper and Its Application to Renewable Transfer Process," Nano Lett. **12**(3), 1448–1452 (2012).
184. S. R. Na, J. W. Suk, L. Tao, D. Akinwande, R. S. Ruoff, R. Huang, and K. M. Liechti, "Selective Mechanical Transfer of Graphene from Seed Copper Foil Using Rate Effects," ACS Nano **9**(2), 1325–1335 (2015).
185. T. L. Chen, D. S. Ghosh, M. Marchena, J. Osmond, and V. Pruneri, "Nanopatterned Graphene on a Polymer Substrate by a Direct Peel-off Technique," ACS Appl. Mater. Interfaces **7**(10), 5938–5943 (2015).
186. C.-S. Chen and C.-K. Hsieh, "An easy, low-cost method to transfer large-scale graphene onto polyethylene terephthalate as a transparent conductive flexible substrate," Thin Solid Films **570**, 595–598 (2014).
187. M. H. Kang, L. O. Prieto López, B. Chen, K. Teo, J. A. Williams, W. I. Milne, and M. T. Cole, "Mechanical Robustness of Graphene on Flexible Transparent Substrates," ACS Appl. Mater. Interfaces **8**(34), 22506–22515 (2016).
188. G. J. M. Fechine, I. Martin-Fernandez, G. Yiapanis, R. Bentini, E. S. Kulkarni, R. V. Bof de Oliveira, X. Hu, I. Yarovsky, A. H. Castro Neto, and B. Özyilmaz, "Direct dry transfer of chemical vapor deposition graphene to polymeric substrates," Carbon **83**, 224–231 (2015).
189. J. R. Klaehn, C. J. Orme, E. S. Peterson, F. F. Stewart, and J. M. Urban-Klaehn, "Chapter 13 - High Temperature Gas Separations Using High Performance Polymers," in *Membrane Science and Technology*, S. T. Oyama and S. M. Stagg-Williams, eds., Inorganic Polymeric and Composite Membranes (Elsevier, 2011), **14**, pp. 295–307.
190. "Genesis Hydraulic Compression Presses from Wabash," https://www.wabashmpi.com/products/compression-presses/four-post-presses/genesis-press.

191. W.-C. Liaw, Y.-L. Cheng, Y.-S. Liao, C.-S. Chen, and S.-M. Lai, "Complementary functionality of SiO_2 and TiO_2 in polyimide/silica–titania ternary hybrid nanocomposites," Polym. J. **43**(3), 249–257 (2011).
192. I.-H. Tseng, Y.-F. Liao, J.-C. Chiang, and M.-H. Tsai, "Transparent polyimide/graphene oxide nanocomposite with improved moisture barrier property," Mater. Chem. Phys. **136**(1), 247–253 (2012).
193. M. D. Hanwell, D. E. Curtis, D. C. Lonie, T. Vandermeersch, E. Zurek, and G. R. Hutchison, "Avogadro: an advanced semantic chemical editor, visualization, and analysis platform," J. Cheminformatics **4**, 17 (2012).
194. Z. Fang, Y. Wang, Z. Liu, A. Schlather, P. M. Ajayan, F. H. L. Koppens, P. Nordlander, and N. J. Halas, "Plasmon-Induced Doping of Graphene," ACS Nano **6**(11), 10222–10228 (2012).
195. D. Yudistira, D. Faccio, C. Corbari, P. G. Kazansky, S. Benchabane, and V. Pruneri, "Electric surface potential and frozen-in field direct measurements in thermally poled silica," Appl. Phys. Lett. **92**(1), 012912 (2008).
196. R. A. Myers, N. Mukherjee, and S. R. J. Brueck, "Large second-order nonlinearity in poled fused silica," Opt. Lett. **16**(22), 1732–1734 (1991).
197. P. G. Kazansky and P. S. J. Russel, "Thermally poled glass: frozen-in electric field or oriented dipoles?," Opt. Commun. **110**(5), 611–614 (1994).
198. H. Mehrer, A. W. Imre, and E. Tanguep-Nijokep, "Diffusion and ionic conduction in oxide glasses," J. Phys. Conf. Ser. **106**(1), 012001 (2008).
199. A. Paradisi, "Ultra-high carrier modulation in two dimensions through space charge doping : graphene and zinc oxide," phdthesis, Université Pierre et Marie Curie - Paris VI (2016).
200. A. L. C. Triques, C. M. B. Cordeiro, V. Balestrieri, B. Lesche, W. Margulis, and I. C. S. Carvalho, "Depletion region in thermally poled fused silica," Appl. Phys. Lett. **76**(18), 2496–2498 (2000).
201. A. L. R. Brennand, "Thermal poling of multioxide silicate glasses and ion-exchanged waveguides," phd, University of Southampton (2002).
202. T. G. Alley, S. R. J. Brueck, and R. A. Myers, "Space charge dynamics in thermally poled fused silica," J. Non-Cryst. Solids **242**(2), 165–176 (1998).
203. H. Takebe, P. G. Kazansky, and P. S. J. Russell, "Effect of poling conditions on second harmonic generation in fused silica," Opt. Lett. **21**(7), 468–470 (1996).
204. F. C. Garcia, I. C. S. Carvalho, E. Hering, W. Margulis, and B. Lesche, "Inducing a large second-order optical nonlinearity in soft glasses by poling," Appl. Phys. Lett. **72**(25), 3252–3254 (1998).
205. M. Dussauze, E. Fargin, M. Lahaye, V. Rodriguez, and F. Adamietz, "Large second-harmonic generation of thermally poled sodium borophosphate glasses," Opt. Express **13**(11), 4064–4069 (2005).
206. E. Franchina, C. Corbari, P. G. Kazansky, N. Chiodini, A. Lauria, and A. Paleari, "Oxygen-deficiency effect on thermal poling of silica-based glasses," Solid State Commun. **136**(5), 300–303 (2005).
207. O. Deparis, P. G. Kazansky, A. Podlipensky, A. Abdolvand, G. Seifert, and H. Graener, "Poling-assisted bleaching of soda-lime float glasses containing silver nanoparticles with a decreasing filling factor across the depth," J. Appl. Phys. **100**(4), 044318 (2006).

208. H. An and S. Fleming, "Second-order optical nonlinearity and accompanying near-surface structural modifications in thermally poled soda-lime silicate glasses," JOSA B **23**(11), 2303–2309 (2006).
209. M. Dussauze, E. Fargin, V. Rodriguez, A. Malakho, and E. Kamitsos, "Enhanced Raman scattering in thermally poled sodium-niobium borophosphate glasses," J. Appl. Phys. **101**(8), 083532 (2007).
210. M. Dussauze, V. Rodriguez, A. Lipovskii, M. Petrov, C. Smith, K. Richardson, T. Cardinal, E. Fargin, and E. I. Kamitsos, "How Does Thermal Poling Affect the Structure of Soda-Lime Glass?," J. Phys. Chem. C **114**(29), 12754–12759 (2010).
211. A. V. Redkov, V. G. Melehin, V. V. Statcenko, and A. A. Lipovskii, "Nanoprofiling of alkali-silicate glasses by thermal poling," J. Non-Cryst. Solids **409**, 166–169 (2015).
212. A. Lepicard, T. Cardinal, E. Fargin, F. Adamietz, V. Rodriguez, K. Richardson, and M. Dussauze, "Surface Reactivity Control of a Borosilicate Glass Using Thermal Poling," J. Phys. Chem. C **119**(40), 22999–23007 (2015).
213. A. N. Kamenskii, I. V. Reduto, V. D. Petrikov, and A. A. Lipovskii, "Effective diffraction gratings via acidic etching of thermally poled glass," Opt. Mater. **62**, 250–254 (2016).
214. Luo Jiawei, He Hongtu, Podraza Nikolas J., Qian Linmao, Pantano Carlo G., Kim Seong H., and Mauro J., "Thermal Poling of Soda-Lime Silica Glass with Nonblocking Electrodes—Part 1: Effects of Sodium Ion Migration and Water Ingress on Glass Surface Structure," J. Am. Ceram. Soc. **99**(4), 1221–1230 (2016).
215. T. Weckman and K. Laasonen, "First principles study of the atomic layer deposition of alumina by TMA–H2O-process," Phys. Chem. Chem. Phys. **17**(26), 17322–17334 (2015).
216. S. Kim, J. Nah, I. Jo, D. Shahrjerdi, L. Colombo, Z. Yao, E. Tutuc, and S. K. Banerjee, "Realization of a high mobility dual-gated graphene field-effect transistor with Al2O3 dielectric," Appl. Phys. Lett. **94**(6), (2009).
217. L. Skuja and B. Güttler, "Detection of Interstitial Oxygen Molecules in Si O 2 Glass by a Direct Photoexcitation of the Infrared Luminescence of Singlet O 2," Phys. Rev. Lett. **77**(10), 2093–2096 (1996).